Title

Input-output formulation of quantum light spectroscopy and its application to study photosynthetic complexes

Author

Ko, Liwen J.

Publication Date

2024

Peer reviewed|Thesis/dissertation

Input-output formulation of quantum light spectroscopy and its application to study photosynthetic complexes

by

Liwen J. Ko

A dissertation submitted in partial satisfaction of the
requirements for the degree of
Doctor of Philosophy
in
Chemistry
in the Graduate Division
of the
University of California, Berkeley

Committee in charge:
Professor K. Birgitta Whaley, Chair
Professor Hartmut Haeffner
Professor Graham R. Fleming

Summer 2024

Abstract

Input-output formulation of quantum light spectroscopy and
its application to study photosynthetic complexes

by

Liwen J. Ko

Doctor of Philosophy in Chemistry

University of California, Berkeley

Professor K. Birgitta Whaley, Chair

Due to recent technological advances in the generation, manipulation, and detection of non-classical light, quantum light spectroscopy has gained attention as a candidate for expanding the current capabilities of classical laser light spectroscopy. In this dissertation, I develop an input-output formulation of quantum light spectroscopy by combining the input-output theory, traditionally used in the quantum optics community, with the perturbative expansion method for nonliear spectroscopy, traditionally used in the chemical physics community. Using this new spectroscopic formalism, we show that the optical signal in a class of quantum light spectroscopy experiments can be emulated by classical laser spectroscopy experiments. This class of quantum light spectroscopy experiments uses $n = 0, 1, 2, \cdots$ classical light pulses and an entangled photon pair (a biphoton state) where one photon acts as a reference without interacting with the matter sample.

To model the interaction between non-classical light and photosynthetic light harvesting systems, we develop a method to simulate the excitonic dynamics coupled to non-Markovian phonon degrees of freedom and to an N-photon Fock state pulse. This method combines the input-output and the hierarchical equations of motion (HEOM) formalisms into a double hierarchy of density matrix equations. We show analytically that, under weak field excitation relevant to natural photosynthesis conditions, an N-photon Fock state input and a corresponding coherent state input give rise to equal density matrices in the excited manifold. However, an N-photon Fock state input induces no off-diagonal coherence between the ground and excited subspaces, in contrast with the coherences created by a coherent state input. Detailed analysis of the absorption and emission behavior are discussed.

Contents

Preface

The potential of quantum light spectroscopy

Due to recent technological advances in the generation, manipulation, and detection of non-classical light, non-classical properties of light, such as photon antibunching [1–5], entanglement [6–10], squeezing [11–15], or Hong-Ou-Mandel interference [16–20], have become commonly observed in the laboratory. Researchers have exploited, or have proposed to exploit, these non-classical properties in various applications, such as quantum computation [21–23], enhancing the detection of gravitational waves [24, 25], imaging [2, 26, 27], x-ray diffraction [28], optical lithography [29], and molecular spectroscopy [30, 31].

In particular, quantum light spectroscopy aims to enhance or surpass traditional spectroscopy experiments that use classical-like coherent state laser light. This can be done either by probing the matter systems with non-classical light or by detecting the non-classical properties of the emitted light. For example, entangled photon pairs can be used to perform sub-shot-noise absorption spectroscopy [32], to excite doubly excited states with high spectral specificity [33], or to act as an analog of two-dimensional electronic spectroscopy [34]. They have also been claimed to increase the probability of two-photon absorption [35,36]. Squeezed light can be used as a low-noise light source for spectroscopy [37,38]. The second order coherence function $g^{(2)}(\tau)$ of the fluorescent light has been claimed to reveal information about the quantum coherence and the transient dynamics in the matter system [3,39–42].

The study of the energy transfer dynamics in natural photosynthetic complexes is a field that can potentially benefit from quantum light spectroscopy. Classical laser spectroscopy experiments, together with x-ray diffraction studies, have revealed much information about the structure and the ultrafast (100 fs to ps timescale) energy transfer dynamics of these complexes [43, 44]. However, due to the large number of pigments in each protein-pigment complex, the electronic interaction between the pigments, and the complex protein environment, experimental analysis and theoretical simulation tend to be very difficult. The experimental spectra can be highly congested, and there are often many different interpretations of the same spectra. This is because the interpretation of spectra often relies on theoretical simulations, which are based on various simplifying assumptions. Depending on the specific assumptions and the level of theory, different energy transfer dynamics and different simulated spectra can be obtained for the same system. Due to these difficulties, many important questions in the field are still left without consensus. For example: "what is the microscopic mechanism for the high transfer efficiency?", "whether quantum coherence plays a role in the high efficiency?", "is the condition of ultrafast spectroscopy representative of the nature condition under sunlight?", or "how do the excitons move in space and time?". New experimental tools and theoretical methods are needed to understand the energy transfer dynamics in greater detail and hopefully answer some of these questions. The recently developed two-dimensional electronic-vibrational spectroscopy (2DEV) has greatly expanded the possibilities of classical spectroscopy by resolving the electronic state in both the visible and the infrared dimensions [45]. Quantum light spectroscopy is another potential tool that

can further our understanding of photosynthetic energy transfer dynamics. For example, an entangled photon pair can have the time-frequency uncertainty $\Delta(t_1 - t_2)\Delta(\omega_1 + \omega_2)$ be as small as possible, while for classical light pulses, this uncertainty has to be greater than an $\mathcal{O}(1)$ constant because of the Fourier transform limit and the lack of correlation between the pulses. These entangled photons could help understand the energy transfer dynamics with higher energy and time resolution. Detecting the $g^{(2)}$ intensity correlation function of emitted light could provide a new dimension of information, as demonstrated theoretically in [39–42].

My PhD scientific journey

I did my undergraduate study also at UC Berkeley. My first undergraduate research project was to synthesize molecular catalysts for electrochemical reduction of carbon dioxide and for photochemical reduction of water into hydrogen gas. There I was introduced to the concept of energy transfer and electron transfer in molecules, and I learned about the various chemical factors affecting these reaction rates. After more than a year, I decided to switch field to do research in theoretical chemistry because of difficult and unsuccessful reactions as well as my realization that my interest lies perhaps more in mathematics and physics than in experimental chemistry. I found a research opportunity in Birgitta Whaley's group, where I studied the nonlinear spectroscopy of one-dimensional array of strongly coupled chromophores. This is when I was first exposed to the perturbative formalism for nonlinear spectroscopy, developed by Mukamel [46].

After I finished my undergraduate degree in 2018, I continued my PhD study with Birgitta. I was assigned the project of simulating the energy transfer dynamics under a single photon Fock state excitation. This project was coupled to experiments performed in Graham Fleming's group. Understanding the interaction between photosynthetic complexes and a single photon was an initial step to understand the interaction with other types of non-classical light. To treat the effect of both phonons and Fock state photons simultaneously, Robert Cook, the postdoc wrote down the double hierarchical equations by simply merging the Fock state master equations [47] with the hierarchical equations of motion (HEOM) [48, 49]. These double hierarchical equations turned out to be correct, but at the time, it was not clear to us whether these equations were indeed correct, although they looked very reasonable. To derive the double hierarchical equations rigorously, I started to learn about the derivation of the Fock state master equation and the HEOM. Working through these derivations carefully helped me later on to develop variations of the commonly used overdamped HEOM [49] and to develop the input-output formulation for quantum light spectroscopy.

The Fock state master equation [47] was first derived using the language of quantum stochastic differential equations (QSDE), which originate in the input-output theory developed in the 1980s [50, 51]. I found the QSDE formalism quite mathematical. In my attempt to find a way to understand it intuitively, I realized one can express many results in QSDE using ordinary calculus, and that the results can also be derived using ordinary calculus. The ordinary calculus corresponds to the Stratonovich form of QSDE, which is more physically intuitive. In QSDE, one often works in the Ito form, which is mathematically more convenient, so one usually has to convert a Stratonovich QSDE into an Ito QSDE using some formula. Working in ordinary calculus, I realized that, in some rough sense, the Ito QSDE corresponds to normal-ordered equations in ordinary calculus, and the Stratonovich QSDE corresponds to time-ordered equations in ordinary calculus. The conversion between the Stratonovich form and the Ito form can be done alternatively in the language of ordinary calculus by using the commutator identity $[a(t), U(t)] = \frac{1}{2}LU(t)$ (see Eq. (5.16)), where $a(t)$ is the field annihilation operator, L is proportional to the system dipole operator, and $U(t)$ is the time evolution operator. This insight helped me later on to recast the perturbative expansion of the reduced system state, usually expressed in a time-ordered form, as a normal-ordered expansion (see Ch. 5).

After showing the correctness of the double hierarchical equations describing the excitonic dynamics of light harvesting systems under the influences from both phonons and Fock state photons, I started to study the equations numerically and to study the analytical properties of these equations. One important result is that under weak light-matter coupling strength, Fock state excitation is quite similar to the classical-like coherent state excitation, giving rise to the same dynamics within the matter excited states. This is due to the fact that given the same temporal profile, a Fock state pulse has the same two-point correlation function as a coherent state pulse. The similarity between Fock states and coherent states is a theme that would come up again, when I later showed the equivalence between a class of quantum light spectroscopy and classical light spectroscopy. The similarity between Fock states and coherent states in the weak-coupling regime is not particularly well-known in the atomic physics and quantum optics community, but it is perhaps more well-known in the chemical physics community [36]. I suspect that this is because in atomic physics and quantum optics, the experiments are more commonly done in the intermediate- to strong-coupling regime, whereas in chemical physics, the experiments are typically done in the weak-coupling perturbative regime.

In 2022, after the theory of single photon excitation [52, 53] and the complementary experiment with heralded single photon [54] had been completed, we started to discuss with Graham Fleming's group about what type of experiment to do next. In the chemical physics literature, there were many theoretical proposals of using quantum light to perform nonlinear spectroscopy on molecular systems [16, 55–58], due to the recent interest in exploring the use of quantum light. The theoretical analysis in these studies used the perturbative formalism for quantum light spectroscopy [30,31], which is an extension of the perturbative formalism for classical nonlinear spectroscopy [46]. In reading these paper, I would try to understand the analysis from the perspective of the input-output theory, which I had become familiar with. I would later develop these connections between the input-output theory and the perturbative formalism into the input-output formulation of quantum light spectroscopy, which is the main part of my thesis.

At that time, it had become clear to the experimentalists in the Fleming group that experiments involving two single photons interacting with the sample were beyond their experimental capabilities, since the probability for two photons interacting with a single molecule is very small. The probability is orders of magnitude smaller than the small probability for a single photon interacting with a single molecule, which is already at most on the order of $\sim 10^{-6}$ [52,59]. So we turned to a theoretical proposal [56] using a classical pump and a heralded single photon probe. The classical pump containing a large number of photons is supposed to increase the absorption probability, thereby increasing the signal strength. We read the paper to try to understand the advantage it could offer. Working through its derivation, I realized that the optical signal can be equivalently obtained by replacing the heralded single photon with a coherent state (i.e., laser light) probe pulse containing one photon on average. Furthermore, using not just a coherent state containing one photon on average, but a coherent state containing a large number of photons, the signal strength can be enhanced further. We then generalized this equivalence to show that a large class of quantum light spectroscopy experiments can be emulated by classical light spectroscopy experiments [60].

In my PhD career, I have also contributed to the study of vibrationally assisted energy transfer (VAET) [61, 62], quantum trajectory of energy transport in photosynthesis [53], and quantum algorithm for ab initio simulation of nonlinear spectroscopy [63]. A brief discussion of these works and my contribution is given at the end of the thesis.

Introduction

The materials in Ch. 1, 2, 3, and 5 are adapted from [64], to be published. The materials in Ch. 4 are adapted from [60]. The materials in Ch. 6 and 7 are adapted from [52].

Part I: A new input-output formalism to study quantum light spectroscopy

A popular theoretical framework to study the interaction between quantum light and matter is the input-output theory, which is commonly used in the quantum optics community to study atoms or cavities interacting with a one-dimensional propagating photon field. The input-output formalism provides an exact expression, known as the input-output relation, that relates the input field to the output field. It also provides formally exact results for the master equation and the Heisenberg equation of motion of the system operators, known as the Heisenberg-Langevin equation [50, 51]. However, the exact formal results often need to be further simplified in a case-by-case basis. For example, the master equations of the matter system under the excitation of a coherent state [65], a thermal state [50], a squeezed state [50], and an m-photon Fock state [47] take different forms.

Another theoretical framework to treat the fully quantum light-matter interaction is the perturbative approach [30,31], which has found its use in the chemical physics community as a generalization of the perturbative formalism used for describing classical nonlinear spectroscopy [46]. In classical nonlinear spectroscopy, one perturbs just the matter state under the influence of a classical photon field, while in the generalization to quantum light spectroscopy, one perturbs the combined matter+field state [57, 66]. The perturbative framework is restricted to weak light-matter coupling, but it provides a unified method to treat the effects from all types of input photon states. This is because the effects from different orders of light-matter interaction appear as photon field correlation functions, which can be evaluated for all types of photon field states.

In Part I of the thesis, we develop a new input-output formulation of quantum light spectroscopy by combining the input-output theory, traditionally used in the quantum optics community, with the perturbative expansion method for nonliear spectroscopy, traditionally used in the chemical physics community. In the analysis of optical signals, we make use of the input-output relation and work in the Heisenberg picture, in contrast to the conventional perturbative formalism for quantum light spectroscopy that is derived in the interaction picture. The new input-output approach is more natural and provides a unified framework for analyzing the optical signal in both the perturbative and non-perturbative regimes.

Besides combining the input-output theory and the perturbative method, we also describe mathematical methods to perform normal-ordered perturbative expansions, both for the optical signal and for the reduced matter system state. In these normal-ordered expansions, the field operators

are always normal-ordered when their expectation values are evaluated. In comparison, in the conventional perturbative approach, the field operators are time-ordered, and they are in general not expressed in normal-ordered form. Photon coherence functions, as well as many standard results in quantum optics, are expressed in normal-ordered form [67], so expressing the perturbative expansions in normal-ordered form simplifies the calculation. We find that the normal-ordered expansion for the reduced system state provides insights to the coherent state master equation and the Fock state master equation. Given a coherent state input, the normal-ordered expansion allows us to see clearly that the quantum correction to the semi-classical master equation is the spontaneous emission effect [65]. Given an m-photon Fock state input, the normal-ordered expansion for the reduced system state truncates exactly at the $2m$-th order. Therefore, the $2m$-th order normal-ordered perturbative expansion becomes exact, regardless of the light-matter coupling strength. This result is closely related to the Fock state master equation [47]. These results are discussed in Ch. 5.

Now, we give an overview of Part I. Ch. 1 expands upon our previous work [52] to show how to rigorously describe the interaction between a matter system and the 3-dimensional photon field as the interaction between the matter system and a finite number of 1-dimensional photon field modes. We then derive the single-molecule and N-molecule Hamiltonians that will be used throughout the paper. Ch. 2 reviews the input-output relation examines several common spectroscopic setups. Through these examples, we demonstrate how the input-output formalism provides an intuitive method to analyze the optical signal. These results derived from the input-output relation hold in the general non-perturbative regime. However, for numerical evaluation, these formal results need to be further analyzed in a case-by-case basis depending on the input field state. To provide some correspondence between the quantum and the classical theories, we derive the classical version of the input-output relation using the macroscopic Maxwell's equations in Appendix B. In Ch. 3, we work in the weak-coupling regime and show how to perturbatively expand the input-output relation in the Heisenberg picture. The perturbative expansion provides a unified approach to treat all types of photon input states. We compare our input-output approach in the Heisenberg picture to the conventional perturbative approach in the interaction picture by analyzing the second order signal as an example. Ch. 4 applies the perturbative expansion of the input-output relation to show an equivalence between a class of quantum light spectroscopy experiments and a class of classical light spectroscopy experiments. In Ch. 5, we switch our focus from analyzing the optical signal in Heisenberg picture operators to analyzing the reduced system state in the interaction picture. There, we develop the normal-ordered expansion for the reduced system state.

We now highlight the key equations and sections. The input-output relation for N molecules and for a single molecule are summarized in Eqs. (2.5) and (2.6), respectively. Under the single molecule Hamiltonian (Eq. 1.32) or the N-molecule Hamiltonian (Eq. (1.33)), the input-output relations are exact results, regardless of the light-matter coupling strength. When the coupling is weak, the input-output relations are expanded perturbatively in Eq. (3.7) for the case of N molecules and in Eq. (3.8) for the case of a single molecule. Sec. 3.4 describes a procedure to enforce normal-ordering in the perturbative expansion of the Heisenberg picture operators. The normal-ordered expansion for the reduced system state is given in Eq. (5.32), which is then applied to a coherent state input and an m-photon Fock state input.

Part II: Simulating photosynthetic complexes interacting with quantum light

Exciton dynamics in natural photosynthetic systems have been studied extensively in recent years, using a range of theoretical techniques [49, 68–71]. Most of such studies assume that an initial excitation is present or created at some initial time. Behind this assumption is the implicit further assumption that light absorption and exciton transfer happen sequentially, while in reality they hap-

pen simultaneously. A related issue is that while it is well known that under weak light conditions natural photosynthetic systems have very high efficiency in utilizing absorbed photons to initiate charge transfer reactions in the reaction center [72], the probability to absorb incoming photons in the first place is seldom discussed and is not well characterised at the microscopic level. A number of publications have focused on the nature of exciton dynamics following incoherent thermal light excitation under continuous illumination [73–79]. These previous studies focused upon solving for the system's steady-state properties. In Part II of the thesis, we are interested in the non-equilibrium dynamics generated by the arrival of a definite photon. As a proxy for a randomly generated solar photon, our group has previously studied the absorption and exciton dynamics under excitation by pulses of weak coherent state light in the presence of a phonon bath [59]. The constraint of a finite pulse envelope gives the photon a notion of a well defined arrival time, in addition to being readily comparable to experiments.

In Part II of the thesis, we study the light excitation and subsequent exciton dynamics of a photosynthetic system under non-classical Fock state pulses including single photon pulses and contrast the behavior under this excitation with that under correspondingly weak coherent state pulses and under continuous illumination by incoherent light. We focus on the exciton system density matrix under the influences of both the photon and phonon environments, including a realistic treatment of the non-Markovian phonon bath. A related paper considers the dynamics of individual quantum trajectories post-selected on measuring emitted fluorescent photons [53].

Probing a light harvesting system with N-photon Fock state pulses has the advantage that, upon observing m outgoing photons, we can deduce (ignoring experimental imperfections) that the system has exactly $N - m$ excitons, due to the excitation conserving property of the total Hamiltonian. The coherent state laser pulses commonly used in experimental studies are superpositions of different photon number (Fock) states, so they do not allow for this type of precise knowledge about the state of the photosynthetic system.

A critical difference between the master equations for quantum systems interacting with Fock states and coherent states of light is that the influence of a Fock state on the system is non-Markovian [47], while the influence of a coherent state of light is Markovian [65] and can be treated by considering the system interacting with a classical electric field plus the quantum theory of spontaneous emission. Employing the input-output formalism [50,51], Baragiola et. al. [47] used the closely related quantum stochastic differential equation (QSDE) formalism to derive a set of Fock state master equations that propagate a physical density matrix coupled with a hierarchy of auxiliary density matrices. For completeness we present here an alternative derivation using the language of ordinary calculus to derive quantum Langevin equations in a more accessible formalism. A key fact that allows us to apply the input-output formalism to light harvesting systems interacting with the three-dimensional (3-d) electromagnetic field is that under the dipole approximation, the interaction with the 3-d electromagnetic field can be described as the interaction with a finite number of 1-d fields because the electric field operator is linear in the field bosonic operators.

To model the non-Markovian effects of the phonon bath, we employ here the hierarchical equations of motion (HEOM) [48]. When these are combined with the Fock state hierarchy, the final master equations for the excitonic density matrix take the form of a double hierarchical structure of linearly coupled differential equations. While numerically accurate, this comes at the cost of increased computational complexity. For a system with N chromophores interacting with a N_p-photon Fock state using the HEOM truncated at N_c cutoff levels, a set of $(N_p+1)^2(N+N_c)!/(N!N_c!)$ coupled density matrix equations need to be simultaneously solved. Because of this cost we limit our numerical studies here to consider the 14 site LHCII monomer, a 2 site dimer and a 7-site subsystem of LHCII considered previously [59]. We note that the original HEOM formalism [48] has since been generalized to treat systems interacting with multiple bosonic and fermionic baths [73, 80, 81], resulting in an equation of

motion consisting of multiple hierarchies. Our double hierarchy method differs from these approaches in that the photon degrees of freedom are treated in our work by the input-output formalism, not by the HEOM formalism. Indeed, due to the non-Gaussian correlations of N-photon Fock states, the photon degrees of freedom cannot be treated within the HEOM formalism.

In the interest of gaining important insights applicable also to larger systems, we additionally develop here analytical studies of the double hierarchy of equations in certain regimes. These studies focus primarily on the case of a single Fock state photon, since the analytical solution for the reduced exciton system state is most readily obtained where there is only one photon. A key result of our analysis is the demonstration in Section 7.1.3 that in the weak chromophore-light coupling limit (relevant to natural photosynthesis, since the intensity of natural sunlight is about 10^{-3} photons per second on a single chlorophyll molecule [72]), the chromophore system dynamics under the excitation of an N-photon Fock state bears a close relationship to the dynamics under the excitation of a single photon Fock state.

The analysis underlying this key result hinges on the natural separation of time scales between the exciton-exciton and exciton-phonon couplings, and the exciton-light dynamics. In natural photosynthetic systems, the exciton-light coupling is about 5-6 orders of magnitude weaker than the exciton-exciton or exciton-phonon couplings. Thus the spontaneous emission occurs at a much longer (ns) time scale than the exciton-exciton and exciton-phonon dynamics, both of which occur on sub-ps time scales. Because of this separation of time scales we can ignore the effect of spontaneous emission at short times. Under this approximation, we can solve the single photon Fock state master equation exactly. The solution is most easily obtained not by solving the non-Markovian Fock state master equations or the HEOM directly, but by considering the chromophore system, the vibrations coupled to this, and the optical field together as a pure state evolving according to the Schrödinger equation. Somewhat surprisingly, the solution to this equation is similar to the second order perturbative solution for a coherent state input. The only difference is that a Fock state input cannot induce any coherence between exciton system subspaces of different exciton number. The resulting solutions to the single photon Fock state master equations enable us to write down analytical expressions for the absorption probability and to understand its dependence on various parameters, most importantly, on pulse duration (or equivalently, inverse bandwidth). Due to the similarity between Fock state and coherent state input light, we can then further understand the coherent state absorption probability using the new Fock state absorption probability expressions.

At long times, the electronic excitation decays via spontaneous emission. Note that we do not include any additional non-radiative decay pathways from the excitonic manifold in the present model. We find that due to the steady state in the excitonic manifold with respect to the phonon bath, the exciton system dynamics follows a single exponential decay to the ground state, giving us a single well-defined decay constant at long times. It is sometimes assumed that the chromophores emit independently of one another (see e.g., [59]), but more rigorous treatment of the light-matter interaction [82] shows that the chromophores should emit collectively [83–85]. The collective emission rate can show enhancements ranging from 0 to N, the number of chromophores. We show that for natural photosynthetic systems the collective emission rates are usually very similar to the independent emission states, as a result of the non-uniform orientations of the dipole moments and the interaction with phonons.

Chapter 6 introduces the basics of the input-output formalism and provides a detailed modeling of the absorption and energy transport problem in the language of this formalism. Analytical solutions of the system+field pure state and system+vibration+field pure state are presented in Eqs. (6.38), (6.43b), (6.116), and (6.117). Our new double hierarchy method that combines the input-output formalism and the HEOM is presented in Eq. (6.138). These equations are used to derive the analytical results in Chapter 7. In Section 7.1 we discuss the similarities and differences between

excitation under a Fock state and excitation under a coherent state input optical fields (see Eqs. (7.1) - (7.4) and Fig. (7.3)), as well as the relationship of the dynamics under a single photon state and an N-photon Fock state (see Eq. (7.7) and Fig. (7.4)). Connections to excitation under incoherent thermal light are also discussed here. Section 7.2 analyzes the short time absorption probability and its dependence on the pulse duration and the presence or absence of exciton-phonon coupling. For short pulses, we show a universal behavior of the absorption probability (Eq. (7.29)) by defining an effective energy spread parameter Δ that characterizes the range of system energies. Fig. (7.6) illustrates this universal behavior. For long pulses, we analyze the absorption probabilities under several different parameter regimes (see Eqs. (7.35), (7.36), and (7.41)). Fig. (7.9) shows how the absorption probabilities transition from the short pulse regime to the long pulse regime. Section 7.3 analyzes the long time emission behavior in the presence of phonons. Analytical descriptions of the system dynamics at long times are given by Eqs. (7.46) and (7.47). Numerical examples in Sections 7.1-7.3 are given using dimeric and 7-mer chromophore systems from the LHCII monomer. In Section 7.4 we then describe a numerical simulation of the double hierarchy of equations describing the Fock state master equation + HEOM on the full LHCII monomer (14-mer) system. Finally in Section 7.5 we provide a summary and assessment.

Acknowledgement

This work was supported by the Photosynthetic Systems program of the U.S. Department of Energy, Office of Science, Basic Energy Sciences, within the Division of Chemical Sciences, Geosciences, and Biosciences, under Award No. DESC0019728. I was supported by the Kavli Energy NanoScience Institute (ENSI) Philomathia graduate fellowship. I was supported by the US Department of Energy, Office of Science, Office of Workforce Development for Teachers and Scientists, Office of Science Graduate Student Research (SCGSR) program. The SCGSR program is administered by the Oak Ridge Institute for Science and Education for the DOE under contract number DE-SC0014664.

I want to thank Birgitta Whaley for her scientific advices, and thank Robert Cook for the discussions that stimulated many ideas. I thank my family and my girlfriend for their love, support, and encouragement.

Part I

Input-output formulation of quantum light spectroscopy

Chapter 1

Quantum description of light-matter interaction

We take the dipole – electric field Hamiltonian as the fundamental Hamiltonian for light-matter interaction. The electric field is a 3-dimensional field, i.e., its degrees of freedom are indexed by the 3-dimensional real space or wavevector space coordinates. However, the conventional perturbative treatment of quantum light spectroscopy [30] and the input-output formalism [50,86] treat the photon field as 1-dimensional fields. The 1-dimensional field is usually considered as a model for plane wave photons or photons confined in an infinite cylinder with cross section area A. This picture is correct for photons in waveguides, but it is not a satisfactory description of photons in 3-dimensional space, as it does not properly account for all 3-dimensional degrees of freedom. To bridge this gap in the different descriptions of the photon field, we will show in Sec. 1.2 how to rigorously decompose the 3-dimensional electric field operator into a finite number of 1-dimensional fields. The Hamiltonian, on the other hand, is decomposed into an infinite number of 1-dimensional fields, but only a finite number of them couple to the matter degrees of freedom. In the discussion of the input-output formulation of quantum light spectroscopy, we use specifically the small solid angle decomposition. We study the small solid angle decomposition in detail in Sec. 1.3. We show that the decomposition to a finite number of 1-dimensional fields is valid only within an interaction region in real space. We also show that under the narrow-band approximation, the small solid angle modes resemble Gaussian beams in real space and time.

1.1 Total Hamiltonian with the dipole - electric field interaction

We take the combined matter system plus photon field Hamiltonian to be

$$H_{\text{sys+field}} = H_{\text{sys}} + H_{\text{field}} + H_{\text{coup}}, \tag{1.1}$$

where H_{sys}, H_{field}, and H_{coup} are the Hamiltonian for the matter system, the photon field, and the coupling between the matter system and the photon field. For molecular systems, H_{sys} would typically contain both the electronic and nuclear degrees of freedom. H_{field} is

$$H_{\text{field}} = \int d^3k \sum_{\lambda} \hbar c|\mathbf{k}| a^{\dagger}_{\mathbf{k},\lambda} a_{\mathbf{k},\lambda}, \tag{1.2}$$

where $\mathbf{k}$ is the three-dimensional wavevector, and λ indexes the two possible polarization corresponding to each $\mathbf{k}$. $\hbar$ and c are the reduced Planck constant and the speed of light, respectively. $a_{\mathbf{k},\lambda}$ and $a^\dagger_{\mathbf{k},\lambda}$ are the bosonic annihilation and creation operators for the field mode $(\mathbf{k}, \lambda)$, and they satisfy the bosonic commutation relations:

$$[a_{\mathbf{k},\lambda}, a_{\mathbf{k}',\lambda'}] = [a^\dagger_{\mathbf{k},\lambda}, a^\dagger_{\mathbf{k}',\lambda'}] = 0 \tag{1.3a}$$

and

$$[a_{\mathbf{k},\lambda}, a^\dagger_{\mathbf{k}',\lambda'}] = \delta(\mathbf{k} - \mathbf{k}')\delta_{\lambda,\lambda'}. \tag{1.3b}$$

For atomic or molecular systems, the size of the matter system is usually small compare to the wavelength of light it interacts with, so that the dipole approximation holds, and the coupling Hamiltonian H_{coup} takes the dipole – electric field form $H_{\text{coup}} = -\mathbf{d} \cdot \mathbf{E}(\mathbf{x})$, where $\mathbf{x}$ is the position of the matter system. The electric field operator $\mathbf{E}(\mathbf{x})$, expressed in terms of $a_{\mathbf{k},\lambda}$, is

$$\mathbf{E}(\mathbf{x}) = \int \frac{d^3\mathbf{k}}{(2\pi)^{3/2}} \sum_\lambda \sqrt{\frac{\hbar\omega}{2\epsilon_0}} (i a_{\mathbf{k},\lambda} e^{i\mathbf{k}\cdot\mathbf{x}} - i a^\dagger_{\mathbf{k},\lambda} e^{-i\mathbf{k}\cdot\mathbf{x}}) \hat{\mathbf{e}}_{\mathbf{k},\lambda}, \tag{1.4}$$

where ϵ_0 is the permittivity of free space and $\hat{\mathbf{e}}_{\mathbf{k},\lambda}$ is the unit vector in the direction of the polarization in the field mode $(\mathbf{k}, \lambda)$.

The electric field $\mathbf{E}(\mathbf{x})$ can be written as the sum $\mathbf{E}(\mathbf{x}) = \mathbf{E}^{(+)}(\mathbf{x}) + \mathbf{E}^{(-)}(\mathbf{x})$. The positive frequency component $\mathbf{E}^{(+)}(\mathbf{x})$ is the part that contains annihilation operators $a_{\mathbf{k},\lambda}$. The negative frequency component $\mathbf{E}^{(-)}(\mathbf{x})$ is the part that contains creation operators $a^\dagger_{\mathbf{k},\lambda}$. $\mathbf{E}^{(+)}(\mathbf{x})$ and $\mathbf{E}^{(-)}(\mathbf{x})$ are hermitian conjugates of each other. We also separate the matter dipole operator $\mathbf{d}$ into a excitation component $\mathbf{d}^{(+)}$ that creates an excitation in the matter and a de-excitation component $\mathbf{d}^{(-)}$ that removes an excitation in the matter, so that $\mathbf{d} = \mathbf{d}^{(+)} + \mathbf{d}^{(-)}$ and $\mathbf{d}^{(+)} = \mathbf{d}^{(-)\dagger}$. Under the rotating wave approximation, the total number of excitations is conserved, and the interaction term becomes

$$H_{\text{coup}} = -\mathbf{d}^{(+)} \cdot \mathbf{E}^{(+)}(\mathbf{x}) - \mathbf{d}^{(-)} \cdot \mathbf{E}^{(-)}(\mathbf{x}). \tag{1.5}$$

In spectroscopy experiments, the material sample usually consists of a large number of matter systems (e.g., atoms or molecules) that do not interact with one another. We will hereafter refer to the matter systems as molecules. In this case, the interaction term is a sum over all molecules, i.e.,

$$H_{\text{coup}} = \sum_{j=1}^{N} -\mathbf{d}_j^{(+)} \cdot \mathbf{E}^{(+)}(\mathbf{x}_j) - \mathbf{d}_j^{(-)} \cdot \mathbf{E}^{(-)}(\mathbf{x}_j), \tag{1.6}$$

where j indexes the N non-interacting molecules. $\mathbf{d}_j$ is the dipole operator for the j-th molecule, and $\mathbf{x}_j$ is the position of the j-th molecule.

1.2 Expressing the 3-dimensional photon field in terms of 1-dimensional fields

To decompose the 3-dimensional field operators $a_{\mathbf{k},\lambda}$ into 1-dimensional field operators, we first rewrite the multi-index $(\mathbf{k}, \lambda)$ as $(|\mathbf{k}|, \Omega, \lambda)$, where Ω is the orientation of $\mathbf{k}$. One can further expand Ω into a polar angle θ and an azimuthal angle ϕ, but we will use Ω for simplicity. The radial parameter $|\mathbf{k}|$ will be proportional to the 1-dimensional index. We will perform a change of basis to represent Ω and λ with a countably infinite set of basis functions $g_l(\Omega, \lambda)$, indexed by l.

We find a complete and orthonormal set of functions $g_l(\Omega, \lambda)$ such that

$$\int d\Omega \sum_{\lambda} g_l^*(\Omega, \lambda) g_{l'}(\Omega, \lambda) = \delta_{l,l'} \tag{1.7a}$$

and

$$\sum_{l=1}^{\infty} g_l^*(\Omega, \lambda) g_l(\Omega', \lambda') = \delta(\Omega - \Omega') \delta_{\lambda,\lambda'}. \tag{1.7b}$$

The integral over orientation $\int d\Omega$ can also be expressed as $\int_0^{\pi} d\theta \int_0^{2\pi} d\phi \sin\theta$. The delta function $\delta(\Omega - \Omega')$ can also be expressed as $\delta(\theta - \theta')\delta(\phi - \phi')/\sin\theta$.

Let the frequency ω be equal to $c|\mathbf{k}|$. The 1-dimensional field $a_l(\omega)$ is defined as

$$a_l(\omega) = \sqrt{\frac{\omega^2}{c^3}} \int d\Omega \sum_{\lambda} g_l(\Omega, \lambda) a_{|\mathbf{k}|,\Omega,\lambda}. \tag{1.8}$$

Using Eq. (1.7) and the delta-function identity $\delta(\mathbf{k} - \mathbf{k}') = \delta(|\mathbf{k}| - |\mathbf{k}'|)\delta(\Omega - \Omega')/|\mathbf{k}|^2$, one can show that the 1-dimensional field operators $a_l(\omega)$ satisfy the bosonic commutation relations:

$$[a_l(\omega), a_{l'}(\omega')] = [a_l^{\dagger}(\omega), a_{l'}^{\dagger}(\omega')] = 0 \tag{1.9a}$$

and

$$[a_l(\omega), a_{l'}^{\dagger}(\omega')] = \delta(\omega - \omega')\delta_{l,l'}. \tag{1.9b}$$

Now, with the use of the completeness relation (i.e., Eq. (1.7)), we can re-write H_{field} (Eq. (1.2) of the main text) in terms of the 1-dimensional fields $a_l(\omega)$ as

$$H_{\text{field}} = \sum_{l=1}^{\infty} \int_0^{\infty} d\omega \, \hbar\omega a_l^{\dagger}(\omega) a_l(\omega). \tag{1.10}$$

To re-write the electric field operator in terms of $a_l(\omega)$, we first re-write the integral $\int d^3k$ in Eq. (1.4) of the main text as $\frac{1}{c}\int d\omega \int d\Omega$. Then

$$\mathbf{E}(\mathbf{x} = \mathbf{0}) = \int_0^{\infty} d\omega \sqrt{\frac{\hbar\omega^3}{16\pi^3 c^3 \epsilon_0}} \sqrt{\frac{\omega^2}{c^3}} \int d\Omega \sum_{\lambda} i a_{|\mathbf{k}|,\Omega,\lambda} \hat{\mathbf{e}}_{|\mathbf{k}|,\Omega,\lambda} + \text{h.c.} \tag{1.11}$$

The abbreviation h.c. denotes the Hermitian conjugate of the previous term. We suppose there is a finite number $l_{\max}$ of real-valued mode functions $g_l(\Omega, \lambda)$ such that

$$\hat{\mathbf{e}}_{|\mathbf{k}|,\Omega,\lambda} = \sum_{l=1}^{l_{\max}} C_l g_l(\Omega, \lambda) \hat{\mathbf{e}}_l \tag{1.12}$$

for some constants C_l and unit vectors $\hat{\mathbf{e}}_l$. We will provide two examples of Eq. (1.12) shortly, corresponding to the polarization mode decomposition and the small solid angle mode decomposition [52]. Substituting Eq. (1.12) into Eq. (1.11) and using Eq. (1.8), we can now express $\mathbf{E}(\mathbf{x} = \mathbf{0})$ in terms of a finite number of 1-dimensional fields $a_l(\omega)$, i.e.,

$$\mathbf{E}(\mathbf{x} = \mathbf{0}) = \sum_{l=1}^{l_{\max}} C_l \int_0^{\infty} d\omega \sqrt{\frac{\hbar\omega^3}{16\pi^3 c^3 \epsilon_0}} i a_l(\omega) \hat{\mathbf{e}}_l + \text{h.c.} \tag{1.13}$$

This is the general form for writing $\mathbf{E}(\mathbf{x}=\mathbf{0})$ in terms of 1-dimensional fields $a_l(\omega)$. Depending on the choice of mode decomposition (i.e., Eqs. (1.7) and (1.12)), C_l and $\hat{\mathbf{e}}_l$ will be different. We now present two examples of Eq. (1.12), where the finitely many $g_l(\Omega,\lambda)$ are orthonormal to one another. From these finite number of orthonormal mode functions, it is then possible, in principle, to construct countably infinitely many more orthonormal $g_l(\Omega,\lambda)$ to form a complete set that satisfies Eq. (1.7b). We will not construct the complete set of $g_l(\Omega,\lambda)$ explicitly, since we are only interested in expressing the electric field using a finite number of modes.

In the polarization mode decomposition scheme, we decompose the electric field into three 1-dimensional fields, indexed by $l=x$, y, and z. The three 1-dimensional fields correspond to the three spatial components of the electric field. The mode functions are $g_l(\Omega,\lambda)=\hat{\epsilon}_l\cdot\hat{\epsilon}_{\Omega,\lambda}$. The mode unit vectors are $\hat{\epsilon}_x=\hat{x}$, $\hat{\epsilon}_y=\hat{y}$, and $\hat{\epsilon}_z=\hat{z}$. The constants are $C_l=\sqrt{\frac{3}{8\pi}}$. One can then check directly that Eq. (1.12) is satisfied and that g_x, g_y, and g_z are indeed orthonormal to one another (i.e., satisfying Eq. (1.7a)).

In the small solid angle decomposition scheme, we partition all possible orientations Ω into M number of small solid angle sections, indexed by m. Each small solid angle section can have two different polarizations, indexed by p (to be distinguished from λ in Eq. (1.12)). The index l in Eq. (1.12) is now a multi-index (m,p), and $l_{\max}=2M$. The mode functions $g_{m,p}$ are

$$g_{m,p}(\Omega,\lambda)=\begin{cases}\frac{1}{\sqrt{\Delta\Omega_m}} & ,\text{if } \Omega \text{ is in the solid angle section } m \text{ and } \lambda=p\\ 0 & ,\text{otherwise.}\end{cases} \tag{1.14}$$

$\Delta\Omega_m$ is the area of the solid angle section m. The mode unit vector $\hat{\mathbf{e}}_{(m,p)}$ is the unit vector of the p-th polarization in the m-th small solid angle section. Note that we have assumed that the small solid angle sections are small enough such that we can define two constant polarization unit vectors within each small solid angle section. The constants are $C_{m,p}=\sqrt{\Delta\Omega_m}$. One can check that Eq. (1.12) is satisfied and $g_{m,p}$ are orthonormal.

1.3 Small solid angle decomposition

Here, we focus specifically on the small solid angle decomposition and study the properties of the small solid angle modes. The small solid angle decomposition provides a natural description for quantum light spectroscopy experiments that excite, probe, or detect the matter sample in different directions.

As discussed in Sec. 1.2, the 4π solid angle for the orientation of $\mathbf{k}$ is partitioned into M small solid angle sections. Each small solid angle section contains two modes, corresponding to the two possible polarizations within each small solid angle section (see Fig. (1.1)). Therefore the electric field operator is described in terms of $2M$ 1-dimensional fields. Combining Eq. (1.8) and Eq. (1.14), the 1-dimensional field annihilation operator $a_l(\omega)$ is defined in terms of the 3-dimensional field annihilation operators as

$$a_l(\omega)=\sqrt{\frac{\omega^2}{c^3\Delta\Omega_l}}\int_{\Omega_l}d\Omega\, a_{|\mathbf{k}|=\omega/c,\Omega,\lambda}. \tag{1.15}$$

l indexes the $2M$ small solid angle modes. We have re-written the 3-dimensional field operator $a_{\mathbf{k},\lambda}$ as $a_{|\mathbf{k}|,\Omega,\lambda}$, where $|\mathbf{k}|$ is the magnitude of $\mathbf{k}$, and Ω is the orientation of $\mathbf{k}$. In the integrand $a_{|\mathbf{k}|,\Omega,\lambda}$, the polarization λ is restricted to be the same as the polarization of the mode l, and $|\mathbf{k}|$ is restricted to be equal to ω/c. The integral $\int_{\Omega_l}d\Omega$ means that the orientation integral is performed on the small solid angle section Ω_l subtended by the l-th mode. $\Delta\Omega_l$ is the area of the l-th small solid angle section, expressed in unit of steradian, or rad^2. $a_l(\omega)$ satisfies the standard bosonic commutation relations (see Eq. (1.9)).

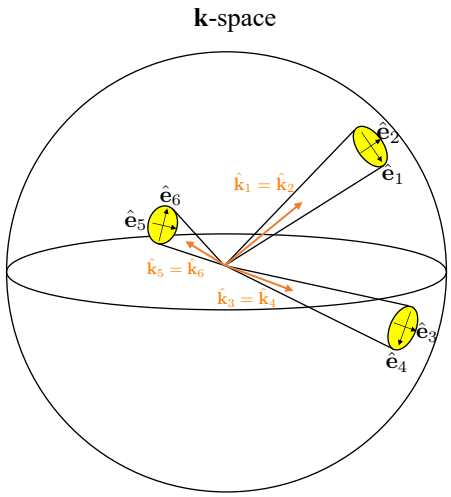

Figure 1.1: Schematics of the small solid angle decomposition. The 4π solid angle in $\mathbf{k}$-space is partitioned into M small solid angle sections (colored yellow). Each small solid angle section is a cone in $\mathbf{k}$-space and contains two spatial modes, corresponding to the two polarizations.

Using the small solid angle decomposition, the electric field operator at position $\mathbf{x} = \mathbf{0}$ is

$$\mathbf{E}(\mathbf{0}) = \sum_{l=1}^{2M} \int_0^\infty d\omega \sqrt{\frac{\hbar\omega^3 \Delta\Omega_l}{16\pi^3\epsilon_0 c^3}} (i a_l(\omega) - i a_l^\dagger(\omega)) \hat{\mathbf{e}}_l, \tag{1.16}$$

(see Eq. (1.13)), where $\hat{\mathbf{e}}_l$ is the unit vector of the polarization in mode l. If the solid angle sections are small enough, then the small variation of the polarization vectors $\hat{\mathbf{e}}_{\mathbf{k},\lambda}$ within a solid angle section can be ignored. Therefore we can define two constant polarization vectors $\hat{\mathbf{e}}_l$ for each solid angle section. Likewise, if the solid angle sections are small enough, we can use one representative wavevector direction $\hat{\mathbf{k}}_l$ (the unit vector of $\mathbf{k}_l$) in each solid angle section to approximate all wavevector directions $\hat{\mathbf{k}}$ in that solid angle section. Near the origin $\mathbf{x} = \mathbf{0}$, we approximate the electric field as

$$\mathbf{E}(\mathbf{x}) \approx \sum_{l=1}^{2M} \int_0^\infty d\omega \sqrt{\frac{\hbar\omega^3 \Delta\Omega_l}{16\pi^3\epsilon_0 c^3}} (i a_l(\omega) e^{i\omega \hat{\mathbf{k}}_l \cdot \mathbf{x}/c} - i a_l^\dagger(\omega) e^{-i\omega \hat{\mathbf{k}}_l \cdot \mathbf{x}/c}) \hat{\mathbf{e}}_l. \tag{1.17}$$

Given a fixed frequency ω (or equivalently, a fixed $|\mathbf{k}|$), we denote the difference between a general $\mathbf{k}$ vector (i.e., $\frac{\omega}{c}\hat{\mathbf{k}}$) in the l-th solid angle section and the representative $\mathbf{k}$ vector (i.e., $\frac{\omega}{c}\hat{\mathbf{k}}_l$) as $\Delta\mathbf{k}$. For the approximation in Eq. (1.17) to be valid, we require the condition $\Delta\mathbf{k} \cdot \mathbf{x} \ll 1$, so that the phase factor $e^{i\omega \hat{\mathbf{k}}_l \cdot \mathbf{x}/c}$ is accurate. Let us define the angular width of a solid angle section as $\Delta\theta$, such that $|\Delta\mathbf{k}| \sim \Delta\theta |\mathbf{k}|$. We will see that $\Delta\theta$ corresponds to the beam divergence angle in real space. Now the condition $\Delta\mathbf{k} \cdot \mathbf{x} \ll 1$ for all solid angle sections becomes $|\mathbf{x}| \ll 1/(\Delta\theta|\mathbf{k}|)$. This means that Eq. (1.17) is valid for $\mathbf{x}$ is an interaction region on the length scale of $1/(\Delta\theta|\mathbf{k}|)$, centered at $\mathbf{x} = \mathbf{0}$. For example, if the beam divergence angles in an experiment are on the order of $\Delta\theta \sim 10^{-3}$ rad and if the wavelengths of the modes are centered at 800 nm (equal to $2\pi/|\mathbf{k}|$), then the interaction region for the sample has a characteristic length of $1/(\Delta\theta|\mathbf{k}|) \approx 100\,\mu$m.

Whereas the electric field is expressed as a sum of a finite number of 1-dimensional field modes, the field Hamiltonian is expressed as a sum over an infinite number of 1-dimensional field modes

$$H_{\text{field}} = \sum_{l=1}^{\infty} \int_0^\infty d\omega\, \hbar\omega a_l^\dagger(\omega) a_l(\omega). \tag{1.18}$$

(see Sec. 1.2). The first $2M$ modes are defined explicitly in Eq. (1.15). The remaining infinitely many modes can be constructed in principle, but we will not define them explicitly. This is because the remaining infinitely many field modes decouple from the matter system and evolve freely. If one is only interested in the finite number of 1-dimensional fields that interact with the matter system, then one can ignore the remaining infinite number of 1-dimensional fields. Practically speaking, for spectroscopy experiments near the visible regime, the remaining infinitely many fields will be in the vacuum state, and stay in the vacuum state under free evolution.

1.3.1 Examining the small solid angle modes in real space and time

The small solid angle modes, defined in the **k**-space, can also be interpreted intuitively in real space by invoking the narrow-band approximation. This approximation makes use of the fact that, in spectroscopy experiments near the visible regime, the matter system only interacts significantly with a narrow band of frequency around some characteristic frequency ω_0 of the matter system (i.e., $\omega \in (\omega_0 - \Delta\omega, \omega_0 + \Delta\omega)$, where $\Delta\omega \ll \omega_0$). To model the effects of a small solid angle mode under the narrow-band approximation, consider a small region in **k**-space in the l-th small solid angle mode, centered around $\mathbf{k}_l = \omega_0/c\hat{\mathbf{k}}_l$ (see Fig. (1.2)). We denote the transverse width of the small region to be $\sigma_\perp$, so that $\sigma_\perp \sim \Delta\theta|\mathbf{k}_l|$. The angular width $\Delta\theta$ is related to the small solid angle area $\Delta\Omega$ by $\Delta\Omega \approx \Delta\theta^2$. The longitudinal width of the region is denoted as $\sigma_\parallel$, and it is related to the frequency bandwidth by $\sigma_\parallel = \Delta\omega/c$. Note that $\sigma_\perp$ and $\sigma_\parallel$ have dimensions of 1/[length], since they are defined as magnitudes in the **k**-space.

To understand the behavior of the photon field due to this small region in **k**-space, let us construct a function $f(\mathbf{k})$, whose value is nonzero and slowly-varying when **k** is in the small region, and we let $f(\mathbf{k})$ drop to 0 quickly away from the small region. In real space and time, the evolution of $f(\mathbf{k})$ is given by

$$\tilde{f}(\mathbf{x}, t) = \int d^3\mathbf{k}\, f(\mathbf{k}) e^{i\mathbf{k}\cdot\mathbf{x}} e^{-ic|\mathbf{k}|t}. \tag{1.19}$$

We show in Appendix A that $\tilde{f}(\mathbf{x}, t)$ resembles a Gaussian paraxial mode in real space and time. As illustrated in Fig. (1.2), at time $t = 0$, the field amplitude is centered at $\mathbf{x} = \mathbf{0}$, and has a cross sectional area on the order of $1/\sigma_\perp^2$. As $t \to \infty$, the field amplitude spreads out into a cone with a solid angle area of $\Delta\Omega$, same as the solid angle area in the **k**-space. The paraxial pulse has a longitudinal width of $\sim 1/\sigma_\parallel$.

In real space, different spatial modes overlap in a region with a characteristic length scale $1/\sigma_\perp$ near the origin (see right side of Fig. (1.2)). This defines an interaction region where multiple spatial modes can interact with the matter sample in a quantum light spectroscopy experiment. The characteristic length scale $1/\sigma_\perp \sim 1/(\Delta\theta|\mathbf{k}_l|)$ is consistent with our previous discussion in the **k**-space.

1.4 The interaction picture Hamiltonian

Consider a molecule located at position **x**. Using the electric field expression in Eq. (1.17), the dipole – electric field coupling Hamiltonian in Eq. (1.5) becomes

$$H_{\text{coup}} = \sum_{l=1}^{2M} \int_{-\infty}^{\infty} \frac{d\omega}{\sqrt{2\pi}} - i a_l(\omega) L_l^\dagger e^{i\omega\hat{\mathbf{k}}_l\cdot\mathbf{x}/c} + i a_l^\dagger(\omega) L_l e^{-i\omega\hat{\mathbf{k}}_l\cdot\mathbf{x}/c}. \tag{1.20}$$

We have combined the prefactor in the electric field with the dipole operator **d** into a scaled dipole operator L_l, defined by

$$L_l = \sqrt{\frac{\hbar\omega_0^3\Delta\Omega_l}{8\pi^2\epsilon_0 c^3}}\mathbf{d}_- \cdot \hat{\mathbf{e}}_l. \tag{1.21}$$

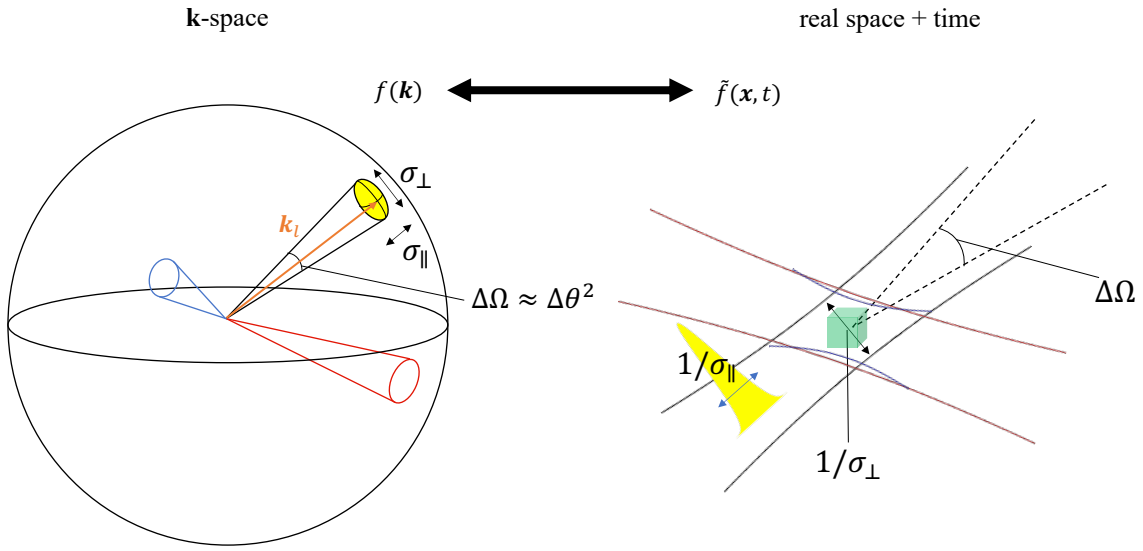

Figure 1.2: Three small solid angle modes, colored black, red, and blue, are represented in the **k**-space and in the real space, under the narrow-band approximation. Under the narrow-band approximation, the mode function $f(\mathbf{k})$ of a small solid angle mode is concentrated in a small region, whose transversal width is $\sigma_\perp$ and longitudinal width is $\sigma_\parallel$. The transversal width $\sigma_\perp$ is related to the angular width $\Delta\theta$ by $\sigma_\perp \sim |\mathbf{k}_l|\Delta\theta$. In real space, the small solid angle mode $\tilde{f}(\mathbf{x},t)$ resembles a paraxial mode. At $t=0$, the waist has a transversal area on the order of $1/\sigma_\perp^2$. As $t \to \infty$, the mode subtends a solid angle area of $\Delta\Omega$ asymptotically. The paraxial pulse has a longitudinal width of $1/\sigma_\parallel$. The green cube is in the overlapping region of different spatial modes, and it represents an interaction region where multiple spatial modes can interact with the matter sample in a quantum light spectroscopy experiment. The interaction region has a characteristic length of $1/\sigma_\perp \sim 1/(\Delta\theta|\mathbf{k}_l|)$.

Note that L_l has a physical dimension of $[1/\sqrt{\text{time}}]$. In Eq. (1.20), we have used the narrow-band approximation (also known as the white noise approximation) to replace the variable ω in the prefactor in Eq. (1.17) with a fixed characteristic frequency ω_0. Under the narrow-band approximation, the integration range $(0, \infty)$ in Eq. (1.17) is extended to $(-\infty, \infty)$ in Eq. (1.20), since only the photons in the narrow frequency window $(\omega_0 - \Delta\omega, \omega_0 + \Delta\omega)$ affect the overall dynamics significantly. The factor of $1/\sqrt{2\pi}$ in Eq. (1.20) is separated out for later convenience, as we will see below. Eq. (1.20) is generalized to the case of many molecules by summing over all molecules, i.e.,

$$H_{\text{coup}} = \sum_{l=1}^{2M} \sum_{j=1}^{N} \int_{-\infty}^{\infty} \frac{d\omega}{\sqrt{2\pi}} - i a_l(\omega) L_{l,j}^{\dagger} e^{i\omega \hat{\mathbf{k}}_l \cdot \mathbf{x}_j / c} + i a_l^{\dagger}(\omega) L_{l,j} e^{-i\omega \hat{\mathbf{k}}_l \cdot \mathbf{x}_j / c}, \tag{1.22}$$

where $L_{l,j}$ is the scaled dipole operator that couples the j-th molecule to the l-th spatial mode, and $\mathbf{x}_j$ is the position of the j-th molecule.

Now, we transform into an interaction picture by writing the total Hamiltonian as

$$H_{\text{sys+field}} = H_0 + H_{\text{coup}}, \tag{1.23}$$

where

$$H_0 = H_{\text{sys}} + H_{\text{field}}. \tag{1.24}$$

A general Schrodinger picture operator A transforms into $A(t) = e^{iH_0(t-t_0)} A e^{-iH_0(t-t_0)}$ in the interaction picture (setting $\hbar = 1$ from now on). In the expression for $A(t)$, t_0 is the initial time with respect to which we define the interaction picture, and t_0 will be set to 0 from now on. In particular, the interaction picture Hamiltonian is

$$H(t) = e^{iH_0 t} H_{\text{coup}} e^{-iH_0 t}. \tag{1.25}$$

For notational simplicity, we have dropped the subscript "coup" and simply denote the interaction picture Hamiltonian as $H(t)$, since this is the main Hamiltonian we will work with. We define the interaction picture time evolution operator $U(t)$ as the solution of the interaction picture Schrodinger equation (in operator form)

$$dU(t)/dt = -iH(t)U(t) \tag{1.26}$$

with the initial condition $U(0) = 1$. The interaction picture time evolution operator $U(t)$ is then related to the Schrodinger picture time evolution operator $e^{-iH_{\text{sys+field}}}$ by

$$e^{-iH_{\text{sys+field}}t} = e^{-iH_0 t} U(t). \tag{1.27}$$

One can check that Eq. (1.27) is indeed correct by taking the time derivative on both sides. Using Eq. (1.27), one can show that a Heisenberg picture operator $A_H(t) = e^{iH_{\text{sys+field}}t} A e^{-iH_{\text{sys+field}}t}$ is related to the interaction picture operator $A(t)$ by

$$A_H(t) = U^{\dagger}(t) A(t) U(t). \tag{1.28}$$

To obtain an explicit expression for the interaction picture Hamiltonian $H(t)$ (Eq. (1.25)), we note that the Schrodinger picture operator $a_l(\omega) e^{i\omega \hat{\mathbf{k}}_l \cdot \mathbf{x}/c}$ in Eq. (1.20) becomes

$$e^{iH_0 t} a_l(\omega) e^{i\omega \hat{\mathbf{k}}_l \cdot \mathbf{x}/c} e^{-iH_0 t} = a_l(\omega) e^{-i\omega(t - \hat{\mathbf{k}}_l \cdot \mathbf{x}/c)} \tag{1.29}$$

in the interaction picture. If we define the retarded time in the paraxial mode l as

$$s_l(t, \mathbf{x}) = t - \frac{\hat{\mathbf{k}}_l \cdot \mathbf{x}}{c}, \tag{1.30}$$

then we can re-write the operator in Eq. (1.29) as $a_l(\omega)e^{-i\omega s_l}$. As time t advances, the plane corresponding to a fixed retarded time s (e.g., $s = 2$ in Fig. (1.3)) moves at the speed of light in the direction of $\hat{\mathbf{k}}_l$.

We now define the retarded time – dependent field operators (or sometimes known as the time-dependent field operators)

$$a_l(s) = \int_{-\infty}^{\infty} \frac{d\omega}{\sqrt{2\pi}}\, a_l(\omega)e^{-i\omega s} \tag{1.31}$$

as the Fourier transform of the frequency-dependent field operators. An important consequence of the definition of $a_l(s)$ is that they satisfy the bosonic commutation relations: $[a_l(s), a_{l'}(s')] = [a_l^\dagger(s), a_{l'}^\dagger(s')] = 0$ and $[a_l(s), a_{l'}^\dagger(s')] = \delta(s - s')\delta_{l,l'}$. Since $a_l(\omega)$ has a physical dimension of $[1/\sqrt{\text{frequency}}]$ (see Eq. (1.8)), by Eq. (1.31), $a_l(s)$ has a physical dimension of $[1/\sqrt{\text{time}}]$. The single-molecule H_{coup} in the interaction picture now becomes

$$H(t) = \sum_{l=1}^{2M} -ia_l(s_l)L_l^\dagger(t) + ia_l^\dagger(s_l)L_l(t). \tag{1.32}$$

$L_l(t)$ is the scaled dipole operator L_l (see Eq. (1.21)) in the interaction picture and it is equal to $e^{iH_{\text{sys}}t}L_l e^{-iH_{\text{sys}}t}$. We have also suppressed the dependence on t and $\mathbf{x}$ in $s_l(t, \mathbf{x})$ for notation simplicity, since the value of t is clear from the context and we are only considering one molecule located at position $\mathbf{x}$. For the case of N molecules, $H(t)$ becomes

$$H(t) = \sum_{l=1}^{2M}\sum_{j=1}^{N} -ia_l\big(s_l(t, \mathbf{x}_j)\big)L_{l,j}^\dagger(t) + ia_l^\dagger\big(s_l(t, \mathbf{x}_j)\big)L_{l,j}(t). \tag{1.33}$$

1.5 Photon field observables

In spectroscopy experiments, the signals are measured in the photon field, and the signal observables can be written in terms of the field creation and annihilation operators, $a_l^\dagger(s)$ and $a_l(s)$. For example, the photon flux $a_l^\dagger(s)a_l(s)$ represents the rate of photons passing through a cross-sectional area in the l-th spatial mode (see Fig. (1.3)). The rate is measured at a position and time that correspond to the retarded time s. The photon flux has a physical dimension of [1/time]. The frequency-dispersed photon count $a^\dagger(\omega)a(\omega)$ represents the density of photons in frequency space, and has a physical dimension of [1/frequency]. Another common observable is the rate of coincidence detection of two photons, one in channel l_1 at retarded time s_1 and one in channel l_2 at retarded time s_2. This is described by the operator $a_{l_1}^\dagger(s_1)a_{l_2}^\dagger(s_2)a_{l_2}(s_2)a_{l_1}(s_1)$, having a physical dimension of [1/time^2]. These operators can also be convolved with detector response functions to account for the finite time-frequency resolution of photon detectors [30, 87].

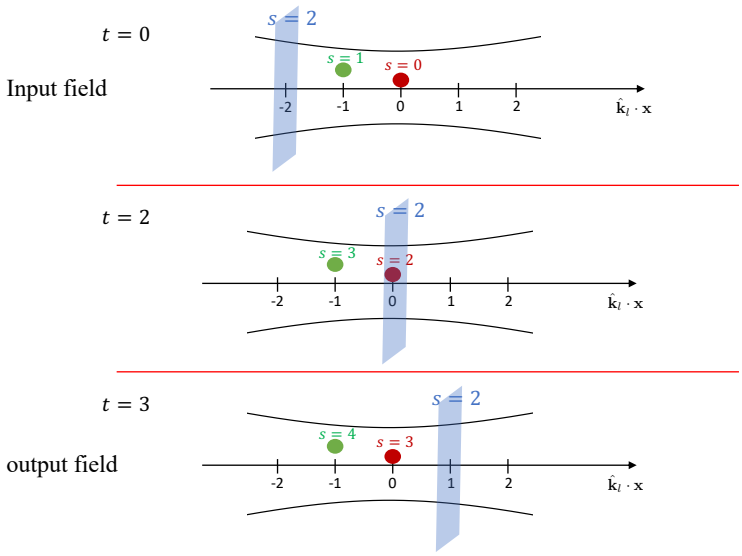

Figure 1.3: Graphical illustration of the input-output relation. The three snapshots at different times ($t = 0, 2, 3$) show the relationship between the retarded time of a traveling field and the retarded time of molecules fixed in position. For simplicity, we set $c = 1$ in this figure. Under the narrow-band approximation, we can define photon field creation and annihilation operators that are localized in retarded time $s = t - \hat{\mathbf{k}}_l \cdot \mathbf{x}$. For example, the field $a_l(s = 2)$ is represented by the blue transversal plane across a paraxial spatial mode. It travels at the speed of light in the direction of $\hat{\mathbf{k}}_l$. Two molecules are located at fixed positions $\hat{\mathbf{k}}_l \cdot \mathbf{x} = -1$ and 0. As time progresses, the retarded time at the positions of the molecules increases. When the retarded time of a field is larger than the retarded time of the position of a molecule, the field is called the input field because it has not interacted with the molecule. When the retarded time of a field is smaller than the retarded time of the position of a molecule, the field is called the output field because the field has finished interacting with the molecule.

Chapter 2

The input-output relation

2.1 Deriving the input-output relation

The input-output formalism describes 1-dimensional fields interacting with quantum systems. Eq. (1.20) represents a basic form of Hamiltonian used in the input-output formalism. Traditionally, the input-output relation is derived by converting between the frequency domain and the time domain, and it is usually described in the language of quantum stochastic differential equations [50, 51, 88, 89]. Here we briefly review the input-output relation. We derive the input-output relation by working only in the (retarded-)time domain and using the language of the more familiar ordinary differential equations.

The input-output relation is in the Heisenberg picture, and it concerns the **time**-evolution of the **retarded time** – dependent field operator $a_l(s)$. By a similar logic to Eq. (1.28), we define the time-evolved retarded time – dependent field operator $a_l(s,t)$ as

$$a_l(s,t) = U^\dagger(t) a_l(s) U(t). \tag{2.1}$$

Here the retarded time s contains both time and position variables implicitly. For this expression to be physically meaningful, the implicit time variable in s needs to be equal to t, hence constraining the position $\mathbf{x}$ of the photon field $a_l(s,t)$ to be on the plane of

$$\frac{\hat{\mathbf{k}}_l \cdot \mathbf{x}}{c} = t - s \tag{2.2}$$

(see Eq. (1.30)). Therefore $a_l(s,t)$ can be thought of as the photon field on the cross section plane $\hat{\mathbf{k}}_l \cdot \mathbf{x}/c = t - s$ at time t (see Fig. 1.3).

To obtain an explicit expression for $a_l(s,t)$, we use the many-molecule Hamiltonian of Eq. (1.33) and the Schrodinger equation (Eq. (1.26)) to take the partial derivative of $a_l(s,t)$ with respect to t (keeping s constant). The partial derivative is evaluated as

$$\begin{aligned} \frac{\partial}{\partial t} a_l(s,t) &= -iU^\dagger(t)\big[a_l(s), H(t)\big]U(t) \\ &= \sum_{j=1}^{N} \delta\big(s - s_l(t, \mathbf{x}_j)\big) L_{Hl,j}(t), \end{aligned} \tag{2.3}$$

where $L_{Hl,j}(t) = U^\dagger(t) L_{l,j}(t) U(t)$ is in the Heisenberg picture (see Eq. (1.28)). Due to the delta function, $a_l(s,t)$ changes value only at time $t = s + \hat{\mathbf{k}}_l \cdot \mathbf{x}_j/c$ for some molecule j. Using Eq. (2.2) to express the retarded time s in terms of time t and real space position $\mathbf{x}$ of the photon field, the condition for nonzero delta function becomes $\hat{\mathbf{k}}_l \cdot \mathbf{x} = \hat{\mathbf{k}}_l \cdot \mathbf{x}_j$, for some molecule j. This means that the field $a_l(s,t)$ changes value (with respect to time propagation) when a molecule is located at the plane of the propagating photon field $a_l(s,t)$.

We shall only consider the field $a_l(s,t)$ with retarded time $s > -\hat{\mathbf{k}}_l \cdot \mathbf{x}_j/c$ for all molecules, so that at initial time $t = 0$, the plane of the photon field, $\hat{\mathbf{k}}_l \cdot \mathbf{x}/c = -s$, is smaller than $\hat{\mathbf{k}}_l \cdot \mathbf{x}_j/c$ for all j (i.e., the photon field $a_l(s, t = 0)$ is upstream of all molecules in the sample). Physically, in spectroscopy experiments, the input light is produced at some distance upstream of the matter sample. As t increases, the plane of the photon field propagates forward in the $\hat{\mathbf{k}}_l$ direction. For small enough t such that the plane of the photon field has not interacted with any molecule (corresponding to the condition $s > s_l(t, \mathbf{x}_j)$ for all j), the right hand side of Eq. (2.3) remains 0. Therefore in this case, $a_l(s,t)$ is equal to $a_l(s)$, which is independent of t as long as $s > s_l(t, \mathbf{x}_j)$ for all j (see top panel of Fig. (1.3)). We call this the input field

$$\text{input field} = a_l(s). \tag{2.4}$$

For large enough t such that the plane of the photon field $a(s)$ has propagated past all molecules (corresponding to the condition $s < s_l(t, \mathbf{x}_j)$ for all j), the right hand side of Eq. (2.3) will remain 0 for all time afterwards, and $a_l(s,t)$ is again independent of t. We call $a_l(s,t)$ in this case the output field, denoted as $a_{l,\text{out}}(s)$. This corresponds to the physical situation where the photon field is detected at some distance downstream of the matter system. By integrating over the delta function in Eq. (2.3), we see that $a_{l,\text{out}}(s)$ is equal to

$$\text{output field} = a_{l,\text{out}}(s) = a_l(s) + \sum_{j=1}^{N} L_{Hl,j}(s + \frac{\hat{\mathbf{k}}_l \cdot \mathbf{x}_j}{c}). \tag{2.5}$$

Eq. (2.5) is the input-output relation in the case of N molecules, for the spatial mode l. In the case of a single molecule located at position $\mathbf{x} = \mathbf{0}$, the input-output relation simplifies to

$$a_{l,\text{out}}(s) = a_l(s) + L_{Hl}(s). \tag{2.6}$$

In classical nonlinear spectroscopy, the output signal's electric field is treated as the sum of the input electric field plus the electric field generated by the matter dipole moment [46]. The input-output relation can be thought of as a quantum mechanical version of this statement. It states that the output field is equal to the input field plus the scaled dipole operators $L_{Hl,j}$ in the Heisenberg picture. The scaled dipole operator $L_{Hl,j}$ is evaluated at time $t = s + \hat{\mathbf{k}}_l \cdot \mathbf{x}_j/c$, which is the time when the propagating plane of the photon field $a_l(s)$ reaches the j-th molecule. Given the Hamiltonian of Eq. (1.33), the input-output relation of Eq. (2.5) is an exact result and it holds for arbitrary light-matter interaction strength (i.e., it is non-perturbative).

In Appendix B, we derive the input-output relation in the classical setting, using Maxwell's equations. In the classical case, the input-output relation is an equation of complex numbers, not operators. As a consequence, the classical input-output relation cannot properly treat non-classical field states or the entanglement between field and matter.

2.2 Examples of analyzing the optical signal using the input-output relation (non-perturbative)

To see how the input-output relation is used in practice, let us consider some examples of output photon field observables in typical quantum light spectroscopy setups. In this section, we shall consider only the case of a single molecule located at $\mathbf{x} = \mathbf{0}$ for simplicity, and the input-output relation is given by Eq. (2.6). To consider the case of having many molecules, one simply sum over all molecules using Eq. (2.5). We note again that the input-output relation is valid for arbitrary matter-field coupling strength. In section 3, we shall restrict our attention to the regime of weak light-matter coupling, as this is the case for most molecular spectroscopy experiments, and then expand the input-output relation perturbatively.

2.2.1 Photon flux

One of the most common type of photon field observable is the photon flux [67]. In classical spectroscopy experiments, the detection of the signal usually takes the form of intensity measurements, and intensity (energy per time in the detection area) is proportion to the photon flux (photon number per time in the detection area). The photon flux signal is defined as $\langle a^\dagger_{l,\mathrm{out}}(s) a_{l,\mathrm{out}}(s)\rangle$, where the expectation value $\langle \cdots \rangle$ is evaluated with respect to the initial state of the matter and the field. We assume the initial state can be factorized into a product of the matter state and the field state. However, the field state may not be factorizable as a product of states in different spatial modes if the input photons are classically correlated or quantum mechanically entangled.

Using the input-output relation (Eq. (2.5)), the output photon flux signal in the l-th mode becomes

$$\langle a^\dagger_{l,\mathrm{out}}(s) a_{l,\mathrm{out}}(s)\rangle = \langle a^\dagger_l(s) a_l(s)\rangle + \langle a^\dagger_l(s) L_{Hl}(s)\rangle + \langle L^\dagger_{Hl}(s) a_l(s)\rangle + \langle L^\dagger_{Hl}(s) L_{Hl}(s)\rangle. \tag{2.7}$$

The first term on the right hand side represents the photon flux of the input light. It is an expectation value of a purely field operator. Since the initial state is a product state between the matter and the field, the first term becomes an expectation value with respect to just the initial field state. The second and the third terms contain the interference between the input light and the field generated by the matter dipole moment, and they are complex conjugates of each other. These two terms together represent absorption and stimulated emission. The time evolution of the scaled dipole operator $L_{Hl}(s)$ is due to not only the interaction with the input light in spatial mode l, but it can also be due to the interaction with the input light in modes other than l. For example, in a pump-probe experiment, the output field is measured in the probe field mode (mode l), but the matter interacts with both the pump field mode (mode l') and the probe field mode (mode l). Note that the Heisenberg-evolved operator $L_{Hl}(s)$ is not purely in the matter degrees of freedom, since the interaction with light mixes the matter and field degrees of freedom. Therefore the expectation value $\langle a^\dagger_l(s) L_{Hl}(s)\rangle$ cannot be factorized as $\langle a^\dagger_l(s)\rangle\langle L_{Hl}(s)\rangle$. This is an important difference to classical light spectroscopy. In classical spectroscopy, the field operator $a_l(s)$ is treated as a complex number instead of an operator, so, for example, the second term factorizes as $a^*_l(s)\langle L_{Hl}(s)\rangle$. Furthermore, in classical spectroscopy, $L_{Hl}(s)$ is purely in the matter degrees of freedom. The last term on the right hand side of Eq. (2.7) represent the spontaneous emission, since it contains no direct contribution from the input field.

For arbitrary light-matter coupling strength, the method to calculate the terms in Eq. (2.7) depends on the specific state of the input light, and in general needs to be considered in a case-by-case basis. To gain insights into the evaluation of these terms, we consider below three different input field states: vacuum state, Fock state, and coherent state.

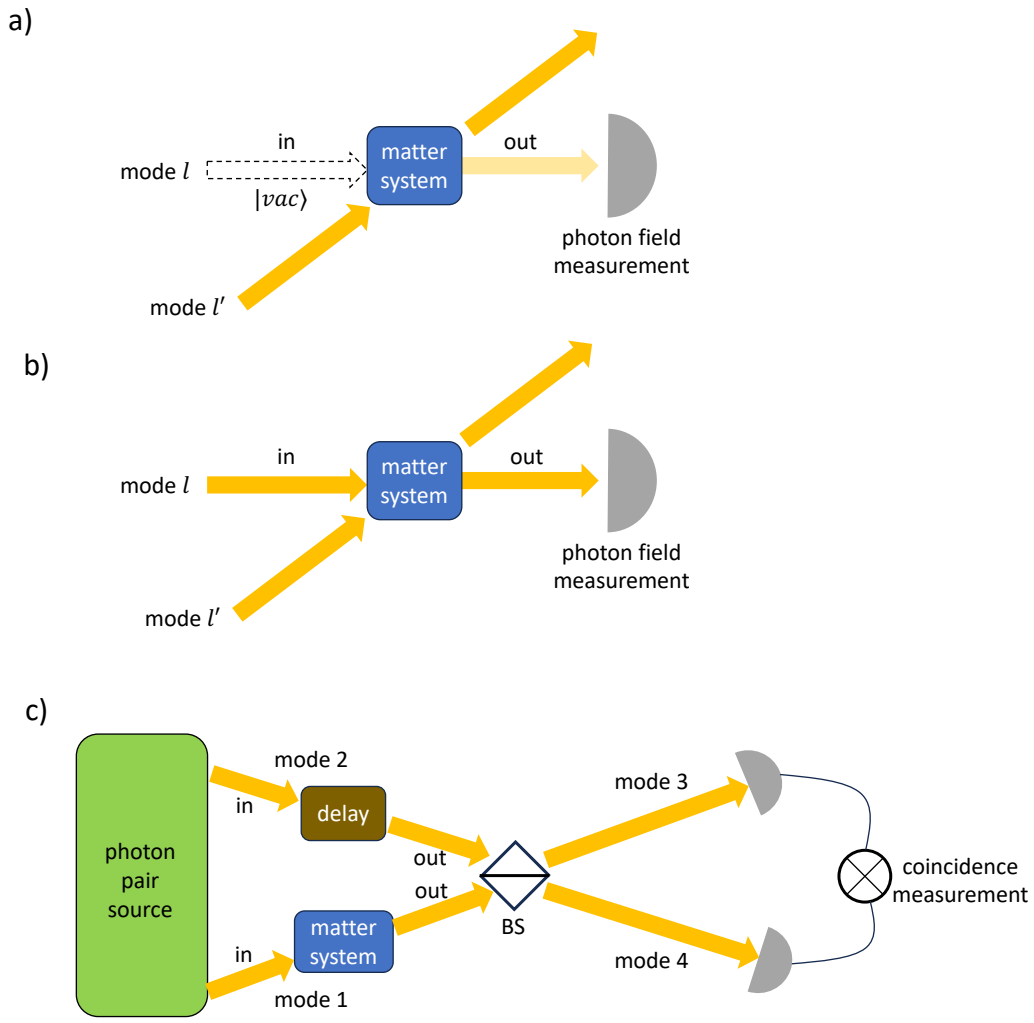

Figure 2.1: Three common quantum light spectroscopy experimental schemes. (a) Measuring the property of the fluorescent light. The matter system interacts with spatial mode l', and the signal is detect in a different spatial mode l. The input of mode l' can be any state of light. The input of the detection mode l is the vacuum state. The analysis can be generalized to consider the matter system interacting with more than one non-detection spatial modes. (b) Measuring the transmitted light. Similar to (a), but the input field state of the detection spatial mode l is not a vacuum state. (c) Hong-Ou-Mandel (HOM) scheme. The input field is typically a photon pair with one photon in mode 1 and another in mode 2. The photon in mode 1 interact with a matter system, while the photon in mode 2 is delayed. The two photons interfere with each other in a beamsplitter (BS). The coincidence count probability between modes 3 and 4 is measured as a function of the time delay, which provides information about the matter system.

Vacuum input

If the spatial mode l is initially in the vacuum state and the matter system is excited by photons in other spatial modes (see Fig. (2.1a)), then the photon flux in the l-th spatial mode corresponds to the fluorescence intensity as a function of time. Evaluating the expectation values with respect to the vacuum state, the first three terms in Eq. (2.7) are equal to zero. Only the last term (i.e. spontaneous emission) contributes to the output photon flux. To evaluate the expectation value $\langle L_{Hl}^\dagger(s)L_{Hl}(s)\rangle$, one can transform from the Heisenberg picture back into the Schrodinger picture, i.e.,

$$\begin{aligned}\langle L_{Hl}^\dagger(s)L_{Hl}(s)\rangle &= \mathrm{Tr}(L_l^\dagger L_l \rho_{\mathrm{tot}}(s)) \\ &= \mathrm{Tr}_{\mathrm{sys}}(L_l^\dagger L_l \rho_{\mathrm{sys}}(s)),\end{aligned} \tag{2.8}$$

where $\rho_{\mathrm{sys}} = \mathrm{Tr}_{\mathrm{field}}(\rho_{\mathrm{tot}})$ is the reduced density matrix for the system. On the right hand side of the first equality, the Schrodinger picture operator $L_l^\dagger L_l$ only acts on the system degrees of freedom. Therefore in the second equality, we can trace out the field degrees of freedom from $\rho_{\mathrm{sys+field}}$. Note that the photon flux expectation value is now re-expressed as an expectation value in the system degrees of freedom. For an arbitrary initial field state, there is no general method to evaluate $\rho_{\mathrm{sys}}(t)$ in the non-perturbative regime, but there are different master equations to treat the effects of different input states [47, 50, 65]. In the case that the matter system reaches a steady state due to a stationary input from a spatial mode other than l, then the photon flux expectation value is obtained by substituting the system steady state ρ_{steady} into Eq. (2.8). In Appendix C, we show that Eq. (2.8) is consistent with the the spontaneous emission rate given by Fermi's golden rule in a simple example.

m-photon Fock state input

Fig. (2.1b) illustrates the situation when the input field state in mode l is not a vacuum state. As an example, we consider an m-photon Fock state as the input in the l-th mode. An m-photon Fock state is defined as

$$|m_\xi\rangle_l = \frac{1}{\sqrt{m!}}\Big(\int ds\, \xi(s) a_l^\dagger(s)\Big)^m |\mathrm{vac}\rangle, \tag{2.9}$$

where $\xi(s)$ is the temporal profile of the pulse, and $|\mathrm{vac}\rangle$ means the vacuum state. ξ is normalized such that $\int ds\, |\xi(s)|^2 = 1$. The last term in Eq. (2.7) is evaluated in a similar way as in Eq. (2.8). The first term in Eq. (2.7) is evaluated with respect to the initial field state of Eq. (2.9), and it is equal to $m|\xi(s)|^2$. The second and the third term in Eq. (2.7) require a more careful treatment. To do so, we first write the combined initial state as $\rho_{\mathrm{tot}}(0) = \rho_{\mathrm{sys}}(0) \otimes \rho_{\mathrm{field},\neq l} \otimes |m_\xi\rangle_l\langle m_\xi|$, where $\rho_{\mathrm{field},\neq l}$ is the field state of all modes other than l. Then the second term (similarly for the third term) becomes

$$\begin{aligned}\langle a_l^\dagger(s)L_{Hl}(s)\rangle &= \mathrm{Tr}\Big(L_{Hl}(s)\big(\rho_{\mathrm{sys}}(0)\otimes\rho_{\mathrm{field},\neq l}\otimes|m_\xi\rangle_l\langle m_\xi|\big)a_l^\dagger(s)\Big) \\ &= \sqrt{m}\xi^*(s)\mathrm{Tr}\Big(U^\dagger(s)L_l U(s)\big(\rho_{\mathrm{sys}}(0)\otimes\rho_{\mathrm{field},\neq l}\otimes|m_\xi\rangle_l\langle(m-1)_\xi|\big)\Big) \\ &= \sqrt{m}\xi^*(s)\mathrm{Tr}\Big(L_l\mathcal{G}(s)\big(\rho_{\mathrm{sys}}(0)\otimes\rho_{\mathrm{field},\neq l}\otimes|m_\xi\rangle_l\langle(m-1)_\xi|\big)\Big) \\ &= \sqrt{m}\xi^*(s)\mathrm{Tr}_{\mathrm{sys}}\big(L_l\rho_{m,m-1}(s)\big).\end{aligned} \tag{2.10}$$

In the first equality, we have used the invariance of trace under cyclic permutation. In the second equality, we have used the photon annihilation property $a_l(s)|m_\xi\rangle_l = \sqrt{m}\xi(s)|(m-1)_\xi\rangle_l$ and that $L_{Hl}(s) = U^\dagger(s)L_l(s)U(s)$. In the third equality, we define the time evolution superoperator $\mathcal{G}(s)$, whose action on an operator X is given by $\mathcal{G}(s)X = U(s)XU^\dagger(s)$. In the final equality, we define the auxiliary system density matrix $\rho_{m,n}(s)$ as $\mathrm{Tr}_{\mathrm{field}}(\mathcal{G}(s)(\rho_{\mathrm{sys}}(0)\otimes\rho_{\mathrm{field},\neq l}\otimes|m_\xi\rangle_l\langle n_\xi|))$, i.e., the reduced system density matrix for the time-evolved non-physical state $\rho_{\mathrm{sys}}(0)\otimes\rho_{\mathrm{field},\neq l}\otimes|m_\xi\rangle_l\langle n_\xi|$. Note that by definition, the physical reduced system state $\rho_{\mathrm{sys}}(t) = \mathrm{Tr}_{\mathrm{field}}\rho_{\mathrm{tot}}(t)$ is $\rho_{m,m}(t)$. For arbitrary $\rho_{\mathrm{field},\neq l}$, there is no general method to evaluate Eq. (2.10) in the non-perturbative regime.

In the simplest case, we take $\rho_{\text{field},\neq l}$ to be the vacuum state. Then the equations of motion of the auxiliary density matrices $\rho_{m,n}$ are described by the hierarchy of Fock state master equations (see [47, 52] or Sec. 5.3). We note that this method of calculating the photon flux was first derived in [47] using the mathematics of quantum stochastic differentials, and we have re-formulated the derivation in terms of ordinary calculus in [52].

Coherent state input

A coherent state with a coherent amplitude $\alpha(s)$ in mode l is defined as

$$|\alpha\rangle_l = \exp\Big(\int ds\, \alpha(s)a_l^\dagger(s) - \alpha^*(s)a_l(s)\Big)|\text{vac}\rangle, \tag{2.11}$$

and it has the property $a_l(s)|\alpha\rangle = \alpha(s)|\alpha\rangle$. If this is used as the input in spatial mode l, then Eq. (2.7) becomes

$$\langle a_{l,\text{out}}^\dagger(s)a_{l,\text{out}}(s)\rangle = |\alpha(s)|^2 + \alpha^*(s)\langle L_{Hl}(s)\rangle + \alpha(s)\langle L_{Hl}^\dagger(s)\rangle + \langle L_{Hl}^\dagger(s)L_{Hl}(s)\rangle, \tag{2.12}$$

where the $a_l(s)$ and $a_l^\dagger(s)$ in Eq. (2.7) are replaced with $\alpha(s)$ and $\alpha^*(s)$. The expectation values $\langle L_{Hl}(s)\rangle$, $\langle L_{Hl}^\dagger(s)\rangle$, and $\langle L_{Hl}^\dagger(s)L_{Hl}(s)\rangle$ in Eq. (2.12) are evaluated in a similar way as in Eq. (2.8).

The system density matrix in the Schrodinger picture $\rho_{\text{sys}}(t)$ is needed to evaluate the expectation values, but again, there is no general method to evaluate $\rho_{\text{sys}}(t)$ for an arbitrary initial field state $\rho_{\text{field},\neq l}$ in modes other than l. If $\rho_{\text{field},\neq l}$ is the vacuum state, then ρ_{sys} can be obtained by solving the coherent state master equation [52, 65, 86]

$$\frac{d\rho_{\text{sys}}}{dt} = [-iH_{\text{sys}} - \alpha(t)L_l^\dagger + \alpha^*(t)L_l, \rho_{\text{sys}}] + \sum_l \Big(L_l\rho_{\text{sys}}L_l - \frac{1}{2}L_l^\dagger L_l\rho_{\text{sys}} - \frac{1}{2}\rho_{\text{sys}}L_l^\dagger L_l\Big). \tag{2.13}$$

2.2.2 Intra-mode second order photon coherence function

The second order photon coherence function $g^{(2)}$ has been increasingly recognized as a useful observable that can reveal information about the matter system, especially when its value lies in the non-classical regime [3, 16, 39, 40, 57, 58]. We consider the intra-mode correlation in this section, and discuss an example of the inter-mode correlation in Sec. 2.2.3.

The intra-mode, un-normalized, second-order photon coherence function of mode l output is defined as

$$G_{l,l}^{(2)}(s_1, s_2) = \langle a_{l,\text{out}}^\dagger(s_1)a_{l,\text{out}}^\dagger(s_2)a_{l,\text{out}}(s_2)a_{l,\text{out}}(s_1)\rangle, \tag{2.14}$$

where we impose the time-ordering $s_2 > s_1$ [40]. Physically, $G^{(2)}(s_1, s_2)dt^2$ is the joint probability of observing a photon at $(s_1, s_1 + dt)$ and observing another photon at $(s_2, s_2 + dt)$, where dt is the infinitesimal time increment. The normalized second order coherence function, $g_{l,l}^{(2)}(s_1, s_2)$, is related to $G_{l,l}^{(2)}(s_1, s_2)$ by $g_{l,l}^{(2)}(s_1, s_2) = G_{l,l}^{(2)}(s_1, s_2)/(\langle a_l^\dagger(s_1)a_l(s_1)\rangle\langle a_l^\dagger(s_2)a_l(s_2)\rangle)$, where we have dropped the subscript "out" for generality. Using the input-output relation (Eq. (2.6)), Eq. (2.14) becomes

$$\begin{aligned} G_{l,l}^{(2)}(s_1, s_2) = \Big\langle &\big(a_l^\dagger(s_1) + L_{Hl}^\dagger(s_1)\big)\big(a_l^\dagger(s_2) + L_{Hl}^\dagger(s_2)\big) \\ &\big(a_l(s_2) + L_{Hl}(s_2)\big)\big(a_l(s_1) + L_{Hl}(s_1)\big)\Big\rangle. \end{aligned} \tag{2.15}$$

For arbitrary light-matter coupling strength, this expression needs to be evaluated in a case-by-case basis, depending on the state of the input light.

If the input state in mode l is the vacuum state (see Fig. (2.1a)), then this situation corresponds to measuring the photon correlation $G^{(2)}_{l,l}$ of the fluorescent light. It has been shown that the fluorescence $g^{(2)}$ of a molecular aggregate can be used as an indicator for the quantum coherence between individual chromophores [39, 40]. When the expectation value in Eq. (2.15) is evaluated with respect to the vacuum state in mode l, terms involving $a_l(s)$ or $a^\dagger_l(s)$ in Eq. (2.15) will be zero, so $G^{(2)}_{l,l}(s_1, s_2)$ reduces to

$$\begin{aligned} G^{(2)}_{l,l}(s_1, s_2) &= \Big\langle L^\dagger_{Hl}(s_1) L^\dagger_{Hl}(s_2) L_{Hl}(s_2) L_{Hl}(s_1) \Big\rangle \\ &= \mathrm{Tr}\Big(L^\dagger_{Hl}(s_2) L_{Hl}(s_2) L_{Hl}(s_1) \rho_{\mathrm{tot}}(0) L^\dagger_{Hl}(s_1) \Big) \\ &= \mathrm{Tr}\Big(L^\dagger_l L_l \mathcal{G}(s_2 - s_1) \big(L_l \, \rho_{\mathrm{tot}}(s_1) L^\dagger_l \big) \Big). \end{aligned} \tag{2.16}$$

We note that the trace is performed in the matter and field degrees of freedom, which include photon mode l that initializes in the vacuum state and all other photon modes that excite the matter system. To obtain the third line from the second line, one expands the Heisenberg picture operators $A_H(s)$ as $e^{iH_{\mathrm{sys+field}}t} A e^{-iH_{\mathrm{sys+field}}t}$ and use the invariance of trace under cyclic permutation. The final line in Eq. (2.16) has an intuitive physical interpretation. As a photon is observed at time s_1, the combined state $\rho_{\mathrm{tot}}(s_1)$ undergoes a de-excitation jump to the (un-normalized) state $L_l \rho_{\mathrm{tot}}(s_1) L^\dagger_l$. After evolving this state from s_1 to s_2 (described by $\mathcal{G}(s_2 - s_1)$), another photon is observed, corresponding to another de-excitation jump. The joint probability of observing two photons is obtained by taking the trace at the end.

The fluorescent $G^{(2)}_{l,l}(s_1, s_2)$ in Eq. (2.16) can be further simplified if the matter system is driven by a stationary photon source in mode l' (i.e., a mode other than l), and if the combined system+field state reaches a steady state. Now, $G^{(2)}_{l,l}(s_1, s_2)$ only depends on the time difference $s = s_2 - s_1$, so we write the second order coherence function as $G^{(2)}_{l,l}(s)$. The total state $\rho_{\mathrm{tot}}(s_1)$ is replaced with ρ_{steady}, the steady state in the combined system+field degrees of freedom. Eq. (2.16) now becomes

$$G^{(2)}_{l,l}(s) = \mathrm{Tr}\Big(L^\dagger_l L_l \mathcal{G}(s) \big(L_l \, \rho_{\mathrm{steady}} L^\dagger_l \big) \Big). \tag{2.17}$$

From this equation, we see that the time-dependence of $G^{(2)}_{l,l}(s)$ contains information about the transient time evolution of the perturbed steady state $L_l \rho_{\mathrm{steady}} L^\dagger_l$.

2.2.3 Hong-Ou-Mandel (HOM) interference

As an example of the inter-mode second order coherence function, we consider the Hong-Ou-Mandel (HOM) interferometry scheme in Fig. (2.1c). A photon pair with one photon in spatial mode 1 and the other photon in spatial mode 2 is used as the input. The photon pair state

$$|\Psi\rangle = \int ds_1 ds_2 \, f(s_1, s_2) a^\dagger_1(s_1) a^\dagger_2(s_2) |\mathrm{vac}\rangle \tag{2.18}$$

is specified by the biphoton wavefunction $f(s_1, s_2)$. Normalization of $|\Psi\rangle$ requires that $f(s_1, s_2)$ be normalized as $\int ds_1 \, ds_2 |f(s_1, s_2)|^2 = 1$. In the HOM scheme, one photon (photon in mode 1 in Fig. (2.1c)) in the photon pair interacts with a matter system, while the other photon (photon in mode 2 in Fig. (2.1c)) propagates freely with a time delay τ. The relative time delay τ between the two photons is varied in the HOM experiment. The output photons in modes 1 and 2 pass through a 50:50 beamsplitter and transform into photons in modes 3 and 4. The beamsplitter transformation is given by

$$\begin{pmatrix} a_3(s) \\ a_4(s) \end{pmatrix} = \frac{1}{\sqrt{2}} \begin{pmatrix} 1 & i \\ i & 1 \end{pmatrix} \begin{pmatrix} a_{1,\mathrm{out}}(s) \\ a_{2,\mathrm{out}}(s) \end{pmatrix}. \tag{2.19}$$

Given a pair of input photon, the probability $P_{34}(\tau)$ of observing a coincidence count in modes 3 and 4 are measured as a function of the time delay τ.

The coincidence probability is given by the expectation value

$$P_{34}(\tau) = \int ds\, ds' \langle a_3^\dagger(s) a_4^\dagger(s') a_4(s') a_3(s) \rangle. \tag{2.20}$$

Using the beamsplitter transformation (Eq. (2.19)) and using the fact that mode 1 and mode 2 each contains at most one photon, $P_{34}(\tau)$ becomes

$$\begin{aligned} P_{34}(\tau) &= \frac{1}{4} \int ds\, ds' \Big\langle \big(a_{1,\text{out}}^\dagger(s) a_{2,\text{out}}^\dagger(s') - a_{1,\text{out}}^\dagger(s') a_{2,\text{out}}^\dagger(s)\big) \\ &\qquad \big(a_{2,\text{out}}(s') a_{1,\text{out}}(s) - a_{2,\text{out}}(s) a_{1,\text{out}}(s')\big) \Big\rangle \\ &= \frac{1}{2} \int ds\, ds' \Big\langle a_{1,\text{out}}^\dagger(s) a_{2,\text{out}}^\dagger(s') a_{2,\text{out}}(s') a_{1,\text{out}}(s) \Big\rangle \\ &\qquad - \Big\langle a_{1,\text{out}}^\dagger(s) a_{2,\text{out}}^\dagger(s') a_{2,\text{out}}(s) a_{1,\text{out}}(s') \Big\rangle. \end{aligned} \tag{2.21}$$

Since the output $a_{2,\text{out}}(s)$ has a time delay τ relative to the input $a_2(s)$, it is related to the input field by $a_{2,\text{out}}(s) = a_2(s+\tau)$. Combining this with the input-output relation for mode 1 (i.e., $a_{1,\text{out}}(s) = a_1(s) + L_{H1}(s)$), we have

$$\begin{aligned} P_{34}(\tau) = \frac{1}{2} \int ds\, ds' &\Big\langle \big(a_1^\dagger(s) + L_{H1}^\dagger(s)\big) a_2^\dagger(s'+\tau) a_2(s'+\tau) \big(a_1(s) + L_{H1}(s)\big) \Big\rangle \\ &- \Big\langle \big(a_1^\dagger(s) + L_{H1}^\dagger(s)\big) a_2^\dagger(s'+\tau) a_2(s+\tau) \big(a_1(s') + L_{H1}(s')\big) \Big\rangle. \end{aligned} \tag{2.22}$$

In the absence of light-matter coupling, L_{H1} is equal to 0. Then evaluating Eq. (2.22) using the photon pair state of Eq. (2.18), we see that

$$\begin{aligned} P_{34}(\tau) &= \frac{1}{2} \int ds\, ds' f^*(s, s'+\tau) f(s, s'+\tau) - f^*(s, s'+\tau) f(s', s+\tau) \\ &= \frac{1}{2} \Big(1 - \int ds\, ds' f^*(s, s') f(s'-\tau, s+\tau)\Big). \end{aligned} \tag{2.23}$$

If the biphoton wavefunction is symmetric (i.e., $f(s_1, s_2) = f(s_2, s_1)$), then $P_{34}(0)$ is zero and $P_{34}(\tau)$ is a symmetric function of τ. To see that the integral in the last line is symmetric in τ, one can switch the time arguments in $f(s_1, s_2)$ (i.e., $f(s_1, s_2) \to f(s_2, s_1)$), and then switch the variable names $(s, s') \to (s', s)$. If there is coupling between the photon in mode 1 and the matter system, $P_{34}(0)$ will no longer be 0, and $P_{34}(\tau)$ will no longer be symmetric. These deviations will then provide information about the matter system [16].

Chapter 3

Perturbative expansion of the output optical signal

Typical molecular spectroscopy experiments operate in the weak coupling perturbative regime, meaning that the energy scale of the light-matter interaction strength is small compared to other energy scales relevant to the dynamics. The perturbative approach for quantum light spectroscopy provides a unified method to treat arbitrary photon input states under the weak coupling regime. To analyze the output optical signal perturbatively, we perform a perturbative expansion on the input-output relation by expanding the Heisenberg picture operator $L_{Hl}(s)$ in terms of purely system and purely field operators.

The conventional perturbative approach for quantum light spectroscopy works in the interaction picture, where the system+field state $\rho_{\text{tot}}(t)$ is expanded perturbatively, and then the expectation values are evaluated with respect to the time-evolved system+field state [30,31]. One can alternatively view the conventional perturbing-the-state approach in the interaction picture as a perturbing-the-observable approach in the Heisenberg picture, a view that is more closely related to our input-output approach. In this section, we will review these two perspectives of the conventional perturbative approach, and then present our input-output approach that perturbs the input-output relation in the Heisenberg picture. The input-output formulation is more natural and intuitive for analyzing the optical signal. It has led us to discover an equivalence between a class of quantum light spectroscopy experiments using entangled biphotons and a class of classical spectroscopy experiments [60]. We will see that the input-output approach also avoids an issue regarding a tricky integration bound in the conventional approach, which has not been addressed in the literature.

3.1 Perturbative expansion of Heisenberg-evolved operators

As a preliminary to the following discussion, we show how to perturbatively expand a Heisenberg picture operator in terms of interaction picture operators. We will present the perturbative expansion in the context of light matter interaction Hamiltonian, but in fact the perturbative expansion of Heisenberg picture operators in terms of interaction picture operators works for any Hamiltonian.

We showed in Eq. (1.28) that a general operator $A(t)$ in the interaction picture is transformed into the corresponding operator $A_H(t)$ in the Heisenberg picture by $A_H(t) = U^\dagger(t)A(t)U(t)$, where $U(t)$ is the interaction picture time evolution operator, defined in Eq. (1.26). To express $A_H(t)$ as a perturbative series, we show in Appendix D that a time-ordered expansion of $A_H(t)$ from $A(t)$

produces the result

$$\begin{aligned} A_H(t) =& A(t) - i\int_0^t dt_1\,[A(t), H_H(t_1)] \\ &+ (-i)^2 \int_0^t dt_2 \int_0^{t_2} dt_1\,[[A(t), H_H(t_1)], H_H(t_2)] \\ &+ (-i)^3 \int_0^t dt_3 \int_0^{t_3} dt_2 \int_0^{t_2} dt_1\,[[[A(t), H_H(t_1)], H_H(t_2)], H_H(t_3)] + \cdots . \end{aligned} \tag{3.1}$$

The commutators with the Hamiltonian are applied in a time-ordered manner, where the Hamiltonians with smaller time arguments are applied first. While this expansion is correct, the Hamiltonians in the expansion are in the Heisenberg picture, not in the interaction picture. In the context of quantum light spectroscopy, the Heisenberg-evolved $H_H(t)$ is a complicated object that mixes the matter and the field degrees of freedom. Therefore this is not a useful expansion for analyzing the optical signal. We note that a different time-ordered expansion of a Heisenberg-evolved operator $A_H(t)$ from $A_H(0)$ has been derived in Appendix 5B of Ref. [46] using the Liouville space representation, in the context of classical spectroscopy.

In Appendix D, we also show that one can perform the expansion in an anti-time-ordered manner as

$$\begin{aligned} A_H(t) =& A(t) - i\int_0^t dt_1\,[A(t), H(t_1)] \\ &+ (-i)^2 \int_0^t dt_2 \int_0^{t_2} dt_1\,[[A(t), H(t_2)], H(t_1)] \\ &+ (-i)^3 \int_0^t dt_3 \int_0^{t_3} dt_2 \int_0^{t_2} dt_1\,[[[A(t), H(t_3)], H(t_2)], H(t_1)] + \cdots , \end{aligned} \tag{3.2}$$

Now, the Hamiltonians with larger time arguments are applied first, and the Hamiltonians are in the interaction picture. In the context of quantum light spectroscopy, $H(t)$ (see Eqs. (1.32) and (1.33)) is expressed neatly in terms of purely system and purely field operators, allowing one to decompose the expectation value of $A_H(t)$ into expectation values in purely matter degrees of freedom and expectation values in purely field degrees of freedom. This is the expansion that we will use below in the input-output formulation of quantum light spectrosocpy.

3.2 Conventional perturbative approach

3.2.1 Perturbing the state in the interaction picture

In the conventional perturbative approach, one perturbs the combined system+field density matrix $\rho_{\rm tot}(t)$ in the interaction picture. The perturbative series is written as

$$\begin{aligned} \rho_{\rm tot}(t) =& \rho(0) - i\int_0^t dt_1\,[H(t_1), \rho_{\rm tot}(0)] \\ &+ (-i)^2 \int_0^t dt_2 \int_0^{t_2} dt_1\,[H(t_2), [H(t_1), \rho_{\rm tot}(0)]] \\ &+ (-i)^3 \int_0^t dt_3 \int_0^{t_3} dt_2 \int_0^{t_2} dt_1\,[H(t_3), [H(t_2), [H(t_1), \rho_{\rm tot}(0)]]] + \cdots . \end{aligned} \tag{3.3}$$

As discussed in Sec. 1.5, the photon field observables can be expressed in the interaction picture, and they are usually a function of retarded times s. The expectation value of a photon field observable

$A(s)$ is given by $\mathrm{Tr}(A(s)\rho_{\mathrm{tot}}(t))$. Substituting Eq. (3.3) into this expectation value, we obtain the perturbative expansion of the optical signal

$$\begin{aligned}\langle A(s)\rangle =& \mathrm{Tr}\big(A(s)\rho_{\mathrm{tot}}(0)\big) - i\int_0^t dt_1\,\mathrm{Tr}\big(A(s)[H(t_1),\rho_{\mathrm{tot}}(0)]\big)\\ &+(-i)^2\int_0^t dt_2\int_0^{t_2} dt_1\,\mathrm{Tr}\big(A(s)[H(t_2),[H(t_1),\rho_{\mathrm{tot}}(0)]]\big)\\ &+(-i)^3\int_0^t dt_3\int_0^{t_3} dt_2\int_0^{t_2} dt_1\,\mathrm{Tr}\big(A(s)[H(t_3),[H(t_2),[H(t_1),\rho_{\mathrm{tot}}(0)]]]\big)+\cdots .\end{aligned} \tag{3.4}$$

Since the optical signal is measured after the photon field has interacted with the matter system, we require that the interaction time t be large enough such that the plane of the photon field $a(s)$ has propagated past all molecules. Mathematically, this condition is expressed as $s_l(t,\mathbf{x}_j) = t-\hat{\mathbf{k}}_l\cdot\mathbf{x}_j/c > s$ for all molecules j (see Fig. (1.3) for an illustration and Sec. 2.1 for more detailed discussion on retarded times). If the field observable involves more than one retarded time variable or more than one field mode (e.g., the second order coherence function $a_l^\dagger(s_1)a_{l'}^\dagger(s_2)a_{l'}(s_2)a_l(s_1)$), then one needs to make sure that t is large enough such that $s_l(t,\mathbf{x}_j)$ is greater than all retarded time variables s_i, for all spatial modes l_i. For convenience, t can simply be set to ∞. In the literature [30, 31], the distinction between the interaction time t and the retarded time s is often overlooked. This has resulted in inconsistencies in the choice of the interaction time t in the literature. In the input-output approach, the choice of the integration time is automatically taken care of by the input-output relation. We will discuss this issue in more detail using an example in Sec. 3.6.

3.2.2 Perturbing the observable in the Heisenberg picture

Instead of perturbing the state $\rho_{\mathrm{tot}}(t)$ in the interaction picture, we can also expand the Heisenberg picture observable $U^\dagger(t)A(s)U(t)$ in terms of interaction picture operators. This method is simply a different perspective of the conventional perturbative approach, and it results in identical expressions as the perturbing-the-state approach. We present this alternative point of view because this approach is more closely related to our input-output method, to be discussed in Sec. 3.3.

Since the expansion of Heisenberg picture operators is in fact an expansion of the time-evolution superoperator $U^\dagger(t)\bullet U(t)$ (see Appendix D), we can generalize Eq. (3.2) slightly to expand $U^\dagger(t)A(s)U(t)$ as

$$\begin{aligned}U^\dagger(t)A(s)U(t) =& A(s) - i\int_0^t dt_1\,[A(s),H(t_1)]\\ &+(-i)^2\int_0^t dt_2\int_0^{t_2} dt_1\,[[A(s),H(t_2)],H(t_1)]\\ &+(-i)^3\int_0^t dt_3\int_0^{t_3} dt_2\int_0^{t_2} dt_1\,[[[A(s),H(t_3)],H(t_2)],H(t_1)]+\cdots .\end{aligned} \tag{3.5}$$

The output optical signal $\langle A(s)\rangle$ is given by the expectation value $\mathrm{Tr}(U^\dagger(t)A(s)U(t)\rho_{\mathrm{tot}}(0))$. Substituting Eq. (3.5) into the trace expression, we have

$$\begin{aligned}\langle A(s)\rangle =& \mathrm{Tr}\big(A(s)\rho_{\mathrm{tot}}(0)\big) - i\int_0^t dt_1\,\mathrm{Tr}\big([A(s),H(t_1)]\rho_{\mathrm{tot}}(0)\big)\\ &+(-i)^2\int_0^t dt_2\int_0^{t_2} dt_1\,\mathrm{Tr}\big([[A(s),H(t_2)],H(t_1)]\rho_{\mathrm{tot}}(0)\big)\\ &+(-i)^3\int_0^t dt_3\int_0^{t_3} dt_2\int_0^{t_2} dt_1\,\mathrm{Tr}\big([[[A(s),H(t_3)],H(t_2)],H(t_1)]\rho_{\mathrm{tot}}(0)\big)+\cdots .\end{aligned} \tag{3.6}$$

By applying the identity $\mathrm{Tr}([A,B]C) = \mathrm{Tr}(A[B,C])$ repeatedly, we can see that Eq. (3.6) is equal to Eq. (3.4). Therefore, the perturbing-the-state approach is equivalent to the perturbing-the-observable approach.

3.3 Perturbative expansion of the input-output relation

In our input-output formalism, we first treat $a_l(s)$ in the photon field observable $A(s)$ as the output field $a_{l,\mathrm{out}}(s)$, and then apply the input-output relation to each $a_{l,\mathrm{out}}(s)$. Examples of this procedure are describe in Eqs. (2.7), (2.15), and (2.22). Then we perturbatively expand the Heisenberg picture system operators L_H in these expressions.

Applying the Heisenberg perturbative expansion (Eq. (3.2)) to $L_{Hl}(s + \hat{\mathbf{k}}_l \cdot \mathbf{x}_j/c)$ in the many-molecule input-output relation (Eq. (2.5)), we have

$$\begin{aligned} a_{l,\mathrm{out}}(s) =& a_l(s) + \sum_{j=1}^{N} L_{l,j}(s + \frac{\hat{\mathbf{k}}_l \cdot \mathbf{x}_j}{c}) - i \sum_{j=1}^{N} \int_0^{s+\hat{\mathbf{k}}_l\cdot\mathbf{x}_j/c} dt_1 \left[L_{l,j}(s + \frac{\hat{\mathbf{k}}_l \cdot \mathbf{x}_j}{c}), H(t_1) \right] \\ &+ (-i)^2 \sum_{j=1}^{N} \int_0^{s+\hat{\mathbf{k}}_l\cdot\mathbf{x}_j/c} dt_2 \int_0^{t_2} dt_1 \left[\left[L_{l,j}(s + \frac{\hat{\mathbf{k}}_l \cdot \mathbf{x}_j}{c}), H(t_2) \right], H(t_1) \right] \\ &+ (-i)^3 \sum_{j=1}^{N} \int_0^{s+\hat{\mathbf{k}}_l\cdot\mathbf{x}_j/c} dt_3 \int_0^{t_3} dt_2 \int_0^{t_2} dt_1 \left[\left[\left[L_{l,j}(s + \frac{\hat{\mathbf{k}}_l \cdot \mathbf{x}_j}{c}), H(t_3) \right], H(t_2) \right], H(t_1) \right] + \cdots . \end{aligned} \tag{3.7}$$

In the case of a single molecule located at $\mathbf{x} = \mathbf{0}$, the expansion of the input-output relation (Eq. (2.6)) becomes

$$\begin{aligned} a_{l,\mathrm{out}}(s) =& a_l(s) + L_l(s) - i \int_0^{s} dt_1 \left[L_l(s), H(t_1) \right] \\ &+ (-i)^2 \int_0^{s} dt_2 \int_0^{t_2} dt_1 \left[\left[L_l(s), H(t_2) \right], H(t_1) \right] \\ &+ (-i)^3 \int_0^{s} dt_3 \int_0^{t_3} dt_2 \int_0^{t_2} dt_1 \left[\left[\left[L_l(s), H(t_3) \right], H(t_2) \right], H(t_1) \right] + \cdots . \end{aligned} \tag{3.8}$$

This expansion can be thought of as the perturbative expansion of the Heisenberg-evolved field operator $U^\dagger(t) a_l(s) U(t)$ (see Eq. (3.5)), where the interaction time t is large enough such that the plane of the photon field $a_l(s)$ has propagated past the matter system. To see this more explicitly, we consider the single molecule case and take $A(s) = a_l(s)$ in Eq. (3.5). Since the molecule is at $\mathbf{x} = \mathbf{0}$, the condition $s_l(t, \mathbf{x} = \mathbf{0}) > s$ becomes $t > s$. Using the single-molecule Hamiltonian (Eq. (1.32)), the first order expansion term in Eq. (3.5) then becomes

$$\sum_{l'} \int_0^{t} dt_1 [a_l(s), -a_{l'}(t_1) L_{l'}^\dagger(t_1) + a_{l'}^\dagger(t_1) L_{l'}(t_1)] = L_l(s). \tag{3.9}$$

This is exactly the second term in Eq. (3.8). The higher order terms in Eq. (3.8) also match with the higher order terms in the Heisenberg expansion of $U^\dagger(t) a_l(s) U(t)$. Notice that in the input-output approach, the condition $s_l(t, \mathbf{x}_j) > s$ is automatically taken care of when we apply the input-output relation.

3.4 Normal-ordered perturbative expansion of the optical signal

To evaluate the nested commutators in Eq. (3.7), we introduce a commutator identity. Given arbitrary field operators A_1 and A_2, and system operators B_1 and B_2,

$$[A_1B_1, A_2B_2] = A_1A_2[B_1, B_2] + [A_1, A_2]B_2B_1 \tag{3.10a}$$

$$= A_2A_1[B_1, B_2] + [A_1, A_2]B_1B_2. \tag{3.10b}$$

If the light-matter interaction is treated semi-classically (i.e., the field is described by complex numbers), then the first terms in both Eqs. (3.10a) and (3.10b), are identical, and the second terms in both Eqs. (3.10a) and (3.10b) are zero, since complex numbers always commute. For ease of reference, we shall call the first terms the "matter commutator" terms and the second terms the "field commutator" terms.

Having two different representations of the commutator in Eq. (3.10) allows us to write the perturbative expansion only in terms of normal-ordered field operators. In the perturbative expansion of Heisenberg-evolved operators (Eq. (3.2)), A_2B_2 comes from the Hamiltonian $H(t)$ (see Eqs. (1.32) and (1.33)), and the field operator A_2 is either of the type $a(t)$ or of the type $a^\dagger(t)$. If A_1 is a normal-ordered field operator, then we can ensure that the commutator $[A_1B_1, A_2B_2]$ contains only normal-ordered field operators by using the identity Eq. (3.10a) if A_2 is of the type $a(t)$, and using the identity Eq. (3.10b) if A_2 is of the type $a^\dagger(t)$. We will see how this works in an example in Sec. 3.6.

We note that, in the literature, a different form of commutator identity is used to perform perturbative expansions in quantum light spectroscopy [31, 90]. This identity is usually expressed in superoperator form as

$$(A_1B_1)_- = A_{1+}B_{1-} + A_{1-}B_{1+}, \tag{3.11}$$

where $A_-X = [A, X]$ is the commutator superoperator, and $A_+X = \{A, X\}/2$ is the anti-commutator superoperator. Again, the first term on the right hand side is the matter commutator term, and the second term is the field commutator term, which vanishes in the semi-classical treatment of light-matter interaction. This identity is in fact closely related to the identities of Eq. (3.10). If we take the arithmatic average of Eqs. (3.10a) and (3.10b), we have

$$(A_1B_1)_-(A_2B_2) = A_{1+}B_{1-}(A_2B_2) + A_{1-}B_{1+}(A_2B_2), \tag{3.12}$$

which is just the superoperators in Eq. (3.11) applied to the operator A_2B_2. The identity of Eq. (3.11) takes a more symmetric form, but it does not provide a direct way to perform normal-ordered perturbative expansion.

3.5 Order of magnitude estimates

For the perturbative expansion to be a good description for the dynamics, we require that the magnitude of the Hamiltonian $H(t)$ (i.e., the light-matter interaction strength) times the interaction time be much less than 1. To provide a rough estimate of the magnitude of $H(t)$, we note that there are two types of operators in $H(t)$: the $a(t)$-type field operator (including $a^\dagger(t)$) and the $L(t)$-type matter operator (including $L^\dagger(t)$). From Sec. 1.4, we see that both $a(t)$ and $L(t)$ have the same physical dimension of 1/[Time], and therefore we can compare their relative magnitudes directly. Given a light pulse having a temporal width of $\sim \Delta$ and containing m photons on average, we have $\int dt \langle a^\dagger(t)a(t)\rangle = m$. Therefore to account for the effects of the pulse, we assign an order of magnitude of $\sqrt{m_l/\Delta_l}$ to each $a_l(t)$ and $a_l^\dagger(t)$, where m_l and Δ_l are the number of photons and pulse width in the

l-th spatial mode. In the case that the l-th spatial mode is in vacuum, we have $\int_0^T dt \langle a_l(t) a_l^\dagger(t') \rangle = 1$. Therefore we assign an order of magnitude of $1/\sqrt{T}$ to $a_l(t)$ and $a_l^\dagger(t)$, where T is the total amount of time considered. The order of magnitude of $L(t)$ is

$$L(t) \sim \sqrt{\frac{\omega_0^3 |\mathbf{d}|^2 \Delta\Omega}{8\pi^2 \epsilon_0 c^3}}, \tag{3.13}$$

as can be seen from Eq. (1.21). We note that the case of $\Delta\Omega = 8\pi/3$ corresponds to maximal coupling between the molecule and the spatial mode, since Eq. (3.13) then becomes the square root of the total spontaneous emission rate into all spatial directions ($\Gamma = \omega_0^3 |\mathbf{d}|^2 / 3\pi\epsilon_0 \hbar c^3$) [67]. To obtain a different estimate for L, we connect the solid angle area $\Delta\Omega$ to the the cross section area of the beam A, since the cross section area may be accessed more directly in experiments. Using the order of magnitude estimates $k_0^2 \Delta\Omega \sim \sigma_\perp^2$ and $A \sim 1/\sigma_\perp^2$ (see Fig. (1.2)), we have $\Delta\Omega \sim \lambda_0^2 / 4\pi^2 A$, where the wavelength λ_0 is given by $k_0 = 2\pi/\lambda_0$. Re-writting Eq. (3.13) in terms of A, we have

$$L(t) \sim \sqrt{\Gamma \frac{3\lambda_0^2}{32\pi^3 A}}. \tag{3.14}$$

We now see that as the cross section area of the beam A increases, the electric field felt by the molecule decreases, and the coupling between molecule and the photon field in the spatial mode decreases.

Table (3.1) lists these order of magnitude estimates of the various quantities discussed above. Numerical values of these quantities are evaluated using typical values encountered in nonlinear spectroscopy with visible light pulses [91–94]. We use the following values (unless otherwise noted): pulse width $\Delta = 30$ fs, $\lambda_0 = 650$ nm, number of photon $m = 3 \times 10^{10}$ (corresponding to a 10 nJ pulse), total experimental time $T = 10$ ps, beam cross section area $A = (100\,\mu\text{m})^2$, and dipole moment $|\mathbf{d}| = 4$ Debye.

operator	order of magnitude	typical numerical value ($\text{ps}^{-1/2}$)
$a(t)$ vacuum effect	$\sim 1/\sqrt{T}$	0.3
$a(t)$ pulse effect, single photon	$\sim 1/\sqrt{\Delta}$	6
$a(t)$ pulse effect, 3×10^{10} photons	$\sim \sqrt{m/\Delta}$	1×10^6
$\sqrt{\Gamma}$	$\sim \sqrt{\omega_0^3 \lvert\mathbf{d}\rvert^2 / 3\pi\epsilon_0 \hbar c^3}$	4×10^{-3}
$L(t)$	$\sim \sqrt{\Gamma}\sqrt{3\lambda_0^2/32\pi^3 A}$	2×10^{-6}

Table 3.1: Order of magnitude estimates of various operators and parameters in the perturbative expansion.

To confirm that the perturbative expansion is a good description under these numerical values, we consider for example a molecule interacting with a light pulse containing 3×10^{10} photons. In this case, $||H|| \sim a(t) L(t) \sim 2\,\text{ps}^{-1}$. Multiplying by the interaction time (i.e., the pulse width Δ), we have $||H||t \sim 0.06 \ll 1$. Hence the perturbative expansion provides a good description for the dynamics. The magnitudes of $a(t)$ for single photon pulse effects and for the vacuum effect are even smaller, ensuring that these effects are well within the perturbative regime.

3.6 Comparing the input-output formalism to the conventional perturbative approach — photon flux

We now compare the input-output formalism to the conventional perturbative approach. We consider the photon flux as the field observable and restrict ourselves to the case of one spatial mode interacting with one molecule located at the origin. We will collect the expansion terms in orders of $L(t)$, since this is typically the smallest parameter in the expansion (see Table (3.1)). The lowest order non-trivial terms are the second order ($\sim L(t)^2$) terms. These terms correspond to spontaneous emission and linear response effects such as absorption and stimulated emission.

The only zeroth order ($\sim L(t)^0$) term is the input photon flux $a_l^\dagger(t)a_l(t)$. The terms that are first order in $L(t)$ are proportional to the expectation values $\langle L(t)\rangle$ and $\langle L^\dagger(t)\rangle$ in the matter degrees of freedom. These expectation values are nonzero only when the initial state contains nonzero coherence between different excitation subspaces(e.g., $\langle e|\rho_{\rm sys}(0)|g\rangle \neq 0$) because $L(t)$ is proportional to the part of dipole operator that removes a matter excitation (e.g. $|g\rangle\langle e|$, also see Eq. (1.21)). We assume the typical situation where the initial state of the matter system is the thermal state, which contains zero coherence between different excitation subspaces. Therefore the first order ($\sim L(t)^1$) terms are zero.

3.6.1 Input-output approach

In the input-output formalism, the output photon flux is given by $\langle a_{l,\rm out}^\dagger(s)a_{l,\rm out}(s)\rangle$, where the bracket $\langle\cdots\rangle$ denotes the expectation value with respect to the initial state $\rho_{\rm tot}(0)$, which is assumed to be a product state between the matter system state and the field state. Expanding $a_{l,\rm out}(s)$ and $a_{l,\rm out}^\dagger(s)$ using Eq. (3.8), we have

$$\begin{aligned}\langle a_{l,\rm out}^\dagger(s)a_{l,\rm out}(s)\rangle = \Big\langle \big(a_l^\dagger(s) + L_l^\dagger(s) - i\int_0^s dt_1[L_l^\dagger(s),H(t_1)] + \cdots\big) \\ \big(a_l(s) + L_l(s) - i\int_0^s dt_1[L_l(s),H(t_1)] + \cdots\big)\Big\rangle\end{aligned} \tag{3.15}$$

Now we collect the expansion terms in orders of $L(t)$. The zeroth order term is $\langle a_l^\dagger(s)a_l(s)\rangle$, which is the input photon flux. The first order terms are $\langle a_l^\dagger(s)L_l(s)\rangle$ and its complex conjugate, $\langle L_l^\dagger(s)a_l(s)\rangle$. Due to the factorizable initial state, the first order term $\langle a_l^\dagger(s)L_l(s)\rangle$ can be factorized into $\langle a_l^\dagger(s)\rangle\langle L_l(s)\rangle$, which is equal to zero, as noted above.

There are two types of second order terms. The first type of second order terms are products between a zeroth order term and a second order term, i.e.,

$$\int_0^s dt_1 \Big\langle a_l^\dagger(s)\big[L_l(s), -a_l(t_1)L_l^\dagger(t_1) + a_l^\dagger(t_1)L_l(t_1)\big]\Big\rangle + \text{c.c.}, \tag{3.16}$$

where c.c. means the complex conjugate. After expanding the commutator, we drop the term involving $\langle LL\rangle$ and $\langle L^\dagger L^\dagger\rangle$ because this is zero by the assumption that there is no initial coherence between different excitation subspaces. Keeping only the terms involving $\langle LL^\dagger\rangle$ and $\langle L^\dagger L\rangle$, we now have

$$\int_0^s dt_1 \Big\langle a_l^\dagger(s)a_l(t_1)\Big\rangle\Big\langle L_l^\dagger(t_1)L_l(s) - L_l(s)L_l^\dagger(t_1)\Big\rangle + \text{c.c.} \tag{3.17}$$

The terms involving the matter correlation function $\langle L_l(s)L_l^\dagger(t_1)\rangle$ correspond to the linear absorption process. The negative sign in front of $L_l(s)L_l^\dagger(t_1)$ is consistent with the fact that the absorption process reduces the output photon flux. The terms involving the matter correlation function $\langle L_l^\dagger(t_1)L_l(s)\rangle$ correspond to the stimulated emission process. The positive sign in front of this term is consistent with the fact that stimulated emission increases the output photon flux.

The second type of second order terms is $\langle L_l^\dagger(s)L_l(s)\rangle$, a product between a first order term and another first order term. This is the spontaneous emission rate into the spatial mode that we are considering. In the perturbative expansion to second order in $L(t)$, the spontaneous emission rate is evaluated with respect to the initial matter state $\rho_{\rm sys}(0)$. This is to be compared with the non-perturbative treatment of spontaneous emission in Eq. (2.8), where the exact spontaneous emission rate is evaluated with respect to the matter state $\rho_{\rm sys}(s)$ at time s.

3.6.2 Conventional perturbing-the-state approach

Now we derive the same expressions for the photon flux due to the absorption, stimulated emission, and spontaneous emission processes using the conventional approach. The conventional approach perturbatively expands the system+field state $\rho_{\rm tot}(t)$ in the interaction picture, and then evaluate expectation values with respect to the state. However, we have shown in Sec. 3.2.2 that this approach is in fact equivalent to perturbing the Heisenberg-evolved observable directly. Therefore the real difference between the conventional and the input-output approach is that, in the conventional approach, one applies the perturbative expansion to the photon field observables directly without first using the input-output relation.

We let the molecule to be located at $\mathbf{x}=\mathbf{0}$, so the output photon flux takes the form

$$a_{l,\rm out}^\dagger(s)a_{l,\rm out}(s) = U^\dagger(t)a_l^\dagger(s)a_l(s)U(t), \tag{3.18}$$

where $t>s$ so that the plane of the photon field $a_l(s)$ has propagated past the molecule at $\mathbf{x}=\mathbf{0}$. Applying the perturbative expansion of Eq. (3.6) to this Heisenberg-evolved operator to the second order, we have

$$\begin{aligned}\Big\langle a_{l,\rm out}^\dagger(s)a_{l,\rm out}(s)\Big\rangle =& \Big\langle a_l^\dagger(s)a_l(s)\Big\rangle - i\int_0^t dt_1 \Big\langle [a_l^\dagger(s)a_l(s), H(t_1)]\Big\rangle \\ &- \int_0^t dt_2\int_0^{t_2} dt_1 \Big\langle [[a_l^\dagger(s)a_l(s), H(t_2)], H(t_1)]\Big\rangle.\end{aligned} \tag{3.19}$$

Note that the upper bound of the first integral is t, not s, since the output field is measured **after** interacting with the molecule.

The zeroth order term is the input photon flux. The first order term evaluates to

$$\begin{aligned}&\int_0^t dt_1\,\delta(s-t_1)\Big\langle a_l(s)L_l^\dagger(t_1) + a_l^\dagger(s)L_l(t_1)\Big\rangle \\ &= \Big\langle a_l(s)L_l^\dagger(s)\Big\rangle + \Big\langle a_l^\dagger(s)L_l(s)\Big\rangle,\end{aligned} \tag{3.20}$$

which is the same as the first order term obtained in the input-output approach, and it is equal to 0. It is important to note that the delta function is integrated fully, since $t'>t$. The second order term is

$$\int_0^t dt_2\int_0^{t_2} dt_1\,\delta(s-t_2)\Big\langle\Big[a_l(s)L_l^\dagger(t_2)+a_l^\dagger(s)L_l(t_2), -a_l(t_1)L_l^\dagger(t_1)+a_l^\dagger(t_1)L_l(t_1)\Big]\Big\rangle. \tag{3.21}$$

To evaluate this commutator, we use the commutator identities of Eq. (3.10) to ensure normal-ordering of the field operators. We will also drop the terms involving the matter correlations $\langle LL\rangle$ or $\langle L^\dagger L^\dagger\rangle$ because we assume that in the initial state there is no matter coherence between difference

excitation subspaces. Now Eq. (3.21) becomes

$$\int_0^t dt_2 \int_0^{t_2} dt_1\, \delta(s-t_2)\Big(\Big\langle a_l^\dagger(t_1)a_l(s)\Big\rangle\Big\langle [L_l^\dagger(t_2), L_l(t_1)]\Big\rangle - \Big\langle a_l^\dagger(s)a_l(t_1)\Big\rangle\Big\langle [L_l(t_2), L_l^\dagger(t_1)]\Big\rangle + \delta(s-t_1)\Big(\Big\langle L_l^\dagger(t_2)L_l(t_1)\Big\rangle + \Big\langle L_l^\dagger(t_1)L_l(t_2)\Big\rangle\Big)\Big) \tag{3.22}$$

In the big parenthesis, the first two terms are the matter commutator terms, and the last two terms are the field commutator terms. The sum of the first two terms is equal to Eq. (3.17) after one integrates over the delta function. The last two terms require a careful treatment of the delta functions. First, we simplify the sum of the last two terms as

$$2\big\langle L_l^\dagger(s)L_l(s)\big\rangle \int_0^t dt_2 \int_0^{t_2} dt_1\, \delta(s-t_2)\delta(s-t_1). \tag{3.23}$$

We treat the delta function $\delta(\tau)$ as the $\epsilon \to 0$ limit of the square function centered at $\tau = 0$ with a width of ϵ and a height of $1/\epsilon$, so that the integral $\int d\tau\, \delta(\tau) = 1$ (see Fig. (3.1a)). We choose the square function for simplicity. In fact, any symmetric function with integral equal to 1 and becomes infinitely narrow in the $\epsilon \to 0$ limit works as well. As shown in Fig. (3.1b), the product of the two delta functions in Eq. (3.23) is nonzero only on a square region centered at $(t_1, t_2) = (s, s)$, having a width of ϵ (taking $\epsilon \to 0$ at the end). The integral of this square region is 1. The double integral integrates over a triangular region in the (t_1, t_2) plane, which cuts the square region in half. Therefore the double integral in Eq. (3.23) is equal to 1/2, and the entire term of Eq. (3.23) becomes $\langle L^\dagger(s)L(s)\rangle$, equal to the second order spontaneous emission term derived using the input-output approach.

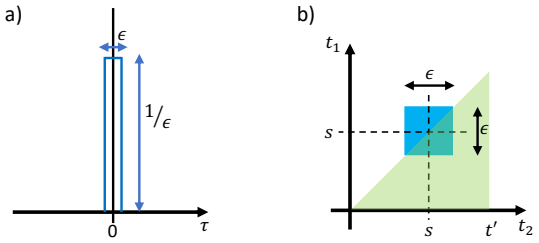

Figure 3.1: Evaluating the double integral in Eq. (3.23). (a) The delta function is treated as the $\epsilon \to 0$ limit of the square function with width ϵ and height $1/\epsilon$. (b) The product of the two delta functions in Eq. (3.23) is nonzero only in the blue square area. The nested integral over t_2 and t_1 is represented by the green area, and covers half of the delta function. Therefore, the double integral evaluates to 1/2.

3.6.3 Comparing the two approaches

We see that in the conventional approach, extra care needs to be taken to ensure the upper bound t of the first integral is larger than the retarded time argument s in the field operator (e.g., $a^\dagger(s)a(s)$). If the position $\mathbf{x}$ of the molecule is not the origin $\mathbf{0}$, then we need to make sure that $s < s_l(t, \mathbf{x}) = t - \hat{\mathbf{k}}_l \cdot \mathbf{x}/c$. In the literature, sometimes, this upper bound t is taken to ∞ [56], while sometimes, this upper bound is taken to be the retarded time variable s [30,31,95], and other times, the upper bound is not specified [57,58], leading to potential confusion as to whether the delta function should be integrated in full or in half. On the other hand, in the input-output approach, one expands the Heisenberg-evolved

system operator $L_H(s)$, and the upper bound of the first integral is s, the same as the time argument in the Heisenberg operator. In a sense, the subtle integration bound in the conventional approach has been taken care of by the input-output relation. We also see that the derivation of terms like the spontaneous emission photon flux is also much simpler using the input-output formalism.

When the conventional approach is used with the normal-ordered perturbative expansion using the method of Sec. 3.4, one can obtain a perturbative expansion where all the field operators are normal-ordered. This is because if the photon field observable is normal-ordered, then by choosing whether to apply Eq. (3.10a) or Eq. (3.10b) to each commutator term in the expansion, the normal-ordering of the field operator can be preserved throughout the expansion. On the other hand, in the input-output approach, one expands the Heisenberg-evolved operators $L_H(s)$ in the signal expression (see Eqs. (2.7), (2.14), and (2.22)). The expansion of each $L_H(s)$ can be normal-ordered by applying Eq. (3.10) judiciously. However, since the final signal expressions usually involve a product of multiple $L_H(s)$, the field operator in the expansion of the final signal is a product of normal-ordered operators, which is typically not normal-ordered.

3.7 Conclusion

We have shown how to calculate the optical signal by using the input-output relation and working in the Heisenberg picture. A key element that makes our approach more intuitive than the conventional method for quantum light spectroscopy is that the input-output relation closely resembles the classical intuition of how the signal electric field is generated. The input-output relation (written in simplified form)

$$a_{\mathrm{out}}(s) = a_{\mathrm{in}}(s) + L_H(s)$$

states that the output field is equal to the input field plus the field generated by the matter dipole moment. Both the photon field $a(s)$ and the matter dipole moment $L(s)$ are treated as quantum mechanical operators in the fully quantum treatment of light-matter interaction. However, in the semi-classical treatment of light-matter interaction, used in classical nonlinear spectroscopy, the input-output relation is treated as an equation of c-numbers. The expectation value of the matter dipole moment is evaluated before applying the input-output relation, i.e.,

$$a_{\mathrm{out}}(s) = a_{\mathrm{in}}(s) + \langle L_H(s) \rangle.$$

In this sense, our input-output formulation of quantum light spectroscopy is a very direct generalization of the semi-classical formalism used in classical nonlinear spectroscopy, and it treats the light-matter interaction fully quantum mechanically. The input-output approach for quantum light spectroscopy also avoids the ambiguous integration bound that arises in the conventional approach for quantum light spectroscopy, since the input-output relation accounts for this integration already.

Chapter 4

Emulating a class of quantum light spectroscopy using classical light pulses

Spectroscopy using quantum light, in particular, using non-classical pulses containing individual or entangled pairs of photons, has attracted much interest in recent years, both theoretically and experimentally, due to its potential to exploit the non-classical properties of light to outperform classical spectroscopy [16, 30, 31, 33, 36, 56, 96–105]. Quantum light spectroscopy (QLS) has been proposed to enable simplification of congested spectra [56], to target specific doubly excited states [33], to improve the signal-to-noise ratio of linear spectroscopy [102], and to measure dephasing rates with high temporal resolution [16]. Understanding the extent to which such QLS experiments provide a quantum advantage requires careful comparison with experiments using classical states of light. For example, the relationship between a quantum pump - quantum probe experiment and classical two-dimensional (2D) spectroscopy experiments is examined in [55].

In this chapter, we show that for a certain class of QLS experiments, the use of entangled photon pairs can be replaced with coherent states of light, which behave classically when normal-ordered field correlations are evaluated (see Fig. (4.1)). This is done in two steps. First, we show that for QLS experiments using entangled photon pairs with one photon being measured without interacting with the matter system [56, 98–102, 104, 105], the entangled photon pair can be replaced with a specially designed single photon Fock state, since measuring one photon effectively collapses the other photon into a single photon state. Thus two-photon entanglement offers no true quantum advantage in these QLS experiments. This has been pointed out previously by [106] using quantum information theory arguments, and an analysis of the quantum information that one can extract from a two-level system using an entangled photon pair versus that extracted using a single photon Fock state has been provided in [107]. In the context of single molecule biphoton spectroscopy that measures photon in the longer time scale of fluorescence, [108] has recently shown that if all scattered photons can be measured, then the entanglement in the photon pair offers no advantage over a single photon. Nevertheless, there may still be practical advantages when using such entangled photon pairs with one photon acting as a reference without interacting with matter. For example, pure single photon Fock states are more difficult to produce experimentally than entangled photon pairs [109], and a visible idler photon may be easier to detect than an infrared signal photon [103].

Second, and this is the main theoretical result of the chapter, we show that for a class of experiments

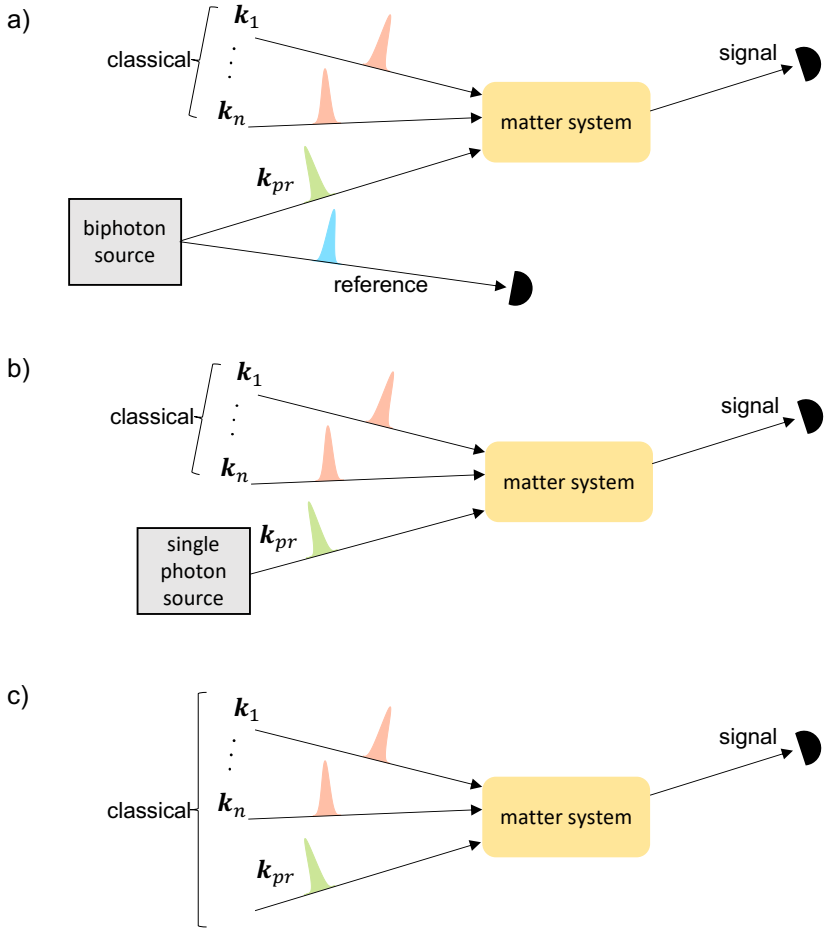

Figure 4.1: Spectroscopic schemes with $n = 0, 1, 2, \cdots$ classical pulses and (a) a biphoton probe pulse with one of the photons acting as a reference without interacting with matter, (b) a single photon Fock state probe pulse, (c) a classical probe pulse containing one photon on average. The signal is measured in all cases in the direction of the probe field. The equivalence between schemes (a) and (b) is referred to as Equivalence 1 in the paper. The equivalence between schemes (b) and (c) is referred to as Equivalence 2 in the paper. Equivalence 2 holds under the conditions that (1) there is no phase matching of the n classical pulses into the direction of the probe field and (2) the signal takes the form of a two-point correlation function (e.g., photon flux, frequency-resolved photon count, or $g^{(1)}$ coherence function).

using n classical pulses ($n = 0, 1, 2, \cdots$) and a single photon Fock state probe pulse, identical signals can also be obtained using a coherent state pulse having the same temporal profile and containing one photon on average. Furthermore, if one uses a coherent state probe with the same temporal profile but containing many photons on average, the signal can be amplified by a factor equal to the average number of photons. Taken together with the equivalence of biphoton and single Fock state probes, this means that the spectral features obtained from experiments with biphoton probe pulses can be exactly reproduced and also amplified by carefully designed coherent state probe pulses. Such quantum-inspired coherent state probes are much simpler to implement and are thus far more preferable than biphoton states for experimental implementation.

We focus our analysis here on spectroscopy experiments for which the signal is measured in the direction of the probe. For the case of a single classical pump, $n = 1$, this allows direct comparison with conventional classical pump-probe spectroscopy and the entangled biphoton probe version of this that was proposed in [56]. Other spectroscopy experiments where the signal is measured in directions other than the probe are not considered here, but can be analyzed similarly using the method we present here. For the equivalence between a single photon Fock state and a single photon coherent state to hold, we require that the classical pulses are incident from different directions than the probe pulse, and that there is no phase matching of the classical pulses into the direction of the probe pulse. In fact, the latter requirement includes the former as a special case. Neither of these are onerous requirements for experiments.

We restrict the signal detection to normal-ordered two-point correlation measurements that contain one creation operator and one annihilation operator in the transmitted probe field, for example, photon flux $\langle a^\dagger(t)a(t)\rangle$, frequency-resolved photon count $\langle a^\dagger(\omega)a(\omega)\rangle$, or the unnormalized $g^{(1)}$ correlation function $\langle a^\dagger(t_2)a(t_1)\rangle$. We note that $g^{(1)}$ is complex-valued and therefore not a quantum mechanical observable in the strict sense, but the real and imaginary parts of $g^{(1)}$ can be measured separately using, for example, a Mach-Zehnder interferometer [67]. The detection of higher-order coherence functions such as $g^{(2)}$ (a four-point correlation function) is not considered here. The key reason for the equivalence between the Fock state probe and the coherent state probe in this class of experiments lies in the fact that they have the same two-point correlation function $\langle a^\dagger(t_2)a(t_1)\rangle$. While the one-point correlation functions $\langle a(t)\rangle$, $\langle a^\dagger(t)\rangle$, and other two-point correlation functions such as $\langle a(t_2)a(t_1)\rangle$ and $\langle a^\dagger(t_2)a^\dagger(t_1)\rangle$ are different for the two probes, their corresponding signals appear only in other phase matching conditions and do not appear in the direction of the probe field. So measuring the signal in this direction, as indicated in Fig. (4.1), isolates signals that are dependent only on $\langle a^\dagger(t_2)a(t_1)\rangle$ and thereby ensures the desired equivalence. We note that this result is a generalization of our other result [52] that the output photon flux is the same under single photon Fock state and single photon coherent state excitation of a matter system in the ground state.

The matter system in this work consists of many molecules distributed over a volume of space, thus giving rise to the phase matching conditions. A single photon Fock state can generate entanglement between different uncoupled molecules, while a coherent state cannot generate such entanglement. Regardless of the difference in the collective matter state, we show here that the two-point correlation signals of the output light are the same. In a different context of a single molecule system, it has been shown [36, 52] that a single photon Fock state and a coherent state containing one photon on average give rise to the same excited state dynamics in the molecule. However, it is important to recognize that despite this similarity, there is also a difference in the overall dynamics of the reduced matter system, since the ground-excited state coherence is identically zero under a single photon Fock state excitation and nonzero under a coherent state excitation [52].

Combining the equivalence between signals from biphotons and single photon Fock states and the equivalence between signals from single photon Fock states and single photon coherent states, we can then establish a class of QLS experiments that can be equivalently performed using only classical

light. We now begin the formal analysis.

4.1 Equivalence 1: Equivalence between signals from biphoton and single photon Fock state probes

Consider an experiment where one probes a matter system using an entangled photon pair, whose density matrix is denoted as ρ_{AB}. Photon A (e.g., the green pulse in Fig. (4.1a)) interacts with the system and the resulting output optical field is measured subsequently. Photon B (e.g., the blue pulse in Fig. (4.1a)) is measured directly, without interacting with anything. Note that in this section focused on the equivalence between signals from biphoton and single photon Fock state probes, we shall impose no restriction on the observables to be measured in each of the two photon fields. For each realization of the experiment, a joint measurement of both photon fields is recorded as (α, β), where α represents the signal in photon field A in that experimental realization, (e.g., whether or not a photon is present, or the measured frequency of the photon), and β represents the measurement outcome of photon field B in the same experimental realization. Averaging over the signal α for fixed β with repeated measurements, one obtains the final reference-averaged signal as (S, β), where S is the averaged signal of photon field A. Each β corresponds to a value of the averaged signal S, so we shall henceforth abbreviate (S, β) as S_β, representing the averaged signal of photon field A that is conditioned on the measurement outcome β of photon field B. It is sometimes suggested that the correlation between the pair of photons A and B enhances the signal S_β [56, 105]. However, we show below that the conditional signal S_β can in fact be constructed alternatively using just single photon states that are parameterized by β. In other words, in the experimental scheme of Fig. (4.1a), quantum entanglement between the two probe photons offers no fundamental advantage in learning about the matter system, since exactly the same results can be obtained using just single photon states. This has also been pointed out by Stefanov in [106].

To derive the single photon state that produces the same signal S_β, we first note that measuring photon B projects the photon pair state to $\Pi_\beta \rho_{AB} \Pi_\beta$, where Π_β is the projector onto the eigenspace of the measurement outcome β. Since no further measurement is performed on photon B, photon A is then completely characterized by the reduced density matrix obtained by tracing the projected state over photon B:

$$\rho_{A|\beta} = \mathcal{N} \mathrm{Tr}_\mathrm{B}\big(\Pi_\beta \rho_{AB} \Pi_\beta\big). \tag{4.1}$$

Here $\mathcal{N} = 1/\mathrm{Tr}(\Pi_\beta \rho_{AB} \Pi_\beta)$ is a normalization factor to ensure unit trace. Eq. (4.1) tells us that measuring the reference photon field B with outcome β effectively collapses the input field of photon A into the single photon state $\rho_{A|\beta}$. Therefore the conditional signal S_β can also be obtained exactly by probing the system with the single photon state $\rho_{A|\beta}$.

As an example, consider the frequency-entangled photon pair

$$|\Psi\rangle = \int d\omega_A \int d\omega_B \Phi(\omega_A, \omega_B) a_A^\dagger(\omega_A) a_B^\dagger(\omega_B) |\mathrm{vac}\rangle, \tag{4.2}$$

where $\Phi(\omega_A, \omega_B)$ is the biphoton wavefunction [67], $a_A(\omega_A)$ ($a_B(\omega_B)$) is the bosonic annihilation operator of frequency mode ω_A (ω_B) in photon field A (B), and $|\mathrm{vac}\rangle$ is the vacuum state of both fields. The operators $a_j(\omega)$ satisfy the bosonic commutation relations: $[a_j(\omega), a_{j'}(\omega')] = [a_j^\dagger(\omega), a_{j'}^\dagger(\omega')] = 0$ and $[a_j(\omega), a_{j'}^\dagger(\omega')] = \delta_{j,j'}\delta(\omega - \omega')$. If we condition the experiment on measuring photon B at some reference frequency $\omega_B = \omega_r$, then the corresponding projection operator Π_{ω_r} is proportional to the outer product of the unnormalized state $a_B^\dagger(\omega_r)|\mathrm{vac}\rangle$ and its adjoint, i.e.,

$$\Pi_{\omega_r} \propto a_B^\dagger(\omega_r)|\mathrm{vac}\rangle_B\langle\mathrm{vac}|a_B(\omega_r), \tag{4.3}$$

where $|\text{vac}\rangle_A$ or $|\text{vac}\rangle_B$ denotes the vacuum state for the photon field A or B. The projected photon pair state becomes

$$\Pi_{\omega_r}|\Psi\rangle \propto \int d\omega_A \Phi(\omega_A, \omega_r) a_A^\dagger(\omega_A) a_B^\dagger(\omega_r)|\text{vac}\rangle, \tag{4.4}$$

which turns out to be a product state between the two photon fields A and B in this case. Therefore the reduced state of photon field A, $\text{Tr}_B(\Pi_{\omega_r}|\Psi\rangle\langle\Psi|\Pi_{\omega_r})$, is a pure state, i.e.,

$$\rho_{A|\omega_r} = |\psi\rangle_{\omega_r}\langle\psi|, \tag{4.5}$$

with

$$|\psi\rangle_{\omega_r} = \mathcal{N}_{\omega_r} \int d\omega_A \Phi(\omega_A, \omega_r) a_A^\dagger(\omega_A)|\text{vac}\rangle_A, \tag{4.6}$$

where $\mathcal{N}_{\omega_r} = \sqrt{1/\int d\omega |\Phi(\omega, \omega_r)|^2}$ is the normalization factor. Now the conditional signal can be alternatively obtained using the single photon state of Eq. (4.6). Note that the frequency profile of this single photon state is explicitly given by evaluating the biphoton wavefunction $\Phi(\omega_A, \omega_B)$ at $\omega_B = \omega_r$.

The equivalence between signals from biphoton and single photon Fock state probes can be understood in a slightly different way by considering the photon correlation functions. For example, if one is interested in some property of the photon field A, represented by the quantum operator O_A, given that a photon with a frequency of ω_r is observed in the photon field B, one would typically need to evaluate the correlation function [56, 105]

$$\langle\Psi|a_B^\dagger(\omega_r) O_A a_B(\omega_r)|\Psi\rangle. \tag{4.7}$$

Since $a_B(\omega_r)|\Psi\rangle = \int d\omega_A\, \Phi(\omega_A, \omega_r) a_A^\dagger(\omega_A)|\text{vac}\rangle = \mathcal{N}_{\omega_r}^{-1}|\psi\rangle_{\omega_r}|\text{vac}\rangle_B$, Eq. (4.7) is equal to the expectation value

$$\mathcal{N}_{\omega_r}^{-2}\, {}_{\omega_r}\langle\psi|O_A|\psi\rangle_{\omega_r} \tag{4.8}$$

with respect to the reduced single photon state $|\psi\rangle_{\omega_r}$, up to a normalization constant $\mathcal{N}_{\omega_r}$ that can be determined from the biphoton wavefunction $\Phi(\omega_A, \omega_B)$.

4.2 Equivalence 2: Equivalence between signals from single photon Fock state and single photon coherent state probes

We now consider the class of experiments where n classical pump pulses (with wavevectors $\mathbf{k}_1, \cdots, \mathbf{k}_n$) and a single photon Fock state or a single photon coherent state probe pulse (with wavevector $\mathbf{k}_{\text{pr}}$), treated quantum mechanically, interact with a matter system. These are illustrated in Fig. (4.1b) and Fig. (4.1c), for a single photon Fock state probe and a single photon coherent state probe, respectively. The classical pulses are incident at different directions from the quantum probe pulse, with the directions selected so that there is no phase matching of the classical pulses into the direction of the single photon probe. These conditions can be summarized as

$$\mathbf{k}_{\text{pr}} \text{ not proportional to } b_1\mathbf{k}_1 \pm \cdots \pm b_n\mathbf{k}_n \tag{4.9}$$

where $b_i = 0, 1, 2, \cdots$ can be any non-negative integer, up to a reasonable number of orders of interaction. The case of $n = 0$ corresponds to the linear absorption of the single photon probe pulse; the case of $n = 1$ corresponds to a classical pump - single photon probe experiment. We place no restriction on the relative time-ordering of the pulses. The signal is restricted to be normal-ordered two-point correlations that contain one creation operator and one annihilation operator in the probe field, e.g., photon flux $\langle a_{\text{pr,out}}^\dagger(t) a_{\text{pr,out}}(t)\rangle$, frequency-resolved photon count $\langle a_{\text{pr,out}}^\dagger(\omega) a_{\text{pr,out}}(\omega)\rangle$, or

the $g^{(1)}$ coherence function $\langle a^\dagger_{\mathrm{pr,out}}(t_2)a_{\mathrm{pr,out}}(t_1)\rangle$. We claim that the final signal coming from the single photon Fock state probe

$$|F_1\rangle = \int dt\, \xi(t) a^\dagger_{\mathrm{pr}}(t)|\mathrm{vac}\rangle \tag{4.10}$$

is equal to the signal from a coherent state probe

$$|C_1\rangle = \exp\big(\int dt\, \xi(t)a^\dagger_{\mathrm{pr}}(t) - \xi^*(t)a_{\mathrm{pr}}(t)\big)|\mathrm{vac}\rangle \tag{4.11}$$

having the same temporal profile $\xi(t)$ and containing on average a single photon. The temporal profile $\xi(t)$ is normalized according to $\int dt|\xi(t)|^2 = 1$. If the coherent state has m photons on average, i.e., the state

$$|C_m\rangle = \exp\big(\sqrt{m}\int dt\, \xi(t)a^\dagger_{\mathrm{pr}}(t) - \xi^*(t)a_{\mathrm{pr}}(t)\big)|\mathrm{vac}\rangle, \tag{4.12}$$

then the probe field absorption and stimulated emission signal will be amplified by a factor of m.

The key to this equivalence between experiments carried out with Fock state probes and coherent state probes is that pulses from these two probes have the same two-point correlation function $\langle a^\dagger_{\mathrm{pr}}(t_2)a_{\mathrm{pr}}(t_1)\rangle$. As already noted in the introduction, even though they have different two-point correlation functions $\langle a^\dagger_{\mathrm{pr}}(t_2)a^\dagger_{\mathrm{pr}}(t_1)\rangle$ and $\langle a_{\mathrm{pr}}(t_2)a_{\mathrm{pr}}(t_1)\rangle$ and different one-point correlation functions $\langle a^\dagger_{\mathrm{pr}}(t)\rangle$ and $\langle a_{\mathrm{pr}}(t)\rangle$, these other correlation functions do not contribute to the observed signal due to phase matching. Together with the explicit parameterization of the coherent state pulse in terms of the single photon frequency profile $\xi(\omega) = \Phi(\omega, \omega_r)$ obtained from the biphoton state in Eq. (4.6), this will allow replacement of a spectroscopic experiment using an entangled probe by experiments using a coherent state probe.

We now prove the equivalence explicitly by analyzing the signals using an input-output formulation of quantum nonlinear spectroscopy. This approach is based on a perturbative expansion of the signal observables in the Heisenberg picture, distinct from the more common approach of perturbing the combined system plus field density matrix in the interaction picture [30, 31]. The input-output formulation simplifies the theoretical analysis by focusing on the signal observables and using standard results from the input-output formalism of quantum optics [50–52].

Our analysis will focus on the frequency-resolved photon count signal $\langle a^\dagger_{\mathrm{pr}}(\omega)a_{\mathrm{pr}}(\omega)\rangle$. The analysis for other two-point correlation signals, such as photon flux and $g^{(1)}$ coherence function, follows almost identically. In the Heisenberg picture, the photon count of the transmitted probe at frequency ω is proportional to

$$\int_{-\infty}^{\infty} dt_2 \int_{-\infty}^{\infty} dt_1 e^{i\omega(t_1-t_2)}\mathrm{Tr}\big(\rho(-\infty)a^\dagger_{\mathrm{pr,\ out}}(t_2)a_{\mathrm{pr,\ out}}(t_1)\big). \tag{4.13}$$

Here $\rho(-\infty)$ is the initial combined system plus probe field state, assumed to be a product state between the matter system ρ_M and the field ρ_F, and the trace operator is evaluated over both the matter and the field degrees of freedom. $a_{\mathrm{pr,out}}(t)$ is the output field operator of the probe field. This output field operator is the result of time-evolving the input field operator in the Heisenberg picture with the combined matter and field Hamiltonian, and thus it mixes the field and matter degrees of freedom [52]. The time domain field operator $a(t)$ is related to the frequency domain field operator $a(\omega)$ by the Fourier relation

$$a(t) = \frac{1}{\sqrt{2\pi}}\int d\omega e^{-i\omega t}a(\omega). \tag{4.14}$$

Therefore $a(t)$ also satisfies the bosonic commutation relations [67].

Although not necessary for the remaining derivation in this paper, we note that Eq. (4.13) is expressed in [56] in a different form in the interaction picture as

$$\int dt_2 dt_1 e^{i\omega(t_1-t_2)} \mathrm{Tr}\big(\rho(\infty) a^\dagger_{\mathrm{pr}}(t_2) a_{\mathrm{pr}}(t_1)\big), \tag{4.15}$$

where $a_{\mathrm{pr}}(t)$ is now the input field operator of the probe field. $\rho(\infty)$ is the combined system plus field state in the interaction picture, evolved to a time longer than t_1 and t_2. The term $\rho(\infty)$ is somewhat non-intuitive. To show the equality between Eqs. (4.13) and (4.15), one considers how the input and output operators are related by unitary time-evolution operators. This is explained in Sec. 3.2.1 and described more explicitly in Appendix E.

Under the dipole-electric field interaction and taking the zeroth order Hamiltonian as the pure system plus pure field Hamiltonian, we can write the interaction picture Hamiltonian as

$$\begin{aligned} H(t) = &- i a_{\mathrm{pr}}(t) L^\dagger_{\mathrm{pr}}(t) + i a^\dagger_{\mathrm{pr}}(t) L_{\mathrm{pr}}(t) \\ &+ \sum_{i=1}^{n} -i\alpha_i(t) L^\dagger_i(t) + i\alpha^*_i(t) L_i(t). \end{aligned} \tag{4.16}$$

Eq. (4.16) consists of the system interaction with the quantum probe field, represented by the field operator $a_{\mathrm{pr}}(t)$, and with n other classical pulses, represented by their complex-valued coherent amplitudes $\alpha_i(t)$. The operators L_{pr} and L_i are the matter de-excitation components of the dipole operator corresponding to the probe field and the field of the i-th classical pulse, respectively. In the interaction picture, $L(t) = e^{iH_{\mathrm{sys}}t} L e^{-iH_{\mathrm{sys}}t}$ is a purely system operator (setting $\hbar = 1$).

Under the Hamiltonian of Eq. (4.16), the input-output relation for the probe field is [50–52]

$$a_{\mathrm{pr,out}}(t) = a_{\mathrm{pr}}(t) + L_{\mathrm{pr,H}}(t), \tag{4.17}$$

with $a_{\mathrm{pr,out}}(t)$ the output probe field operator and $a_{\mathrm{pr}}(t)$ the input probe field operator. Here $L_{\mathrm{pr,H}}(t)$ is the Heisenberg evolved operator, defined as $U^\dagger(t) L_{\mathrm{pr}}(t) U(t)$, where $U(t)$ is the time-evolution operator that solves the Schrodinger equation in the interaction picture, i.e., $dU(t)/dt = -iH(t)U(t)$. The physical interpretation of Eq. (4.17) is that the output electric field is equal to the input electric field plus the electric field generated by the matter dipole moment. $L_{\mathrm{pr}}(t)$, without the subscript "H", will denote the operator in the interaction picture, which as noted above, is a purely system operator. In contrast, $L_{\mathrm{pr,H}}(t)$ now mixes the system and field degrees of freedom. Performing a perturbative expansion on the backward Heisenberg equation of motion for $L_{\mathrm{pr,H}}(t)$ [64], we have

$$\begin{aligned} L_{\mathrm{pr,H}}(t) = &L_{\mathrm{pr}}(t) - i\int_{-\infty}^{t} dt_1 [L_{\mathrm{pr}}(t), H(t_1)] \\ &+ (-i)^2 \int_{-\infty}^{t} dt_2 \int_{-\infty}^{t_2} dt_1 [[L_{\mathrm{pr}}(t), H(t_2)], H(t_1)] \\ &+ (-i)^3 \int_{-\infty}^{t} dt_3 \int_{-\infty}^{t_3} dt_2 \int_{-\infty}^{t_2} dt_1 [[[L_{\mathrm{pr}}(t), H(t_3)], H(t_2)], H(t_1)] \\ &+ \cdots . \end{aligned} \tag{4.18}$$

The first term on right-hand side of Eq. (4.18) can be interpreted as the matter dipole moment without interacting with the light, the second term as the matter dipole moment due to interacting with the field once, the third term as the matter dipole moment due to two interactions with the field, and so on. After expanding the commutators, each term becomes a product of a pure system operator and a pure field operator. Therefore the expectation values of $L_{\mathrm{pr,H}}(t)$ with respect to an initial product state can be readily evaluated.

Substituting Eqs. (4.17) and (4.18) into the Tr operator in Eq. (4.13), we obtain the following expansion for the two-point correlation function of the output signal:

$$\begin{aligned}\mathrm{Tr}\big(\rho(-\infty)a^\dagger_{\mathrm{pr,out}}(t_2)a_{\mathrm{pr,out}}(t_1)\big) &= \Big\langle a^\dagger_{\mathrm{pr,out}}(t_2)a_{\mathrm{pr,out}}(t_1)\Big\rangle \\ &= \Big\langle \Big(a^\dagger_{\mathrm{pr}}(t_2) + L^\dagger_{\mathrm{pr}}(t_2) - i\int_{-\infty}^{t_2} d\tau[L^\dagger_{\mathrm{pr}}(t_2), H(\tau)] + \cdots\Big) \\ &\qquad \Big(a_{\mathrm{pr}}(t_1) + L_{\mathrm{pr}}(t_1) - i\int_{-\infty}^{t_1} d\tau[L_{\mathrm{pr}}(t_1), H(\tau)] + \cdots\Big)\Big\rangle.\end{aligned} \tag{4.19}$$

Here we have adopted the conventional notation of using an angled bracket $\langle\hat{O}\rangle = \mathrm{Tr}(\rho(-\infty)\hat{O})$ to denote the expectation value of an operator $\hat{O}$ with respect to the initial system plus field state $\rho(-\infty)$.

We now expand the right-hand side of Eq. (4.19) in orders of L_{pr}. To show that L_{pr} is indeed proportional to a small parameter, first notice that L_{pr}, a_{pr}, and the L_{i} and α_i from the semi-classical terms of the Hamiltonian (Eq. (4.16)) all have the same dimension of $1/\sqrt{\mathrm{time}}$ (setting $\hbar = 1$). Since $\langle L^\dagger_{\mathrm{pr}}(t)L_{\mathrm{pr}}(t)\rangle$ ($\langle L^\dagger_i(t)L_i(t)\rangle$) is at most equal to the spontaneous emission rate into the probe field (i^{th} classical field), where the maximum rate is obtained when the matter state is in the bright state of the corresponding field mode, we assign an order of magnitude value

$$L \sim \sqrt{\eta/\tau_{\mathrm{emission}}} \tag{4.20}$$

to each L, where τ_{emission} is the time scale of spontaneous emission into the polarization of that field mode, and η is the geometric factor of the field mode [52,53]. η is less than 1 because a paraxial mode in an experiment usually covers only a small fraction of all light with the polarization of that paraxial mode. For a light pulse containing an average of m photons, we have $\int dt\langle a^\dagger(t)a(t)\rangle = m$ (for classical pulses, we replace the operator $a(t)$ with the coherent amplitude $\alpha(t)$). Therefore we assign an order of magnitude value

$$a(t), \alpha(t) \sim \sqrt{m/\tau_{\mathrm{pulse}}} \tag{4.21}$$

to each $a(t)$ or $\alpha(t)$, where τ_{pulse} characterizes the pulse duration. In typical visible spectroscopy experiments with atomic and molecular samples, $\tau_{\mathrm{emission}} \gg \tau_{\mathrm{pulse}}$, so that the matter system dynamics is observable before spontaneous emission removes the excitation. Furthermore, since $m \gg 1$ for typical classical pulses and $m = 1$ for the single photon probe pulse, we conclude that the magnitude of L is much smaller than the magnitude of a_{pr} and α_i, justifying an expansion in powers of the L operators. We then choose to expand Eq. (4.19) only in orders of L_{pr}, since the orders of L_i do not affect the main result, i.e., the equivalence of signals originating from a single photon Fock state probe and a single photon coherent state probe. Furthermore, since L_i always appears together with the classical pulse amplitude α_i, the effect of L_i is amplified by a factor of $\sqrt{m}$, so L_{pr} becomes indeed the smallest parameter in the expansion of Eq. (4.19). We now analyze the three lowest order contributions to the expansion.

Zeroth order term ($\sim {L_{pr}}^0$). The only zeroth order term in Eq. (4.19) is $\langle a^\dagger_{\mathrm{pr}}(t_2)a_{\mathrm{pr}}(t_1)\rangle$, the transmitted probe without any interaction with matter. This expectation value is the same for both the single photon Fock state (Eq. (4.10)) and the single photon coherent state (Eq. (4.11)), namely

$$\langle a^\dagger_{\mathrm{pr}}(t_2)a_{\mathrm{pr}}(t_1)\rangle = \xi^*(t_2)\xi(t_1), \tag{4.22}$$

where $\xi(t)$ is the pulse shape. For the m-photon coherent state (Eq. (4.12)), Eq. (4.22) is amplified by a factor of m.

First order terms ($\sim {L_{pr}}^1$). Any first-order term in Eq. (4.19) must be the expectation value of a product between $a^{(\dagger)}_{\mathrm{pr}}$ and another term containing a single factor of L_{pr}, or its complex conjugate.

In other words, only the semi-classical part of the Hamiltonian can contribute in the commutators of Eq. (4.19); otherwise, there will be more than one factor of L_{pr}. Specifically, the first-order terms take the form

$$\int d\tau_l \cdots d\tau_1 \Big\langle a_{\mathrm{pr}}^\dagger(t_2) \Big[\big[\cdots \big[L_{\mathrm{pr}}(t_1), \alpha_{i_l}^{(\pm)}(\tau_l) L_{i_l}^{(\mp)}(\tau_l) \big], \cdots \big], \alpha_{i_1}^{(\pm)}(\tau_1) L_{i_1}^{(\mp)}(\tau_1) \Big] \Big\rangle, \tag{4.23}$$

and its complex conjugates. Here $l = 0, 1, 2, \cdots$, and each i index can denote any one of the n classical field interactions. The probe field operators (i.e., a_{pr} or $a_{\mathrm{pr}}^\dagger$) are highlighted in blue, while the matter operator associated with the probe field (i.e., L_{pr} or $L_{\mathrm{pr}}^\dagger$) are highlighted in yellow. When $l = 0$, Eq. (4.23) reduces to $\langle a_{\mathrm{pr}}^\dagger(t_2) L_{\mathrm{pr}}(t_1) \rangle$. The notation $\alpha_i^{(\pm)}(\tau) L_i^{(\mp)}(\tau)$ means either $\alpha_i^*(\tau) L_i(\tau)$ or $\alpha_i(\tau) L_i^\dagger(\tau)$.

We note that the optical signal expression of Eq. (4.23) applies not just to the case of a single molecule, but also to the case of many molecules. This is because the matter operators L of different molecules commute with each other, so that Eq. (4.23) is nonzero only if all the L operators in the commutator originate from the same molecule. This argument applies to all signal expressions in the remainder of the paper. The fact that there are many molecules in our matter system gives rise to phase matching conditions, which we describe in the following paragraph.

Physically, Eq. (4.23) represents the heterodyne measurement between the probe field (i.e., the $a_{\mathrm{pr}}^\dagger$ in the first line) and the field generated by the matter polarization that is induced by the interactions with the classical fields (the second line). In all of the first order terms, the probe field expectation value factorizes out as $\langle a_{\mathrm{pr}}^\dagger(t) \rangle$ or $\langle a_{\mathrm{pr}}(t) \rangle$. These one-point correlation functions are zero for Fock state inputs and nonzero for coherent state inputs; therefore Eq. (4.23) is different for Fock state and coherent state inputs. However, the optical signal generated by the matter polarization has the phase matching condition [46, 64, 110]

$$\mathbf{k}_{\mathrm{sig}} = \mathbf{k}_{i_1} \pm \cdots \pm \mathbf{k}_{i_l}, \tag{4.24}$$

where the k_i on the right-hand side are the wavevectors of the classical pulses. This means that $\mathbf{k}_{\mathrm{sig}}$ must be in a different direction than the probe field direction $\mathbf{k}_{\mathrm{pr}}$, due to our assumption of the beam geometry in Eq. (4.9), i.e., the probe pulse is not phase matched with any of the classical pulses. Therefore the probe field signal of Eq. (4.23) will vanish because it is not phase-matched to the matter polarization. At the molecular level, this means that in our beam geometry, the polarization from different molecules will generate destructively interfering signals and result in zero overall signal. Hence the first order ($\sim {L_{\mathrm{pr}}}^1$) signal does not contribute to the probe field output.

Second order terms ($\sim {L_{pr}}^2$). There are two types of second order terms. The first type is related to spontaneous emission and takes the form

$$\text{Type 1: } \int d\tau_l \cdots d\tau_1 d\sigma_p \cdots d\sigma_1 \Big\langle \Big[\big[\cdots \big[L_{\mathrm{pr}}^\dagger(t_2), \alpha_{i_l}^{(\pm)}(\tau_l) L_{i_l}^{(\mp)}(\tau_l) \big], \cdots \big], \alpha_{i_1}^{(\pm)}(\tau_1) L_{i_1}^{(\mp)}(\tau_1) \Big] \Big[\big[\cdots \big[L_{\mathrm{pr}}(t_1), \alpha_{j_p}^{(\pm)}(\sigma_l) L_{j_p}^{(\mp)}(\sigma_l) \big], \cdots \big], \alpha_{j_1}^{(\pm)}(\sigma_1) L_{j_1}^{(\mp)}(\sigma_1) \Big] \Big\rangle. \tag{4.25}$$

The integrand is a product of two nested commutators. Here l and p can take values of $0, 1, 2, \cdots$. Each of the i and j indices can be any one of the n semi-classical interactions of the Hamiltonian. We take only the semi-classical part of the Hamiltonian in the commutators, since there is already one L_{pr} in each of the two nested commutators. Otherwise Eq. (4.25) will contain more than two L_{pr}, becoming a higher-order term. In the case of $l = p = 0$, Eq. (4.25) becomes $\langle L_{\mathrm{pr}}^\dagger(t_2) L_{\mathrm{pr}}(t_1) \rangle$: this represents spontaneous emission into the probe field without any interaction with the classical pulses.

Since Eq. (4.25) contains no probe field operator (i.e., no a_{pr} or $a_{\mathrm{pr}}^\dagger$ terms), the expectation value is the same for all input field states, regardless of the phase matching conditions. For completeness, we note that the phase matching condition for these terms is [64]

$$0 = \mathbf{k}_{i_1} \pm \cdots \pm \mathbf{k}_{i_l} \pm \mathbf{k}_{j_1} \pm \cdots \pm \mathbf{k}_{j_p}. \tag{4.26}$$

The second type of second-order terms is related to absorption and stimulated emission, and has the form of

$$\text{Type 2: } \int d\tau_l \cdots d\tau_1 \Big\langle a_{\mathrm{pr}}^\dagger(t_2) \Big[\big[\cdots [[\cdots [L_{\mathrm{pr}}(t_1), \alpha_{i_l}^{(\pm)}(\tau_l) L_{i_l}^{(\mp)}(\tau_l)], \cdots], a_{\mathrm{pr}}^{(\pm)}(\tau_j) L_{\mathrm{pr}}^{(\mp)}(\tau_j) \big], \cdots \big], \alpha_{i_1}^{(\pm)}(\tau_1) L_{i_1}^{(\mp)}(\tau_1) \Big] \Big\rangle \tag{4.27}$$

and its complex conjugate. In the nested commutator expression here, there is exactly one interaction with the quantum probe field. Physically, Eq. (4.27) represents the heterodyne measurement between the probe field (i.e., the $a_{\mathrm{pr}}^\dagger$ in the first line) and the field generated by the matter polarization that is induced by one interaction with the quantum probe field and a number of interactions with the classical fields (the second line). The notation of the probe interaction term $a_{\mathrm{pr}}^{(\pm)}(\tau_j) L_{\mathrm{pr}}^{(\mp)}(\tau_j)$ stands for either the product $a_{\mathrm{pr}}^\dagger(\tau_j) L_{\mathrm{pr}}(\tau_j)$ or $a_{\mathrm{pr}}(\tau_j) L_{\mathrm{pr}}^\dagger(\tau_j)$.

When the probe field interaction is $a_{\mathrm{pr}}^\dagger(\tau_j) L_{\mathrm{pr}}(\tau_j)$, the probe field correlation in Eq. (4.27) factorizes out as $\langle a_{\mathrm{pr}}^\dagger(t_2) a_{\mathrm{pr}}^\dagger(\tau_j) \rangle$, which is zero for Fock state inputs and nonzero for coherent state inputs. Now the optical signal generated by the matter polarization has the phase matching condition of

$$\mathbf{k}_{\mathrm{sig}} = \mathbf{k}_{i_1} \pm \cdots - \mathbf{k}_{\mathrm{pr}} \cdots \pm \mathbf{k}_{i_l}, \tag{4.28}$$

where the right hand side contains only one probe field wavevector k_{pr}, and all other k_i are the classical pulse wavevectors. But as discussed above, $\mathbf{k}_{\mathrm{sig}}$ cannot be in the same direction as $\mathbf{k}_{\mathrm{pr}}$ due to our assumption of the beam geometry in Eq. (4.9). Therefore the final signal is not phase matched in the probe field direction $\mathbf{k}_{\mathrm{pr}}$ and will vanish. So neither a Fock state input nor a coherent state input will produce any signal from the $a_{\mathrm{pr}}^\dagger(\tau_j) L_{\mathrm{pr}}(\tau_j)$ interaction in this direction.

On the other hand, when the probe field interaction in Eq. (4.27) is $a_{\mathrm{pr}}(\tau_j) L_{\mathrm{pr}}^\dagger(\tau_j)$, the field correlation now factorizes as $\langle a_{\mathrm{pr}}^\dagger(t_2) a_{\mathrm{pr}}(\tau_j) \rangle$, which is the same for both the single-photon Fock state and single-photon coherent state inputs, regardless of the phase-matching condition. These terms represent the transient absorption/stimulated emission of the probe field due to the interaction with the classical pulses. In this case the phase matching condition of the optical signal generated by the matter polarization is now

$$\mathbf{k}_{\mathrm{sig}} = \mathbf{k}_{i_1} \pm \cdots + \mathbf{k}_{\mathrm{pr}} \cdots \pm \mathbf{k}_{i_l}, \tag{4.29}$$

where the right hand side consists of only one probe field wavevector k_{pr}, and all other k_i are the classical pulse wavevectors. We see that now if the classical pulse wavevectors cancel each other out pairwise, then we will have the correct phase matching condition of $k_{\mathrm{sig}} = k_{\mathrm{pr}}$ that results in a non-zero final signal in the probe field.

Due to the weak nature of the interaction between a single photon and a molecule (for example the probability for a chlorophyll molecule to absorb a single photon is at most on the order of $\sim 10^{-6}$ due to phonon dephasing [52, 59]), it is reasonable to truncate Eq. (4.19) up to second order in L_{pr}. This second-order truncation corresponds to one interaction with the probe field in the language of classical nonlinear spectroscopy [46].

We may then combine the analysis for all of the terms up to second order in L_{pr} (i.e., Eqs. (4.22), (4.23), and (4.25), and the two cases in Eq. (4.27)). Doing this, we see first that while the first-order contribution Eq. (4.23) and the first case of the second type of second-order contribution Eq. (4.27) yield different values for Fock state and coherent state inputs, neither of these terms appears in the final signal due to the phase matching constraint, so they cannot contribute to a difference between Fock and coherent state inputs. In contrast, the zeroth-order contribution Eqs. (4.22), the first type of the second-order contribution (4.25), and the second case of the second type of second order contribution Eq. (4.27) yield the same value for both Fock state and coherent state inputs, and these terms do have the correct phase matching condition to contribute to the final signal. Therefore, provided that the coherent state has the same temporal profile as the Fock state, a single photon Fock state probe and a single photon coherent state probe will produce exactly the same signal in the experimental setups of Fig. (4.1b) and (4.1c). Furthermore, a many photon coherent state probe with the same temporal profile will amplify the signals of Eq. (4.22) and the second case of Eq. (4.27) by a factor of m, where m is the average number of photons.

4.3 Example: Pump quantum-inspired probe (PQIP) spectroscopy

To demonstrate this equivalence between an entangled photon probe and a coherent state probe, we consider here the specific example of the classical pump - quantum probe experiment described theoretically in [56], which corresponds to the case of a single classical pump pulse, i.e., $n = 1$ in Fig. (4.1). We then compare this experiment to the corresponding classical pump - quantum-inspired classical probe experiment, which we shall refer to as "pump quantum-inspired probe" (PQIP). In this experiment, a delta-function classical pump first excites a four-level matter system from the ground state $|g\rangle$ to the singly excited state $|e\rangle$, which transfers the excitation to another lower-energy singly excited state $|e'\rangle$ irreversibly with a rate k (see Fig. (4.2a)). These energy transfer dynamics are monitored by the transient absorption of a probe pulse (delayed by time t_0 from the pump pulse) that excites $|e\rangle$ or $|e'\rangle$ into the doubly excited state $|f\rangle$. In [56], the probe pulse was taken to be either a classical pulse or an entangled photon pair. Fig. (4.2c) shows the calculated transient absorption spectrum using a conventional classical probe pulse consisting of a single gaussian with frequency width $\sigma = 600\ \mathrm{cm}^{-1}$, covering both transition frequencies from $|e\rangle$ and $|e'\rangle$ to $|f\rangle$. The structure of the two peaks centered at different delay times reveal the energy transfer dynamics from $|e\rangle$ to $|e'\rangle$.

In the case of a biphoton probe, the photon pair state $|\Psi\rangle$ is given by Eq. (4.2), with the biphoton wavefunction $\Phi(\omega_{\mathrm{pr}}, \omega_r)$. One photon (the reference photon) of the probe photon pair does not interact with the matter system and its frequency ω_r is measured. The other photon (the probe signal photon) interacts with the matter system and is frequency-resolved. For each ω_r, there is a transient absorption spectrum as a function of the signal frequency ω and delay time t_0. As discussed in [56], due to the frequency correlation in the entangled photon pair, by selecting different values of ω_r, one can target specific frequency windows of the transient absorption spectrum, thereby simplifying the spectrum.

The theoretical analysis of these spectra obtained from biphoton pulses proceeds as follows. The pump-probe signal for a fixed reference photon frequency ω_r is the difference between the output and the input signals

$$\langle a_r^\dagger(\omega_r) a_r(\omega_r) a_{\mathrm{pr,out}}^\dagger(\omega) a_{\mathrm{pr,out}}(\omega)\rangle - \langle a_r^\dagger(\omega_r) a_r(\omega_r) a_{\mathrm{pr}}^\dagger(\omega) a_{\mathrm{pr}}(\omega)\rangle. \tag{4.30}$$

If no reference photon is used, the pump-probe signal becomes

$$\langle a_{\mathrm{pr,out}}^\dagger(\omega) a_{\mathrm{pr,out}}(\omega)\rangle - \langle a_{\mathrm{pr}}^\dagger(\omega) a_{\mathrm{pr}}(\omega)\rangle. \tag{4.31}$$

Applying Eqs. (4.17) and (4.18), the lowest order term of Eq. (4.30), represented by the double-sided

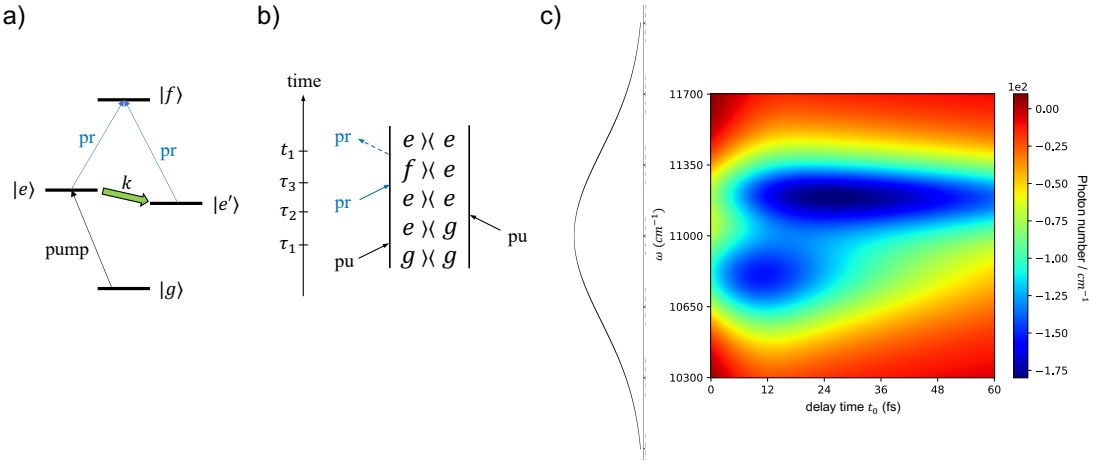

Figure 4.2: (a) Energy level scheme with four levels from [56], which we use for our numerical example. The pump pulse is resonant to only the $|g\rangle \to |e\rangle$ transition. The probe pulse is resonant to only the $|e\rangle \to |f\rangle$ and $|e'\rangle \to |f\rangle$ transitions. (b) Double-sided Feynman diagram representing the excited state absorption of the pump-probe signal. The order of the first two pump interactions can be switched. (c) Transient absorption spectrum due to a conventional classical probe. The spectrum plots the change in the probe field frequency-resolved photon count $\langle a^\dagger_{\rm pr}(\omega) a_{\rm pr}(\omega)\rangle$ at frequency ω, i.e., the signal photon number spectral density. This conventional classical probe has a Gaussian frequency profile $E(\omega) \propto e^{-(\omega-\omega_0)^2/2\sigma^2}$ ($\omega_0 = 11000$ cm^{-1}, $\sigma = 600$ cm^{-1}) and contains on average 10^6 photons. The frequency distribution $|E(\omega)|^2$ of the input probe pulse is plotted on the left of the spectrum.

Feynman diagram of Fig. (4.2b), is

$$-\int_{-\infty}^{\infty}\frac{dt_2}{\sqrt{2\pi}}\int_{-\infty}^{\infty}\frac{dt_1}{\sqrt{2\pi}}e^{i\omega(t_1-t_2)}\int_{-\infty}^{t_1}d\tau_3\int_{-\infty}^{\tau_3}d\tau_2\int_{-\infty}^{\tau_3}d\tau_1 \\ \Big\langle a_r^\dagger(\omega_r)a_r(\omega_r)a^\dagger_{\rm pr}(t_2)a_{\rm pr}(\tau_3)\Big\rangle\Big\langle L_{\rm pu}(\tau_1)L_{\rm pr}(t_1)L^\dagger_{\rm pr}(\tau_3)L^\dagger_{\rm pu}(\tau_2)\Big\rangle\alpha^*_{\rm pu}(\tau_1)\alpha_{\rm pu}(\tau_2) + \text{c.c.} \tag{4.32}$$

Note that Eq. (4.32) originates from the second-order ($\sim L^2_{\rm pr}$) expansion term of the form of Eq. (4.27). Substituting in the delta-function classical pump $\alpha_{\rm pu}(t) \propto \delta(t)$, Eq. (4.32) is now proportional to

$$-\int_{-\infty}^{\infty}d\omega'\Big\langle a_r^\dagger(\omega_r)a_r(\omega_r)a^\dagger_{\rm pr}(\omega)a_{\rm pr}(\omega')\Big\rangle \\ \int_0^\infty dt_1\int_0^{t_1}d\tau_3\, e^{i\omega t_1}e^{-i\omega'\tau_3}\Big\langle L_{\rm pu}(0)L_{\rm pr}(t_1)L^\dagger_{\rm pr}(\tau_3)L^\dagger_{\rm pu}(0)\Big\rangle + \text{c.c.} \tag{4.33}$$

Since the field correlation function in Eq. (4.33) with a time delay of t_0 evaluates to

$$\langle a_r^\dagger(\omega_r)a_r(\omega_r)a^\dagger_{\rm pr}(\omega)a_{\rm pr}(\omega')\rangle = \Phi^*(\omega,\omega_r)\Phi(\omega',\omega_r)e^{i(\omega'-\omega)t_0}, \tag{4.34}$$

The signal Eq. (4.33) can be expressed compactly as [56]

$$-\text{Re}\int d\omega'\Phi^*(\omega,\omega_r)\Phi(\omega',\omega_r)\tilde{F}(\omega',\omega;t_0), \tag{4.35}$$

where

$$\tilde{F}(\omega',\omega;t_0) = \int_0^\infty dt_1\int_0^{t_1}d\tau_3\, e^{i\omega(t_1-t_0)}e^{-i\omega'(\tau_3-t_0)}\Big\langle L_{\rm pu}(0)L_{\rm pr}(t_1)L^\dagger_{\rm pr}(\tau_3)L^\dagger_{\rm pu}(0)\Big\rangle \tag{4.36}$$

is the frequency-domain matter correlation function defined in [56].

The detailed model of the matter system, the corresponding analytical form of $\tilde{F}(\omega', \omega; t_0)$, and the analytical form of $\Phi(\omega_{\rm pr}, \omega_r)$ are discussed in [56] and summarized in Appendix F. Similarly, if a single photon Fock state or a coherent state is used as the probe, then the pump-probe signal Eq. (4.31) becomes

$$-\mathrm{Re} \int d\omega' \xi^*(\omega) \xi(\omega') \tilde{F}(\omega', \omega; t_0), \tag{4.37}$$

where $\xi(\omega)$ is the frequency profile of the probe pulse (see Eqs. (4.10)-(4.12)).

Comparing Eq. (4.35) and Eq. (4.37), we observe that if we choose a quantum-inspired coherent state probe with coherent amplitude $\xi_{\rm pr}(\omega) = \Phi(\omega, \omega_r)$, the final signal is exactly proportional to Eq. (4.35) at a fixed reference photon frequency ω_r. Therefore the classical pump - quantum probe experiment can be exactly reproduced using a standard classical pump - classical probe setup, with the only additional feature of requiring a pulse shaper for the quantum-inspired classical probe pulse. The shape of the quantum-inspired classical probe is parameterized by ω_r, together with the other parameters of the biphoton pulse (see Appendix F).

The classical pump - quantum probe spectra with biphoton pulses, characterized by two choices of ω_r, are shown in the left-hand panels (a) and (b) of Fig. (4.3). The signal is detected in the probe beam direction, in accordance with the phase matching requirement discussed in Equivalence 2. The simplification of the spectra relative to the conventional pump-probe spectrum in Fig. (4.2) is immediately evident, with the two peaks now clearly resolved, permitting a more detailed analysis of the coupled dynamics underlying the two spectra.

The corresponding PQIP spectra are shown in the right-hand panels (c) and (d) of Fig. (4.3). In the numerical simulation, we use a classical probe containing an average of $m = 10^6$ photons to amplify the final signal by a factor of 10^6. As noted above, this has the additional benefit of making the signal detection much easier experimentally than when using an entangled biphoton probe. When the amplified signals are normalized to the same reference value as that for panels (a) and (b), the left- and right-hand panels of Fig. (4.3) are identical to within numerical precision, validating the PQIP analysis. The specific quantum-inspired pulses that produce the same spectra as the biphoton probe with ω_r values in panels (a) and (b) of Fig. (4.2) are given explicitly in Section B of the Supporting Information.

4.4 Reflection on quantum advantage of QLS

We have shown that for a class of QLS experiments consisting of $n = 0, 1, 2 \cdots$ classical pulses and an entangled photon pair probe in the scheme of Fig. (4.1a), the use of the entangled photon pair can be replaced with a specially designed coherent state pulse, which behaves as classical light when normal-ordered field correlations are evaluated. The two main requirements for this equivalence to hold are the following: (1) there is no phase matching of the classical pulses into the direction of the probe field, and (2) signal measurement takes the form of (time-integrated) photon flux, frequency-resolved photon count, or $g^{(1)}(t)$ correlation function. In this work we also demonstrated the validity of the analysis by explicit calculations of the signal for a classical pump – entangled photon probe experiment, showing numerical equivalence with the signal obtained from a classical pump with a coherent state pulse that is constructed according to the two equivalences.

There is in fact a larger class of QLS experiments that can be emulated using classical light pulses. More generally, whenever a biphoton input is used and one of the photons is measured at frequency ω_r, without interacting with anything, so that the signal consists of field correlation functions of the form $\langle a_r^\dagger(\omega_r) a_r(\omega_r) a^\dagger(t_2) a(t_1) \rangle$, the signal can be reproduced using coherent state

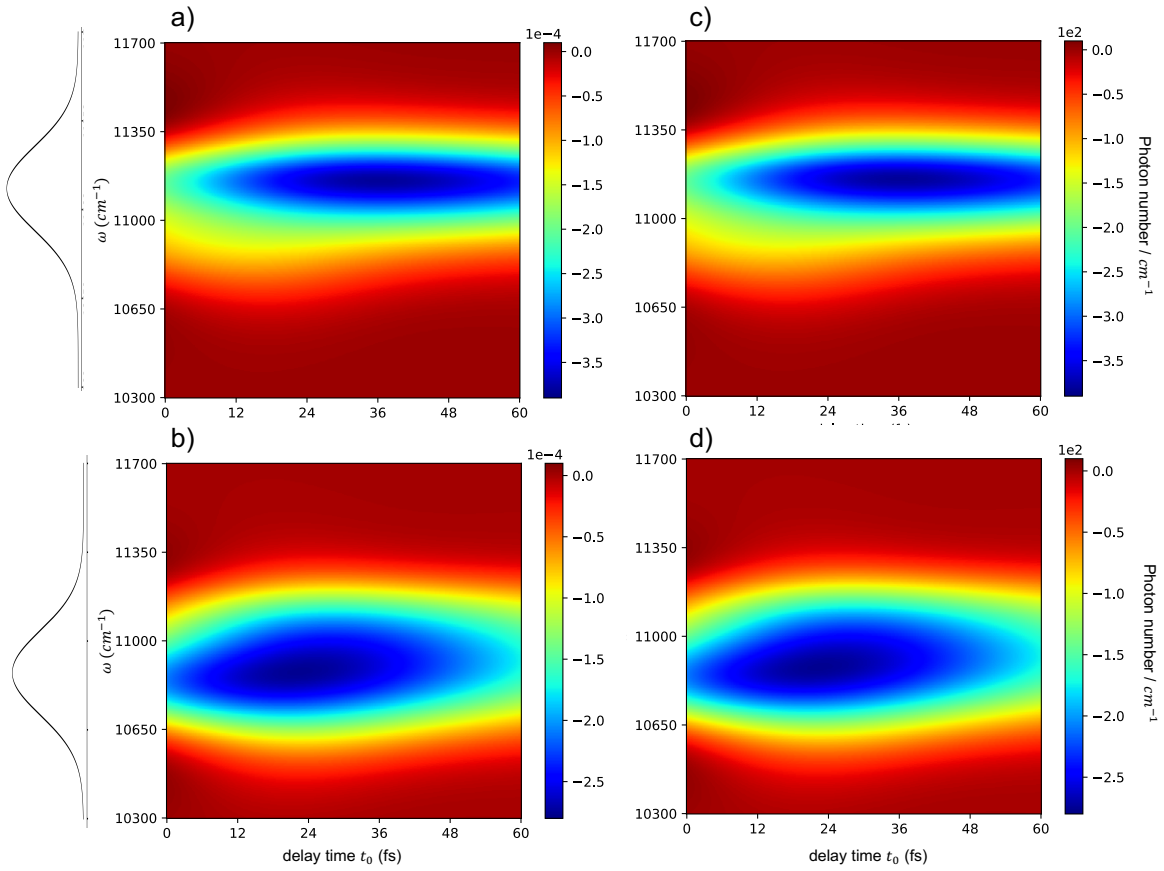

Figure 4.3: Transient absorption spectra obtained using (a-b) an entangled biphoton probe or (c-d) quantum-inspired classical probes. The signal is the change of the probe field frequency-resolved photon count $\langle a^\dagger(\omega)a(\omega)\rangle$ at frequency ω, i.e., the signal photon number spectral density. In panels (a) and (b), the signal is conditioned on the reference photon frequencies of (a) $\omega_r = 11400$ cm^{-1} (b) $\omega_r = 10400$ cm^{-1}. On the left of each spectrum is the frequency distribution $|\Phi(\omega, \omega_r)|^2$ of the probe single photon for fixed ω_r. In panels (c) and (d), classical probes with frequency profiles $\xi(\omega) = \Phi(\omega, \omega_r)$ are used, where $\omega_r = 11400$ cm^{-1} in (c) and $\omega_r = 10400$ cm^{-1} in (d), corresponding to panels (a) and (b), respectively. The classical probe pulses contain 10^6 photons on average, resulting in 10^6 times signal amplification. Note that the scales of the color bars in (c) and (d) are 10^6 larger than those in (a) and (b).

pulses that are specifically designed for the biphoton state and reference frequency. For example, we can go beyond the dipole – electric field interaction used in this paper and allow for Raman scattering interactions. The intensity correlated Raman signal in [105] and the (1,0) component of the interferometric stimulated Raman signal in [101] depend on the biphoton input through the correlation function $\langle a_r^\dagger(\omega_r) a_r(\omega_r) a_{\rm pr}^\dagger(t_2) a_{\rm pr}(t_1)\rangle$. These experiments also use a biphoton state as an input, with one of the photons acting as the reference. The reference photon does not interact with anything and its frequency ω_r is measured. Therefore these QLS experiments can also be reproduced by classical pulses parameterized by the biphoton wavefunction and the reference photon frequency.

Going beyond the scope of analysis in this paper, one may also consider the effect of the environmental background photon noise (i.e., dark counts) on spectroscopy with entangled photons [102]. Here the signal-to-dark-count improvement offered by entangled photon pairs described in [102], can be achieved by using pulsed classical light in only the signal arm and detecting the output photon only in the time window Δt that is set to be equal to the pulse duration. This is because the number of dark count photons during the detection time window is linearly proportional to Δt, so by using a classical pulse with a short duration (i.e., small Δt), one can reduce the number of dark count photons and increase the signal-to-dark-count ratio.

We can also consider the effect of noise due to the uncertainty of the photon number or the noise due to detector inefficiency. For simplicity, we shall refer here to both of these uncertainties as measurement shot noise. Using a 100% efficient photon detector, the detection of a single photon has zero shot noise. Therefore the signal-to-noise of a single photon from one half of an entangled photon pair cannot be achieved using classical pulses. However if the photon detector is not perfectly efficient, the detection of a single photon will contain a nonzero shot noise. Then the signal-to-noise ratio for the detection of a single photon can be achieved or surpassed by using a coherent state pulse with large enough amplitude. This is because the signal-to-noise ratio of a coherent state under both perfectly efficient or inefficient photon detectors is equal to $\sqrt{\text{average number of photons detected}}$ [22]. Therefore by increasing the coherent state amplitude, one can systematically improve the signal-to-noise ratio.

Finally, we note that while some QLS experiments can be reproduced using carefully designed classical light sources as shown here, at the same time the technologies for generation and detection of quantum light are maturing, raising the possibility of a new generation of QLS experiments. The equivalence between entangled biphoton probes and classical-like coherent state probes shown in this work leads to a new category of quantum-inspired classical spectroscopy experiments, such as the pump quantum-inspired probe experiment. An understanding of the range of applicability of the equivalence demonstrated here will provide insights for future design of more powerful QLS experiments that cannot be replicated by suitably designed quantum-inspired classical pulses and that could provide a true quantum advantage for the study of electronic dynamics in complex systems.

Chapter 5

Normal-ordered perturbative expansion of the reduced system state

So far, we have focused on the perturbative expansion of the output photon field in the Heisenberg picture. We have shown in Sec. 3.4 that this expansion can be written in a form that contains only normal-ordered field operators, simplifying the calculation of the field expectation value. In this chapter, we will work in a modified interaction picture to show how to obtain a normal-ordered perturbative expansion of the reduced system state $\rho_{\text{sys}}(t) = \text{Tr}_{\text{field}}(\rho_{\text{tot}}(t))$. In this normal-ordered expansion of the reduced system state, the field expectation values only consist of normal-ordered field operators. We note that this normal-ordered expansion relies on the assumption that the initial total state $\rho_{\text{tot}}(0) = \rho_{\text{sys}}(0) \otimes \rho_{\text{field}}(0)$ is a product state between the initial system state $\rho_{\text{sys}}(0)$ and the initial field state $\rho_{\text{field}}(0)$. Conventional perturbative expansion of the reduced system state does not enforce normal-ordering, and one usually needs to evaluate expectation values of non-normal-ordered field operators. Since evaluating the expectation values of normal-ordered field operators is usually simpler than evaluating the expectation values of non-normal-ordered operators, this normal-ordered expansion can be more convenient to use. We shall first consider the case of a single molecule interacting with one spatial mode. Then we will generalize the normal-ordered expansion to many spatial modes.

5.1 Derivation

5.1.1 A different interaction picture

The normal-ordered perturbative expansion works in a modified interaction picture. We rotate out H_{field} from the total Hamiltonian

$$H_{\text{sys+field}} = H_{\text{sys}} + H_{\text{field}} + H_{\text{coup}} \tag{5.1}$$

(see Eq. (1.1)). Note that this is a different interaction picture Hamiltonian from the Hamiltonian used from Ch. 1 to Ch. 3. Previously, the interaction picture rotates out $H_{\text{sys}} + H_{\text{field}}$ from $H_{\text{sys+field}}$. Here, we only rotate out H_{field}. The Hamiltonian in this modified interaction frame is

$$H'(t) = e^{iH_{\text{field}}t}(H_{\text{sys}} + H_{\text{coup}})e^{-iH_{\text{field}}t}. \tag{5.2}$$

Similar to Eq. (1.26), we define a time evolution operator $U'(t)$ as the solution to

$$dU'(t)/dt = -iH'(t)U'(t) \tag{5.3}$$

with the initial condition $U'(0) = 1$. Therefore the total time evolution operator $e^{-iH_{\text{sys+field}}t}$ can be decomposed as

$$e^{-iH_{\text{sys+field}}t} = e^{-iH_{\text{field}}t}U'(t). \tag{5.4}$$

The total density matrix $\rho_{\text{S,tot}}(t)$ in the Schrodinger picture is transformed into the corresponding density matrix $\rho'_{\text{tot}}(t)$ in this interaction picture by the transformation

$$\rho'_{\text{tot}}(t) = e^{iH_{\text{field}}t}\rho_{\text{S,tot}}(t)e^{-iH_{\text{field}}t}. \tag{5.5}$$

Taking the partial trace over field and using the fact that Tr_{field} is invariant under the cyclic permutation of field operators, we have

$$\rho_{\text{sys}}(t) = \text{Tr}_{\text{field}}\big(\rho'_{\text{tot}}(t)\big) = \text{Tr}_{\text{field}}\big(\rho_{\text{S,tot}}(t)\big). \tag{5.6}$$

Therefore, the reduced system state obtained by the partial trace of $\rho'_{\text{tot}}(t)$ in the modified interaction picture is equal to the reduced system state obtained by the partial trace of $\rho_{\text{S,tot}}(t)$ in the Schrodinger picture.

$\rho'_{\text{tot}}(t)$ can also be expressed in terms of $U'(t)$ as

$$\rho'_{\text{tot}}(t) = U'(t)\rho_{\text{tot}}(0)U'^{\dagger}(t). \tag{5.7}$$

Since at time $t = 0$, $\rho_{\text{tot}}(0)$ in the interaction picture is the same as that in the Schrodinger picture, we will drop the " $'$ " on $\rho'_{\text{tot}}(0)$. Taking the time derivative, we obtain the Liouville-von Neumann equation in the interaction picture

$$\frac{d}{dt}\rho'_{\text{tot}}(t) = -i[H'(t), \rho'_{\text{tot}}(t)]. \tag{5.8}$$

Using the fact that H_{sys} commutes with H_{field} and following the derivation in Sec. 1.4, the Hamiltonian $H'(t)$ in Eq. (5.2) becomes

$$H'(t) = H_{\text{sys}} - ia(t)L^{\dagger} + ia^{\dagger}(t)L \tag{5.9}$$

for the case of a single-molecule and a single spatial mode. See Eq. (1.32) to compare this Hamiltonian with the Hamiltonian in the interaction picture used from Ch. 1 to Ch. 3.

5.1.2 Conventional perturbative expansion for the reduced system state

The usual perturbative expansion of the reduced system state makes use of the weak light-matter coupling strength, so that

$$|H_{\text{sys}}| \gg |-ia(t)L^{\dagger} + ia^{\dagger}(t)L|. \tag{5.10}$$

One way to derive the conventional perturbative expansion for the reduced system state is to first express the Liouville-Von Neumann equation (Eq. (5.8)) in superoperator form as

$$\frac{d}{dt}\rho'_{\text{tot}}(t) = \mathcal{K}'\rho'_{\text{tot}}(t) + \mathcal{L}(t)\rho'_{\text{tot}}(t), \tag{5.11}$$

where $\mathcal{K}'$ and $\mathcal{L}$ are superoperators defined as

$$\mathcal{K}' = -i[H_{\text{sys}}, \bullet] \tag{5.12}$$

and

$$\mathcal{L}(t) = [-a(t)L^\dagger + a^\dagger(t)L, \bullet]. \tag{5.13}$$

The superoperator notation using $\bullet$ means that the action of the superoperator on an operator is performed by substituting the operator into the $\bullet$. For example, $(-i[H_{\rm sys}, \bullet])\rho = -i[H_{\rm sys}, \rho]$. Solving the Liouville-Von Neumann equation (Eq. (5.11)) formally, we have

$$\rho'_{\rm tot}(t) = e^{\mathcal{K}'t}\rho'_{\rm tot}(0) + \int_0^t dt_1 e^{\mathcal{K}'(t-t_1)}\mathcal{L}(t_1)\rho'_{\rm tot}(t_1). \tag{5.14}$$

We note that $\mathcal{K}'(t-t')$ denotes the superoperator $\mathcal{K}'$ times the real-valued number $t-t'$, while $\mathcal{L}(t)$ means the superoperator $\mathcal{L}$ is a function of time t. The first term on the right hand side represents the free evolution due to $H_{\rm sys}$, while the second term represents the perturbation due to the interaction between the matter and the photon field. Substituting this expression into itself iteratively to obtain a perturbative series of $\rho'_{\rm tot}(t)$, and then take the partial trace over the field, we have

$$\begin{aligned}\rho_{\rm sys}(t) = \mathrm{Tr}_{\rm field}\Big(& e^{\mathcal{K}'t}\rho_{\rm tot}(0) \\ &+ \int_0^t dt_1\, e^{\mathcal{K}'(t-t_1)}\mathcal{L}(t_1)e^{\mathcal{K}'(t_1)}\rho_{\rm tot}(0) \\ &+ \int_0^t dt_2 \int_0^{t_2} dt_1\, e^{\mathcal{K}'(t-t_2)}\mathcal{L}(t_2)e^{\mathcal{K}'(t_2-t_1)}\mathcal{L}(t_1)e^{\mathcal{K}'(t_1)}\rho_{\rm tot}(0) \\ &+ \cdots\Big).\end{aligned} \tag{5.15}$$

This is the conventional perturbative expansion for the reduced system state. In this expansion, $\mathcal{K}'$ acts only on the system degrees of freedom. The field operators only appear in $\mathcal{L}$. The action of multiple $\mathcal{L}$ on $\rho_{\rm field}(0)$ will result in expectation values of non-normal-ordered field operators. For example, the second order term of the expansion contains 8 different field expectation values: $\langle a^\dagger(t_2)a^\dagger(t_1)\rangle$, $\langle a^\dagger(t_1)a^\dagger(t_2)\rangle$, $\langle a^\dagger(t_2)a(t_1)\rangle$, $\langle a^\dagger(t_1)a(t_2)\rangle$, $\langle a(t_2)a^\dagger(t_1)\rangle$, $\langle a(t_1)a^\dagger(t_2)\rangle$, $\langle a(t_2)a(t_1)\rangle$, and $\langle a(t_1)a(t_2)\rangle$. Two of these expectation values are not normal-ordered.

In the semi-classical treatment of light-matter interaction, one replaces the field operators $a(t)$ and $a^\dagger(t)$ with the classical complex-valued amplitudes $\alpha(t)$ and $\alpha^*(t)$. This corresponds to evaluating the expectation values of normal-ordered field operators with respect to a coherent state of light, since a coherent state $|\alpha\rangle$ is an eigenstate of the annihilation operator $a(s)$ (see Eq. (2.11)) [67]. However, this replacement is correct only for normal-ordered field operators. and the non-normal-ordered operators will give rise to quantum corrections to the semi-classical treatment. From the conventional expansion of Eq. (5.15), it is not easy to extract the quantum correction to the semi-classical treatment. The normal ordered expansion described in Sec. 3.4 cannot be used here because $\rho_{\rm field}$ usually can not be expressed simply as a normal ordered operator.

5.1.3 Normal-ordered perturbative expansion for the reduced system state

To derive the normal-ordered perturbative expansion of the system state, we first need to derive the identity

$$[a(t), U'(t)] = \frac{1}{2}LU'(t). \tag{5.16}$$

The derivation is very similar to the derivation of the input-output relation in Sec. 2.1. First, we define $a(s,t)$ as $U'^\dagger(t)a(s)U'(t)$. Using Eqs. (5.3) and (5.9), we obtain

$$\frac{\partial a(s,t)}{\partial t} = \delta(s-t)U'^\dagger(t)LU'(t), \tag{5.17}$$

similar to Eq. (2.3). We assume $s > 0$, meaning that at time $t = 0$, the plane of the photon field $a(s)$ has not interacted with the molecule at the origin. Solving Eq. (5.17) using the initial condition $a(s, 0) = a(s)$, we have the input-output relation as

$$a(s,t) = \begin{cases} a(s) & , t < s \\ a(s) + \frac{1}{2}U'^{\dagger}(t)LU'(t) & , t = s \\ a(s) + U'^{\dagger}(t)LU'(t) & , t > s. \end{cases} \tag{5.18}$$

When $t < s$, the Heisenberg-evolved field operator $a(s, t)$ is identified as the input field. When $t > s$, $a(s, t)$ is identified as the output field. When $t = s$, the factor of $1/2$ originates from cutting the delta function in half. In the case of $t = s$, we have $U'^{\dagger}(t)a(t)U'(t) = a(t) + \frac{1}{2}U'^{\dagger}(t)LU'(t)$. Left multiplying both sides of this equation by $U'(t)$, then we arrive at the commutation relation of Eq. (5.16).

Using the commutation relation of Eq. (5.16), we can write the Schrodinger equation (Eq. (5.3)) in a normal-ordered form as

$$\begin{aligned} \frac{dU'(t)}{dt} &= -iH'(t)U'(t) \\ &= -iH_{\rm sys}U'(t) - L^{\dagger}a(t)U'(t) + a^{\dagger}(t)LU'(t) \\ &= -iH_{\rm sys}U'(t) - L^{\dagger}\big(\frac{1}{2}LU'(t) + U'(t)a(t)\big) + a^{\dagger}(t)LU'(t) \\ &= \big(-iH_{\rm sys} - \frac{1}{2}L^{\dagger}L\big)U'(t) - L^{\dagger}U'(t)a(t) + a^{\dagger}(t)LU'(t). \end{aligned} \tag{5.19}$$

This allows us to express the time derivative of the reduced time evolution superoperator as

$$\begin{aligned} &\frac{d}{dt}{\rm Tr}_{\rm field}\Big(U'(t) \bullet U'^{\dagger}(t)\Big) \\ &= {\rm Tr}_{\rm field}\Big(-i\big[H_{\rm sys}, U'(t) \bullet U'^{\dagger}(t)\big] - \frac{1}{2}\big\{L^{\dagger}L, U'(t) \bullet U'^{\dagger}(t)\big\} \\ &\qquad - L^{\dagger}U'(t)a(t) \bullet U'^{\dagger}(t) - U'(t) \bullet a^{\dagger}(t)U'^{\dagger}(t)L \\ &\qquad + U'(t) \bullet U'^{\dagger}(t)L^{\dagger}a(t) + a^{\dagger}(t)LU'(t) \bullet U'^{\dagger}(t)\Big). \end{aligned} \tag{5.20}$$

The notation $\{A, B\} = AB + BA$ denotes the anticommutator. To obtain the normal-ordered perturbative expansion, we want to turn this expression into to a form such that all $a(t)$ appear on the left of $\bullet$ as $U'(t)a(t) \bullet U'^{\dagger}(t)$ and all $a^{\dagger}(t)$ appear on the right of $\bullet$ as $U'(t) \bullet a^{\dagger}(t)U'^{\dagger}(t)$. The reason for this arrangement will be clearer when we later substitute the $\bullet$ with $\rho'_{\rm tot}(0) = \rho_{\rm sys}(0) \otimes \rho_{\rm field}(0)$, so the field expectation value takes the form ${\rm Tr}_{\rm field}(a(t'_1) \cdots a(t'_m)\rho_{\rm field}(0)a^{\dagger}(t''_n) \cdots a^{\dagger}(t''_1))$. By the invariance of cyclic permutation under trace, this becomes the expectation value $\langle a^{\dagger}(t''_n) \cdots a^{\dagger}(t''_1)a(t'_1) \cdots a(t'_m)\rangle$ of a normal-ordered operator with respect to the initial field state $\rho_{\rm field}(0)$.

The final two terms on the right hand side of Eq. (5.20) do not take the desired form and need further manipulation. Under partial trace over the field degrees of freedom, the field operators $a(t)$ and $a^{\dagger}(t)$ can be permuted cyclically. Therefore, the second to last term on the right hand side of Eq. (5.20) becomes

$$\begin{aligned} {\rm Tr}_{\rm field}\big(U'(t) \bullet U'^{\dagger}(t)L^{\dagger}a(t)\big) &= {\rm Tr}_{\rm field}\big(a(t)U'(t) \bullet U'^{\dagger}(t)L^{\dagger}\big) \\ &= {\rm Tr}_{\rm field}\big(U'(t)a(t) \bullet U'^{\dagger}(t)L^{\dagger} + \frac{1}{2}LU'(t) \bullet U'^{\dagger}(t)L^{\dagger}\big), \end{aligned} \tag{5.21}$$

where we have applied the commutation relation of Eq. (5.16) to obtain the last equality. The last term on the right hand side of Eq. (5.20) is simply the Hermitian conjugate of Eq. (5.21).

Now, Eq. (5.20) can be put in the desired form as

$$\begin{aligned}
&\frac{d}{dt}\mathrm{Tr}_{\mathrm{field}}\Big(U'(t)\bullet U'^{\dagger}(t)\Big)\\
&=\mathrm{Tr}_{\mathrm{field}}\Big(-i\big[H_{\mathrm{sys}},U'(t)\bullet U'^{\dagger}(t)\big]-\frac{1}{2}\big\{L^{\dagger}L,U'(t)\bullet U'^{\dagger}(t)\big\}+LU'(t)\bullet U'^{\dagger}(t)L^{\dagger}\\
&\qquad-\big[L^{\dagger},U'(t)a(t)\bullet U'^{\dagger}(t)\big]+\big[L,U'(t)\bullet a^{\dagger}(t)U'^{\dagger}(t)\big]\Big).
\end{aligned}\tag{5.22}$$

This should be compared with the conventional result

$$\begin{aligned}
&\frac{d}{dt}\mathrm{Tr}_{\mathrm{field}}\Big(U'(t)\bullet U'^{\dagger}(t)\Big)\\
&=\mathrm{Tr}_{\mathrm{field}}\Big(-i\big[H_{\mathrm{sys}},U'(t)\bullet U'^{\dagger}(t)\big]\\
&\qquad-\big[a(t)L^{\dagger},U'(t)\bullet U'^{\dagger}(t)\big]+\big[a^{\dagger}(t)L,U'(t)\bullet U'^{\dagger}(t)\big]\Big),
\end{aligned}\tag{5.23}$$

where no normal-ordering is applied. Comparing Eqs. (5.22) and (5.23), we see that by ordering $a(t)$ and $a^{\dagger}(t)$ into the forms $U'(t)a(t)\bullet U'^{\dagger}(t)$ and $U'(t)\bullet a^{\dagger}(t)U'^{\dagger}(t)$, a Lindblad dissipator term (i.e., $-\frac{1}{2}\{L^{\dagger}L,U'(t)\bullet U'^{\dagger}(t)\}+LU'(t)\bullet U'^{\dagger}(t)L^{\dagger}$) has to be added.

Since system operators can be taken out of the partial trace over field, Eq. (5.22) can be re-written as

$$\begin{aligned}
&\frac{d}{dt}\mathrm{Tr}_{\mathrm{field}}\Big(U'(t)\bullet U'^{\dagger}(t)\Big)\\
&=\mathcal{K}\Big(\mathrm{Tr}_{\mathrm{field}}\big(U'(t)\bullet U'^{\dagger}(t)\big)\Big)\\
&\quad-\Big[L^{\dagger},\mathrm{Tr}_{\mathrm{field}}\big(U'(t)a(t)\bullet U'^{\dagger}(t)\big)\Big]+\Big[L,\mathrm{Tr}_{\mathrm{field}}\big(U'(t)\bullet a^{\dagger}(t)U'^{\dagger}(t)\big)\Big],
\end{aligned}\tag{5.24}$$

where $\mathcal{K}=$ is defined as the superoperator

$$\mathcal{K}=-i[H_{\mathrm{sys}},\bullet]-\frac{1}{2}\{L^{\dagger}L\bullet\}+L\bullet L^{\dagger}.\tag{5.25}$$

Solving Eq. (5.24) formally, we have

$$\begin{aligned}
\mathrm{Tr}_{\mathrm{field}}\Big(U'(t)\bullet U'^{\dagger}(t)\Big)=&e^{\mathcal{K}t}\mathrm{Tr}_{\mathrm{field}}(\bullet)+\int_0^t dt_1\,e^{\mathcal{K}(t-t_1)}\\
&\Big(\Big[-L^{\dagger},\mathrm{Tr}_{\mathrm{field}}\big(U'(t_1)a(t_1)\bullet U'^{\dagger}(t_1)\big)\Big]+\Big[L,\mathrm{Tr}_{\mathrm{field}}\big(U'(t_1)\bullet a^{\dagger}(t_1)U'^{\dagger}(t_1)\big)\Big]\Big).
\end{aligned}\tag{5.26}$$

Applying Eq. (5.26) to the combined initial state $\rho_{\mathrm{tot}}(0)$, we have

$$\begin{aligned}
\rho_{\mathrm{sys}}(t)&=\mathrm{Tr}_{\mathrm{field}}\Big(U'(t)\rho_{\mathrm{tot}}(0)U'^{\dagger}(t)\Big)\\
&=e^{\mathcal{K}t}\mathrm{Tr}_{\mathrm{field}}\big(\rho_{\mathrm{tot}}(0)\big)+\int_0^t dt_1\,e^{\mathcal{K}(t-t_1)}\\
&\quad\Big(\Big[-L^{\dagger},\mathrm{Tr}_{\mathrm{field}}\big(U'(t_1)a(t_1)\rho_{\mathrm{tot}}(0)U'^{\dagger}(t_1)\big)\Big]+\Big[L,\mathrm{Tr}_{\mathrm{field}}\big(U'(t_1)\rho_{\mathrm{tot}}(0)a^{\dagger}(t_1)U'^{\dagger}(t_1)\big)\Big]\Big).
\end{aligned}\tag{5.27}$$

We can further expand $\mathrm{Tr}_{\mathrm{field}}\big(U'(t_1)a(t_1)\rho_{\mathrm{tot}}(0)U'^{\dagger}(t_1)\big)$ and its Hermitian conjugate in the integrand by applying Eq. (5.26) to $a(t_1)\rho_{\mathrm{tot}}(0)$ and its Hermitian conjugate. Then $\rho_{\mathrm{sys}}(t)$ becomes

$$\begin{aligned}
\rho_{\mathrm{sys}}(t) =& e^{\mathcal{K}t}\mathrm{Tr}_{\mathrm{field}}\big(\rho_{\mathrm{tot}}(0)\big) \\
&+ \int_0^t dt_1\, e^{\mathcal{K}(t-t_1)}\bigg(\Big[-L^\dagger, e^{\mathcal{K}t_1}\mathrm{Tr}_{\mathrm{field}}\big(a(t_1)\rho_{\mathrm{tot}}(0)\big)\Big] \\
&\qquad\qquad + \Big[L, e^{\mathcal{K}t_1}\mathrm{Tr}_{\mathrm{field}}\big(\rho_{\mathrm{tot}}(0)a^\dagger(t_1)\big)\Big]\bigg) \\
&+ \int_0^t dt_2 \int_0^{t_2} dt_1\, e^{\mathcal{K}(t-t_2)}\bigg(\Big[-L^\dagger, e^{\mathcal{K}(t_2-t_1)}\Big[-L^\dagger, \mathrm{Tr}_{\mathrm{field}}\big(U'(t_1)a(t_1)a(t_2)\rho_{\mathrm{tot}}(0)U'^{\dagger}(t_1)\big)\Big]\Big] \\
&\qquad\qquad + \Big[-L^\dagger, e^{\mathcal{K}(t_2-t_1)}\Big[L, \mathrm{Tr}_{\mathrm{field}}\big(U'(t_1)a(t_2)\rho_{\mathrm{tot}}(0)a^\dagger(t_1))U'^{\dagger}(t_1)\big)\Big]\Big] \\
&\qquad\qquad + \Big[L, e^{\mathcal{K}(t_2-t_1)}\Big[-L^\dagger, \mathrm{Tr}_{\mathrm{field}}\big(U'(t_1)a(t_1)\rho_{\mathrm{tot}}(0)a^\dagger(t_2)U'^{\dagger}(t_1)\big)\Big]\Big] \\
&\qquad\qquad + \Big[L, e^{\mathcal{K}(t_2-t_1)}\Big[L, \mathrm{Tr}_{\mathrm{field}}\big(U'(t_1)\rho_{\mathrm{tot}}(0)a^\dagger(t_2)a^\dagger(t_1)U'^{\dagger}(t_1)\big)\Big]\Big]\bigg).
\end{aligned} \tag{5.28}$$

In this expansion, we have new terms like $\mathrm{Tr}_{\mathrm{field}}\big(U'(t_1)a(t_1)a(t_2)\rho_{\mathrm{tot}}(0)U'^{\dagger}(t_1)\big)$, where there are now two field operators in the partial trace. We can apply Eq. (5.26) again to these new terms. Repeating this iterative procedure, we have

$$\begin{aligned}
\rho_{\mathrm{sys}}(t) =& e^{\mathcal{K}t}\mathrm{Tr}_{\mathrm{field}}\big(\rho_{\mathrm{tot}}(0)\big) \\
&+ \int_0^t dt_1\, e^{\mathcal{K}(t-t_1)}\bigg(\Big[-L^\dagger, e^{\mathcal{K}t_1}\mathrm{Tr}_{\mathrm{field}}\big(a(t_1)\rho_{\mathrm{tot}}(0)\big)\Big] \\
&\qquad\qquad + \Big[L, e^{\mathcal{K}t_1}\mathrm{Tr}_{\mathrm{field}}\big(\rho_{\mathrm{tot}}(0)a^\dagger(t_1)\big)\Big]\bigg) \\
&+ \int_0^t dt_2 \int_0^{t_2} dt_1\, e^{\mathcal{K}(t-t_2)}\bigg(\Big[-L^\dagger, e^{\mathcal{K}(t_2-t_1)}\Big[-L^\dagger, e^{\mathcal{K}t_1}\mathrm{Tr}_{\mathrm{field}}\big(a(t_1)a(t_2)\rho_{\mathrm{tot}}(0)\big)\Big]\Big] \\
&\qquad\qquad + \Big[-L^\dagger, e^{\mathcal{K}(t_2-t_1)}\Big[L, e^{\mathcal{K}t_1}\mathrm{Tr}_{\mathrm{field}}\big(a(t_2)\rho_{\mathrm{tot}}(0)a^\dagger(t_1))\big)\Big]\Big] \\
&\qquad\qquad + \Big[L, e^{\mathcal{K}(t_2-t_1)}\Big[-L^\dagger, e^{\mathcal{K}t_1}\mathrm{Tr}_{\mathrm{field}}\big(a(t_1)\rho_{\mathrm{tot}}(0)a^\dagger(t_2)\big)\Big]\Big] \\
&\qquad\qquad + \Big[L, e^{\mathcal{K}(t_2-t_1)}\Big[L, e^{\mathcal{K}t_1}\mathrm{Tr}_{\mathrm{field}}\big(\rho_{\mathrm{tot}}(0)a^\dagger(t_2)a^\dagger(t_1)\big)\Big]\Big]\bigg) \\
&+ \cdots .
\end{aligned} \tag{5.29}$$

Notice that Eq. (5.26) ensures that the field operators inside the partial traces over field in Eq. (5.29) always take the general form

$$a(t_1')\cdots a(t_m')\rho_{\mathrm{tot}}(0)a^\dagger(t_n'')\cdots a^\dagger(t_1''), \tag{5.30}$$

where $a(t)$ are on the left of $\rho_{\mathrm{tot}}(0)$, and $a^\dagger(t)$ are on the right of $\rho_{\mathrm{tot}}(0)$. We call the ordering of the field operators in Eq. (5.30) normal ordering because when $\rho_{\mathrm{tot}}(0) = \rho_{\mathrm{sys}}(0)\otimes\rho_{\mathrm{field}}(0)$ (i.e., $\rho_{\mathrm{tot}}(0)$ is separable), the partial trace

$$\begin{aligned}
&\mathrm{Tr}_{\mathrm{field}}\big(a(t_1')\cdots a(t_m')\rho_{\mathrm{tot}}(0)a^\dagger(t_n'')\cdots a^\dagger(t_1'')\big) \\
=&\big\langle a^\dagger(t_n'')\cdots a^\dagger(t_1'')a(t_1')\cdots a(t_m')\big\rangle\rho_{\mathrm{sys}}(0).
\end{aligned} \tag{5.31}$$

becomes $\rho_{\mathrm{sys}}(0)$ times the expectation value of a normal-ordered string of field operators. The relative ordering among the annihilation operators $a(t)$ or among the creation operators $a^\dagger(t)$ is not important, since the annihilation operators (or creation operators) commute among themselves.

Eq. (5.29) is the normal-ordered perturbative expansion of the reduced system state, i.e., the state on which the partial trace over the field degrees of freedom has been taken. We can re-write it in a simpler-looking form. Notice that apart from the partial traces, the superoperator $\mathcal{K}$ and the operator L act only on the system degrees of freedom. So we can pull out the $\mathrm{Tr}_{\mathrm{field}}$ to the front and apply this partial trace to all the terms on the right hand side. Also notice that, because normal-ordering of the field operators is preserved throughout the expansion due to the ordering in Eq. (5.26), we do not need to keep track of the exact ordering of the field operators during the expansion. In other words, even if the ordering of the field operators are scrambled, if we re-order the field operators using normal ordering at the end, then the correct operator ordering is recovered. Therefore we now re-express Eq. (5.29) as

$$\begin{aligned}\rho_{\mathrm{sys}}(t) = \mathrm{Tr}_{\mathrm{field}}\hat{\mathcal{N}}\Bigg(& e^{\mathcal{K}t}\rho_{\mathrm{tot}}(0) \\ & + \int_0^t dt_1\, e^{\mathcal{K}(t-t_1)}\mathcal{L}(t_1)e^{\mathcal{K}t_1}\rho_{\mathrm{tot}}(0) \\ & + \int_0^t dt_2 \int_0^{t_2} dt_1\, e^{\mathcal{K}(t-t_2)}\mathcal{L}(t_2)e^{\mathcal{K}(t_2-t_1)}\mathcal{L}(t_1)e^{\mathcal{K}(t_1)}\rho_{\mathrm{tot}}(0) \\ & + \cdots \Bigg).\end{aligned} \tag{5.32}$$

The notation $\mathrm{Tr}_{\mathrm{field}}\hat{\mathcal{N}}$ means to normal-order the field operators according to Eq. (5.30), and then evaluate the partial trace over the field degrees of freedom. We note again that $\mathcal{L}(t)$ is the superoperator $[-a(t)L^\dagger + a^\dagger(t)L, \bullet]$ (see Eq. (5.13)).

The derivation of Eq. (5.32) can be generalized straightforwardly to the case of a single molecule interacting with multiple spatial modes of light (indexed by l). The final result takes the same form as Eq. (5.32), but with the superoperators $\mathcal{K}$ and $\mathcal{L}$ modified to sum over the photon modes, i.e.,

$$\mathcal{K} = -i[H_{\mathrm{sys}}, \bullet] + \sum_l \Big(-\frac{1}{2}\{L_l^\dagger L_l \bullet\} + L_l \bullet L_l^\dagger \Big) \tag{5.33}$$

and

$$\mathcal{L}(t) = \sum_l [-a(t)L_l^\dagger + a^\dagger(t)L_l, \bullet]. \tag{5.34}$$

Comparing this result to the conventional non-normal-ordered expansion of Eq. (5.15), we see that by changing the free evolution generator from $\mathcal{K}'$ (Eq. (5.12)) to $\mathcal{K}$ (Eq. (5.25)), we only need to evaluate normal-ordered field operators now. $\mathcal{K}' = -i[H_{\mathrm{sys}}, \bullet]$ describes the Hamiltonian evolution the free evolution, while $\mathcal{K} = \mathcal{K}' - \frac{1}{2}\{L^\dagger L, \bullet\} + L \bullet L^\dagger$ describes both the Hamiltonian evolution and the dissipation due to spontaneous emission. Hence, the lack of normal ordereding in the conventional expansion is captured by the Lindblad dissipator.

We will see in Sec. 5.4 that given a fixed order of perturbation, the normal-ordered expansion for the reduced system state can provide a more accurate description for the reduced system dynamics than the conventional expansion does. The normal-ordered expansion also provides new perspectives on the time evolution of the reduced system state. Specifically, for a coherent state input (see Sec. 5.2) or a m-photon Fock state input (see Sec. 5.3), the normal-ordered expansion in the integral form (i.e., Eq. (5.32)) can be re-expressed in the differential form as master equations (see Eqs. (5.38) and (5.47)). We also find that, surprisingly, the normal-ordered expansion for an m-photon input truncates exactly at the $2m$-th order, and the truncated perturbative series becomes an exact result.

5.2 Coherent state input

A coherent state with amplitude $\alpha(t)$ is given by

$$|\psi\rangle = \exp\Big(\int dt\, \alpha(t)a^\dagger(t) - \alpha^*(t)a(t)\Big)|\text{vac}\rangle. \tag{5.35}$$

It is an eigenstate of $a(t)$, and the expectation value of a normal-ordered string of $a(t)$ and $a^\dagger(t)$ (e.g., $\langle\psi|a^\dagger(t_4)a^\dagger(t_3)a(t_2)a(t_1)|\psi\rangle$) is obtained by replacing $a(t)$ and $a^\dagger(t)$ with $\alpha(t)$ and $\alpha^*(t)$, respectively. The example above would evaluate to $\alpha^*(t_4)\alpha^*(t_3)\alpha(t_2)\alpha(t_1)$.

Therefore in the normal-ordered perturbative expansion (Eq. (5.32)), we can simply replace all $a(t)$ and $a^\dagger(t)$ by the classical amplitudes $\alpha(t)$ and $\alpha^*(t)$. Let the initial state $\rho_{\text{tot}}(0)$ be a product state $\rho_{\text{sys}}(0)\otimes|\psi\rangle\langle\psi|$, where $|\psi\rangle\langle\psi|$ is the initial coherent state of the field. The expansion now becomes

$$\begin{aligned}\rho_{\text{sys}}(t) =& e^{\mathcal{K}t}\rho_{\text{sys}}(0) + \int_0^t dt_1\, e^{\mathcal{K}(t-t_1)}\mathcal{L}'(t_1)e^{\mathcal{K}t_1}\rho_{\text{sys}}(0)\\ &+ \int_0^t dt_2\int_0^{t_2} dt_1\, e^{\mathcal{K}(t-t_2)}\mathcal{L}'(t_2)e^{\mathcal{K}(t_2-t_1)}\mathcal{L}'(t_1)e^{\mathcal{K}(t_1)}\rho_{\text{sys}}(0)\\ &+\cdots,\end{aligned} \tag{5.36}$$

where $\mathcal{L}'(t) = [-\alpha(t)L^\dagger + \alpha^*(t)L, \bullet]$. Taking the time derivative of Eq. (5.36), we see that

$$\frac{d}{dt}\rho_{\text{sys}}(t) = \mathcal{K}\rho_{\text{sys}}(t) + \mathcal{L}'(t)\rho_{\text{sys}}(t), \tag{5.37}$$

or

$$\begin{aligned}\frac{d}{dt}\rho_{\text{sys}}(t) =& [-iH_{\text{sys}} - \alpha(t)L^\dagger + \alpha^*(t)L, \rho_{\text{sys}}(t)]\\ &- \frac{1}{2}L^\dagger L\rho_{\text{sys}}(t) - \frac{1}{2}\rho_{\text{sys}}(t)L^\dagger L + L\rho_{\text{sys}}(t)L^\dagger.\end{aligned} \tag{5.38}$$

This is the coherent state master equation [52, 65]. Here, we can see that, in the case of a coherent state input, the quantum correction to the semi-classical master equation is the Lindblad dissipator that describes spontaneous emission.

5.3 m-photon Fock state input

Consider an m-photon Fock state, defined as

$$|\xi_m\rangle = \frac{1}{\sqrt{m!}}\Big(\int dt\, \xi(t)a^\dagger(t)\Big)^m|\text{vac}\rangle, \tag{5.39}$$

where the temporal profile $\xi(t)$ is normalized as $\int dt\,|\xi(t)|^2 = 1$, so that $\langle\xi_m|\xi_m\rangle = 1$. The expectation value of the normal-ordered field operator $\langle\xi_m|a^{(\dagger)}\cdots a^{(\dagger)}|\xi_m\rangle$ is nonzero only when the number of creation operators $a^\dagger(t)$ is the same as the number of annihilation operators $a(t)$ and the number of annihilation operators is not greater than m. Specifically,

$$\langle\xi_m|a^\dagger(t_1)\cdots a^\dagger(t_k)a(t'_k)\cdots a(t'_1)|\xi_m\rangle = \frac{m!}{(m-k)!}\xi^*(t_1)\cdots\xi^*(t_k)\xi(t'_k)\cdots\xi(t'_1) \tag{5.40}$$

for $k = 1, 2, \cdots, m$. Since normal-ordered strings of n field operators only appear in the n-th order normal-ordered expansion, only the 0th, 2nd, 4th, $\cdots$, and $2m$-th order terms in the normal-ordered expansion are nonzero. Because normal-ordered strings of field operators whose lengths are longer

than $2m$ result in zero expectation values, expansion terms of order higher than $2m$ vanish identically, and the normal-ordered perturbative expansion truncates exactly at order $2m$. Therefore, the truncated perturbative series becomes the exact description for the reduced system state interacting with an m-photon Fock state input. We note that while the validity of perturbative expansion usually requires weak light-matter coupling strength, this exact result holds for arbitrary light-matter coupling strength.

We can deduce the Fock state master equation [47,52] from the normal-ordered expansion. In the Fock state master equation, we define auxiliary density matrices $\rho_{\mu,\nu}$ as

$$\rho_{\mu,\nu}(t) = \mathrm{Tr}_{\mathrm{field}}\Big(U'(t)\big(\rho_{\mathrm{sys}}(0)\otimes|\xi_\mu\rangle\langle\xi_\nu|\big)U'^{\dagger}(t)\Big). \tag{5.41}$$

$\rho_{m,m}(t)$ is the reduced system state given an m-photon Fock state input. Note that, by definition, the initial state is $\rho_{\mu,\nu}(0) = \delta_{\mu,\nu}\rho_{\mathrm{sys}}(0)$. Following the derivation from Eq. (5.27) to Eq. (5.32), but applying the expansion to $\rho_{\mathrm{sys}}(0)\otimes|\xi_\mu\rangle\langle\xi_\nu|$ instead of $\rho_{\mathrm{tot}}(0)$, we have

$$\rho_{\mu,\nu}(t) = \mathrm{Tr}_{\mathrm{field}}\hat{\mathcal{N}}\Big(R_{\mu,\nu}\Big), \tag{5.42}$$

where

$$\begin{aligned} R_{\mu,\nu}(t) =& e^{\mathcal{K}t}\rho_{\mathrm{sys}}(0)\otimes|\xi_\mu\rangle\langle\xi_\nu| \\ &+\int_0^t dt_1\, e^{\mathcal{K}(t-t_1)}\mathcal{L}(t_1)e^{\mathcal{K}t_1}\rho_{\mathrm{sys}}(0)\otimes|\xi_\mu\rangle\langle\xi_\nu| \\ &+\int_0^t dt_2\int_0^{t_2} dt_1\, e^{\mathcal{K}(t-t_2)}\mathcal{L}(t_2)e^{\mathcal{K}(t_2-t_1)}\mathcal{L}(t_1)e^{\mathcal{K}(t_1)}\rho_{\mathrm{sys}}(0)\otimes|\xi_\mu\rangle\langle\xi_\nu| \\ &+\cdots \end{aligned} \tag{5.43}$$

Taking the time derivative of Eq. (5.42), we see that

$$\begin{aligned} \frac{d}{dt}\rho_{\mu,\nu}(t) &= \mathrm{Tr}_{\mathrm{field}}\hat{\mathcal{N}}\Big(\mathcal{K}R_{\mu,\nu}+\mathcal{L}(t)R_{\mu,\nu}\Big) \\ &= \mathcal{K}\rho_{\mu,\nu}(t)+\mathrm{Tr}_{\mathrm{field}}\hat{\mathcal{N}}\Big(-\big[L^\dagger a(t),R_{\mu,\nu}(t)\big]+\big[La^\dagger(t),R_{\mu,\nu}(t)\big]\Big) \\ &= \mathcal{K}\rho_{\mu,\nu}(t)-\Big[L^\dagger,\mathrm{Tr}_{\mathrm{field}}\hat{\mathcal{N}}\big(a(t)R_{\mu,\nu}(t)\big)\Big]+\Big[L,\mathrm{Tr}_{\mathrm{field}}\hat{\mathcal{N}}\big(a^\dagger(t)R_{\mu,\nu}(t)\big)\Big]. \end{aligned} \tag{5.44}$$

In the second line, we take the system operators $L^\dagger$ and L outside of the partial trace over field. We also combine the field operators $a(t)$ and $a^\dagger(t)$ with $R_{\mu,\nu}$, since under normal-ordering, the placement of the field operators is unimportant. Using the property

$$a(t)|\xi_\mu\rangle = \sqrt{\mu}\xi(t)|\xi_{\mu-1}\rangle, \tag{5.45}$$

we can simplify $\mathrm{Tr}_{\mathrm{field}}\hat{\mathcal{N}}\big(a(t)R_{\mu,\nu}(t)\big)$ as

$$\begin{aligned} \mathrm{Tr}_{\mathrm{field}}\hat{\mathcal{N}}\big(a(t)R_{\mu,\nu}(t)\big) =& \ \mathrm{Tr}_{\mathrm{field}}\hat{\mathcal{N}}\Big(e^{\mathcal{K}t}\rho_{\mathrm{sys}}(0)\otimes a(t)|\xi_\mu\rangle\langle\xi_\nu| \\ &+\int_0^t dt_1\, e^{\mathcal{K}(t-t_1)}\mathcal{L}(t_1)e^{\mathcal{K}t_1}\rho_{\mathrm{sys}}(0)\otimes a(t)|\xi_\mu\rangle\langle\xi_\nu| \\ &+\int_0^t dt_2\int_0^{t_2} dt_1\, e^{\mathcal{K}(t-t_2)}\mathcal{L}(t_2)e^{\mathcal{K}(t_2-t_1)}\mathcal{L}(t_1)e^{\mathcal{K}(t_1)}\rho_{\mathrm{sys}}(0)\otimes a(t)|\xi_\mu\rangle\langle\xi_\nu| \\ &+\cdots\Big) \\ =& \sqrt{\mu}\xi(t)\rho_{\mu-1,\nu}. \end{aligned} \tag{5.46}$$

We have used the fact that due to the normal-ordering, $a(t)$ always acts on the left of $|\xi_\mu\rangle\langle\xi_\nu|$. Similarly, $\mathrm{Tr}_{\mathrm{field}}\hat{\mathcal{N}}\big(a^\dagger(t)R_{\mu,\nu}(t)\big) = \sqrt{\nu}\xi^*(t)\rho_{\mu,\nu-1}$. Therefore we can re-write Eq. (5.44) to obtain the Fock state master equation as

$$\frac{d}{dt}\rho_{\mu,\nu}(t) = \mathcal{K}\rho_{\mu,\nu}(t) - \sqrt{\mu}\xi(t)[L^\dagger, \rho_{\mu-1,\nu}] + \sqrt{\nu}\xi^*(t)[L, \rho_{\mu,\nu-1}]. \tag{5.47}$$

This is a set of differential equations that couples a hierarchy of auxiliary density matrices $\rho_{\mu,\nu}$, with $\rho_{m,m}$ being the physical reduced system state, given an m-photon Fock state input. Using the initial condition $\rho_{\mu,\nu}(0) = \delta_{\mu,\nu}\rho_{\mathrm{sys}}(0)$, this set of equations describe the non-Markovian effects of an m-photon Fock state input [47, 52].

5.4 Numerical evaluation of the perturbative expansions

We now study the numerical accuracy of the conventional expansion (Eq. (5.15)) vs. the normal-ordered expansion (Eq. (5.32)) under various parameter regimes by comparing to the exact system state evolution. We study the excitation by a coherent state and an m-photon Fock state. We consider a matter system consisting of two electronic levels (labeled as ground state $|g\rangle$ and excited state $|e\rangle$) interacting with a bath (e.g., nuclear degrees of freedom) that gives rise to Lindbladian pure dephasing in the electronic subsystem [111]. Tracing out the bath degrees of freedom and focus on the two electronic states, we model the reduced electronic system dynamics as

$$\frac{d}{dt}\rho_{\mathrm{el}} = -i\big[H'_{\mathrm{el}}, \rho_{\mathrm{el}}\big] + \gamma_d\Big(-\frac{1}{2}\big\{P^\dagger P, \rho_{\mathrm{el}}\big\} + P\rho_{\mathrm{el}}P^\dagger\Big), \tag{5.48}$$

where γ_d is the dephasing rate, and $P = |e\rangle\langle e|$. We take $H = \omega|e\rangle\langle e|$. The dipole de-excitation operator L is taken to be $\sqrt{\gamma}|g\rangle\langle e|$, where γ is the coupling strength between the system and the field. γ is also the spontaneous emission rate into the field. We assume the excitation pulse has a normalized Gaussian temporal profile

$$\xi'(t) = \frac{1}{(\pi\sigma^2)^{1/4}}e^{-\frac{(t-t_0)^2}{2\sigma^2}}e^{-i\omega t} \tag{5.49}$$

centered at time t_0, with a pulse duration of σ. The carrier frequency ω is resonant with the energy splitting of the two electronic levels. ξ' is normalized such that $\int dt\,|\xi'(t)|^2 = 1$. We set $t_0 = 5$ ps, $\sigma = 1$ ps, and $\gamma_d = 1(\mathrm{ps})^{-1}$.

In the numerical calculation, we work in a rotating frame where the carrier frequency ω is rotated out. In this frame, the temporal profile becomes

$$\xi(t) = \frac{1}{(\pi\sigma^2)^{1/4}}e^{-\frac{(t-t_0)^2}{2\sigma^2}}, \tag{5.50}$$

and the Hamiltonian becomes $H_{\mathrm{el}} = H'_{\mathrm{el}} - \omega|e\rangle\langle e| = 0$.

The initial state is set to be in the ground state $|g\rangle\langle g|$. We will compute the excited state population as a function of time. The change from the initial ground state $|g\rangle\langle g|$ to the excited state population $|e\rangle\langle e|$ requires at least two interactions (i.e., $L^\dagger|g\rangle\langle g|L = |e\rangle\langle e|$). Therefore, we need to perform the expansion to the second order to see nonzero excited state population. In the conventional expansion (Eq. (5.15)), the superoperator that generates free evolution is $\mathcal{K}' = -i[H_{\mathrm{sys}}, \bullet]$ (see Eq. (5.12)). The matter system consists of both the electronic and the bath degrees of freedom. After tracing out the bath degrees of freedom, the superoperator that generates free evolution in the electronic degrees of freedom becomes

$$\mathcal{K}' = -i\big[H_{\mathrm{el}}, \bullet\big] + \gamma_d\Big(-\frac{1}{2}\{P^\dagger P, \bullet\} + P \bullet P^\dagger\Big). \tag{5.51}$$

Similarly, in the normal-ordered expansion (Eq. (5.32)), the superoperator that generates free evolution in the electronic degrees of freedom is

$$\begin{aligned}\mathcal{K} = -i\big[H_{\rm el}, \bullet\big] + \gamma_d\Big(-\frac{1}{2}\{P^\dagger P, \bullet\} + P \bullet P^\dagger\Big) \\ -\frac{1}{2}\{L^\dagger L, \bullet\} + L \bullet L^\dagger.\end{aligned} \tag{5.52}$$

The perturbative expansion is dominated by the first few terms when the perturbation $\mathcal{L}$ is weak (see Eqs. (5.15) and (5.32)). This corresponds to the situation where the order of magnitude of $\int dt\, a(t)L^\dagger$ (or its Hermitian conjugate) is much less than 1. Since the integrand $a(t)L^\dagger$ contributes significantly only during the pulse duration σ, we assign an order of magnitude of σ to the integral. We also assign an order of magnitude of $\sqrt{m/\sigma}$ to $a(t)$ and an order of magnitude of $\sqrt{\gamma}$ to L (see Table (3.1)). Multiplying the factors together, we have

$$\int dt\, a(t)L^\dagger \sim \sqrt{m\sigma\gamma}. \tag{5.53}$$

Therefore the criterion for being in the weak-coupling perturbative regime is $\sqrt{m\sigma\gamma} \ll 1$.

5.4.1 Coherent state input

The coherent state amplitude $\alpha(t)$ for a coherent state input with an average photon number of m is given by

$$\alpha(t) = \sqrt{m}\xi(t), \tag{5.54}$$

where $\xi(t)$ is the normalized temporal profile (see Eqs. (5.35) and (5.50)). For different values of photon number m and coupling strength γ, we preform direct numerical integrations to compute the conventional perturbative expansion (Eq. (5.15)) and the normal-ordered perturbative expansion (Eq. (5.32)) up to the second order. We then compare the second order expansion results to the exact result obtained by solving the coherent state master equation (Eq. (5.38)). In Fig. (5.1), we plot the excited state population as a function of time to see the accuracy of the perturbative expansions under different parameter regimes.

When there is one photon on average ($m = 1$) in the coherent state input, we examine the cases when $\gamma = 0.001$, 0.05, and 1 ps^{-1}, corresponding to $\sqrt{m\sigma\gamma} \approx 0.03$, 0.22, and 1. When the coupling is very weak ($\gamma = 0.001$ ps^{-1}), both the second order conventional expansion and the second order normal-ordered expansion approximate the exact dynamics well (see Fig. (5.1a)). In Fig. (5.1b and c), as γ increases beyond the weak coupling perturbative regime, both expansions become less accurate. However, the normal-ordered expansion produces significantly more accurate results because it accounts for the spontaneous emission effect. When $\gamma = 1$ ps^{-1} (see Fig. (5.1c)), the second order conventional expansion produces unphysical results where the excited state population is greater than 1 after around 5 ps, while in the second order normal-ordered expansion, the excited state population remains ≤ 1.

In the conventional expansion, a general n-th order expansion term involves the expectation value of a non-normal-ordered string of n field operators $a(t)$ and $a^\dagger(t)$. These non-normal-ordered operators can be expressed in terms of normal-ordered strings with shorter or equal lengths. For example, the non-normal-ordered operator $a(t_3)a^\dagger(t_2)a(t_1)$ can be expressed in terms of normal-ordered operators as $a^\dagger(t_2)a(t_3)a(t_1) + \delta(t_3 - t_2)a(t_1)$. Therefore in the conventional expansion, a general n-th order expansion term reduces to not only terms that are n-th order in the coherent amplitude $\alpha(t)$, but also terms that are lower order in $\alpha(t)$ (i.e., lower than n-th order). In the normal-ordered expansion, a general n-th order expansion term is exactly n-th order in $\alpha(t)$ because the field operators are

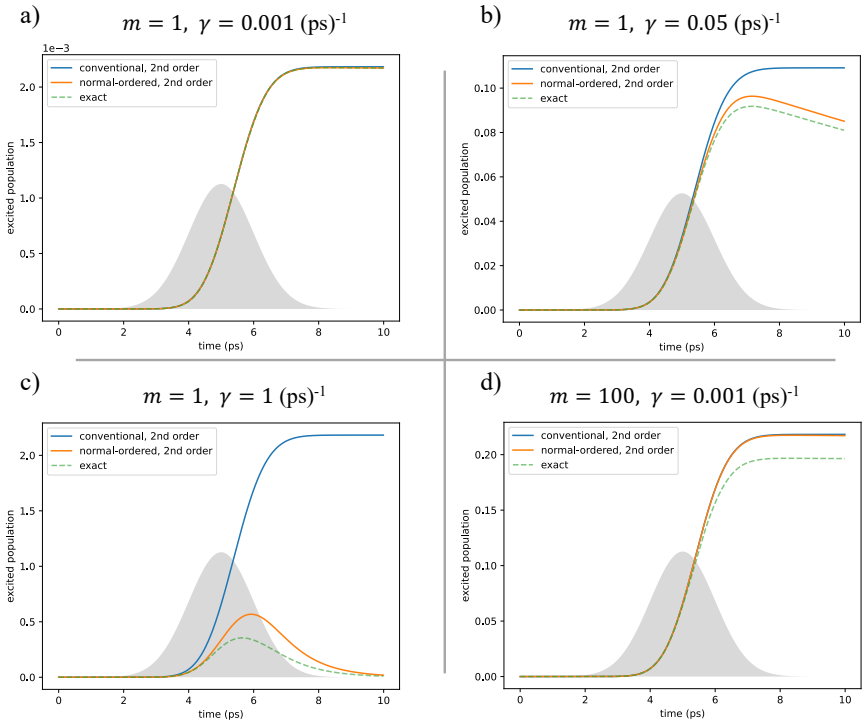

Figure 5.1: Comparing the second order conventional perturbative expansion, the second order normal-ordered perturbative expansion, and the exact time evolution for the reduced system state, under a coherent state input. The matter system is taken to be a simple two-level system with Lindbladian dephasing. See sec. 5.4 for details. Grey area represents the input pulse profile $\xi(t)$ (see Eq. (5.50)), scaled differently in each plot for easier visualization. (a)-(c) Excitation by a coherent state input with $m = 1$ photon on average. Light-matter coupling strengths of $\gamma = 0.001$, 0.05, and $1\,\mathrm{ps}^{-1}$ are considered. (d) Excitation by a coherent state input with $m = 100$ photons on average, $\gamma = 0.001\,\mathrm{ps}^{-1}$.

normal-ordered, and the expectation values of normal-ordered operators with respect to a coherent state is obtained by replacing $a(t)$ or $a^\dagger(t)$ with $\alpha(t)$ or $\alpha^*(t)$. Therefore if we examine expansion terms in orders of $\alpha(t)$, an n-th order normal-ordered expansion contains all terms up to order α^n. In contrast, an n-th order conventional expansion does not contain all terms up to order α^n because a higher-than-n-th order conventional expansion still contains terms that are of order α^n or lower due to the non-normal-ordered-ness of the field operators. This is why normal-ordered expansion tends to be more accurate than the conventional expansion.

In Fig. (5.1d) we consider a coherent state input with a larger average photon number $m = 100$ and set $\gamma = 0.001\ \mathrm{ps}^{-1}$. Due to the large number of photons, this is no longer in the very weak coupling perturbative regime, since $\sqrt{m\sigma\gamma} \approx 0.32$. The difference between the second order expansions and the exact result increases as m increases, but the difference between the second order conventional expansion and the second order normal-ordered expansion (i.e., the spontaneous emission Lindblad dissipator) does not depend on m. Hence, when the photon number is large, we see that the difference between the two second order expansions is small compared to the difference to the exact result. Therefore when the photon number is large and the perturbation parameter $\sqrt{m\sigma\gamma}$ is no longer much smaller than 1, neither expansion provides a good description of the reduced system dynamics.

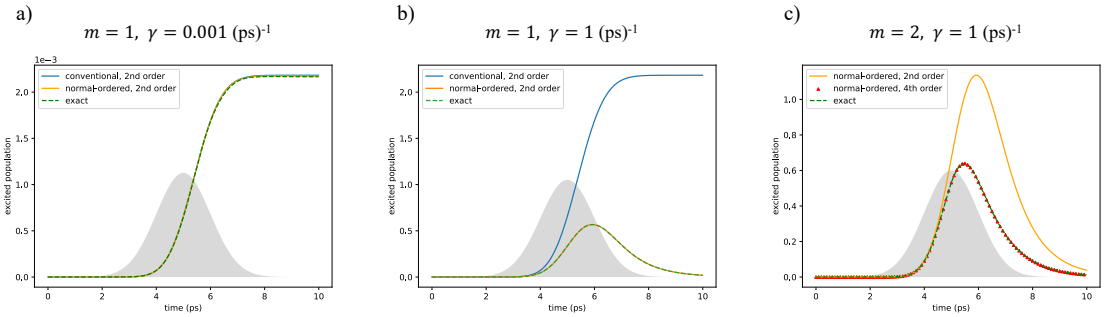

Figure 5.2: Comparing various types of expansion to the exact time evolution for the reduced system state, under an m-photon Fock state input. The normal-ordered expansion to the $2m$-th order reproduces the exact dynamics, regardless of the coupling strength. (a)-(b) Excitation by a single-photon Fock state input. Light matter coupling strengths of $\gamma = 0.001$ and $1\,\mathrm{ps}^{-1}$ are considered. (c) Excitation by a two-photon Fock state input in the strong coupling regime.

5.4.2 m-photon Fock state input

In the case of m-photon Fock state inputs, we first compute the conventional or normal-ordered perturbative expansions through numerical integration, and then the results are compared to exact solutions obtained by solving the Fock state master equation (Eq. (5.47)).

Given a single photon Fock state input (i.e., $m = 1$), the second order ($2m = 2$) normal-ordered expansion provides the exact reduced system dynamics. Fig. (5.2a) shows that when the coupling γ is weak ($\gamma = 0.001\,\mathrm{ps}^{-1}$) such that $\sqrt{m\sigma\gamma} \approx 0.03$ is much smaller than 1, both the second order conventional expansion and the second order normal-ordered expansion approximate the exact solution well. In the strong-coupling regime ($\gamma = 1\,\mathrm{ps}^{-1}$, see Fig. (5.2b)), $\sqrt{m\sigma\gamma} = 1$, and the second order conventional expansion becomes unreliable. However, we see that the second order normal-ordered expansion is still exact in the strong-coupling regime. When the photon number $m = 2$, we see that the fourth order ($2m = 4$) normal-ordered expansion agrees with the exact solution, regardless of the coupling strength (see Fig. (5.2c)). When the photon number m is large and the perturbation parameter $\sqrt{m\sigma\gamma}$ is no longer much smaller than 1, one would need to expand the normal-ordered expansion to very high order (i.e., $2m$-th order) to obtain a good description of the dynamics. Therefore, in this case, a low order normal-ordered expansion will not provide a good description of the reduced system dynamics.

5.5 Conclusion

Working in a interaction picture, a different interaction picture than that used in Ch. 1 to Ch. 3, we have developed a normal-ordered expansion for the reduced system state. This has resulted in new ways to derive the coherent state master equation and the Fock state master equation. Under coherent state and m-photon Fock state excitation, and when the photon number is small, we find that the normal-ordered expansion provides significantly more accurate description of the dynamics in the intermediate to strong coupling regime than the conventional expansion does.

Part II

Dynamics of photosynthetic complexes interacting with quantum light

Chapter 6

Theoretical modeling of photosynthetic complexes and their interaction with photons and phonons

6.1 Chromophoric System Hamiltonian

We model the lowest two accessible electronic states of each chromophore as a two level system, corresponding to the Q_y transition [72]. The dipole-dipole coupling between chromophores, under the rotating wave approximation, does not change the number of electronic excitations. Therefore the chromophoric Hamiltonian will commute with the operator that counts the number of excitons in the system, and the Hamiltonian is block diagonal, with the j^{th} block corresponding to the j-excitation subspace, $\mathcal{H}_j$. The excitation energy of a typical chromophore is $\sim 15,000\,\mathrm{cm}^{-1}$, about 75 times larger than $k_BT \approx 200\ \mathrm{cm}^{-1}$ at room temperature. Therefore, to a very good approximation, we may regard the initial thermal state of the isolated chromophoric system as the absolute ground state of $\mathcal{H}_0$, denoted as $|g\rangle$, which is defined to have zero energy. Due to the weak system-field coupling in a natural photosynthetic system, the probability to have multiple excitations in the system is much smaller than the probability to have a single excitation, so we will only consider the $(1+N)$-dimensional subspace $\mathcal{H}_0 \bigoplus \mathcal{H}_1$. We denote the singly excited state where site j is excited and all other sites are in their ground states as $|j\rangle$. The chromophoric system Hamiltonian is written as

$$H_{\mathrm{sys}} = \sum_{j=1}^{N} \epsilon_j |j\rangle\langle j| + \sum_{j \neq k} J_{jk} |j\rangle\langle k|, \tag{6.1}$$

where ϵ_j is the excited state energy of site j, and J_{jk} are the electronic coupling matrix elements between chromophores j and k. The effects of the phonon environment on the site energies are discussed in Section 6.3.1. The numerical values for the ϵ_j and J_{jk} parameters in an LHCII monomer system are taken from [112]. For simplicity, we shall refer to the chromophore system as the system, unless otherwise noted. The numerical values for the Hamiltonian that we use are given in Appendix H.

6.2 Interaction with photons

6.2.1 System-light interaction as system interacting with finite number of one-dimensional electromagnetic fields

The quantized electromagnetic field in 3-dimensional space is described by harmonic oscillators indexed with a 3-dimensional wavevector and a polarization index [67,113]. However, it is useful to decompose the electric field into 1-dimensional fields, so that the input-output formalism can be applied [50,114]. We will first consider the incoming N-photon Fock state in a fixed paraxial beam mode. The electric field at the center of the beam is written as

$$\mathbf{E}_{\text{para}}(t) = \int_0^\infty d\omega \sqrt{\frac{\hbar\omega}{4\pi\epsilon_0 c}} \tilde{\mathbf{u}}(\mathbf{0})(ia(\omega)e^{-i\omega t} + \text{h.c.}), \tag{6.2}$$

(see derivation in Appendix G and Ref. [115]), where $\tilde{\mathbf{u}}(\mathbf{x})$ is the normalized spatial mode function such that the integral over all transverse area is unity, i.e., $\int dA_T \, |\tilde{\mathbf{u}}|^2 = 1$. Here $a(\omega)$ is the annihilation operator for the frequency ω component of the paraxial mode. Note that the field is now indexed by the 1-dimensional parameter ω.

To capture the spontaneous emission into other modes, we must also consider field modes other than the incoming mode. One way to do this is to partition the 4π solid angle of the 3-dimensional wavevector into finite numbers of small solid angle sections, indexed by m, and write the electric field at position $\mathbf{x} = \mathbf{0}$ as

$$\mathbf{E}(t) = \sum_{m,\lambda} \mathbf{E}_{m,\lambda}(t), \tag{6.3a}$$

where

$$\mathbf{E}_{m,\lambda}(t) = \int_0^\infty d\omega \sqrt{\frac{\hbar\omega^3 \Delta\Omega_m}{16\pi^3\epsilon_0 c^3}} (ia_{m,\lambda}(\omega)e^{-i\omega t}\hat{\epsilon}_{m,\lambda} + \text{h.c.}) \tag{6.3b}$$

(see Sec. 1.2 and Sec. 1.3). Here λ indexes the two polarizations in a small solid angle section, $\Delta\Omega_m$ is the amount of solid angle (in steradian units) of section m, and $\hat{\epsilon}_{m,\lambda}$ is the polarization vector corresponding to m and λ. One can show that in the case of the simplest transverse electromagnetic mode TEM_{00}, if we think of the boundary of the beam as the location where the beam intensity is $1/e^4 \approx 2\%$ of the intensity at the center, then Eq. (6.2) matches Eq. (6.3) for a particular (m, λ). Therefore we can treat the incoming TEM_{00} paraxial mode as one of the (m, λ) modes in the small angle decomposition (Eq. (6.3)), as illustrated in Figs. (1.2) and (6.1).

In Eq. (6.3), the electric field is decomposed into a finite number of 1-D fields, which is not enough to describe all degrees of freedom in the 3-D electromagnetic field. However, Sec. 1.2 shows that one can describe the 3-D electromagnetic field by a set of countably infinite 1-D fields. Then using the small solid angle decomposition (see Eq. (6.3)), we can decompose the 3-D electromagnetic field into a finite number of small solid angle 1-D fields plus a countably infinite number of 1-D fields that are needed to describe all degrees of freedom in the 3-D field. The countably infinite number of 1-D fields are chosen to be orthogonal to each other and to the small solid angle 1-D fields in the sense described in Sec. 1.2. Under this decomposition scheme, the total system+field Hamiltonian under the dipole-electric field coupling $(-\mathbf{d} \cdot \mathbf{E})$ can be written as

$$H_{\text{sys+field}} = H_{\text{sys}} - \mathbf{d} \cdot \sum_{m,\lambda} \mathbf{E}_{m,\lambda} + \sum_{m,\lambda} \int_0^\infty d\omega \, \hbar\omega a^\dagger_{m,\lambda}(\omega) a_{m,\lambda}(\omega) + \sum_s^\infty \int_0^\infty d\omega \, \hbar\omega a^\dagger_s(\omega) a_s(\omega), \tag{6.4}$$

where $\sum_{m,\lambda}$ sums over the finite number of small solid angle modes, and the $\sum_s^\infty$ sums over the remaining countably infinite number of 1-D field modes. Since the last term in Eq. (6.4) involving the

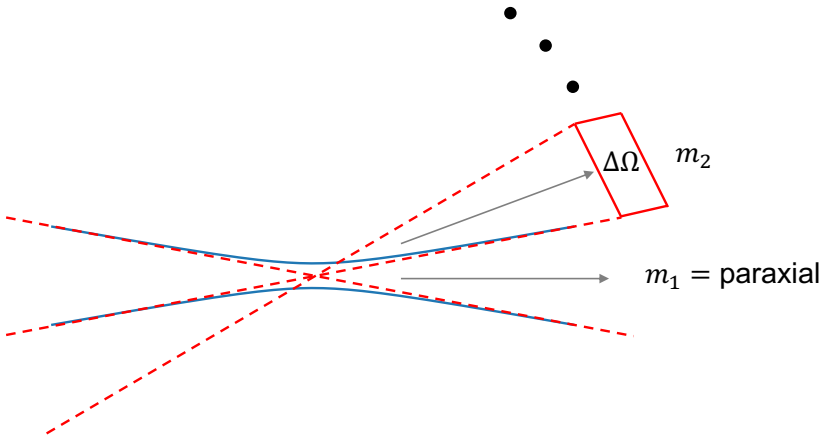

Figure 6.1: Small angle modal decomposition of the electric field in three dimensions defined in reference to a paraxial beam traveling from left to right. The chromophore system will be located at the focus of this beam. Blue solid curves show the contour of the paraxial beam mode. Red dashed lines denote the boundaries of small solid angle modes. Since the paraxial beam mode is concentrated in a small solid angle as shown, we can treat it as the small solid angle mode m_1. m_2 is another small solid angle mode propagating in the upper right direction and covering the solid angle $\Delta\Omega$.

infinite sum is decoupled from the rest of the Hamiltonian, we can describe the system-light interaction as system interacting with just a finite number of 1-D fields.

An alternative way to decompose the electric field into a finite sum of 1-D fields is to write it as a sum of the x, y, and z polarization components, i.e. $\mathbf{E}(t) = E_x(t)\hat{x} + E_y(t)\hat{y} + E_z(t)\hat{z}$. E_x then takes the form

$$E_x(t) = \int_0^\infty d\omega \sqrt{\frac{\hbar\omega^3}{6\pi^2\epsilon_0 c^3}}(ia_x(\omega)e^{-i\omega t} + \text{h.c.}), \tag{6.5}$$

with E_y and E_z defined similarly (see Sec. 1.2).

6.2.2 System-light interaction in the language of input-output formalism

To put the system-light interaction in the language of input-output formalism, we follow the procedure in [51], with addition of some details specific to our modeling of light harvesting systems. We summarize the results here.

We will work in the interaction frame by rotating out the zeroth order Hamiltonian defined by having a constant energy (equal to the carrier frequency of the light pulse) in the singly excited states plus the free field Hamiltonian, i.e.,

$$H_0 = \sum_{j=1}^{N} \hbar\omega_0 |j\rangle\langle j| + \sum_l \int_0^\infty d\omega\, \hbar\omega a_l^\dagger(\omega) a_l(\omega). \tag{6.6}$$

For notational simplicity, we denote the mode indices (m, λ) by l. We define the quantum white noise operator

$$a_l(t) \equiv \sqrt{\frac{1}{2\pi}} \int_{-\infty}^{\infty} d\omega\, a_l(\omega) e^{i(\omega-\omega_0)t}, \tag{6.7}$$

which is a central object in the input-output formalism. With this definition, the field operators $a_l(t)$ satisfy the bosonic commutation relations: $[a_l(t), a_{l'}^\dagger(t')] = \delta_{l,l'}\delta(t-t')$ and $[a_l(t), a_{l'}(t')] =$

$[a_l^\dagger(t), a_{l'}^\dagger(t')] = 0$. The total Hamiltonian in the interaction frame is now expressed as

$$H_{\text{sys+field}}(t) = H + \sum_l \left(-i\hbar a_l(t) L_l^\dagger + i\hbar a_l^\dagger(t) L_l \right), \tag{6.8}$$

where

$$H = \sum_{j=1}^{N} (\epsilon_j - \hbar\omega_0) |j\rangle\langle j| + \sum_{j \neq k} J_{jk} |j\rangle\langle k| \tag{6.9}$$

and

$$L_l = \sqrt{\Gamma_0 \eta_l} \sum_j \mathbf{d}_j \cdot \hat{\epsilon}_l |g\rangle\langle j| \tag{6.10}$$

is a system lowering operator. $\Gamma_0 = \frac{d_0^2 \omega_0^3}{3\pi\epsilon_0 \hbar c^3}$ characterizes the system-light coupling strength and is equal to the spontaneous emission rate of a unit dipole d_0 with transition frequency ω_0 in vacuum. η is a geometric factor that will depend on the type of the spatial mode, e.g., paraxial incoming modes (Eq. (6.2)), small solid angle modes (Eq. (6.3)), or x-, y-, z-polarization modes (Eq. (6.5)). $\mathbf{d}_j$ is the vector transition dipole moment of the j-th site (divided by the unit dipole moment d_0 so that $\mathbf{d}_j$ is dimensionless), and $\hat{\epsilon}_l$ is the unit polarization vector of spatial mode l.

L_l can be written in a useful alternative form as

$$L_l = \sqrt{\Gamma_l} |g\rangle\langle B_l|, \tag{6.11}$$

with Γ_l the effective coupling constant

$$\Gamma_l = \Gamma_0 \eta_l \sum_j |\mathbf{d}_j \cdot \hat{\epsilon}|^2 \tag{6.12}$$

and $|B_l\rangle$ the normalized bright state

$$|B_l\rangle = (\sum_j |\mathbf{d}_j \cdot \hat{\epsilon}|^2)^{-1/2} \sum_j \mathbf{d}_j \cdot \hat{\epsilon} |j\rangle. \tag{6.13}$$

As a physical motivation for this notation, we note that the excited state $|B_l\rangle$ spontaneously emits into mode l at the rate Γ_l. A more detailed discussion of the emission rate, or more generally, of the photon flux, is given in Section 6.2.7.

An N-photon Fock state pulse in mode l with temporal profile $\xi(t)$ is defined as

$$|N_\xi\rangle_l = \frac{1}{\sqrt{N!}} \left(\int d\tau\, \xi(\tau) a_l^\dagger(\tau) \right)^N |\phi\rangle, \tag{6.14}$$

where $\xi(t)$ is normalized according to $\int d\tau\, |\xi(\tau)|^2 = 1$ and $|\phi\rangle$ is the vacuum state of the field. More general N-photon Fock states are possible, as discussed in Ref. [47], but we shall restrict ourselves to this single mode product form here.

Another important object in the input-output formalism is the unitary $U(t)$ defined by

$$\frac{dU(t)}{dt} = -\frac{i}{\hbar} H_{\text{int}}(t) U(t) \tag{6.15}$$

with initial condition $U(0) = 1$. The system+field unitary in the Schrodinger picture, $e^{-\frac{i}{\hbar} H_{\text{sys+field}} t}$, is related to the interaction picture unitary $U(t)$ by

$$e^{-\frac{i}{\hbar} H_{\text{sys+field}} t} = e^{-\frac{i}{\hbar} H_0 t} U(t) \tag{6.16}$$

(see Eq. (6.6)). We will set $\hbar = 1$ from now on.

6.2.3 Some results in the input-output formalism

This section summarizes some results in the input-output formalism that will be used later. The operators $a(t)$ and $U(t)$ satisfy the so-called input-output relation [50]:

$$U^\dagger(t)a_l(t_r)U(t) = \begin{cases} a_l(t_r) & t < t_r \\ a_l(t_r) + \frac{1}{2}L_{Hl}(t_r) & t = t_r \\ a_l(t_r) + L_{Hl}(t_r) & t > t_r, \end{cases} \tag{6.17}$$

with $L_{Hl}(t) \equiv U^\dagger(t)L_lU(t)$ (see Sec. 2.1). At time $t < t_r$, $a_l(t_r)$ has not interacted with the system, so time evolution has no effect on it (i.e., $U^\dagger(t)a_l(t_r)U(t) = a_l(t_r)$). For this reason, $a_l(t_r)$ is called the input field. At time $t > t_r$, $a(t_r)$ has interacted with the system and will not interact with the system anymore. For this reason, the time-evolved operator $U^\dagger(t)a_l(t_r)U(t) = a_l(t_r) + L_{Hl}(t_r) \equiv a_{l,\text{out}}(t_r)$ is called the output field. Using the Markov property that $a(t_r)$ only interacts with the system at time $t = t_r$, we have thereby expressed the time-evolved field operator, which usually mixes the system and field degrees of freedom in some complicated way, as a simple sum of a pure field operator and a time-evolved system operator.

Left-multiplying Eq. (6.17) by $U(t)$, we then obtain the following commutation relation at $t = t_r$,

$$[a_l(t), U(t)] = \frac{1}{2}L_lU(t). \tag{6.18}$$

Using this commutation relation, we can rewrite Eq. (6.15) (also see Eq. (6.8)) in normal-ordered form as

$$\frac{d}{dt}U(t) = \big(-iH - \frac{1}{2}\sum_l L_l^\dagger L_l\big)U(t) - \sum_l L_l^\dagger U(t)a_l(t) + \sum_l a_l^\dagger(t)L_lU(t). \tag{6.19}$$

In the following sections, we will see that the commutation relation and the normal-ordered form of the time evolution derivative ensure that we only need to consider the action of normal-ordered field operators acting on field states, greatly simplifying the calculations.

Input-output theory is traditionally presented in terms of quantum stochastic differential equations (QSDE) where the input field operators are taken to be differentials, e.g. $dA_{l,t} = a_l(t + dt) - a_l(t)$, analogous to the Wiener process increment dW_t in classical stochastic calculus. As in classical stochastic calculus, integrals over the quantum stochastic differential $\int X_t dA_t$ can be interpreted either as Stratonivich integrals or as Ito integrals, resulting in different values [86, 116]. The Stratonovich integral takes a "mid-point" time approximation for the integrand, while the Ito integral takes the initial time approximation for the integrand. To make connections to the QSDE approach, we note that Eq. (6.19) can be written as

$$dU_t = -iHU_tdt - \sum_l L_l^\dagger U_t \circ dA_{l,t} + \sum_l L_lU_t \circ dA_{l,t}^\dagger, \tag{6.20}$$

where the symbol $\circ$ indicates that the differential expression is to be integrated in the Stratonovich sense, or it can also be written as

$$dU_t = \big(-iH - \frac{1}{2}\sum_l L_l^\dagger L_l\big)U_tdt - \sum_l L_l^\dagger U_t \cdot dA_{l,t} + \sum_l L_lU_t \cdot dA_{l,t}^\dagger, \tag{6.21}$$

where the symbol $\cdot$ indicates that the differential expression is to be integrated in the Ito sense.

It was shown in [117] that a usual time-ordered product of iterated time integrals that include products of the field operators $a_l(t)$ and $a_l^\dagger(t)$ should be interpreted as a quantum Stratonovich

integral. Conversely, if the iterated time integrals were instead written in normal-order then that corresponds to a quantum Ito integral. Thus by writing Eq. (6.19) in normal order, the solution will have the same mathematical properties as a quantum Ito integral (Eq. (6.21)), without delving into the mathematics of quantum Ito integration and its modified rules of calculus.

6.2.4 Coherent state master equation

A coherent state with coherent amplitude α and temporal profile $\xi(t_r)$ is given by

$$|\alpha_\xi\rangle = \exp\Big(\int dt_r\, \alpha(t_r) a^\dagger_{\rm inc}(t_r) - \alpha^*(t_r) a_{\rm inc}(t_r)\Big)|{\rm vac}\rangle, \tag{6.22}$$

where $\alpha(t_r) = \alpha\xi(t_r)$. This is an eigenstate of the annihilation operator $a(t)$ for all t, i.e.,

$$a(t)|\alpha_\xi\rangle = \alpha(t)|\alpha_\xi\rangle. \tag{6.23}$$

The system state $\rho(t)$ in the interaction frame is given by

$$\rho(t) = {\rm Tr}_{\rm field}\Big(U(t)\rho(0)\otimes|\alpha\rangle\langle\alpha|U^\dagger(t)\Big). \tag{6.24}$$

Using Eq. (6.19), we have

$$\begin{aligned}\frac{d}{dt}\rho(t) =& -i[H,\rho(t)] + \frac{1}{2}\sum_l\Big(-L_l^\dagger L_l\rho(t) - \rho(t)L_l^\dagger L_l\Big) - \alpha(t)L^\dagger_{\rm inc}\rho(t) - \alpha^*(t)\rho(t)L_{\rm inc}\\ &+\sum_l L_l {\rm Tr}_{\rm field}\Big(U(t)\rho(0)\otimes|\alpha(t_r)\rangle\langle\alpha(t_r)|U^\dagger(t)a_l^\dagger(t)\Big)\\ &+{\rm Tr}_{\rm field}\Big(a_l(t)U(t)\rho(0)\otimes|\alpha(t_r)\rangle\langle\alpha(t_r)|U^\dagger(t)\Big)L_l^\dagger.\end{aligned} \tag{6.25}$$

Using the commutation relation (Eq. (6.18)) to simplify the partial traces yields the coherent state master equation

$$\frac{d}{dt}\rho = -i[H - i\alpha(t)L^\dagger_{\rm inc} + i\alpha^*(t)L_{\rm inc},\rho] + \sum_l L_l\rho L_l^\dagger - \frac{1}{2}L_l^\dagger L_l\rho - \frac{1}{2}\rho L_l^\dagger L_l. \tag{6.26}$$

We identify a time dependent classical electric field $\mathbf{E}(t)$ as the expectation value of the coherent state, i.e.,

$$\mathbf{E}(t) = \langle\alpha_\xi|\hat{\mathbf{E}}(t)|\alpha_\xi\rangle, \tag{6.27}$$

where $\hat{\mathbf{E}}(t)$ is the electric field operator. Then we see that the system evolution follows exactly the semiclassical equation plus spontaneous emission, i.e.,

$$\frac{d}{dt}\rho = -i[H - \mathbf{d}\cdot\mathbf{E}(t),\rho] + \sum_l L_l\rho L_l^\dagger - \frac{1}{2}L_l^\dagger L_l\rho - \frac{1}{2}\rho L_l^\dagger L_l. \tag{6.28}$$

We note the coherent state master equation (Eq. (6.26)) can be alternatively derived from the Fock state master equation. This is because the system density matrix under coherent state excitation can be written as a sum of Fock state auxiliary density matrices, i.e.,

$$\rho = \sum_{m,n}\frac{\alpha^m\alpha^{*n}}{\sqrt{m!n!}}e^{-|\alpha|^2}\rho_{m,n}. \tag{6.29}$$

Then substituting the Fock state master equation into the right hand side of this equation, allows one to obtain Eq. (6.26) in a few lines of algebra.

6.2.5 Fock State Master Equations

Let $|N_\xi\rangle$ be the field state where a single photon pulse with temporal profile $\xi(t)$ is in the incoming mode ($l = \text{inc}$), and all other field modes are in the vacuum state. The system density matrix in the interaction picture, $\tilde{\rho}_{\text{sys}}(t)$, is obtained by evolving the initial state then partially tracing over the field, i.e.,

$$\tilde{\rho}_{\text{sys}}(t) = \text{Tr}_{\text{field}}\Big(U(t)\rho_0 \otimes |N_\xi\rangle\langle N_\xi| U^\dagger(t)\Big). \tag{6.30}$$

We assume at $t = 0$, the system+field state is a factorizable state, $\rho_0 \otimes |N_\xi\rangle\langle N_\xi|$.

A normalized N-photon Fock state in spatial mode $l = \text{inc}$ is specified by

$$|N_\xi\rangle = \frac{1}{\sqrt{N!}}\Big[\int d\tau\, \xi(\tau) a^\dagger_{\text{inc}}(\tau)\Big]^N |\phi\rangle, \tag{6.31}$$

where $\xi(t)$ is the normalized temporal profile of the N-photon Fock state satisfying $\int d\tau\, |\xi(\tau)|^2 = 1$. Using Eq. (6.19) to take the time derivative of $\tilde{\rho}_{\text{sys}}$, we find

$$\begin{aligned}
\frac{d\tilde{\rho}_{\text{sys}}}{dt} =& \big(-iH - \frac{1}{2}\sum_l L_l^\dagger L_l\big)\text{Tr}_{\text{field}}\Big(U(t)\rho_0 \otimes |N_\xi\rangle\langle N_\xi| U^\dagger(t)\Big) \\
&- \sum_l L_l^\dagger \text{Tr}_{\text{field}}\Big(U(t)a_l(t)\rho_0 \otimes |N_\xi\rangle\langle N_\xi| U^\dagger(t)\Big) \\
&+ \sum_l \text{Tr}_{\text{field}}\Big(a_l^\dagger(t) L_l U(t)\rho_0 \otimes |N_\xi\rangle\langle N_\xi| U^\dagger(t)\Big) \\
&+ \text{Tr}_{\text{field}}\Big(U(t)\rho_0 \otimes |N_\xi\rangle\langle N_\xi| U^\dagger(t)\Big)\big(iH - \frac{1}{2}\sum_l L_l^\dagger L_l\big) \\
&- \sum_l \text{Tr}_{\text{field}}\Big(U(t)\rho_0 \otimes |N_\xi\rangle\langle N_\xi| a_l^\dagger(t) U^\dagger(t)\Big) L_l \\
&+ \sum_l \text{Tr}_{\text{field}}\Big(U(t)\rho_0 \otimes |N_\xi\rangle\langle N_\xi| U^\dagger(t) L_l^\dagger a_l(t)\Big)
\end{aligned} \tag{6.32}$$

The second (and similarly the fifth) term on the right hand side can be simplified using the identity

$$a_l(t)|N_\xi\rangle = \begin{cases} \sqrt{N}\xi(t)|(N-1)_\xi\rangle\,, & l = \text{inc} \\ 0 \quad \text{otherwise.} \end{cases} \tag{6.33}$$

Hence when $l = \text{inc}$, the partial trace in the second term becomes

$$\text{Tr}_{\text{field}}\Big(U(t)a_{\text{inc}}(t)\rho_0 \otimes |N_\xi\rangle\langle N_\xi| U^\dagger(t)\Big) = \sqrt{N}\xi(t)\text{Tr}_{\text{field}}\Big(U(t)\rho_0 \otimes |(N-1)_\xi\rangle\langle N_\xi| U^\dagger(t)\Big). \tag{6.34}$$

The sixth (and similarly the third) term can be simplified by applying the cyclic property of trace and the commutation relation Eq. (6.18). For example, when $l = \text{inc}$,

$$\begin{aligned}
&\text{Tr}_{\text{field}}\Big(U(t)\rho_0 \otimes |N_\xi\rangle\langle N_\xi| U^\dagger(t) L_{\text{inc}}^\dagger a_{\text{inc}}(t)\Big) \\
&= \text{Tr}_{\text{field}}\Big(a_{\text{inc}}(t)U(t)\rho_0 \otimes |N_\xi\rangle\langle N_\xi| U^\dagger(t)\Big) L_{\text{inc}}^\dagger \\
&= \text{Tr}_{\text{field}}\Big(U(t)a_{\text{inc}}(t)\rho_0 \otimes |N_\xi\rangle\langle N_\xi| U^\dagger(t)\Big) L_{\text{inc}}^\dagger + \frac{1}{2} L_{\text{inc}} \text{Tr}_{\text{field}}\Big(U(t)\rho_0 \otimes |N_\xi\rangle\langle N_\xi| U^\dagger(t)\Big) L_{\text{inc}}^\dagger.
\end{aligned} \tag{6.35}$$

If we now define

$$\rho_{m,n}(t) \equiv \text{Tr}_{\text{field}}\Big(U(t)\rho_0 \otimes |m_\xi\rangle\langle n_\xi| U^\dagger(t)\Big), \tag{6.36}$$

then following a similar procedure as above, we obtain the full Fock state master equation

$$\begin{aligned}\frac{d\rho_{m,n}}{dt} =& -i[H,\rho_{m,n}] + \sum_l \mathcal{D}[L_l](\rho_{m,n}) \\ &+ \sqrt{m}\xi(t)[\rho_{m-1,n}, L_{\text{inc}}^\dagger] + \sqrt{n}\xi^*(t)[L_{\text{inc}}, \rho_{m,n-1}],\end{aligned} \tag{6.37}$$

with $\rho_{N,N}(t) = \tilde{\rho}_{\text{sys}}(t)$ and $\mathcal{D}[L]$ is the Lindblad superoperator defined as $\mathcal{D}[L](\rho) \equiv -\frac{1}{2}L^\dagger L\rho - \frac{1}{2}\rho L^\dagger L + L\rho L^\dagger$. Here $\rho_{N,N}(t)$ is the physical density matrix that describes the system state given an N-photon Fock state input. $\rho_{N,N}$ couples to other auxiliary density matrices corresponding to smaller number of photons, with lower indices down to $\rho_{0,0}$. Therefore, we need to solve for a hierarchy of $(N+1)^2$ coupled density matrix equations. In the absence of phonon coupling, we can use the property $\rho_{m,n} = \rho_{n,m}^\dagger$ to reduce the number of density matrices to solve for to $(N+1)(N+2)/2$. The initial value $\rho_{m,n} = \delta_{m,n}\,\rho_0$ is obtained from Eq. (6.36).

The Fock state master equation (Eq. (6.37)) was originally derived by Baragiola et. al. [47] using the more mathematical quantum stochastic differential equations (QSDE). Here, we have given a more accessible alternative derivation based on ordinary differential equations (ODE).

6.2.6 System plus field pure state

In the special case of a single photon Fock state input, the Fock state master equations (Eq. (6.37)) can be solved analytically. However, rather than solving Eq. (6.37) directly, a more physically intuitive approach is to write the system+field pure state $|\psi(t)\rangle$ as

$$|\psi(t)\rangle = |\beta(t)\rangle|\text{vac}\rangle + |g\rangle\sum_l \int_{-\infty}^{\infty} dt_r\, \phi_l(t,t_r) a_l^\dagger(t_r)|\text{vac}\rangle, \tag{6.38}$$

where $|\beta(t)\rangle$ is an unnormalized system state in the excited subspace, and $\phi_l(t,t_r)$ is the photon field amplitude of the single photon field state in mode l given unitary evolution up to time t, evaluated at t_r. Eq. (6.38) is in fact the most general form of the system+field pure state when there is exactly one excitation in the system and the field.

Taking the time derivative of Eq. (6.38), we have

$$\frac{d}{dt}|\psi(t)\rangle = \frac{d}{dt}|\beta(t)\rangle|\text{vac}\rangle + |g\rangle\sum_l \int_{-\infty}^{\infty} dt_r\, \frac{\partial}{\partial t}\phi_l(t,t_r) a_l^\dagger(t_r)|\text{vac}\rangle. \tag{6.39}$$

On the other hand, we can write the time derivative as

$$\frac{d}{dt}|\psi(t)\rangle = \frac{d}{dt}U(t)\left[|g\rangle\int_{-\infty}^{\infty} dt_r\, \xi(t_r) a_{\text{inc}}^\dagger(t_r)|\text{vac}\rangle\right], \tag{6.40}$$

where we rewrite $|\psi(t)\rangle$ as $U(t)$ acting on the initial state $|\psi(0)\rangle$. Using Eqs. (6.19) and (6.38), this becomes

$$\begin{aligned}\frac{d}{dt}|\psi(t)\rangle &= (-iH - \frac{1}{2}\sum_l L_l^\dagger L_l)|\psi(t)\rangle - L_{\text{inc}}^\dagger U(t)\xi(t)|g\rangle|\text{vac}\rangle + \sum_l a_l^\dagger(t) L_l|\psi(t)\rangle \\ &= \left[(-iH - \frac{1}{2}\sum_l L_l^\dagger L_l)|\beta(t)\rangle - \xi(t)L_{\text{inc}}^\dagger|g\rangle\right]|\text{vac}\rangle + |g\rangle\sum_l \langle g|L_l|\beta(t)\rangle a_l^\dagger(t)|\text{vac}\rangle.\end{aligned} \tag{6.41}$$

Comparing Eq. (6.39) to (6.41), we have

$$\frac{d}{dt}|\beta(t)\rangle = (-iH - \frac{1}{2}\sum_l L_l^\dagger L_l)|\beta(t)\rangle - \xi(t)L_{\text{inc}}^\dagger|g\rangle \tag{6.42a}$$

$$\frac{\partial}{\partial t}\phi_l(t,t_r) = \langle g|L_l|\beta(t)\rangle\delta(t-t_r). \tag{6.42b}$$

The solution to Eq. (6.42) is

$$|\beta(t)\rangle = -\int_0^t d\tau\, \xi(\tau) e^{(-iH - \frac{1}{2}\sum_l L_l^\dagger L_l)(t-\tau)} L_{\rm inc}^\dagger |g\rangle \tag{6.43a}$$

$$\phi_l(t, t_r) = \begin{cases} \delta_{l,\rm inc}\, \xi(t_r) & t < t_r \quad \text{(upstream)} \\ \delta_{l,\rm inc}\, \xi(t_r) + \frac{1}{2}\langle g|L_l|\beta(t_r)\rangle & t = t_r \\ \delta_{l,\rm inc}\, \xi(t_r) + \langle g|L_l|\beta(t_r)\rangle & t > t_r \quad \text{(downstream).} \end{cases} \tag{6.43b}$$

Since $\langle\psi(t)|\psi(t)\rangle = 1$, we have the property

$$\langle\beta(t)|\beta(t)\rangle + \sum_l \int dt_r\, |\phi_l(t, t_r)|^2 = 1. \tag{6.44}$$

Using Eq. (6.36), we find that the solution to the single photon Fock state master equation (Eq. (6.37)) is

$$\begin{aligned} \rho_{1,1}(t) &= |\beta(t)\rangle\langle\beta(t)| + |g\rangle\langle g| \sum_l \int_{-\infty}^{\infty} dt_r\, |\phi_l(t, t_r)|^2 \\ \rho_{1,0}(t) &= |\beta(t)\rangle\langle g| \\ \rho_{0,0}(t) &= |g\rangle\langle g|. \end{aligned} \tag{6.45}$$

The total probability of being in the excited state is $\langle\beta(t)|\beta(t)\rangle$. However, since the system energy scale $||H||$ is much larger than the spontaneous emission rate $||\sum_l L_l^\dagger L_l||$, if we are interested in the system behavior at short times we will have $||\sum_l L_l^\dagger L_l||\, t \ll 1$. It is then useful to drop the spontaneous emission terms in Eq. (6.43a) and approximate $|\beta(t)\rangle$ as

$$|\beta'_\xi(t)\rangle \equiv -\int_0^t d\tau\, \xi(\tau) e^{-iH(t-\tau)} L_{\rm inc}^\dagger |g\rangle, \tag{6.46}$$

where for later convenience, we added the subscript ξ to emphasize the dependence of the excited state $|\beta'(t)\rangle$ on the temporal profile $\xi(t)$.

6.2.7 Photon Flux

The photon flux of a field mode is defined as the rate at which photons pass through the mode and has the dimension of 1/[time]. At time t, the photon flux immediately downstream of the system is given by $a_{\rm out}^\dagger(t) a_{\rm out}(t)$ [47, 67].

Coherent state input

The expectation value of the photon flux F_l in spatial mode l is the trace over the initial state:

$$F_l = \mathrm{Tr}\Big(a_{l,\rm out}^\dagger(t) a_{l,\rm out}(t) \rho_0 \otimes |\alpha_\xi\rangle\langle\alpha_\xi|\Big). \tag{6.47}$$

Substituting in $a_{l,\rm out}(t) = a_l(t) + L_{Hl}(t)$ (see Eq. (6.17)) and following a similar procedure as in Sec. 6.2.4, we obtain the following explicit expression for the photon flux into mode l

$$F_l = \begin{cases} |\alpha(t)|^2 + \big(\alpha^*(t)\langle L_l\rangle + \text{c.c.}\big) + \langle L_l^\dagger L_l\rangle & , l = \text{inc} \\ \langle L_l^\dagger L_l\rangle & , \text{otherwise,} \end{cases} \tag{6.48}$$

where $\langle X\rangle \equiv \mathrm{Tr}(X\rho(t))$.

N-photon Fock state input

The expectation value of the photon flux F_l in spatial mode l is the trace over the initial state:

$$F_l = \mathrm{Tr}\Big(a^\dagger_{l,\mathrm{out}}(t)a_{l,\mathrm{out}}(t)\rho_0 \otimes |N_\xi\rangle\langle N_\xi|\Big). \tag{6.49}$$

Substituting in $a_{l,\mathrm{out}}(t) = a_l(t) + L_{Hl}(t)$ (see Eq. (6.17)) and following a similar procedure as in Sec. 6.2.5, we obtain the following explicit expression for the photon flux into mode l

$$F_l = \begin{cases} N|\xi(t)|^2 + \big(\sqrt{N}\xi^*(t)\langle L_l\rangle_{N,N-1} + \mathrm{c.c.}\big) + \langle L_l^\dagger L_l\rangle_{N,N} & , l = \mathrm{inc} \\ \langle L_l^\dagger L_l\rangle_{N,N} & , \text{otherwise,} \end{cases} \tag{6.50}$$

where $\langle X\rangle_{n,m} \equiv \mathrm{Tr}(X\rho_{n,m})$. In the expression on the first line for the incoming mode, the first term represents the transmission of the incoming photon and the second term arises from the coherent dynamics between the system and the field. A negative value of the latter term represents the absorption of photons. A positive value for this term corresponds to stimulated emission. It is interesting to note that the second term can be positive also in the case of a single photon input, meaning that a single photon can stimulate its own emission. The final term on the first line for the incoming mode has the same form as the flux expression for the non-incoming modes and represents the spontaneous emission into the particular mode l.

6.3 Interaction with phonons

6.3.1 Vibronic Hamiltonian and vibrational correlation functions

To model the interaction with phonons, we first employ the Born-Oppenheimer approximation to separate electronic and nuclear degrees of freedom. Each chromophore is coupled to a set of nuclear coordinates, and the nuclear coordinates of different chromophores are independent of each other. Next, we use the harmonic approximation to describe the nuclear Hamiltonian near the potential energy minumum as a set of harmonic oscillators. Let the nuclear Hamiltonian for the electronic ground state be

$$H_{\mathrm{vib,g}} = \sum_\xi \frac{p_\xi^2}{2} + \frac{\omega_\xi^2 q_\xi^2}{2}, \tag{6.51}$$

where ξ indexes the normal mode (phonon) coordinates, ω_ξ is the normal mode frequency, q_ξ and p_ξ are the mass-normalized normal mode coordinate and its conjugate momentum. We set the minimum of the ground state potential energy surface to have zero potential energy. We assume the nuclear Hamiltonian for the excited state is described by the same set of normal mode coordinates and that it takes the usual form of shifted harmonic oscillators [49, 118]

$$H_{\mathrm{vib,e}} = E_0 + \sum_\xi \frac{p_\xi^2}{2} + \frac{\omega_\xi^2 (q_\xi + d_\xi)^2}{2}, \tag{6.52}$$

where E_0 is the minimum energy of the excited state potential energy surface, and d_ξ is the coordinate shift of normal mode ξ. $H_{\mathrm{vib,e}}$ can be re-expressed as

$$H_{\mathrm{vib,e}} = \epsilon + H_{\mathrm{vib,g}} + u, \tag{6.53}$$

where

$$\epsilon = E_{0,j} + \sum_\xi \omega_\xi^2 d_\xi^2/2 \tag{6.54}$$

is the energy of the vertical transition from the ground state minimum, and

$$u = \sum_{\xi} \omega_{\xi}^2 d_{\xi} q_{\xi} \tag{6.55}$$

is a linear combination of phonon coordinates. In the continuum limit, the coupling to phonon coordinates can be described by the spectral density $J(\omega)$, defined as

$$J(\omega) = \sum_{\xi} \frac{\pi}{2\omega_{\xi}} (\omega_{\xi}^2 d_{\xi})^2 \delta(\omega - \omega_{\xi}) \tag{6.56}$$

The second term on the right-hand side of Eq. (6.54) is the reorganization energy λ, which is related to the spectral density by

$$\lambda = \frac{1}{\pi} \int_0^{\infty} d\omega \, \frac{J(\omega)}{\omega}. \tag{6.57}$$

The overall system+vibration Hamiltonian in the 0- and 1-electronic excitation subspace is

$$H_{\text{sys+vib}} = |g\rangle\langle g| \sum_k H_{\text{vib,g}}^{(k)} + \sum_j |j\rangle\langle j| \big(H_{\text{vib,e}}^{(j)} + \sum_{k \neq j} H_{\text{vib,g}}^{(k)} \big) + \sum_{j \neq k} J_{jk} |j\rangle\langle k|, \tag{6.58}$$

where the last term on the right hand side describes the dipole-dipole interaction between the singly-excited states. We ignore the small effect of phonons on the dipole-dipole interaction [119]. Note that the nuclear Hamiltonian $H_{\text{vib}}^{(j)}$ for different chromophore sites can have different normal modes, displacements d_{ξ}, and energy shifts E_0. Using Eq. (6.53), we can simplify Eq. (6.58) as

$$H_{\text{sys+vib}} = \underbrace{\sum_j \epsilon_j |j\rangle\langle j| + \sum_{j \neq k} J_{jk} |j\rangle\langle k|}_{H_{\text{sys}}} + \underbrace{\sum_k H_{\text{vib,g}}^{(k)}}_{H_{\text{vib}}} + \underbrace{\sum_j |j\rangle\langle j| u_j}_{H_{\text{sys-vib}}}. \tag{6.59}$$

We have separated the system+vibration Hamiltonian here into a system part H_{sys}, a vibration part H_{vib}, and a system-vibration interaction part $H_{\text{sys-vib}}$. Note that H_{sys} takes exactly the same form as Eq. (6.1). Since the system-vibration coupling term does not involve the system ground state, to a very good approximation, the initial thermal state $\propto e^{-\beta H_{\text{sys+vib}}}$ is a product state between the system ground state $|g\rangle\langle g|$ and the vibrational thermal state $\propto e^{-\beta H_{\text{vib}}}$.

To study the effect of nuclear vibrations on the electronic states, we need to understand some properties of the vibrational correlation functions. First, we rotate out H_{vib} from the system+vibration Hamiltonian, and we write the interaction Hamiltonian as

$$H_{\text{I}}(t) = H_{\text{sys}} + \sum_j |j\rangle\langle j| u_j(t), \tag{6.60}$$

where $u_j(t) \equiv \exp(iH_{\text{vib}}t) u_j \exp(-iH_{\text{vib}}t)$. An important property of $u_j(t)$ is Wick's theorem [120]

$$\big\langle \mathcal{O} u_{j_{2n}}(t_{2n}) u_{j_{2n-1}}(t_{2n-1}) \cdots u_{j_2}(t_2) u_{j_1}(t_1) \big\rangle = \sum_{\text{a.p.p.}} \prod_{k,l} \big\langle \mathcal{O} u_{j_k}(t_k) u_{j_l}(t_l) \big\rangle, \tag{6.61}$$

where $\mathcal{O}$ is an ordering operator that imposes some ordering on $\{t_1, \cdots t_{2n}\}$ and re-orders the operators according to their time arguments t_k. The angled bracket $\langle X \rangle \equiv \text{Tr}(\rho_{\text{thermal}} X)$ denotes averaging with a thermal state. The sum on the right hand side is over all possible pairings (k, l) of the 2n operators. Averaging over an odd number of operators, we have $\langle \mathcal{O} u_{j_{2n-1}}(t_{2n-1}) \cdots u_{j_2}(t_2) u_{j_1}(t_1) \rangle = 0$. Therefore, under thermal averaging, $u_j(t)$ behaves like a mean-zero Gaussian random process. Note that $\langle \mathcal{O} u_{j_k}(t_k) u_{j_l}(t_l) \rangle$ is non-zero only when $j_k = j_l$, meaning that these correlation functions

are non-zero only when they correspond to the phonon operator on the same site, because of the assumption that phonons on different sites are independent. Substituting $q_\xi = \sqrt{\hbar/2\omega_\xi}(a_\xi + a_\xi^\dagger)$ into Eq. (6.55), we find that the two-point correlation function of phonon operators on the same site is

$$\langle u_j(t_2)u_j(t_1)\rangle = \frac{\hbar}{\pi}\int_0^\infty d\omega\, J_j(\omega)\big[\coth(\frac{\beta\hbar\omega}{2})\cos(\omega\tau) - i\sin(\omega\tau)\big], \tag{6.62}$$

where $\tau \equiv t_2 - t_1$ and $\beta = 1/k_BT$ is the inverse temperature.

We will analyze the effect of vibration using two different methods. The first method considers an initial vibrational pure state, and solves for the pure state analogous to Section 6.2.6. Then by averaging the dynamics starting from a thermal distribution of vibrational pure states, we can analyze the behavior given an initial vibrational thermal state. This method can be applied numerically only for a small number of discrete vibration modes, but it gives us useful analytical expressions in the continuum limit. The second method uses the HEOM formalism to trace out the vibration degrees of freedom and represent the effect of a continuum of vibration modes by a set of auxiliary density matrices containing only the system degrees of freedom.

6.3.2 Generalized cumulant expansion

The hierarchical equations of motion (HEOM) is a non-perturbative method to treat the non-Markovian effects of phonons on the system dynamics. They are a set of differential equations that couples the physical density matrix to a hierarchy of auxiliary density matrices. We first discuss the generalized cumulant expansion [121] for the reduced system state, and then use it to derive the HEOM for an overdamped vibrational bath and an underdamped vibrational bath.

The time evolution of the system+vibration density matrix can be expressed as a superoperator acting on the initial system+vibration density matrix

$$\rho_{\text{sys+vib}}(t) = \mathcal{T}\exp\bigg(\int_0^t d\tau\, -\frac{i}{\hbar}H_I^\times(\tau)\bigg)\rho_{\text{sys+vib}}(0).r \tag{6.63}$$

The exponential is time-ordered, and $H_I^\times(\tau)\rho \equiv [H_I(\tau),\rho]$ is the commutator. Assuming an initial factorized state $\rho_{\text{sys+vib}}(0) = \rho_{\text{sys}}(0)\otimes\rho_{\text{vib, thermal}}$, with the vibrational state in thermal equilibrium, the reduced system state is then obtained as the partial trace of the time-evolved system+vibration state

$$\begin{aligned}\rho_{\text{sys}}(t) &= \text{Tr}_{\text{vib}}\Big(\big(\mathcal{T}\exp\int_0^t d\tau\, -\frac{i}{\hbar}H_I^\times(\tau)\big)\rho_{\text{sys+vib}}(0)\Big)\\ &= \Big\langle\mathcal{T}\exp\int_0^t d\tau\, -\frac{i}{\hbar}H_I^\times(\tau)\Big\rangle\rho_{\text{sys}}(0).\end{aligned} \tag{6.64}$$

In the second line, the angled bracket $\langle\cdots\rangle$ means averaging with the vibration thermal state: this maps a superoperator acting on the system+vibration Liouville space to a superoperator acting on the system Liouville space. We will show below that Eq. (6.64) can be expressed as a generalized cumulant expansion as

$$\rho_{\text{sys}}(t) = \mathcal{T}\exp\Big(-\frac{i}{\hbar}\int_0^t dt_1\,\langle H_I^\times(t_1)\rangle - \frac{1}{\hbar^2}\int_0^t dt_2\int_0^{t_2} dt_1\,\langle H_I^\times(t_2)H_I^\times(t_1)\rangle - \langle H_I^\times(t_2)\rangle\langle H_I^\times(t_1)\rangle\Big)\rho_{\text{sys}}(0). \tag{6.65}$$

All higher cumulant terms vanish identically because of Wick's property (Eq. (6.61)).

To fill in some steps leading to Eq. (6.65), we write a commutator superoperator $A^\times = A^l + A^r$ as a sum of a left multiplication superoperator A^l, defined as $A^lB = AB$, and a right multiplication

superoperator A^r, defined with an additional minus sign as $A^r B = -BA$. We also write Eq. (6.58) as a sum of $N+1$ product terms

$$H_I(t) = \sum_{k=0}^{N} S_k(t) B_k(t), \tag{6.66}$$

where $S_k(t)$ are system operators and $B_k(t)$ are phonon bath operators. In particular,

$$S_k(t) = \begin{cases} H_{\text{sys}} & , k = 0 \\ P_j = |j\rangle\langle j| & , k \neq 0 \end{cases}, \tag{6.67}$$

and

$$B_k(t) = \begin{cases} 1 & , k = 0 \\ u_k(t) & , k \neq 0 \end{cases}. \tag{6.68}$$

A general time-ordered product in the expansion of Eq. (6.64) takes the form

$$\begin{aligned} &\Big\langle \mathcal{T}\big(S_{k_n}(t_n)B_{k_n}(t_n)\big)^{\times} \cdots \big(S_{k_1}(t_1)B_{k_1}(t_1)\big)^{\times} \Big\rangle \\ &= \sum_{\alpha_n = l,r} \cdots \sum_{\alpha_1 = l,r} \mathcal{T} S_{k_n}^{\alpha_n}(t_n) \cdots S_{k_1}^{\alpha_1}(t_1) \Big\langle \mathcal{O}_{\{\alpha,t\}} B_{k_n}(t_n) \cdots B_{k_1}(t_1) \Big\rangle, \end{aligned} \tag{6.69}$$

where in the second line the bracket $\langle \cdots \rangle$ means averaging with the phonon thermal state. The ordering of the phonon operators depends on the α and depends on the ordering of the time points t_1 to t_n. We now partition the n different time points, t_1 to t_n, into $N+1$ groups, where in the k-th group the time points correspond to operators S_k and B_k. The time points in the k-th group are re-labeled as $\{t_{k,1}, t_{k,2}, \cdots\}$. To illustrate this notation, Eq. (6.69) may, for example, be rewritten as

$$\Big\langle \mathcal{T}\big(S_4(t_{4,1})B_4(t_{4,1})\big)^{\times} \big(S_3(t_{3,1})B_3(t_{3,1})\big)^{\times} \big(S_3(t_{3,2})B_3(t_{3,2})\big)^{\times} \Big\rangle. \tag{6.70}$$

Since the phonon correlation function factorizes into $N+1$ groups of different B_k operators, Eq. (6.69) can be factorized as

$$\begin{aligned} \text{Eq. (6.69)} &= \mathcal{T} \prod_{k=0}^{N} \sum_{\alpha_{k,1}} \sum_{\alpha_{k,2}} \cdots S_k^{\alpha_{k,1}}(t_{k,1}) S_k^{\alpha_{k,2}}(t_{k,2}) \cdots \Big\langle \mathcal{O}_{\{\alpha,t\}} B_k(t_{k,1}) B_k(t_{k,2}) \cdots \Big\rangle \\ &= \mathcal{T} \prod_{k=0}^{N} \Big\langle \mathcal{T}\big(S_k(t_{k,1})B_k(t_{k,1})\big)^{\times} \big(S_k(t_{k,2})B_k(t_{k,2})\big)^{\times} \cdots \Big\rangle. \end{aligned} \tag{6.71}$$

Using the factorization property (Eq. (6.71)) and the fact that superoperators commute under time-ordering, we can factorize Eq. (6.64) as

$$\rho_{\text{sys}}(t) = \mathcal{T} \prod_{k=0}^{N} \Big\langle \mathcal{T} \exp \int_0^t d\tau \; -\frac{i}{\hbar} \big(S_k(\tau) B_k(\tau)\big)^{\times} \Big\rangle \rho_{\text{sys}}(0). \tag{6.72}$$

For $k = 0$,

$$\Big\langle \mathcal{T} \exp \int_0^t d\tau \; -\frac{i}{\hbar} \big(S_k(\tau) B_k(\tau)\big)^{\times} \Big\rangle = \mathcal{T} \exp \int_0^t d\tau \; -\frac{i}{\hbar} H_{\text{sys}}(\tau)^{\times}. \tag{6.73}$$

For $k \neq 0$, the n-th expansion term of $\Big\langle \mathcal{T} \exp \int_0^t d\tau \, -\frac{i}{\hbar}\big(S_k(\tau)B_k(\tau)\big)^\times \Big\rangle$ is

$$\begin{aligned} &\frac{1}{n!}(\frac{-i}{\hbar})^n \int_0^t dt_n \cdots \int_0^t dt_1 \\ &\qquad \sum_{\alpha_n} \cdots \sum_{\alpha_1} \mathcal{T} P_k^{\alpha_n}(t_n) \cdots P_k^{\alpha_1}(t_1) \Big\langle \mathcal{O}_{\{\alpha,t\}} u_k(t_n) \cdots u_k(t_1) \Big\rangle. \end{aligned} \tag{6.74}$$

Using Wick's property (Eq. (6.61)), the integrand in the equation above is nonzero when n is even. In this case, the integrand becomes

$$\begin{aligned} &\sum_{\text{a.p.p.}} \Big(\sum_{\alpha_n} \cdots \sum_{\alpha_1} \mathcal{T} P_k^{\alpha_n}(t_n) \cdots P_k^{\alpha_1}(t_1) \Big\langle \mathcal{O}_{\{\alpha,t\}} u_k(t_p) u_k(t_q) \Big\rangle \Big\langle \mathcal{O}_{\{\alpha,t\}} u_k(t_r) u_k(t_s) \Big\rangle \cdots \Big) \\ &= \sum_{\text{a.p.p.}} \mathcal{T} \Big(\sum_{\alpha_p} \sum_{\alpha_q} \mathcal{T} P_k^{\alpha_p}(t_p) P_k^{\alpha_q}(t_q) \Big\langle \mathcal{O}_{\{\alpha,t\}} u_k(t_p) u_k(t_q) \Big\rangle \Big) \\ &\qquad \Big(\sum_{\alpha_r} \sum_{\alpha_s} \mathcal{T} P_k^{\alpha_r}(t_r) P_k^{\alpha_s}(t_s) \Big\langle \mathcal{O}_{\{\alpha,t\}} u_k(t_r) u_k(t_s) \Big\rangle \Big) \\ &\qquad \cdots . \end{aligned} \tag{6.75}$$

On the right hand side, we factorize the integrand into products of double interaction terms. Eq. (6.74) becomes

$$\begin{aligned} &\frac{1}{n!} \sum_{\text{a.p.p.}} (\frac{-i}{\hbar})^n \mathcal{T} \Big(\int_0^t dt_2 \int_0^t dt_1 \sum_{\alpha_2} \sum_{\alpha_1} \mathcal{T} P_k^{\alpha_2}(t_2) P_k^{\alpha_1}(t_1) \Big\langle \mathcal{O}_{\{\alpha,t\}} u_k(t_2) u_k(t_1) \Big\rangle \Big)^{n/2} \\ &= \frac{1}{2^{n/2}(n/2)!} (\frac{-1}{\hbar^2})^{n/2} \mathcal{T} \Big(2 \int_0^t dt_2 \int_0^{t_2} dt_1 (P_k(t_2)P_k(t_1) \bullet - P_k(t_1) \bullet P_k(t_2)) \langle u_k(t_2) u_k(t_1) \rangle \\ &\qquad\qquad (\bullet P_k(t_1) P_k(t_2) - P_k(t_2) \bullet P_k(t_1)) \langle u_k(t_1) u_k(t_2) \rangle \Big)^{n/2} \\ &= \frac{1}{(n/2)!} (\frac{-1}{\hbar^2})^{n/2} \mathcal{T} \Big(\int_0^t dt_2 \int_0^{t_2} dt_1 P_k^\times(t_2) P_k^\times(t_1) \Re \langle u_k(t_2) u_k(t_1) \rangle \\ &\qquad\qquad + P_k^\times(t_2) P_k^o(t_1) \Im \langle u_k(t_2) u_k(t_1) \rangle \Big)^{n/2}. \end{aligned} \tag{6.76}$$

Note that in the first line, the summand is independent of the pairing of the n factors. Therefore, the sum $\sum_{\text{a.p.p}}$ becomes a factor of $n!/(2^n(n/2)!)$, which is the number of ways to pair up n terms into $n/2$ pairs (remember n is even). In the second equality, we use the superoperator notation where for example $(A \bullet B)\rho = A\rho B$. Therefore for $k \neq 1$,

$$\begin{aligned} &\Big\langle \mathcal{T} \exp \int_0^t d\tau \, -\frac{i}{\hbar}\big(S_k(\tau)B_k(\tau)\big)^\times \Big\rangle = \\ &\mathcal{T} \exp \big(\int_0^t dt_2 \int_0^{t_2} dt_1 P_k^\times(t_2) P_k^\times(t_1) \Re \langle u_k(t_2) u_k(t_1) \rangle + P_k^\times(t_2) P_k^o(t_1) \Im \langle u_k(t_2) u_k(t_1) \rangle \big). \end{aligned} \tag{6.77}$$

Combining Eqs. (6.72), (6.73), and (6.77), we obtain the generalized cumulant expansion of Eq. (6.65).

6.3.3 Hierarchical equations of motion for overdamped vibration

We assume the spectral density takes the Drude-Lorentz form

$$J_j(\omega) = \frac{2\lambda_j \gamma_j \omega}{\omega^2 + \gamma_j^2}, \tag{6.78}$$

corresponding to the overdamped Brownian oscillator model [46,49], where γ is the exponential decay rate of the imaginary part of the correlation function. It is interesting to note that if we require the imaginary part of the correlation function (proportional to the linear response of phonons) be an exponential decay with decay rate γ, and that Eq. (6.57) be satisfied, then the spectral density has to take the Drude-Lorentz form in Eq. (6.78). In modeling photosynthetic systems, typically $\beta\hbar\gamma < 1$, and we approximate $\coth(\beta\hbar\omega/2)$ in Eq. (6.62) as $2k_BT/\hbar\omega$. Under this high-temperature approximation and using Eq. (6.78), Eq. (6.62) becomes

$$\langle u_j(t_2) u_j(t_1)\rangle = \lambda_j e^{-\gamma_j|\tau|}(2k_BT - i\hbar\gamma_j). \tag{6.79}$$

The first and second generalized cumulants are

$$\langle H_I^\times(t_1)\rangle = H_{\rm sys}^\times(t_1) \tag{6.80a}$$

$$\langle H_I^\times(t_2) H_I^\times(t_1)\rangle - \langle H_I^\times(t_2)\rangle\langle H_I^\times(t_1)\rangle = \sum_j \lambda_j e^{-\gamma_j|\tau|} P_j^\times(t_2)(2k_BT P_j^\times(t_1) - i\hbar\gamma_j P_j^o(t_1)), \tag{6.80b}$$

where $P_j \equiv |j\rangle\langle j|$ and $A^o B \equiv \{A, B\}$ is the anticommutator superoperator. The superoperators $H_{\rm sys}^\times$, $P_j^\times$, and P_j^o do not depend on time. However, they are still indexed by time so that they can be properly time-ordered inside the time-ordering operator.

We write the generalized cumulant expansion (Eq. (6.65)) as

$$\rho_{\rm sys}(t) = \mathcal{T}\mathcal{Z}\rho_{\rm sys}(0), \tag{6.81}$$

where

$$\mathcal{Z} = \exp\Big(-\frac{i}{\hbar}\int_0^t dt_1\, H_{\rm sys}(t_1) - \frac{1}{\hbar^2}\sum_j \int_0^t dt_2 \int_0^{t_2} dt_1\, \lambda_j e^{-\gamma_j(t_2-t_1)} P_j^\times(t_2)(2k_BT P_j^\times(t_1) - i\hbar\gamma_j P_j^o(t_1))\Big). \tag{6.82}$$

We now further define

$$\mathcal{Y}_j \equiv \frac{1}{\hbar}\int_0^t dt_1\, e^{-\gamma_j(t-t_1)}(2k_BT P_j^\times(t_1) - i\hbar\gamma_j P_j^o(t_1)), \tag{6.83}$$

as well as the auxiliary density matrices

$$\rho^{\vec{n}}(t) \equiv \mathcal{T}(\prod_j \mathcal{Y}_j^{n_j})\mathcal{Z}\rho_{\rm sys}(0), \tag{6.84}$$

with $\vec{n} = (n_1, \cdots, n_N)$ is a list of N integers where each integer n_j corresponds to a site. The factor $1/\hbar$ in $\mathcal{Y}$ makes $\mathcal{Y}$ dimensionless and ensures that all auxiliary density matrices have the same dimension. Notice that $\rho^{\vec{0}}$ is the physical density matrix, and that at time $t = 0$,

$$\rho^{\vec{n}}(0) = \begin{cases} \rho_{\rm sys}(0) & , \vec{n} = \vec{0} \\ 0 & , \vec{n} \neq \vec{0}. \end{cases} \tag{6.85}$$

We can then obtain the HEOM by taking the time derivative of $\rho^{\vec{n}}(t)$ (Eq. (6.84)) to arrive at

$$\frac{d}{dt}\rho^{\vec{n}}(t) = -\frac{i}{\hbar}H_{\rm sys}^\times \rho^{\vec{n}} - (\sum_j n_j\gamma_j)\rho^{\vec{n}} - \sum_j \frac{\lambda_j}{\hbar} P_j^\times \rho^{\vec{n}+\hat{e}_j} + n_j(\frac{2k_BT}{\hbar}P_j^\times - i\gamma_j P_j^o)\rho^{\vec{n}-\hat{e}_j}, \tag{6.86}$$

where $\hat{e}_j \equiv (0, \cdots, 0, 1, 0, \cdots, 0)$ is the "unit vector" with the j^{th} element equals to 1 and all other elements equal to 0.

Note that we began the derivation in the interaction picture where we rotated out H_{vib}, but because the auxiliary density matrices contain only the system degrees of freedom, the rotation has no effect on the auxiliary density matrices and one can interpret the HEOM (Eq.(6.86)) as being in the Schrodinger picture. Numerically, a cutoff level N_{cutoff} has to be introduced, so that only the auxiliary density matrices with $\sum_j n_j \leq N_{\mathrm{cutoff}}$ are solved. The total number of auxiliary density matrices is $\binom{N+N_{\mathrm{cutoff}}}{N_{\mathrm{cutoff}}}$.

The numerical values of the parameters in the spectral density are taken from [122]. Specifically, λ is the reorganization energy, taken to be 37 cm^{-1} for all sites, and γ, with physical dimension of frequency, is the decay rate of the phonon correlation function, which characterizes the time scale of vibration-induced fluctuations in the electronic excitation energy. For chlorophyll a, we take $\gamma = 30\,\mathrm{cm}^{-1}$; for chlorophyll b, we take $\gamma = 48\,\mathrm{cm}^{-1}$ (see Appendix H). Under high temperatures (characterized by $\hbar\gamma/k_BT \ll 1$, where k_B and T are the Boltzmann constant and temperature, respectively), the interaction picture system density matrix (i.e., with $\sum_j \omega_0 |j\rangle\langle j|$ rotated out) follows the hierarchical equations of motion [48, 49]

$$\frac{d}{dt}\rho^{\vec{n}}(t) = -iH^{\times}\rho^{\vec{n}} - (\sum_j n_j\gamma_j)\rho^{\vec{n}} - \sum_j \lambda_j P_j^{\times}\rho^{\vec{n}+\hat{e}_j} + n_j(2k_BTP_j^{\times} - i\gamma_j P_j^o)\rho^{\vec{n}-\hat{e}_j}, \tag{6.87}$$

where $P_j \equiv |j\rangle\langle j|$, $A^oB \equiv \{A, B\}$ is the anticommutator superoperator, and $A^{\times}B \equiv [A, B]$ is the commutator superoperator. $\vec{n} = (n_1, \cdots, n_N)$ is a vector of N integers, where the element n_j is the hierarchical level of the j^{th} site. $\hat{e}_j \equiv (0, \cdots, 0, 1, 0, \cdots, 0)$ is the "unit vector" with the j^{th} element equals to 1 and all other elements equal to 0. $\rho^{(\vec{0})}$ is the physical density matrix, and the other $\rho^{(\vec{n})}$'s are non-physical auxiliary density matrices that capture the non-Markovian effects of the phonon environment. The initial contition is

$$\rho^{\vec{n}}(0) = \begin{cases} \rho_{\mathrm{sys}}(0) & , \vec{n} = \vec{0} \\ 0 & , \vec{n} \neq \vec{0}. \end{cases} \tag{6.88}$$

Numerically, a cutoff level N_{cutoff} has to be introduced so that only a finite number of auxiliary density matrices with $\sum_j n_j \leq N_{\mathrm{cutoff}}$ are solved. Given the cutoff, the total number of auxiliary density matrices is $\binom{N+N_{\mathrm{cutoff}}}{N_{\mathrm{cutoff}}}$ [123].

HEOM terminator equations

The auxiliary density matrices having $\sum_j n_j = N_{\mathrm{cutoff}}$ are called the terminators. To capture the effect of the auxiliary density matrices $\rho^{\vec{n}+\hat{e}_j}$ that are one level beyond the terminators, we first write their time derivatives as

$$\frac{d}{dt}\rho^{\vec{n}+\hat{e}_j}(t) = -\frac{i}{\hbar}H_{\mathrm{sys}}^{\times}\rho^{\vec{n}+\hat{e}_j} - (\gamma_j + \sum_k n_k\gamma_k)\rho^{\vec{n}+\hat{e}_j} + \sum_k (n_k + \delta_{j,k})(\frac{2k_BT}{\hbar}P_j^{\times} - i\gamma_j P_j^o)\rho^{\vec{n}+\hat{e}_j-\hat{e}_k}, \tag{6.89}$$

where we have dropped the terms involving auxiliary density matrices that are two levels beyond the terminators. If the cutoff level is high enough such that $(\gamma_j + \sum_k n_k\gamma_k)$ is much larger than the scale of H_{sys}, then Hamiltonian term in Eq. (6.89) can be dropped. Then solving Eq. (6.89) formally, we have

$$\rho^{\vec{n}+\hat{e}_j}(t) = \int_0^t d\tau\, e^{-(\gamma_j + \sum_k n_k\gamma_k)(t-\tau)} \sum_k (n_k + \delta_{j,k})(\frac{2k_BT}{\hbar}P_j^{\times} - i\gamma_j P_j^o)\rho^{\vec{n}+\hat{e}_j-\hat{e}_k}(\tau). \tag{6.90}$$

Approximating $e^{-(\gamma_j+\sum_k n_k\gamma_k)|t-\tau|}$ as $2\delta(t-\tau)/(\gamma_j+\sum_k n_k\gamma_k)$, Eq. (6.90) becomes

$$\rho^{\vec{n}+\hat{e}_j}(t)=\sum_k \frac{n_k+\delta_{j,k}}{\gamma_j+\sum_k n_k\gamma_k}\left(\frac{2k_BT}{\hbar}P_j^{\times}-i\gamma_j P_j^o\right)\rho^{\vec{n}+\hat{e}_j-\hat{e}_k}(t). \tag{6.91}$$

Substituting Eq. (6.91) into Eq. (6.87) for the terminators, the time derivatives of the terminators can now be written explicitly as

$$\begin{aligned}\frac{d}{dt}\rho^{\vec{n}}(t)=&-\frac{i}{\hbar}H_{\rm sys}^{\times}\rho^{\vec{n}}-\left(\sum_j n_j\gamma_j\right)\rho^{\vec{n}}+\sum_j n_j\left(\frac{2k_BT}{\hbar}P_j^{\times}-i\gamma_jP_j^o\right)\rho^{\vec{n}-\hat{e}_j}\\&-\sum_{j,k}\frac{\lambda_j}{\hbar}\frac{n_k+\delta_{j,k}}{\gamma_j+\sum_l n_l\gamma_l}P_j^{\times}\left(\frac{2k_BT}{\hbar}P_k^{\times}-i\gamma_kP_k^o\right)\rho^{\vec{n}+\hat{e}_j-\hat{e}_k}.\end{aligned} \tag{6.92}$$

6.3.4 Hierarchical equations of motion for underdamped vibration and its equivalence to Lindblad equation on an extended Hilbert space

In this Section, we derive the non-Markovian HEOM for treating the effects of a specific form of underdamped modes on the reduced electronic system, and we show that the reduced system dynamics can be equivalently obtained by solving a Markovian Lindblad master equation on the larger Hilbert space consisting of the electronic plus vibrational degrees of freedom and then tracing out the vibrational degrees of freedom.

We begin with a microscopic model for the electronic degrees of freedom, a single vibrational mode, and a quantum white noise bath that damps the vibrational mode. The total Hamiltonian is written as

$$H=H_{\rm el}+S\frac{b+b^\dagger}{\sqrt{2}}+\nu b^\dagger b+\int_{-\infty}^{\infty}d\omega\,\omega a^\dagger(\omega)a(\omega)+\sqrt{\frac{\gamma}{2\pi}}\int_{-\infty}^{\infty}d\omega\,a^\dagger(\omega)b+a(\omega)b^\dagger. \tag{6.93}$$

$H_{\rm el}$ is the electronic Hamiltonian; S is an arbitrary electronic system operator that couples to the single vibrational mode b with frequency ν; the mode b is then coupled to a white noise bath $a(\omega)$ with coupling constant γ. The initial state is assumed to be a product state of an arbitrary system state, a thermal state with average phonon number of $\bar{n}$ in the b vibrational mode, and a quasi-thermal state in the white noise bath, where every $a(\omega)$ mode is in a thermal state with the same occupation number $\bar{n}$. Note that a true thermal state of the white noise bath at some fixed temperature will have the occupation number of each mode dependent on the mode frequency ω.

First, we treat the electronic degrees of freedom and the single vibrational mode as the reduced system. Rotating out the free bath evolution (i.e., $\int_{-\infty}^{\infty}d\omega\,\omega a^\dagger(\omega)a(\omega)$), the total Hamiltonian becomes

$$H(t)=H_{\rm el+vib}+\sqrt{\gamma}(a^\dagger(t)b+a(t)b^\dagger), \tag{6.94}$$

where $H_{\rm el+vib}=H_{\rm el}+S(b+b^\dagger)/\sqrt{2}+\nu b^\dagger b$ and

$$a(t)=\frac{1}{\sqrt{2\pi}}\int_{-\infty}^{\infty}d\omega\,a(\omega)e^{-i\omega t}, \tag{6.95}$$

similar to Eq. (6.7). The reduced system density matrix is formally expressed as a time-ordered exponential

$$\rho_{\rm el+vib}(t)=\left\langle\mathcal{T}\exp\Big(\int_0^t d\tau\;-iH_{\rm el+vib}^{\times}-i\sqrt{\gamma}(a^\dagger(\tau)b+a(t)b^\dagger)^{\times}\Big)\right\rangle\rho_{\rm el+vib}(0), \tag{6.96}$$

where the bracket $\langle \cdots \rangle$ means averaging over the initial state of the white noise bath. Since the quasi-thermal white noise bath satisfies the Gaussian property [120] of Eq. (6.61), where u_j are replaced by either $a(\tau)$ or $a^\dagger(\tau)$, we can write the generalized cumulant expansion of Eq. (6.96) as

$$\begin{aligned}\rho_{\text{el+vib}}(t) = \mathcal{T}\exp\Bigg(\int_0^t d\tau\ -iH^\times_{\text{el+vib}}(\tau) - \frac{\gamma}{2}\int_0^t d\tau_2\int_0^t d\tau_1 \\ \langle a^\dagger(\tau_2)a^\dagger(\tau_1)\rangle(b(\tau_2)b(\tau_1)\bullet - b(\tau_1)\bullet b(\tau_2)) + \langle a^\dagger(\tau_1)a^\dagger(\tau_2)\rangle(\bullet b(\tau_1)b(\tau_2) - b(\tau_2)\bullet b(\tau_1)) \\ + \langle a(\tau_2)a(\tau_1)\rangle(b^\dagger(\tau_2)b^\dagger(\tau_1)\bullet - b^\dagger(\tau_1)\bullet b^\dagger(\tau_2)) + \langle a(\tau_1)a(\tau_2)\rangle(\bullet b^\dagger(\tau_1)b^\dagger(\tau_2) - b^\dagger(\tau_2)\bullet b^\dagger(\tau_1)) \\ + \langle a(\tau_2)a^\dagger(\tau_1)\rangle(b^\dagger(\tau_2)b(\tau_1)\bullet - b(\tau_1)\bullet b^\dagger(\tau_2)) + \langle a^\dagger(\tau_1)a(\tau_2)\rangle(\bullet b(\tau_1)b^\dagger(\tau_2) - b^\dagger(\tau_2)\bullet b(\tau_1)) \\ + \langle a^\dagger(\tau_2)a(\tau_1)\rangle(b(\tau_2)b^\dagger(\tau_1)\bullet - b^\dagger(\tau_1)\bullet b(\tau_2)) + \langle a(\tau_1)a^\dagger(\tau_2)\rangle(\bullet b^\dagger(\tau_1)b(\tau_2) - b(\tau_2)\bullet b^\dagger(\tau_1))\Bigg) \\ \times \rho_{\text{el+vib}}(0).\end{aligned} \tag{6.97}$$

Note that $H_{\text{el+vib}}$ is time-independent, but we have added a time index here so that it can be properly time-ordered inside the time-ordering operator. The delta function correlations

$$\begin{aligned}\langle a^\dagger(\tau_2)a^\dagger(\tau_1)\rangle &= \langle a(\tau_2)a(\tau_1)\rangle = 0 \\ \langle a^\dagger(\tau_2)a(\tau_1)\rangle &= \bar{n}\delta(\tau_2-\tau_1) \\ \langle a(\tau_2)a^\dagger(\tau_1)\rangle &= (\bar{n}+1)\delta(\tau_2-\tau_1)\end{aligned} \tag{6.98}$$

allow us to reduce the double integral inside the time-ordered exponential of Eq. (6.97) to a single integral. Therefore Eq. (6.97) becomes

$$\begin{aligned}\rho_{\text{el+vib}}(t) = \mathcal{T}\exp\Bigg(\int_0^t d\tau\ -iH^\times_{\text{el+vib}}(\tau) + \gamma(\bar{n}+1)\Big(b(\tau)\bullet b^\dagger(\tau) - \frac{1}{2}b^\dagger(\tau)b(\tau)\bullet) - \frac{1}{2}\bullet b^\dagger(\tau)b(\tau)\Big) \\ + \gamma\bar{n}\Big(b^\dagger(\tau)\bullet b(\tau) - \frac{1}{2}b(\tau)b^\dagger(\tau)\bullet - \frac{1}{2}\bullet b(\tau)b^\dagger(\tau)\Big)\Bigg)\rho_{\text{el+vib}}(0),\end{aligned} \tag{6.99}$$

which is the solution to the Lindblad equation on the electronic plus vibrational degrees of freedom

$$\begin{aligned}\frac{d}{dt}\rho_{\text{el+vib}} = -i[H_{\text{el+vib}},\rho_{\text{el+vib}}] + \gamma(\bar{n}+1)\Big(b\rho_{\text{el+vib}}b^\dagger - \frac{1}{2}b^\dagger b\rho_{\text{el+vib}} - \frac{1}{2}\rho_{\text{el+vib}}b^\dagger b\Big) \\ + \gamma\bar{n}\Big(b^\dagger\rho_{\text{el+vib}}b - \frac{1}{2}bb^\dagger\rho_{\text{el+vib}} - \frac{1}{2}\rho_{\text{el+vib}}bb^\dagger\Big).\end{aligned} \tag{6.100}$$

On the other hand, we can also use the HEOM formalism to treat only the electronic degrees of freedom as the reduced system. Working now in the interaction frame where we rotate out

$$H_0 = \nu b^\dagger b + \int_{-\infty}^{\infty} d\omega\,\omega a^\dagger(\omega)a(\omega) + \sqrt{\frac{\gamma}{2\pi}}\int_{-\infty}^{\infty} d\omega\, a^\dagger(\omega)b + a(\omega)b^\dagger \tag{6.101}$$

from Eq. (6.93), the electronic system density matrix has the formal solution of

$$\rho_{\text{el}}(t) = \Big\langle \mathcal{T}\exp\Big(\int_0^t d\tau\ -iH^\times_{\text{el}}(\tau) - i(S(\tau)q(\tau))^\times\Big)\Big\rangle\rho_{\text{el}}(0), \tag{6.102}$$

where $q(\tau) = (b(\tau)+b^\dagger(\tau))/\sqrt{2}$ and the bracket $\langle\cdots\rangle$ means to average over the initial states of both the vibration mode b and the white noise bath $a(\omega)$. Next, we want to show that $q(\tau)$ is Gaussian, so that the cumulant expansion of Eq. (6.102) only contains up to the second cumulants.

Defining $U_0(t) \equiv \exp(-iH_0 t)$, $b(t) \equiv U_0^\dagger(t) b U_0(t)$ follows the Heisenberg equation of motion

$$\frac{d}{dt}b(t) = -iU_0^\dagger(t)[b, H_0]U_0(t) = -i\nu b(t) - i\sqrt{\frac{\gamma}{2\pi}}\int_{-\infty}^{\infty} d\omega\, a(\omega, t), \tag{6.103}$$

where $a(\omega, t) = U_0^\dagger(t) a(\omega) U_0(t)$. $a(\omega, t)$ follows another Heisenberg equation of motion

$$\frac{d}{dt}a(\omega, t) = -i\omega a(\omega, t) - i\sqrt{\frac{\gamma}{2\pi}}b(t), \tag{6.104}$$

which has the solution

$$a(\omega, t) = e^{-i\omega t}a(\omega) - i\sqrt{\frac{\gamma}{2\pi}}\int_0^t d\tau\, e^{-i\omega(t-\tau)}b(\tau). \tag{6.105}$$

Substituting Eq. (6.105) into Eq. (6.103), we have

$$\frac{d}{dt}b(t) = -i\nu b(t) - i\sqrt{\gamma}a(t) - \frac{\gamma}{2}b(t), \tag{6.106}$$

which has the solution

$$b(t) = e^{(-i\nu-\gamma/2)t}b - i\sqrt{\gamma}\int_0^t d\tau\, e^{(-i\nu-\gamma/2)(t-\tau)}a(\tau). \tag{6.107}$$

Notice that $b(t)$ is a sum of operators that satisfy the Gaussian property when averaged over the initial thermal state. Therefore $b(t)$ and $q(t)$ also satisfy the Gaussian property. The mean, or the first cumulant, of $q(t)$ is $\langle q(t)\rangle = 0$. The two-point correlation function, or the second cumulant, is

$$\begin{aligned}
\langle q(t_2)q(t_1)\rangle &= \frac{1}{2}\big(\langle b^\dagger(t_2)b(t_1)\rangle + \langle b(t_2)b^\dagger(t_1)\rangle\big) \\
&= \frac{1}{2}\Big(e^{i\nu(t_2-t_1)}e^{-\gamma/2(t_2+t_1)}\big(\langle b^\dagger b\rangle + \gamma\int_0^{t_2}d\tau_2\int_0^{t_1}d\tau_1\, e^{-i\nu(\tau_2-\tau_1)}e^{\gamma/2(\tau_2+\tau_1)}\langle a^\dagger(\tau_2)a(\tau_1)\rangle\big) \\
&\qquad e^{-i\nu(t_2-t_1)}e^{-\gamma/2(t_2+t_1)}\big(\langle bb^\dagger\rangle + \gamma\int_0^{t_2}d\tau_2\int_0^{t_1}d\tau_1\, e^{i\nu(\tau_2-\tau_1)}e^{\gamma/2(\tau_2+\tau_1)}\langle a(\tau_2)a^\dagger(\tau_1)\rangle\big)\Big) \\
&= \frac{\bar{n}}{2}e^{i\nu(t_2-t_1)}e^{-\gamma/2|t_2-t_1|} + \frac{\bar{n}+1}{2}e^{-i\nu(t_2-t_1)}e^{-\gamma/2|t_2-t_1|}.
\end{aligned} \tag{6.108}$$

Using this correlation function and the Gaussian property, we can now write the cumulant expansion of Eq. (6.102) as

$$\begin{aligned}
\rho_{\rm el}(t) = \mathcal{T}\exp\Bigg(&\int_0^t d\tau\ -iH_{\rm el}^\times(\tau) \\
&-\int_0^t d\tau_2 S^\times(\tau_2)\int_0^{\tau_2}d\tau_1\, e^{(i\nu-\gamma/2)(\tau_2-\tau_1)}\Big(\frac{\bar{n}}{2}S(\tau_1)\bullet - \frac{\bar{n}+1}{2}\bullet S(\tau_1)\Big) \\
&\qquad + e^{(-i\nu-\gamma/2)(\tau_2-\tau_1)}\Big(\frac{\bar{n}+1}{2}S(\tau_1)\bullet - \frac{\bar{n}}{2}\bullet S(\tau_1)\Big)\Bigg)\rho_{\rm el}(0) \\
\equiv\ &\mathcal{T}\mathcal{Z}\rho_{\rm el}(0),
\end{aligned} \tag{6.109}$$

where we defined $\mathcal{Z}$ as the superoperator exponential in the equation. Now we further define the superoperators

$$\mathcal{A} = \int_0^t d\tau e^{(i\nu-\gamma/2)(t-\tau)}\Big(\frac{\bar{n}}{2}S(\tau)\bullet - \frac{\bar{n}+1}{2}\bullet S(\tau)\Big) \tag{6.110}$$

and

$$\mathcal{B} = \int_0^t d\tau e^{(-i\nu-\gamma/2)(t-\tau)}\Big(\frac{\bar{n}+1}{2}S(\tau)\bullet - \frac{\bar{n}}{2}\bullet S(\tau)\Big), \tag{6.111}$$

so the repeated time derivatives of Eq. (6.109) consist of terms of the form $\rho_{\rm el}^{\vec{m}} = \rho_{\rm el}^{m_A,m_B} \equiv \mathcal{T}\mathcal{A}^{m_A}\mathcal{B}^{m_B}\mathcal{Z}\rho_{\rm el}(0)$. Taking the time derivative of $\rho_{\rm el}^{\vec{m}}$

$$\begin{aligned}\frac{d}{dt}\rho_{\rm el}^{\vec{m}} =& -i[H_{\rm el},\rho_{\rm el}^{\vec{m}}] + m_A(i\nu-\frac{\gamma}{2})\rho_{\rm el}^{\vec{m}} + m_B(-i\nu-\frac{\gamma}{2})\rho_{\rm el}^{\vec{m}}\\ &+ m_A(\frac{\bar{n}}{2}S\rho_{\rm el}^{\vec{m}-\hat{e}_A} - \frac{\bar{n}+1}{2}\rho_{\rm el}^{\vec{m}-\hat{e}_A}S)\\ &+ m_B(\frac{\bar{n}+1}{2}S\rho_{\rm el}^{\vec{m}-\hat{e}_B} - \frac{\bar{n}}{2}\rho_{\rm el}^{\vec{m}-\hat{e}_B}S)\\ &- [S,\rho_{\rm el}^{\vec{m}+\hat{e}_A}+\rho_{\rm el}^{\vec{m}+\hat{e}_B}],\end{aligned} \tag{6.112}$$

we obtain the HEOM for the electronic degrees of freedom coupled to a single underdamped vibrational mode with the Hamiltonian of Eq. (6.93). $\hat{e}_A$ and $\hat{e}_B$ are the unit vectors in the A and B indices of $\vec{m} = (m_A, m_B)$. $\rho^{\vec{0}}$ is the physical density matrix, and the initial condition is $\rho^{\vec{m}}(0) = \delta_{\vec{0},\vec{m}}\rho_{\rm el}(0)$.

The main result in this section is that solving the Markovian Lindblad master equation (Eq. (6.100)) on the electronic degrees of freedom plus the single vibrational degree of freedom and then tracing out the vibrational degree of freedom is equivalent to solving the non-Markovian HEOM of Eq. (6.112) on the electronic degrees of freedom alone. This is because both equations are derived exactly from the same Hamiltonian (Eq. (6.93)) and the same initial condition.

This result can be generalized straightforwardly to an electronic system coupling to N independent underdamped vibrational modes. To do so in the Lindblad description, we enlarge the Hilbert space to include all N underdamped modes and then add a pair of Lindblad dissipators for each underdamped mode, so that the Lindblad equation becomes

$$\begin{aligned}\frac{d}{dt}\rho_{\rm el+vib} =& -i[H_{\rm el+vib},\rho_{\rm el+vib}]\\ &+\sum_{\alpha=1}^{N}\Big(\gamma_\alpha(\bar{n}_\alpha+1)\Big(b_\alpha\rho_{\rm el+vib}b_\alpha^\dagger - \frac{1}{2}b_\alpha^\dagger b_\alpha\rho_{\rm el+vib} - \frac{1}{2}\rho_{\rm el+vib}b_\alpha^\dagger b_\alpha\Big)\\ &\quad+\gamma_\alpha\bar{n}_\alpha\Big(b_\alpha^\dagger\rho_{\rm el+vib}b_\alpha - \frac{1}{2}b_\alpha b_\alpha^\dagger\rho_{\rm el+vib} - \frac{1}{2}\rho_{\rm el+vib}b_\alpha b_\alpha^\dagger\Big)\Big),\end{aligned} \tag{6.113}$$

where α indexes the N underdamped modes. In the HEOM description, we add a pair of HEOM indices (m_A, m_B) to Eq. (6.112) for each underdamped mode, so that $\vec{m} = (m_A^1, m_B^1, \cdots, m_A^N, m_B^N)$. Eq. (6.112) then becomes

$$\begin{aligned}\frac{d}{dt}\rho_{\rm el}^{\vec{m}} =& -i[H_{\rm el},\rho_{\rm el}^{\vec{m}}]\\ &+\sum_{\alpha=1}^{N}\Big(m_A^\alpha(i\nu_\alpha-\frac{\gamma_\alpha}{2})\rho_{\rm el}^{\vec{m}} + m_B^\alpha(-i\nu_\alpha-\frac{\gamma_\alpha}{2})\rho_{\rm el}^{\vec{m}}\\ &\quad+ m_A^\alpha(\frac{\bar{n}_\alpha}{2}S_\alpha\rho_{\rm el}^{\vec{m}-\hat{e}_A^\alpha} - \frac{\bar{n}_\alpha+1}{2}\rho_{\rm el}^{\vec{m}-\hat{e}_A^\alpha}S_\alpha)\\ &\quad+ m_B^\alpha(\frac{\bar{n}_\alpha+1}{2}S_\alpha\rho_{\rm el}^{\vec{m}-\hat{e}_B^\alpha} - \frac{\bar{n}_\alpha}{2}\rho_{\rm el}^{\vec{m}-\hat{e}_B^\alpha}S_\alpha)\\ &\quad- [S_\alpha,\rho_{\rm el}^{\vec{m}+\hat{e}_A^\alpha}+\rho_{\rm el}^{\vec{m}+\hat{e}_B^\alpha}]\Big).\end{aligned} \tag{6.114}$$

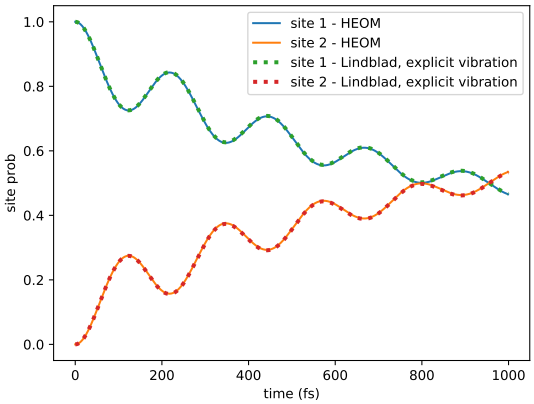

Figure 6.2: Comparison between solving the Lindblad Eq. (6.113) on the electronic plus vibrational Hilbert space then tracing out vibrations and solving the HEOM Eq. (6.114) on the electronic states alone, for a dimer system coupled to two underdamped modes. The parameter values are $(\nu_1, \nu_2, \kappa_1, \kappa_2, \gamma_1, \gamma_2) = (200, 200, 50, 50, 100, 100)\,\mathrm{cm}^{-1}$. The temperature of the initial vibrational state is 300 K. The electronic initial state is $|1\rangle$. In solving the Lindblad equation, both harmonic oscillators are truncated to the 8 lowest eigenstates. In solving the HEOM, we propagate only the auxiliary density matrices $\rho^{\vec{m}}$ satisfying $\mathrm{sum}(\vec{m}) = m_A^1 + m_B^1 + m_A^2 + m_B^2 \leq 5$.

Due to the fact that in the Lindblad description, the dimension of Hilbert space scales exponentially with the number of underdamped modes, HEOM can be more computationally efficient in simulating the reduced electronic system dynamics.

Fig. (6.2) illustrates the equivalence of solving Eq. (6.113) then tracing out vibrations and solving Eq. (6.114), for a dimer system coupled to two underdamped modes. The following vibronic Hamiltonian is considered

$$H_{\mathrm{el+vib}} = H_{\mathrm{dimer}} + \nu_1 b_1^\dagger b_1 + \nu_2 b_2^\dagger b_2 + \kappa_1 |1\rangle\langle 1| \frac{b_1 + b_1^\dagger}{\sqrt{2}} + + \kappa_2 |2\rangle\langle 2| \frac{b_2 + b_2^\dagger}{\sqrt{2}}, \tag{6.115}$$

where H_{dimer} is given in Appendix H. $|1\rangle$ and $|2\rangle$ represent states with excitations on site 1 or 2.

6.4 Interaction with both photons and phonons

6.4.1 System plus field plus vibration pure state

Generalizing the analysis presented in Section 6.2.6, one can write down a system+field+vibration pure state as a function of time, given the system+vibration state initialized in the pure product state $|g\rangle \otimes |v\rangle$, where $|v\rangle$ is an arbitrary vibration state. In Section 7.2, we shall take $|v\rangle$ to be the eigenstate of H_{vib}, the vibrational Hamiltonian in the electronic ground state with energy E_v, so that $H_{\mathrm{vib}}|v\rangle = E_v|v\rangle$. The overall pure state $|\psi(t)\rangle$ is written as

$$|\psi(t)\rangle = |\gamma(t)\rangle|\mathrm{vac}\rangle + |g\rangle \sum_l \int_{-\infty}^{\infty} dt_r \, |\chi_l(t, t_r)\rangle a_l^\dagger(t_r)|\mathrm{vac}\rangle, \tag{6.116}$$

with

$$|\gamma(t)\rangle = -\int_0^t d\tau\, \xi(\tau) e^{(-iH_{\text{sys+vib}} - \frac{1}{2}\sum_l L_l^\dagger L_l)(t-\tau)} L_{\text{inc}}^\dagger |g\rangle e^{-iH_{\text{vib}}\tau}|v\rangle \tag{6.117a}$$

$$\chi_l(t,t_r) = \begin{cases} \delta_{l,\text{inc}}\xi(t_r)e^{-iH_{\text{vib}}t}|v\rangle & ,t<t_r \\ \delta_{l,\text{inc}}\xi(t_r)e^{-iH_{\text{vib}}t}|v\rangle + \frac{1}{2}e^{-iH_{\text{vib}}(t-t_r)}\langle g|L_l|\gamma(t_r)\rangle & ,t=t_r \\ \delta_{l,\text{inc}}\xi(t_r)e^{-iH_{\text{vib}}t}|v\rangle + e^{-iH_{\text{vib}}(t-t_r)}\langle g|L_l|\gamma(t_r)\rangle & ,t>t_r. \end{cases} \tag{6.117b}$$

Here $|\gamma(t)\rangle$ is an unnormalized system+vibration state with the system being in the excited subspace, and $\chi_l(t,t_r)$ is an unnormalized vibration state at time t. One can check that

$$\begin{aligned} \rho_{1,1}(t) &= |\gamma(t)\rangle\langle\gamma(t)| + |g\rangle\langle g| \sum_l \int_{-\infty}^{\infty} dt_r\, |\chi_l(t,t_r)\rangle\langle\chi_l(t,t_r)| \\ \rho_{1,0}(t) &= |\gamma(t)\rangle\langle g|\langle v|e^{iH_{\text{vib}}t} \\ \rho_{0,0}(t) &= e^{-iH_{\text{vib}}t}|v\rangle|g\rangle\langle g|\langle v|e^{iH_{\text{vib}}t} \end{aligned} \tag{6.118}$$

solves the single photon Fock state master equation (Eq. (6.37)) with vibration. For later convenience, we drop the spontaneous emission terms and define

$$|\gamma'_{\xi,v}(t)\rangle \equiv -\int_0^t d\tau\, \xi(\tau) e^{-iH_{\text{sys+vib}}(t-\tau)} L_{\text{inc}}^\dagger |g\rangle e^{-iH_{\text{vib}}\tau}|v\rangle \tag{6.119}$$

to emphasize the dependence on the temporal profile $\xi(t)$ and the initial vibrational state $|v\rangle$.

6.4.2 Combining the input-output and HEOM formalisms

To simultaneously study the effects of the single photon and the phonon bath on the excitonic system, we now combine the input-output and HEOM formalisms. Two different formalisms are needed to treat the effects of these two bosonic baths because of their different properties. The input-output formalism is based on the frequency-independent coupling and the wide-band approximation (see Section 6.2.2), which has been used extensively in quantum optics to treat the interaction of matter with the photon field. The coupling to phonons, on the other hand, is frequency-dependent, and therefore cannot be treated with the assumptions of the input-output formalism. The input-output formalism allows us to explicitly calculate properties of the outgoing photon field (see Section 6.2.7), while the HEOM formalism traces out the bath degrees of freedom. The HEOM formalism is well-suited to treat the coupling to phonons, since the phonon correlation function is Gaussian, while the correlation function (e.g. $\langle a^\dagger(t_2)a^\dagger(t_1)\rangle$, $\langle a^\dagger(t_2)a(t_1)\rangle$, etc.) of an N-photon Fock state is not Gaussian. As an aside, we note that in contrast to a Fock state, for a multimode coherent state the correlation function is Gaussian, and for a coherent state input one can in fact treat the interaction with photons using the HEOM formalism. In addition, because the second cumulant $\langle a(t_2)a^\dagger(t_1)\rangle - \langle a(t_2)\rangle\langle a^\dagger(t_1)\rangle$ is proportional to a delta function for a coherent state, the resulting reduced system dynamics is Markovian and does not involve auxiliary density matrices (see Section 7.1.1) [59, 65].

To combine the input-output and HEOM formalisms, we use Eqs. (6.6), (6.8), and (6.59) to write the full Hamiltonian as

$$H_{\text{total}} = H_{\text{field}} + H_{\text{vib}} + \sum_j \omega_0 |j\rangle\langle j| + \underbrace{(H_{\text{sys}} - \sum_j \omega_0 |j\rangle\langle j|)}_{H} + H_{\text{sys-field}} + H_{\text{sys-vib}}. \tag{6.120}$$

Here the term inside the parenthesis is the Hamiltonian appearing in the Fock state master equation, and will be denoted simply as H. Moving into the interaction picture where we now rotate out

$H_{\rm field} + H_{\rm vib} + \sum_j \omega_0 |j\rangle\langle j|$, the full Hamiltonian becomes

$$H_{\rm total}(t) = H + \sum_j |j\rangle\langle j| u_j(t) + \sum_l (-i a_l(t) L_l^\dagger + \text{h.c.}). \tag{6.121}$$

This is to be compared with the interaction picture Hamiltonian for the system+field state alone, Eq. (6.8). Given a multimode Fock state photon in one spatial mode as the input field, the reduced dynamics in the system+vibration degrees of freedom is then given by the Fock state master equation Eq. (6.37), with H replaced by $H + \sum_j |j\rangle\langle j| u_j(t)$. To apply the HEOM formalism to this, we rewrite the Fock state master equation in the block matrix form

$$\frac{d}{dt}\begin{pmatrix} \rho_{N,N} \\ \vdots \\ \rho_{m,n} \\ \vdots \\ \rho_{0,0} \end{pmatrix} =$$
$$\begin{pmatrix} -i\sum_j (P_j u_j(t))^\times \rho_{N,N} + \big(-iH^\times + \sum_l \mathcal{D}[L_l]\big)\rho_{N,N} - \sqrt{N}\xi(t) L_{\rm inc}^{\dagger\times}\rho_{N-1,N} + \sqrt{N}\xi^*(t) L_{\rm inc}^\times \rho_{N,N-1} \\ \vdots \\ -i\sum_j (P_j u_j(t))^\times \rho_{m,n} + \big(-iH^\times + \sum_l \mathcal{D}[L_l]\big)\rho_{m,n} - \sqrt{m}\xi(t) L_{\rm inc}^{\dagger\times}\rho_{m-1,n} + \sqrt{n}\xi^*(t) L_{\rm inc}^\times \rho_{m,n-1} \\ \vdots \\ -i\sum_j (P_j u_j(t))^\times \rho_{0,0} + \big(-iH^\times + \sum_l \mathcal{D}[L_l]\big)\rho_{0,0} \end{pmatrix}. \tag{6.122}$$

Eq. (6.122) can be written in a more compact notation as

$$\frac{d}{dt}\Xi(t) = (\mathcal{V}(t) + \mathcal{W}(t))\Xi(t), \tag{6.123}$$

where

$$\Xi(t) = \begin{pmatrix} \rho_{N,N} \\ \vdots \\ \rho_{0,0} \end{pmatrix}, \tag{6.124}$$

and $\mathcal{V}(t)$ and $\mathcal{W}(t)$ are linear operators on Ξ. $\mathcal{V}(t)$ is the operator that acts nontrivially on the vibrational degrees of freedom. Its effect on Ξ is given by

$$\mathcal{V}(t)\Xi = \begin{pmatrix} -i\sum_j (P_j u_j(t))^\times \rho_{N,N} \\ \vdots \\ -i\sum_j (P_j u_j(t))^\times \rho_{0,0} \end{pmatrix}. \tag{6.125}$$

The effect of $\mathcal{W}(t)$ on Ξ is to produce the rest of the terms in Eq. (6.122). We note that $\mathcal{W}(t)$ acts trivially on the vibrational degrees of freedom. Now, from Eq. (6.123), we can write the vector $\chi(t)$ of reduced Fock state auxiliary density matrices on the system, i.e.,

$$\chi(t) = \text{Tr}_{\rm vib}(\Xi(t)) = \begin{pmatrix} \text{Tr}_{\rm vib}(\rho_{N,N}) \\ \vdots \\ \text{Tr}_{\rm vib}(\rho_{0,0}) \end{pmatrix} \tag{6.126}$$

formally as a time-ordered exponential

$$\chi(t) = \text{Tr}_{\rm vib}\Big(\mathcal{T}\exp\big(\int_0^t d\tau\, (\mathcal{V}(\tau) + \mathcal{W}(\tau))\rho_{\rm vib,thermal}\Big)\chi(0), \tag{6.127}$$

where we have used the fact $\Xi(0) = \chi(0) \otimes \rho_{\text{vib,thermal}}$ to pull out $\chi(0)$ from the partial trace.

Following Sec. 6.3.2, first we need to show that Eq. (6.127) factorizes as

$$\chi(t) = \mathcal{T}\Big\langle \mathcal{T} \exp \int_0^t d\tau \mathcal{W}(\tau) \Big\rangle \prod_{j=1}^{N} \Big\langle \mathcal{T} \exp \int_0^t d\tau \mathcal{V}_j(\tau) \Big\rangle \chi(0), \tag{6.128}$$

where $\sum_j \mathcal{V}_j = \mathcal{V}$ and $\mathcal{V}_j$'s action on χ is given by

$$\mathcal{V}_j(t)\chi = \begin{pmatrix} -i\big\langle (P_j u_j(t))^{\times} \big\rangle \rho_{N,N} \\ \vdots \\ -i\big\langle (P_j u_j(t))^{\times} \big\rangle \rho_{1,1} \end{pmatrix}. \tag{6.129}$$

The brackets $\langle \cdots \rangle$ represent averaging with the phonon thermal state. To prove Eq. (6.128), it suffices to show that any mixed generalized moment, written as a time-ordered product of $\mathcal{V}$ and $\mathcal{W}$ at different time points, can be factored into a time-ordered product of a generalized moment with $\mathcal{V}$ only and a generalized moment with $\mathcal{W}$ only. Using similar notations as in Eq. (6.70), a general mixed moment

$$\Big\langle \mathcal{T}\, \mathcal{W}(t_{w,1})\mathcal{W}(t_{w,2}) \cdots \prod_{j=1}^{N} \mathcal{V}_j(t_{j,1})\mathcal{V}_j(t_{j,2}) \cdots \Big\rangle \tag{6.130}$$

can be expanded as

$$\mathcal{T}\, \mathcal{W}(t_{w,1})\mathcal{W}(t_{w,2}) \cdots \prod_{j=1}^{N} \Big(\sum_{\alpha_{j,1}} \sum_{\alpha_{j,2}} \cdots (-i) P_j^{\alpha_{j,1}}(t_{j,1}) (-i) P_j^{\alpha_{j,2}}(t_{j,2}) \cdots \Big\langle \mathcal{O}_{\{\alpha,t\}} u_j(t_{j,1}) u_j(t_{j,2}) \cdots \Big\rangle \Big), \tag{6.131}$$

where the meaning of P_j^l (P_j^r) is augmented from that in Sec. 6.3.2 to mean left- (right-) multiplying each Fock state auxiliary density matrix $\rho_{m,n}$ by P_j. Eq. (6.131) can be simplified as

$$\mathcal{T}\Big\langle \mathcal{T}\mathcal{W}(t_{w,1})\mathcal{W}(t_{w,2}) \cdots \Big\rangle \prod_{j=1}^{N} \Big\langle \mathcal{T}\mathcal{V}_j(t_{j,1})\mathcal{V}_j(t_{j,2}) \cdots \Big\rangle. \tag{6.132}$$

Thus Eq. (6.128) is proved.

Following the steps in Sec. 6.3.2, one can show that

$$\Big\langle \mathcal{T} \exp \int_0^t d\tau\, \mathcal{W}(\tau) \Big\rangle = \mathcal{T} \exp \int_0^t d\tau\, \mathcal{W}(\tau) \tag{6.133}$$

and

$$\begin{aligned} &\Big\langle \mathcal{T} \exp \int_0^t d\tau\, \mathcal{V}_j(\tau) \Big\rangle = \\ &\mathcal{T} \exp \Big(\int_0^t dt_2 \int_0^{t_2} P_j^{\times}(t_2) P_j^{\times}(t_1) \Re \langle u_j(t_2) u_j(t_1) \rangle + P_j^{\times}(t_2) P_j^{o}(t_1) \Im \langle u_j(t_2) u_j(t_1) \rangle \Big), \end{aligned} \tag{6.134}$$

where $P_j^{\times}$ and P_j^o are augmented to act on every Fock state auxiliary density matrices.

Overdamped vibration

In the overdamped case, we write $\chi(t)$ as

$$\chi(t) = \mathcal{T}\mathcal{Z}\chi(0), \tag{6.135}$$

where $\mathcal{Z}$ is defined as

$$\mathcal{Z} = \exp(\int_0^t dt_1\, \mathcal{W}(t_1) - \sum_j \int_0^t dt_2 \int_0^{t_2} dt_1\, \lambda_j e^{-\gamma_j(t_2-t_1)} P_j^\times(t_2)(2k_BTP_j^\times(t_1) - i\gamma_j P_j^o(t_1))). \quad (6.136)$$

The integrand of the double integral is now understood as an operator that applies to every block matrix $\mathrm{Tr}_{\mathrm{vib}}(\rho_{m,n})$ of χ. Following a similar procedure as employed for the derivation of HEOM in Sec. 6.3.2, we then obtain the Fock state + HEOM master equation

$$\frac{d}{dt}\chi^{\vec{n}}(t) = \mathcal{W}(t)\chi^{\vec{n}} - (\sum_j n_j\gamma_j)\chi^{\vec{n}} - \sum_j \lambda_j P_j^\times \chi^{\vec{n}+\hat{e}_j} + n_j(2k_BTP_j^\times - i\gamma_j P_j^o)\chi^{\vec{n}-\hat{e}_j}. \quad (6.137)$$

Written in terms of individual auxiliary density matrices, this is equivalent to

$$\begin{aligned}\frac{d}{dt}\rho_{m,n}^{\vec{n}} =& (-iH^\times + \sum_l \mathcal{D}[L_l])\rho_{m,n}^{\vec{n}} - \sqrt{m}\xi(t)L_{\mathrm{inc}}^{\dagger\times}\rho_{m-1,n}^{\vec{n}} + \sqrt{n}\xi^*(t)L_{\mathrm{inc}}^\times\rho_{m,n-1}^{\vec{n}} \\ & - (\sum_j n_j\gamma_j)\rho_{m,n}^{\vec{n}} - \sum_j \lambda_j P_j^\times \rho_{m,n}^{\vec{n}+\hat{e}_j} + n_j(2k_BTP_j^\times - i\gamma_j P_j^o)\rho_{m,n}^{\vec{n}-\hat{e}_j},\end{aligned} \quad (6.138)$$

with the initial condition

$$\rho_{m,n}^{\vec{n}}(0) = \begin{cases}\rho_{\mathrm{sys}}(0) & , \vec{n} = \vec{0} \text{ and } m = n \\ 0 & , \text{otherwise.}\end{cases} \quad (6.139)$$

Note that $\rho_{N,N}^{\vec{0}}$ is the only physical density matrix.

The set of equations in Eq. (6.138) consist of a double hierarchical structure. The supercripted index $\vec{n}$ indexes the HEOM auxiliary density matrices, and the subscripted index (m,n) indexes the Fock state master equation auxiliary density matrices. The total number of auxiliary density matrices is $\binom{N+N_{\mathrm{cutoff}}}{N_{\mathrm{cutoff}}}(N_{\mathrm{photon}}+1)^2$. Note that in general $\rho_{m,n}^{\vec{n}} \neq \rho_{n,m}^{\vec{n}\dagger}$, while the equality holds without HEOM. Since the photon flux operators act trivially on the vibrational degrees of freedom, the expressions for photon fluxes are the same as Eq. (6.50), with the replacement of $\rho_{m,n}$ by $\rho_{m,n}^{\vec{0}}$.

We note that Eq. (6.138) is exact, given the Hamiltonian of Eq. (6.120) and the spectral density of Eq. (6.78), which describes coupling to overdamped vibrational modes. The Hamiltonian does not include any direct interaction between photons and phonons, consistent with the very different energy scales between photons and phonons. It also does not include non-Condon effects such as the Herzberg-Teller effect (i.e., photons exciting both excitons and phonons simultaneously) [124], signs of which have recently been speculated to exist in LHCII [125].

The double hierarchical structure of Eq. (6.138) makes the computation quite expensive, so we first turn to analytical studies to understand some of its features and consequences in Sections 7.1, 7.2, and 7.3. Following this, in Section 7.4, we present a numerical simulation using the double hierarchical structure for single photon Fock state absorption and excitonic energy transfer in the LHCII monomer (14-mer) system.

underdamped vibration

To describe excitonic interactions with phonon spectral densities or phonon correlation functions other than those arising from the Drude-Lorentz spectral density (Eq. (6.78)), one can simply replace the HEOM part of the double hierarchy in Eq. (6.138) with the corresponding HEOM for the new spectral densities (which are determined by the form of the phonon correlation functions). For example, to

simulate the vibronic effects of underdamped phonon modes, we can combine the Fock state master equation with Eq. (6.114).

Given an N-photon Fock state input light, we can combine the Lindblad equation (Eq. (6.113)) or the HEOM (Eq. 6.114)) with the Fock state master equation Eq. (6.37). After combining with the Fock state master equation, Eq. (6.113) now becomes

$$\begin{aligned}\frac{d}{dt}\rho_{\text{el+vib }m,n} =& -i[H_{\text{el+vib}}, \rho_{\text{el+vib }m,n}] + \sum_l \mathcal{D}[L_l](\rho_{\text{el+vib }m,n}) \\ &+ \sqrt{m}\xi(t)[\rho_{\text{el+vib }m-1,n}, L_{\text{inc}}^\dagger] + \sqrt{n}\xi^*(t)[L_{\text{inc}}, \rho_{\text{el+vib }m,n-1}] \\ &+ \sum_{\alpha=1}^{M}\Big(\gamma_\alpha(\bar{n}_\alpha+1)\mathcal{D}[b_\alpha](\rho_{\text{el+vib }m,n}) + \gamma_\alpha\bar{n}_\alpha\mathcal{D}[b_\alpha^\dagger](\rho_{\text{el+vib }m,n})\Big),\end{aligned} \tag{6.140}$$

and Eq. (6.114) becomes

$$\begin{aligned}\frac{d}{dt}\rho^{\vec{m}}_{\text{el }m,n} =& -i[H_{\text{el}}, \rho^{\vec{m}}_{\text{el }m,n}] + \sum_l \mathcal{D}[L_l](\rho^{\vec{m}}_{\text{el }m,n}) \\ &+ \sqrt{m}\xi(t)[\rho^{\vec{m}}_{\text{el }m-1,n}, L_{\text{inc}}^\dagger] + \sqrt{n}\xi^*(t)[L_{\text{inc}}, \rho^{\vec{m}}_{\text{el }m,n-1}] \\ &+ \sum_{\alpha=1}^{M}\Big(m_A^\alpha(i\nu_\alpha - \frac{\gamma_\alpha}{2})\rho^{\vec{m}}_{\text{el }m,n} + m_B^\alpha(-i\nu_\alpha - \frac{\gamma_\alpha}{2})\rho^{\vec{m}}_{\text{el }m,n} \\ &\quad + m_A^\alpha(\frac{\bar{n}_\alpha}{2}S_\alpha\rho^{\vec{m}-\hat{e}_A^\alpha}_{\text{el }m,n} - \frac{\bar{n}_\alpha+1}{2}\rho^{\vec{m}-\hat{e}_A^\alpha}_{\text{el }m,n}S_\alpha) \\ &\quad + m_B^\alpha(\frac{\bar{n}_\alpha+1}{2}S_\alpha\rho^{\vec{m}-\hat{e}_B^\alpha}_{\text{el }m,n} - \frac{\bar{n}_\alpha}{2}\rho^{\vec{m}-\hat{e}_B^\alpha}_{\text{el }m,n}S_\alpha) \\ &\quad - [S_\alpha, \rho^{\vec{m}+\hat{e}_A^\alpha}_{\text{el }m,n} + \rho^{\vec{m}+\hat{e}_B^\alpha}_{\text{el }m,n}]\Big).\end{aligned} \tag{6.141}$$

Eq. (6.141) is the double hierarchical equation describing the excitonic system dynamics coupled to underdamped vibrational modes under Fock state excitation. It should be compared with the double hierarchical equation of Eq. (6.138), which describes the excitonic system dynamics coupled to overdamped vibrational modes (with Drude-Lorentz spectral density) under Fock state excitation. The initial condition of Eq. (6.140) is $\rho_{\text{el+vib }m,n} = \rho_{\text{el+vib}}(0)\delta_{m,n}$, and $\rho_{\text{el+vib }N,N}$ is the physical density matrix given an N-photon Fock state input. The initial condition of Eq. (6.141) is $\rho^{\vec{m}}_{\text{el }m,n} = \rho_{\text{el}}(0)\delta_{m,n}\delta_{\vec{m},\vec{0}}$, and $\rho^{\vec{0}}_{\text{el }N,N}$ is the physical density matrix given an N-photon Fock state input.

Following the derivation of Section 6.4.2 and Section 6.3.4, one can show that solving the Fock state master equation with Lindblad dissipators on the electronic plus vibrational degrees of freedom (Eq. (6.140)) and then tracing out the vibrations is equivalent to solving the Fock state master equation + underdamped HEOM (Eq. (6.141)). Fig. (6.3) demonstrates this equivalence numerically for a dimer system coupled to two underdamped vibrational modes under a two-photon Fock state excitation. The vibronic Hamiltonian takes the form

$$H_{\text{el+vib}} = H_{\text{dimer}} + \nu_1 b_1^\dagger b_1 + \nu_2 b_2^\dagger b_2 + \kappa_1|1\rangle\langle 1|\frac{b_1+b_1^\dagger}{\sqrt{2}} + +\kappa_2|2\rangle\langle 2|\frac{b_2+b_2^\dagger}{\sqrt{2}}, \tag{6.142}$$

where H_{dimer} is given in Appendix H. $|1\rangle$ and $|2\rangle$ represent states with excitations on site 1 or 2. The system-light coupling strength Γ_0 is increased by a factor of 10^5 from the physical value in order to show that the equivalence is not due to the weak system-light interaction. This numerical equivalence between the two different equations further verifies the correctness of our general approach to combine Fock state master equations and HEOM equations into a double hierarchy.

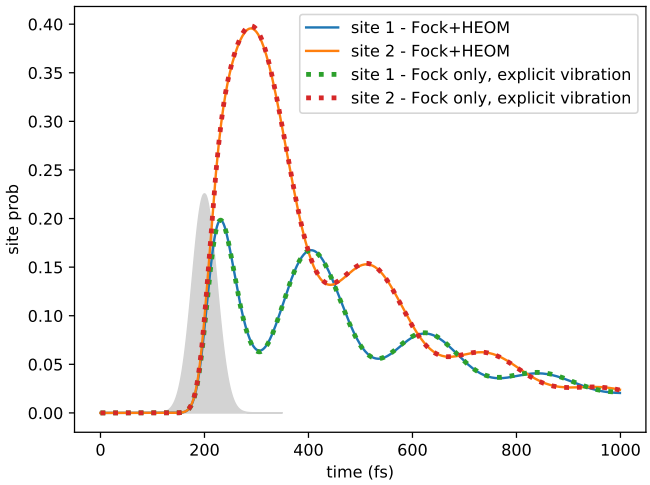

Figure 6.3: Comparison between solving the Fock state master equation (Eq. (6.140)) with a vibronic Hamiltonian then tracing out the vibrations and solving the Fock state + underdamped HEOM master equation (Eq. (6.141)). Calculations are performed on a dimer system with the vibronic Hamiltonian of Eq. (6.142). The parameter values are $(\nu_1, \nu_2, \kappa_1, \kappa_2, \gamma_1, \gamma_2) = (200, 200, 50, 50, 100, 100)\,\mathrm{cm}^{-1}$. The temperature of the initial vibrational state is 300 K. In solving the Lindblad equation, both harmonic oscillators are truncated to the 5 lowest eigenstates. In solving the HEOM, we propagate only the auxiliary density matrices $\rho^{\vec{m}}$ satisfying $\mathrm{sum}(\vec{m}) = m_A^1 + m_B^1 + m_A^2 + m_B^2 \leq 5$. Gray area: temporal profile of the two-photon Fock state light pulse.

Chapter 7

Analytical and numerical analysis of the system dynamics

7.1 Fock state vs coherent state input

In this section we shall examine the relationship between the dynamics under Fock state input photon fields and under coherent state input fields. We show that unlike coherent state inputs, Fock state inputs do not induce any coherence between excited states with different total number of excitations. If a Fock state input and a coherent state have the same average photon number and the same temporal profile, then when the weak coupling condition $N\Gamma_{\rm inc}\tau_{\rm pulse} \ll 1$ (where N is the average photon number, $\Gamma_{\rm inc}$ is the coupling strength between system and the incoming paraxial mode (see Eq. (6.12)), and $\tau_{\rm pulse}$ is the pulse duration) holds, the system density matrices in the single excitation subspace are the same. Furthermore, the output photon flux is also the same for both Fock and coherent state input fields. We derive these results by first examining the case of a single input photon, then generalizing to the case of N input photons to show that the excited part of the system state is directly proportional to the number of photons.

7.1.1 System state

We first compare the system state under a coherent state input with that under an N-photon Fock state input. We will neglect spontaneous emission here, since it has a small effect in the timescale of the light pulse. In Appendix I, we perform a second order perturbation (PT2) analysis on the initial state $|g\rangle\langle g|$, and show that the system state can be written in the block matrix form as

$$\rho_c(t) = \begin{pmatrix} \big(1 - \langle\beta'_\alpha(t)|\beta'_\alpha(t)\rangle\big)|g\rangle\langle g| & |g\rangle\langle\beta'_\alpha(t)| \\ |\beta'_\alpha(t)\rangle\langle g| & |\beta'_\alpha(t)\rangle\langle\beta'_\alpha(t)| \end{pmatrix}, \tag{7.1}$$

where $|\beta'_\alpha(t)\rangle$ is defined in Eq. (6.46). In the presence of phonons, writing the initial phonon thermal state as a mixture of pure states $\sum_v P_v|v\rangle\langle v|$, the system+vibration state in PT2 is given by

$$\rho_{c'}(t) = \sum_v P_v \begin{pmatrix} \big(1 - \langle\gamma'_{\alpha,v}(t)|\gamma'_{\alpha,v}(t)\rangle\big)|g\rangle\langle g| & {\rm Tr}_{\rm vib}\,|g\rangle\langle\gamma'_{\alpha,v}(t)| \\ {\rm Tr}_{\rm vib}\,|\gamma'_{\alpha,v}(t)\rangle\langle g| & {\rm Tr}_{\rm vib}\,|\gamma'_{\alpha,v}(t)\rangle\langle\gamma'_{\alpha,v}(t)| \end{pmatrix}, \tag{7.2}$$

where $|\gamma'_{\alpha,v}(t)\rangle$ is defined in Eq. (6.119). Using the form for $|\gamma'_{\alpha,v}(t)\rangle$ from Eq. (6.119), Eq. (7.2) shows that the ground-excited state coherences will be proportional to α, i.e., to $\sqrt{N}$, while the excited state

populations will be proportional to $|\alpha|^2$, i.e., to N, where N is the average number of photons in the coherent state.

The perturbative approach works well when product of the perturbation $\alpha(t)L_{\text{inc}}^\dagger$ (or its Hermitian conjugate) and the interaction time is $\ll 1$. The coherent amplitude $\alpha(t) = \alpha\xi(t)$ is on the order of $\sqrt{N/\tau_{\text{pulse}}}$, where N is the average photon number and τ_{pulse} is the pulse duration, since $N = |\alpha|^2$ and $\xi(t)$ has the normalization $\int dt|\xi(t)|^2 = 1$. L_{inc} is on the order of $\sqrt{\Gamma_{\text{inc}}}$ because $L_{\text{inc}} = \sqrt{\Gamma_{\text{inc}}}|g\rangle\langle B_{\text{inc}}|$ (see Eq. (6.11)). Combining the order of magnitude estimates, we can conclude that the PT2 analysis is accurate when $N\Gamma_{\text{inc}}\tau_{\text{pulse}} \ll 1$.

As a comparison, given a single photon Fock state input, neglecting spontaneous emission, the system state without the influence of phonons is given exactly by

$$\rho_{F1}(t) = \begin{pmatrix} \big(1 - \langle\beta'_\xi(t)|\beta'_\xi(t)\rangle\big)|g\rangle\langle g| & 0 \\ 0 & |\beta'_\xi(t)\rangle\langle\beta'_\xi(t)| \end{pmatrix} \tag{7.3}$$

(see Eq. (6.45)), and in the presence of phonons it is given by

$$\rho_{F1'}(t) = \sum_v P_v \begin{pmatrix} \big(1 - \langle\gamma'_{\xi,v}(t)|\gamma'_{\xi,v}(t)\rangle\big)|g\rangle\langle g| & 0 \\ 0 & \text{Tr}_{\text{vib}}\,|\gamma'_{\xi,v}(t)\rangle\langle\gamma'_{\xi,v}(t)| \end{pmatrix}. \tag{7.4}$$

Thus with or without phonons, when the Fock state temporal profile $\xi(t)$ is equal to the coherent amplitude $\alpha(t)$, the block diagonal terms of $\rho_{F1}(t)$ turn out to be the same as those of $\rho_c(t)$ in this weak coupling situation. In contrast, the off-diagonal blocks representing the coherence between ground and singly excited states are nonzero in $\rho_c(t)$, while these blocks are 0 in $\rho_{F1}(t)$. The fact that the coherence terms between subspaces of different excitation number are zero for Fock state input fields derives from a much more general observation, namely that: **for the reduced system density matrix,** given the system initializes in the electronic ground state, an n-photon Fock state input does not induce any direct coherence between system subspaces of different electronic excitation number.

The proof of this statement makes use of the excitation conserving property of the overall Hamiltonian. Defining the total excitation number as the number of photons plus the number of electronic excitations in the system, the total excitation is equal to n, the photon number of the input Fock state, at all times, since both the system-field and the system-vibration interactions conserve the total excitation number. Any pure state $|\Psi\rangle$ with n total excitations lives in the subspace

$$|\Psi\rangle \in \bigoplus_{m=0}^{n} \mathcal{S}_m \otimes \mathcal{F}_{n-m},$$

where $\mathcal{S}_m$ is the system m-excitation subspace, and $\mathcal{F}_m$ is the m-photon subspace of the field. Since $\mathcal{F}_m$ and $\mathcal{F}_{m'}$ are orthogonal to each other if $m \neq m'$, the reduced system density matrix $\text{Tr}_{\text{field}}|\Psi\rangle\langle\Psi| = \sum_{m=0}^{n} \rho_m$ is block-diagonal, with ρ_m being nonzero only in the m-excitation block. Any matrix element connecting states with different excitation numbers is identically zero. In the more general case that the system+field+vibration state is a mixture of different pure states with n total excitations, the reduced system density matrix becomes a mixture of block-diagonal matrices, which is still block-diagonal. Thus, the conservation of total excitation number by the Hamiltonian results in a coherence selection rule on the reduced system density matrix which states that, under N photon Fock state excitation, there are no coherences between reduced system states with different numbers of electronic excitations.

For example under a single photon Fock state excitation, we note that coherence in the form

$$|\text{excited, 0 photon}\rangle\langle\text{ground, 1 photon}|$$

is indeed generated in the system+field degrees of freedom. However, after tracing over the field, the resulting matter coherence term $|\text{excited}\rangle\langle\text{ground}|$ in the reduced system density matrix vanishes because $\langle 1 \text{ photon}|0 \text{ photon}\rangle = 0$. This fact is implicit in the Fock state hierarchy (Eq. (6.37)). The necessity of including $\rho_{0,1}$ to describe the dynamics of $\rho_{1,1}$ shows that there are nevertheless relevant ground-excited state coherences that are mediated via field states with different photon numbers.

The above proof of no coherence between system subspaces with different numbers of electronic excitations (including no ground-excited state coherence), can be generalized to consider an initial incoherent thermal state of light, i.e.,

$$\rho_{\text{field,thermal}} = \prod_{\mathbf{k},\lambda} \sum_{n_{\mathbf{k},\lambda}} P_{n_{\mathbf{k},\lambda}} |n_{\mathbf{k},\lambda}\rangle\langle n_{\mathbf{k},\lambda}|, \tag{7.5}$$

where $|n_{\mathbf{k},\lambda}\rangle$ is the n-th number state of the mode of wavevector $\mathbf{k}$ and polarization λ. $P_{n_{\mathbf{k},\lambda}}$ is the probability described by the Bose-Einstein distribution. We assume that only photons whose energies are close to ω_0, the energy difference between exciton manifolds, interact with the system. Furthermore, these interactions cause transitions between electronic excitation manifolds in a manner that conserves the total number of excitations (i.e., absorption or emission). Since a thermal state is a mixture of number states, by the same arguments as above, we can then conclude that: **given the system initializes in the electronic ground state, a thermal state does not induce any coherence between system subspaces of different electronic excitation number.** A similar result was obtained in Ref. [76] using first order perturbation theory. We emphasize that this absence of coherence between different system excitation subspaces is not due to the lack of temporal coherence in the thermal state of light. Instead, it is due to the conservation of total excitation number and the fact that thermal state is a mixture of number states and so inherits the selection rule on these that we have shown above is imposed by the excitation conserving property of the overall Hamiltonian.

An alternative derivation based on perturbative expansion

The conclusion that an N-photon Fock state induces no coherence between system subspaces of different electronic excitation number holds true regardless of the system-field coupling strength. The argument in the previous section only makes use of the excitation-number-conserving property of the system-field coupling. However, under weak system-field coupling (more precisely, for $N\Gamma_{\text{inc}}\tau_{\text{pulse}} \ll 1$), the second-order perturbative expansion of the system state provides a unified comparison between Fock state excitation and coherent state excitation. To second order, the system state is

$$\rho(t) = \rho(0) - i\text{Tr}_{\text{field}} \int_0^t dt_1 \, [H_I(t_1), \rho(0)] - \text{Tr}_{\text{field}} \int_0^t dt_1 \int_0^{t_1} dt_2 \, [H_I(t_1), [H_I(t_2), \rho(0)]], \tag{7.6}$$

where H_I is the dipole-electric field coupling in the interaction picture, and $\rho(0) = |g\rangle\langle g|$. The first order perturbation term gives rise to ground-excited coherence and is proportional to the one-point field correlation functions $\langle E(t)\rangle$ and $\langle E^\dagger(t)\rangle$. These are nonzero for a coherent state input, but zero for a N-photon Fock state input. Therefore the ground-excited coherence is zero (nonzero) under Fock (coherent) state excitation. The second order term contributes to the singly excited block of the density matrix, and the contribution is proportional to the two-point correlations $\langle E^\dagger(t_2)E(t_1)\rangle$ and $\langle E(t_2)E^\dagger(t_1)\rangle$. Therefore when an N-photon Fock state input and a coherent state input have the same two-point correlations, they will induce the same dynamics in the singly excited block of the system density matrix.

A thermal state input has one-point correlations equal to zero, so it does not induce any ground-excited coherence. Different forms of the two-point correlations have been used to study the dynamics under thermal light excitation [73, 78, 79]. But due to the short coherence time of the two-point

correlations for black body radiation [126], it is common to let the two-point correlation functions (for example $\langle E(t_2)E^\dagger(t_1)\rangle$) be proportional to $\delta(t_2 - t_1)$. In that case, the effects of the second order term are described by Lindblad dissipation channels [74, 77].

7.1.2 Photon flux

The photon flux under a single photon coherent state input, also an averaged quantity, is similarly identical to the flux under a single photon Fock state input. Substituting Eqs. (7.1) or (7.2) into Eq. (6.48), and substituting Eqs. (7.3) or (7.4) into Eq. (6.50), we see that if the single photon Fock state temporal profile $\xi(t)$ is equal to the coherent amplitude $\alpha(t)$, then the photon fluxes from the single photon Fock state input are the same as the photon fluxes from the coherent state within a PT2 description. Numerical comparison of the photon fluxes of a single photon Fock state and a coherent state interacting with a dimer system is shown in Fig. 7.1.

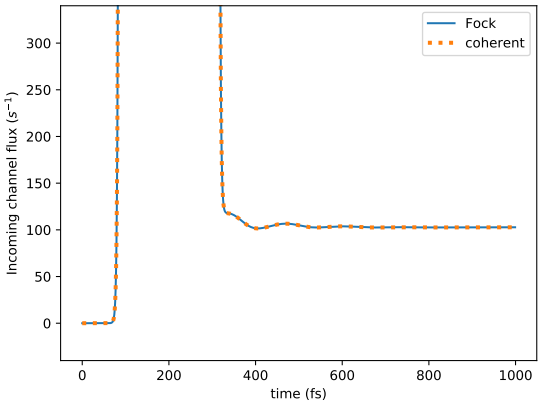

Figure 7.1: Photon flux in the paraxial channel for single photon Fock state and single photon coherent state inputs interacting with a dimer system. Consistent with our analysis in Section 7.1.2, under weak field excitation, the photon fluxes are identical.

7.1.3 N-photon Fock state input

In this section, we show that when $N\Gamma_{\text{inc}}\tau_{\text{pulse}} \ll 1$, the singly excited part of the system density matrix under excitation by an N-photon Fock state is on the order of $N\Gamma_{\text{inc}}\tau_{\text{pulse}}$ and is equal to N times that under excitation by a single photon Fock state. Since the single excitation probability $\sim N\Gamma_{\text{inc}}\tau_{\text{pulse}} \ll 1$, saturation effects can be ignored under this condition. If $N \geq 2$, the probability of double excitation is on the order of $(N\Gamma_{\text{inc}}\tau_{\text{pulse}})^2$, much smaller than the single excitation probability. Therefore we can restrict our analysis to the ground and singly excited states, and the absorption probability from ground to the singly excited state is given by $\sim N\Gamma_{\text{inc}}\tau_{\text{pulse}}$.

To understand this result, consider the N-photon Fock state hierarchy, which is shown schematically in Figure (7.2). The diagonal density matrices $\rho_{m,m}$, indicated by the solid orange boxes, are initialized in $|g\rangle\langle g|$, and are considered as the "source" terms of the master equations. The off-diagonal density matrices $\rho_{m,n}$ $(m \neq n)$ are initialized in 0, and are considered as the "non-source" terms. An auxiliary density matrix $\rho_{m,n}$ couples downward to $\rho_{m-1,n}$ and $\rho_{m,n-1}$, with coupling strength $\sqrt{m\Gamma}$ and $\sqrt{n\Gamma}$, respectively (see Eq. (6.37)). The couplings are drawn as bonds between auxiliary density matrices. Perturbatively speaking, changes in the physical density matrix $\rho_{N,N}$ are due to its coupling to other "source" density matrices because they have nonzero initial values. Therefore if $N\Gamma_{\text{inc}}\tau_{\text{pulse}} \ll 1$ (i.e.

if the coupling $\sqrt{N\Gamma_{\rm inc}}\xi(t)$ times the interaction time $\tau_{\rm pulse}$ is $\ll 1$), the dynamics of $\rho_{N,N}$ is dominated by its 2-bond couplings to $\rho_{N-1,N-1}$. The couplings to other source density matrices require more than 2 bonds, which contribute much less than the 2-bond coupling. Double excitations in the system require at least 4 bonds, so the probability for such events is much lower than for single excitations. This justifies our restriction to the ground and singly excited states.

Focusing on the four auxiliary density matrices involved in the 2-bond coupling (i.e., $\rho_{N,N}$, $\rho_{N-1,N}$, $\rho_{N,N-1}$, and $\rho_{N-1,N-1}$) and dropping all other auxiliary density matrices, we notice that the four auxiliary density matrices follow the same master equations as the single photon master equations, with the replacement of $\Gamma_{\rm inc}$ in the single photon master equations by $N\Gamma_{\rm inc}$. Since $|\beta'_\xi(t)\rangle$ in Eq. (7.3) and $|\gamma'_{\xi,v}(t)\rangle$ in Eq. (7.4) are both proportional to $\sqrt{\Gamma_{\rm inc}}$, , the system state under the excitation of an N-photon Fock state in the absence of phonons is

$$\rho_{FN}(t) = \begin{pmatrix} \big(1 - N\langle\beta'_\xi(t)|\beta'_\xi(t)\rangle\big)|g\rangle\langle g| & 0 \\ 0 & N|\beta'_\xi(t)\rangle\langle\beta'_\xi(t)| \end{pmatrix}, \tag{7.7}$$

to the lowest order in $N\Gamma_{\rm inc}\tau_{\rm pulse}$. The corresponding equation in the presence of phonon coupling follows similarly. Thus with or without phonons, the entire single excitation block of the system density matrix (lower right block in Eq. 7.7), containing both population and coherence terms, is now a factor of N times that derived from excitation by a single photon Fock state.

Comparing Eq. (7.7) and its generalization in the presence of phonons to the coherent state results in Eqs. (7.1) and (7.2), and using the properties $|\beta'_\alpha(t)\rangle = \alpha|\beta'_\xi(t)\rangle$ and $|\gamma'_{\alpha,v}(t)\rangle = \alpha|\gamma'_{\xi,v}(t)\rangle$, we see that the $|\text{ground}\rangle\langle\text{ground}|$ and the $|\text{excited}\rangle\langle\text{excited}|$ blocks of the system density matrix under the excitation by a N-photon Fock state is the same as those under the excitation by a coherent state with the same temporal profile and average photon number. This relationship is verified numerically below for a dimer system under excitations with average 20 photons. It should be emphasized again that this relationship holds when $N\Gamma_{\rm inc}\tau_{\rm pulse} \ll 1$. It is well known that in the case of average single photon, when $\Gamma_{\rm inc}\tau_{\rm pulse} \sim 1$, a Fock state input and a coherent state input with the same temporal profile can generate very different dynamics in a two-level system [127].

7.1.4 Numerical comparison between Fock state vs coherent state input

To give numerical verifications to the analysis above, we first calculate the system dynamics and photon fluxes of a dimer system under excitation by a single photon Fock state pulse and by a coherent state with coherent amplitude $\alpha = 1$ (average $|\alpha|^2 = 1$ photon). Details of the dimer Hamiltonian and transition dipoles are given in Appendix H. The temporal profile of both coherent state and Fock state pulses are set to equal to the Gaussian form

$$\xi(t) = \Big(\frac{\Omega^2}{2\pi}\Big)^{1/4} e^{-\Omega^2(t-t_0)^2/4}, \tag{7.8}$$

where the bandwidth Ω is chosen to be $0.06\,\text{fs}^{-1}$, and the time delay $t_0 = 200\,\text{fs}$. 5 HEOM levels were used for all calculations in this section. For Fock state inputs, the double hierarchical equations Eq. (6.138) are used. For coherent state inputs, only the HEOM hierarchy is needed, since the coherent state master equation does not involve any Fock state hierarchy.

If we characterize the pulse duration $\tau_{\rm pulse}$ by the inverse bandwidth $1/\Omega \approx 16.6\,\text{fs}$, then $\Gamma_{\rm inc}\tau_{\rm pulse} \approx 8.9\times10^{-7} \ll 1$. Therefore we expect the numerical results to show good agreement with the analyses in Sections 7.1.1 and 7.1.2. Figure (7.3a) shows for example the site 2 probabilities, $\langle 2|\rho|2\rangle$, and the coherence term between site 1 and site 2, $\langle 1|\rho|2\rangle$, under Fock state and coherent state inputs. Both the population and the coherence terms are nearly identical under the two input light states, with the

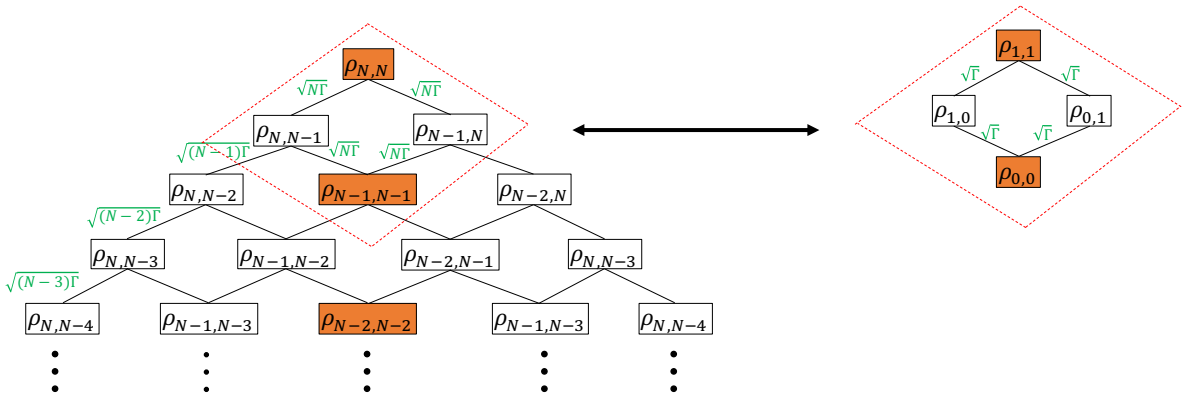

Figure 7.2: Fock state hierarchy for the (left) N-photon Fock state master equations and (right) single photon Fock state master equations. Each box represents an auxiliary density matrix. Solid orange boxes are the diagonal "source" terms, and the other boxes are the off-diagonal "non-source" terms. The "bonds" between auxiliary density matrices represent the coupling between them. We label the coupling strengths for some of the bonds. To the lowest order in $\Gamma_{\text{inc}}\tau_{\text{pulse}}$, only the top four auxiliary density matrices (enclosed in red dashed lines) contribute to the dynamics of the physical density matrix. The equations for the top four density matrices are the same as those for the single photon master equations, with the replacement of Γ_{inc} by $N\Gamma_{\text{inc}}$.

relative difference smaller than the numerical accuracy of the numerical integrator (relative tolerance $= 10^{-3}$). The main difference between the two system states is in the ground-excited state coherence. Figure (7.3b) shows for example the coherence term $\langle g|\rho|2\rangle$ under the two input light. As predicted in Section 7.1.1 above, $\langle g|\rho|2\rangle$ is zero for a Fock state input, but nonzero for a coherent state input.

Similar results are obtained for the photon flux, since these are obtained by averaging over the excited state density matrix (see Eqs. (6.50) and (6.48)).

To confirm the photon number dependence of Eq. (7.7), we consider a dimer system under excitation by a 20-photon Fock state and under the excitation by a coherent state with $\alpha = \sqrt{20}$, corresponding to an average photon number of 20. For this example $N\Gamma_{\text{inc}}\tau_{\text{pulse}} \approx 1.8 \times 10^{-5}$. Similar to the result in Fig. 7.3 for excitation by single photons, Fig. (7.4a) shows that both the population and coherence terms in the $|\text{excited}\rangle\langle\text{excited}|$ block of the system density matrix are almost the same under excitation by a 20-photon Fock state as under and excitation by a coherent state with an average of 20 photons. The difference between the singly excited blocks is again less than the numerical accuracy of the numerical integrator. Furthermore, these values are 20 times larger than the values from single photon calculations in Fig. (7.3a), confirming the dependence on N in Eq. (7.7). Matrix elements between the ground state and the excited subspace are identically zero under Fock state excitation, and are non-zero under coherent state excitation (see Fig. (7.4b)). We note that the ground-excited coherence under a 20-photon coherent state excitation in Fig. (7.4b) is $\sqrt{20}$ times larger than the corresponding values in Fig. (7.3b), obtained under a single photon coherent state excitation, consistent with the $\sqrt{N}$ enhancement predicted by Eq. 7.2) (see also appendix *I*).

The fact that the coherent state and Fock state inputs give similar results when $N\Gamma_{\text{inc}}\tau_{\text{pulse}} \ll 1$ means that we can in fact simulate the average dynamics under N-photon Fock state excitation by simulating the dynamics under a coherent state and then setting the ground-excited coherence terms to be zero. This can drastically reduce the computational runtime by avoiding the Fock state hierarchy. For example, for the 20-photon input light fields above, the computational runtime of this Fock state calculation is $\approx$ 500 s on a 1.6GHz dual-core CPU, while the runtime of the corresponding coherent

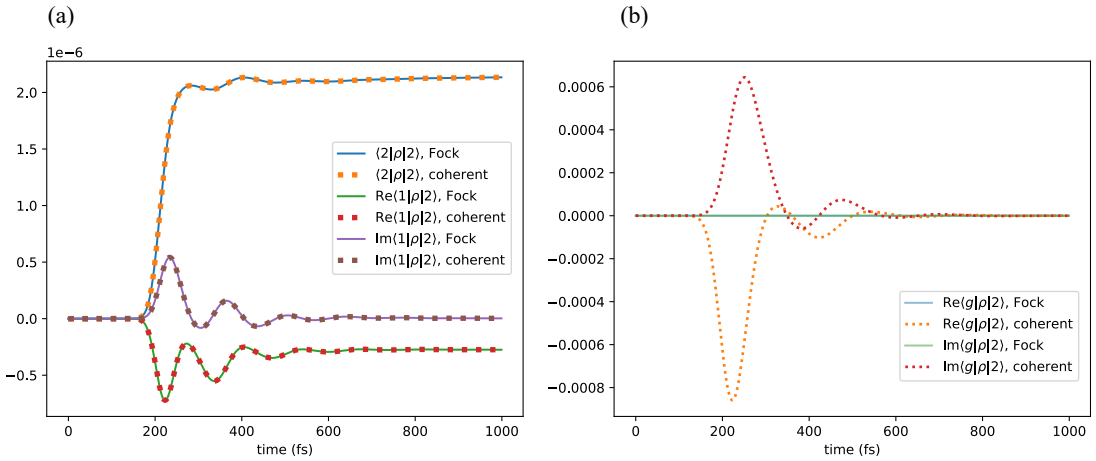

Figure 7.3: Time dependence of selected excitonic density matrix elements of a dimer under excitation by a single photon Fock state pulse of light and by a coherent state pulse of light containing an average of one photon. (a) Comparison of matrix elements $\langle 2|\rho|2\rangle$ and $\langle 1|\rho|2\rangle$ with indexing referring to the excitations at sites 1 or 2, showing that density matrix component in the first excitation subspace is almost identical under excitation by a Fock state (solid lines) and by a coherent state of light (dotted lines) with the same average photon number. The differences between the matrix elements under excitation by these two states of light are less than the numerical accuracy of the numerical integrator. (b) Real and imaginary parts of matrix elements between the dimer ground state and the excited state of chromophore 2, $\langle g|\rho|2\rangle$, under Fock state excitation (solid lines) and under coherent state input light (dotted lines). For this single-photon excitation, the ground-excited coherence terms are identically zero for a Fock state input (solid lines), but non-zero for a coherent state input (dotted lines).

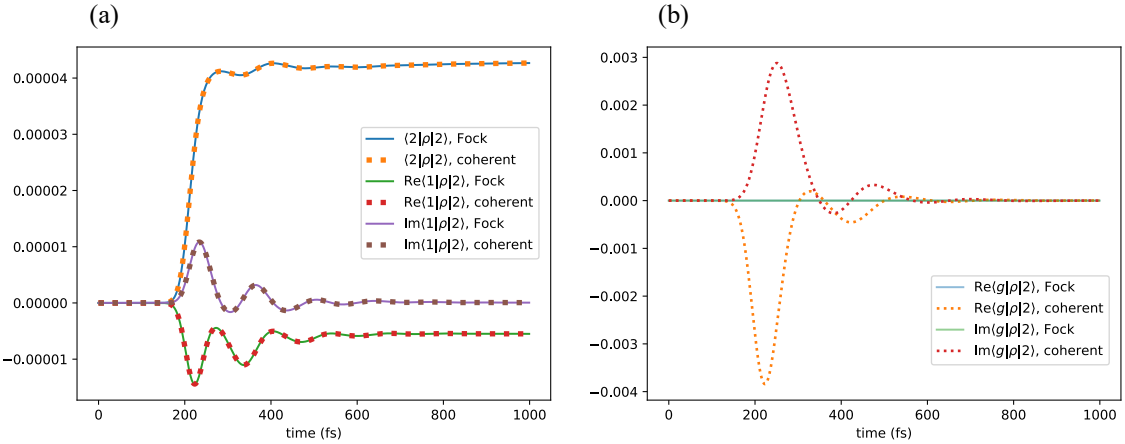

Figure 7.4: Time dependence of selected excitonic density matrix elements of a dimer under excitation by a 20-photon Fock state pulse of light and by a coherent state pulse of light containing an average of 20 photons. (a) Comparison of matrix elements $\langle 2|\rho|2\rangle$ and $\langle 1|\rho|2\rangle$ in the $|\text{excited}\rangle\langle\text{excited}|$ block under Fock state excitation (solid lines) and under coherent state input light (dotted lines). (b) Comparison of the matrix element $\langle g|\rho|2\rangle$ under Fock state excitation (solid lines) and under coherent state input light (dotted lines).

state calculation is ≈ 1 s.

To assess the implications of this analysis for light absorption by photosynthetic systems, we consider absorption by the Q_y absorption bands of chlorophyll molecules, taking Chla as an example [72]. Regarding the absorption as a measurement process whereby the chlorophyll molecules detect incoming light only at frequencies inside the width of the Q_y band, then the corresponding duration of optimally detectable light pulses is the inverse bandwidth $\tau_{\text{pulse}} = 1/\Omega \sim 1/(400\,\text{cm}^{-1}) \approx 13\,\text{fs}$. This leads to an absorption probability from a single incident photon that is equal to $\Gamma_{\text{inc}}\tau_{\text{pulse}} \approx 4 \times 10^{-7}$ for a single chromophore with a transition dipole of 4 Debye (a value typical of chlorophyll molecules [112]). This small value of absorption probability is consistent with results of previous calculations for coherent states with an average of one photon and with bulk absorption cross-sections [59]. Given the very low flux of natural sunlight, estimated using spectral irradiance data [128] and the size of a Chla molecule [72], to be approximately 74 photons/nm^2/s for a Chla monomer under full sunlight [59], it is evident that incident single photons with temporal pulse durations ~ 13 fs under natural sunlight conditions will show the equivalence derived above for the excited states of the photosynthetic system under Fock and coherent state excitation, as well as the difference derived above in the ground-excited state coherences.

7.2 Analysis of Absorption

The spontaneous emission time scale $\tau_{\text{emission}} \sim 10$ ns is much longer than the system+vibration time scale $\tau_{\text{sys+vib}} \sim 10 - 100$ fs. If we let the pulse duration τ_{pulse} be much shorter than τ_{emission}, we can study the dynamics within short times $t \ll \tau_{\text{emission}}$ without considering the effects of spontaneous emission, since spontaneous emission only reduces the total excitation probability by a small fraction. Within the short time regime, we can define the absorption probability as the total excitation probability $\sum_j \langle j|\rho|j\rangle$ immediately after all but an exponentially small tail of the pulse has passed. After this time the interaction with the phonon bath can redistribute the excitation between the chromophores, but it does not change the total excitation probability.

From the solution to the pure state equations without phonons (Eq. (6.46)), we know that the absorption probability as a function of time is

$$\text{abs. prob.}_{\text{no phonon}} = \langle \beta'_\xi(t)|\beta'_\xi(t)\rangle. \tag{7.9}$$

To find the absorption probability at time t when almost all of the pulse has passed, we notice that the magnitude of the integrand in Eq. (6.46) is very small outside of the integration bounds $(0, t)$, since the temporal profile $\xi(\tau)$ is localized in this interval. Therefore we can extend the range of integration to $(-\infty, \infty)$. Next, we replace the L_{inc} in Eq. (6.46) with $\sqrt{\Gamma_{\text{inc}}}|g\rangle\langle B_{\text{inc}}|$ (see Eq. (6.11)), where Γ_{inc} is the effective coupling constant to the incoming paraxial mode and $|B_{\text{inc}}\rangle$ is the normalized bright state corresponding to the incoming mode polarization. Then Eq. (6.46) becomes

$$|\beta'_\xi\rangle = -\sqrt{\Gamma_{\text{inc}}} \sum_n \int_{-\infty}^{\infty} d\tau\, \xi(\tau) e^{-i(E_n - E_0)(t-\tau)} \langle n|B_{\text{inc}}\rangle |n\rangle, \tag{7.10}$$

where we inserted a resolution of identity $\sum_n |n\rangle\langle n| = 1$ with n indexing the eigenstates of the exciton system Hamiltonian H_{sys} of Eq (6.1). Since the H in the exponential of Eq. (6.46) already has a carrier frequency $E_0 = \hbar\omega_0$ rotated out (see Eq. (6.6)), the eigenvalue of H is the original system eigenenergy E_n minus the carrier frequency E_0, hence the factor $E_n - E_0$ appearing in the exponential in Eq. (7.10). Substituting Eq. (7.10) into Eq. (7.9), the absorption probability without phonon becomes

$$\text{abs. prob.}_{\text{no phonon}} = \Gamma_{\text{inc}} \sum_n c_n |\tilde{\xi}(E_n - E_0)|^2, \tag{7.11}$$

where

$$c_n = |\langle n|B_{\text{inc}}\rangle|^2 \tag{7.12}$$

is the overlap between the system eigenstate and the bright state, and

$$\tilde{\xi}(E) = \int_{-\infty}^{\infty} d\tau\, \xi(\tau) e^{iE\tau} \tag{7.13}$$

is the Fourier transform of the temporal profile. Note that $\sum_n c_n = 1$, so the sum in Eq. (7.11) can be thought of as a weighted average of the frequency components of the incoming pulse.

The analysis above can be generalized to take into account the effects of phonons. To distinguish between the analysis without or with phonons, we denote the eigenstate and eigenenergy of H_{sys} (Eq. (6.1)) as $|n\rangle$ and E_n, respectively. We denote the eigenstate and eigenenergy of $H_{\text{sys+vib}}$ (Eq. (6.59)) as $|\widetilde{n}\rangle$ and $\widetilde{E}_n$, respectively.

First, we assume an initial phonon state $|v\rangle$ that is an eigenstate of H_{vib}, the vibrational Hamiltonain in the ground electronic state, with energy E_v. Following the same procedure that we used to obtain Eq. (7.10), we rewrite Eq. (6.119) as

$$|\gamma'_{\xi,v}\rangle = -\sqrt{\Gamma_{\text{inc}}} \sum_n \int_{-\infty}^{\infty} d\tau\, \xi(\tau) e^{-i(\widetilde{E}_n - E_0)t} e^{i(\widetilde{E}_n - E_0 - E_v)\tau} \langle \widetilde{n}|B_{\text{inc}}, v\rangle |\widetilde{n}\rangle. \tag{7.14}$$

$|B_{\text{inc}}, v\rangle$ denotes the product state $|B_{\text{inc}}\rangle \otimes |v\rangle$. The absorption probability $\langle \gamma'_{\xi,v}|\gamma'_{\xi,v}\rangle$ given a pure initial vibrational state $|v\rangle$ is evaluated as

$$\text{abs. prob.}_{\text{ pure phonon},v} = \Gamma_{\text{inc}} \sum_n c'_{n,v} |\tilde{\xi}(\widetilde{E}_n - E_v - E_0)|^2, \tag{7.15}$$

with $c'_{n,v} = |\langle \widetilde{n}|B_{\text{inc}}, v\rangle|^2$. Note that the vibronic eigenstates $|\widetilde{n}\rangle$ can be expanded in the eigenbasis of the shifted harmonic oscillators corresponding to the vibrational Hamiltonian in the excited electronic states. This will result in Franck-Condon vibration overlap factors appearing in the expression of $c'_{n,v}$. However, due to the fact that the vibrational modes are distributed over all sites and that dipole-dipole coupling mixes the excitonic states, one cannot in general decompose $|\widetilde{n}\rangle$ into a simple product of an electronic state and a vibrational state. Therefore we will simply use the symbol $|\widetilde{n}\rangle$ to represent the complicated superposition of different vibrational states in the electronically excited subspace.

To obtain the absorption probability given an initial phonon thermal state, note that the thermal state can be treated as a classical mixture of energy eigenstates $|v\rangle$. Therefore the total absorption probability becomes

$$\text{abs. prob.}_{\text{thermal phonon}} = \sum_v P_v \,\text{abs. prob.}_{\text{pure phonon},v} = \Gamma_{\text{inc}} \sum_{\widetilde{n},v} \widetilde{c}_{n,v} |\tilde{\xi}(\widetilde{E}_n - E_v - E_0)|^2, \tag{7.16}$$

where P_v is the Boltzmann weight

$$P_v = \frac{\exp(-E_v/k_B T)}{\sum_u \exp(-E_u/k_B T)}, \tag{7.17}$$

and we introduce a thermally weighted squared overlap of the vibronic eigenstate $|\widetilde{n}\rangle$ with the bright state,

$$\widetilde{c}_{n,v} = P_v c'_{n,v} = P_v |\langle \widetilde{n}|B_{\text{inc}}, v\rangle|^2. \tag{7.18}$$

Since $\sum_{\widetilde{n},v} \widetilde{c}_{n,v} = 1$, Eq. (7.16) can be thought of as a weighted average of $|\tilde{\xi}(\widetilde{E}_n - E_v - E_0)|^2$.

To understand the factor $\widetilde{E}_n - E_v - E_0$ in Eq. (7.16), we consider the sys+vib eigenenergy $\widetilde{E}_n$ to be in the range $[E_{\text{sys}} + E_v - \mathcal{O}(E_{\text{int}}), E_{\text{sys}} + E_v + \mathcal{O}(E_{\text{int}})]$, where E_{int} is the energy scale of the system-vibration interaction. Then

$$\widetilde{E}_n - E_v - E_0 \in [E_{\text{sys}} - E_0 - \mathcal{O}(E_{\text{int}}), E_{\text{sys}} - E_0 + \mathcal{O}(E_{\text{int}})]. \tag{7.19}$$

This indicates that the interaction with vibration broadens the photon frequency range that the system can interact with, from exactly $E_{\text{sys}} - E_0$ in Eq. (7.11), to the range $[E_{\text{sys}} - E_0 - \mathcal{O}(E_{\text{int}}), E_{\text{sys}} - E_0 + \mathcal{O}(E_{\text{int}})]$ in Eq. (7.16). In the case of zero system-vibration interaction, $E_{\text{int}} = 0$ and Eq. (7.16) reduces to Eq. (7.11).

7.2.1 Absorption probability is proportional to system-field coupling

From Eqs. (7.11) and (7.16), we see that the absorption probability is proportional to Γ_{inc}, with or without phonons. The only assumption we have made to arrive at these results is that the spontaneous emission time scale ($1/\Gamma_l \sim \tau_{\text{emission}} \sim 10$ ns) is much longer than both the system+vibration time scale ($\tau_{\text{sys+vib}} \sim 10 - 100$ fs) and the pulse duration τ_{pulse}. In other words, Γ_{inc} is the small parameter in the problem.

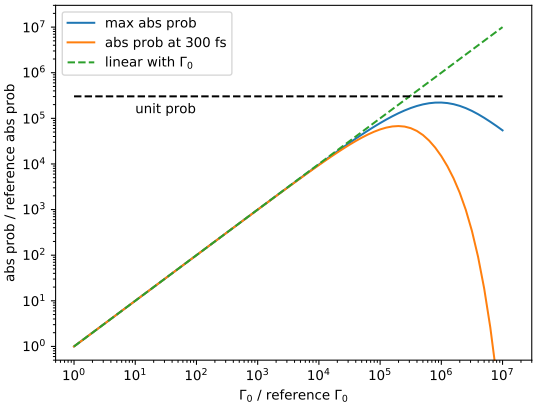

Figure 7.5: Effect of artificially increasing the system-field coupling strength Γ_0. Here Γ_0 is artificially increased by 7 orders of magnitude from the reference physical value (see Sec. 6.2.2). The resulting increase in absorption probability is plotted in the vertical axis as the ratio of this to the reference physical absorption probability. The temporal profile of the single photon pulse is a Gaussian centered at 150 fs, with FWHM of 55.5 fs. Two types of absorption probabilities are plotted: maximum absorption probability (blue) and the absorption probability at 300 fs (orange). The absorption probability depends linearly on Γ_0 across many orders of magnitude until the emission time scale $\tau_{\text{emission}} \sim 1/\Gamma$ becomes comparable to the pulse time scale τ_{pulse}. At very large Γ_0, spontaneous emission causes deviation from the linear relationship. The black dotted line represents unit absorption probability.

Figure (7.5) examines to what extent the linear relationship between the absorption probability and Γ_{inc} holds, or equivalently, to what extent can Γ_{inc} be consider a small parameter. Since $\Gamma_{\text{inc}} = \Gamma_0 \eta \sum_j |\mathbf{d}_j \cdot \hat{\epsilon}|^2$, we artificially increased the unit spontaneous emission rate Γ_0 by a factor of 1 to 10^7 in order to change the value for Γ_{inc}. The absorption probability as a function of Γ_0 was then evaluated numerically for a dimer system with 5 HEOM levels, using a Gaussian pulse with temporal profile $\xi(t)$ (Eq. (7.8)) centered at 150 fs with a pulse duration of $\tau_{\text{pulse}} = 1/\Omega = 16.7$ fs. The emission time scale τ_{emission} is on the order of $1/\Gamma_{\text{inc}} = 18.7$ ns. In Figure (7.5) we plot the maximum

absorption probability and the absorption probability at 300 fs. We see that the linear relationship between absorption probability and Γ_0 holds up to $\simeq 10^4$ times the physical value of Γ_0, indicating that for up to 10^4 times the physical value of Γ_0, Γ_{inc} can still be treated as the small parameter in the absorption process. At a value 10^5 times the reference physical Γ_0 value, the emission time scale $\tau_{\text{emission}} \sim 187\,\text{fs}$ becomes comparable to $\tau_{\text{pulse}} \sim 16.7\,\text{fs}$, so that spontaneous emission occurs before the tail of the Gaussian pulse has passed, making the absorption porbability at 300 fs significantly smaller than the maximum absorption probability. Another reason that the linear relationship cannot hold for large Γ_0 is of course that the absorption probability cannot exceed one. This limit is plotted as the black dashed line in Figure 7.5.

The simple observation that the absorption probability is proportional to $\Gamma_{\text{inc}} = \Gamma_0 \eta \sum_j |\mathbf{d}_j \cdot \hat{\epsilon}|^2$ allows us to quantitatively predict the absorption probability upon varying many different parameters. For example, changing the paraxial beam geometry or the position of the system inside the paraxial spatial mode results in changes in the geometric factor η. The effect of the dielectric environment is contained in the factor Γ_0. The effect of light polarization and dipole orientations is described by the factor $\sum_j |\mathbf{d}_j \cdot \hat{\epsilon}|^2$. One can analyze the factor $\sum_j |\mathbf{d}_j \cdot \hat{\epsilon}|^2$ using a singular value decomposition, as described in detail in Appendix M. Numerical illustrations of this method for a dimeric system are also given there.

7.2.2 How absorption probability depends on pulse duration

To analyze the dependence of absorption probability on pulse duration, we first write a general single photon Fock state photon temporal profile $\xi(t)$ in the scaling form

$$\xi(t) = \frac{1}{\sqrt{\tau_{\text{pulse}}}} f\left(\frac{t - t_0}{\tau_{\text{pulse}}}\right) \tag{7.20}$$

in order to focus on its dependence on the pulse duration τ_{pulse}. Here $f(x)$ is the scale-invariant pulse shape function, which is dimensionless and square-normalized, i.e., $\int |f(x)|^2 dx = 1$. The prefactor $1/\sqrt{\tau_{\text{pulse}}}$ gives $\xi(t)$ the correct dimension and ensures that $\int |\xi(t)|^2\, dt = 1$. We note that τ_{pulse} simply characterizes the pulse duration in a general sense, as long as the pulse is reasonably localized in time. Given a pulse shape, one has the freedom to define τ_{pulse} up to some $\mathcal{O}(1)$ factors. For example, for the Gaussian temporal profile (Eq. 7.8), one could define $\tau_{\text{pulse}} = \sqrt{2}/\Omega$ as the standard deviation of $\xi(t)$; alternatively, one could define $\tau_{\text{pulse}} = 1/\Omega$ as the standard deviation of $|\xi(t)|^2$.

Using Eq. (7.20), we rewrite the absorption probability without phonons (Eq. (7.11)) as

$$\text{abs. prob.}_{\text{no phonon}} = \Gamma_{\text{inc}} \tau_{\text{pulse}} \sum_n c_n A((E_n - E_0)\tau_{\text{pulse}}) \tag{7.21}$$

or with (Eq. (7.16)) phonons as

$$\text{abs. prob.}_{\text{thermal phonon}} = \Gamma_{\text{inc}} \tau_{\text{pulse}} \sum_{\widetilde{n},v} \widetilde{c}_{n,v} A((\widetilde{E}_n - E_v - E_0)\tau_{\text{pulse}}), \tag{7.22}$$

where we have defined the function

$$A(E\tau_{\text{pulse}}) = \Big| \int dx\, f(x) e^{iE\tau_{\text{pulse}} x} \Big|^2. \tag{7.23}$$

In the following analysis, we assume that the pulse shape function $\xi(t)$ is real, so that $f(t)$ is real and $A(E\tau_{\text{pulse}})$ is a real and even function.

7.2.3 Absorption probability in the short pulse regime

For short pulses, characterized by $\tau_{\text{pulse}} \ll \tau_{\text{sys+vib}}$, $(E_n - E_0)\tau_{\text{pulse}}$ in Eq. (7.21) or $(\widetilde{E}_n - E_v - E_0)\tau_{\text{pulse}}$ in Eq. (7.22) will be much less than 1. Furthermore, if $A(E\tau_{\text{pulse}})$ is analytic at $\tau_{\text{pulse}} = 0$, then for short pulses, we can Taylor expand it to the second order as

$$A(E\tau_{\text{pulse}}) = a - bE^2\tau_{\text{pulse}}^2. \tag{7.24}$$

The linear term vanishes because $A(E\tau_{\text{pulse}})$ is an even function. The expansion coefficients a and b are determined by the pulse shape alone and not by the pulse duration.

Substituting Eq. (7.24) into Eqs. (7.21) and (7.22), we obtain for the short pulse regime,

$$\text{abs. prob.}_{\text{no phonon}} = \Gamma_{\text{inc}}\tau_{\text{pulse}}\left(a - b\tau_{\text{pulse}}^2 \sum_n c_n (E_n - E_0)^2\right) \tag{7.25}$$

and

$$\text{abs. prob.}_{\text{thermal phonon}} = \Gamma_{\text{inc}}\tau_{\text{pulse}}\left(a - b\tau_{\text{pulse}}^2 \sum_{\widetilde{n},v} \widetilde{c}_{n,v} (\widetilde{E}_n - E_v - E_0)^2\right). \tag{7.26}$$

The term $\sum_n c_n (E_n - E_0)^2$ in Eq. (7.25) is a bright-state weighted average of the system eigenenergy detunings squared. If the pulse center frequency is set to the average of the system eigenenergies, then this quantity is a skewed variance of the eigenenergies in which eigenstates with more overlap with the bright state have more weight. Similarly, the term $\sum_{\widetilde{n},v} \widetilde{c}_{n,v} (\widetilde{E}_n - E_v - E_0)^2$ in Eq. (7.26) is a thermally weighted and bright-state weighted average of $(\widetilde{E}_n - E_v - E_0)^2$, where more weight is placed on eigenstates (indexed by $\widetilde{n}$) having high overlaps with the bright state and on vibration states (indexed by v) with higher Boltzmann weights. Next, we define an effective energy spread parameter

$$\Delta^2 = \sum_n c_n (E_n - E_0)^2 = \sum_n |\langle n|B_{\text{inc}}\rangle|^2 (E_n - E_0)^2 \tag{7.27}$$

or

$$\Delta^2 = \sum_{\widetilde{n},v} \widetilde{c}_{n,v} (\widetilde{E}_n - E_v - E_0)^2 = \sum_{\widetilde{n},v} P_v |\langle \widetilde{n}|B_{\text{inc}}, v\rangle|^2 (\widetilde{E}_n - E_v - E_0)^2, \tag{7.28}$$

depending on whether or not the interaction with phonons is taken into account. Since Δ characterizes the energy spread of a system, we can identify $1/\Delta$ as a characteristic system+vibration time scale, $\tau_{\text{sys+vib}}$. Substituting Eqs. (7.27) and (7.28) into Eqs. (7.25) and (7.26), we have a universal expression for the absorption probability in the short pulse regime:

$$\text{universal short pulse abs. prob.} = \Gamma_{\text{inc}}\tau_{\text{pulse}}(a - b\Delta^2\tau_{\text{pulse}}^2). \tag{7.29}$$

We thus find that despite the complexity of the system and the interaction with phonons, we can describe the absorption probability of the chromophore system in the short pulse regime by only two parameters, Γ_{inc} and Δ.

One important implication of Eq. (7.29) is that a single photon with a delta function temporal profile does not interact with the system, since in the limit $\tau_{\text{pulse}} \to 0$, the quantity abs. prob. $= 0$. An analogous situation in atomic physics is that to make a π-pulse, the electric field E times the pulse duration τ times some constants must be equal to π (i.e., $E\tau \sim \pi$, or $E \sim \tau^{-1}$). The photon number, proportional to the energy, in a π-pulse is proportional to the electric field squared times pulse duration ($E^2\tau$), which is proportional to τ^{-1}. Therefore to make a π-pulse infinitely short in time requires an infinite number of photons. Hence, a single photon with a delta function temporal profile cannot interact with the system.

To test the validity of Eq. (7.29), we first consider a Gaussian pulse as in Eq. (7.8), and define $\tau_{\text{pulse}} = 1/\Omega$. Comparing Eq. (7.8) to Eq. (7.20), yields the scale-invariant pulse shape function

$$f(x) = \frac{1}{(2\pi)^{1/4}} e^{-x^2/4}, \tag{7.30}$$

from which we obtain (using Eq. (7.23))

$$A(y) = \sqrt{8\pi} e^{-2y^2}. \tag{7.31}$$

This results in parameter values $a = \sqrt{8\pi}$ and $b = 2\sqrt{8\pi}$ for the Taylor expansion coefficients of $A(y)$ in Eq. (7.24).

We can then evaluate the absorption probability for different systems, with and without phonons, and test Eq. (7.29) by plotting the scaled absorption probability, abs. prob./$\Gamma_{\text{inc}}\tau_{\text{pulse}}$, as a function of τ_{pulse} with the latter given in system-independent units of $1/\Delta$. For systems without phonons, Δ is computed directly using Eq. (7.27) by diagonalizing the system Hamiltonian and calculating the overlaps between the eigenstates and the bright state. For systems with coupling to phonons, Δ cannot be computed directly, and is obtained instead by fitting Eq. (7.29) to values of the scaled absorption probability.

To fit the energy spread parameter Δ numerically, we simulate the absorption dynamics with a 5-level HEOM in each calculation. The pulse is centered at time $t = 10\tau_{\text{pulse}}$. The absorption probability is taken as the total excitation probability at time $t = 20\tau_{\text{pulse}}$. We calculate data points for shorter and shorter pulses until the fitted Δ converges. Numerically, we find that the estimated variance of the fitted Δ decreases to some minimum value and then increases as the pulse shortens. We take the Δ value with the smallest estimated variance as the Δ for the system. As a check, applying this fitting procedure to numerical calculations for systems without phonons yields good agreement with the analytically calculated Δ. The resulting values of Δ for various different size systems with and without phonons are tabulated in table (7.1).

	monomer no phonon	monomer with phonon	dimer no phonon	dimer with phonon	7-mer no phonon	7-mer with phonon	14-mer no phonon
Δ (cm^{-1})	50	124.1	75.3	145.2	306.7	330.8	383.1
$1/\Delta$ (fs)	106.1	42.7	70.4	36.5	17.3	16.0	13.8

Table 7.1: Δ and $1/\Delta$ for various chromophore systems, with or without phonons. For systems without phonons, Δ was calculated directly using Eq. (7.27). In the monomer system without phonons, a 50 cm^{-1} detuning was introduced, so Δ is exactly equal to 50 cm^{-1}. For systems with phonons, Δ was obtained by numerically fitting to the scaled absorption probability obtained from numerical calculations with a 5-level HEOM at temperature $T = 300$ K.

Figure (7.6) plots the scaled absorption probability, namely abs. prob./$\Gamma_{\text{inc}}\tau_{\text{pulse}}$, as a function of τ_{pulse} in units of $1/\Delta$ for various systems, calculated with or without phonons. For short enough pulse durations ($\tau_{\text{pulse}} <\approx 0.15/\Delta$ in this case), it is evident that the numerically calculated absorption probabilities match Eq. (7.29) very well for all of the systems considered here. We note that for carrier frequencies similar to the excitation energies of chromophores, pulse durations τ_{pulse} as short as ≈ 33 fs have been produced experimentally [109, 129].

We further note that as the temperature of the initial phonon state increases, the effective energy spread parameter Δ also increases. The temperature dependence of Δ for the dimer system with phonons is shown in Fig. (7.7).

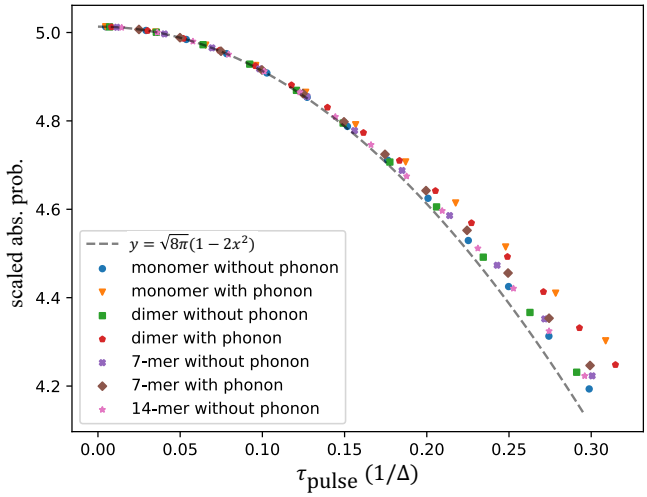

Figure 7.6: Scaled absorption probability (defined as abs. prob./$\Gamma_{\text{inc}}\tau_{\text{pulse}}$) plotted against τ_{pulse} for various systems under Gaussian pulses. τ_{pulse} is measured in system-dependent time units of $1/\Delta$. The values of $1/\Delta$ are tabulated in table (7.1). For short enough pulse duration, the absorption probability follows the analytical expression of Eq. (7.29), shown as the gray dashed line. For systems with phonons, the absorption probability was obtained from numerical calculations with a 5-level HEOM at temperature $T = 300$K. To reduce the runtime of the computations, the special HEOM terminator equations (Eq. (6.92)) were not used here.

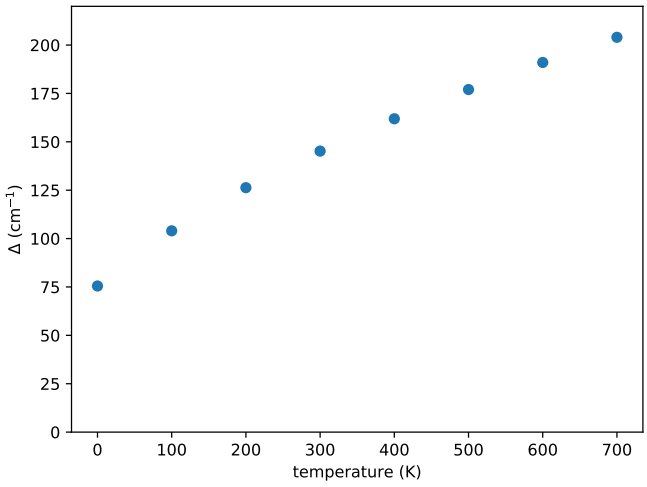

Figure 7.7: Temperature dependence of the effective energy spread parameter Δ for a dimer system.

Since Δ is independent of pulse shape, having measured it with one pulse form allows us to quantitatively understand the absorption probability under many other pulse shapes. For example, we previously measured $1/\Delta = 37.1$ fs for the dimer system with phonons under short Gaussian pulses. We can use this information to predict the absorption probability under short square pulses and short exponential pulses by inserting the corresponding expansion coefficients a and b. For example, consider the square pulse specified by

$$f(x) = \begin{cases} 1 & , |x| \leq 0.5 \\ 0 & , \text{otherwise} \end{cases} , \tag{7.32}$$

and the exponential pulse, specified by

$$f(x) = \begin{cases} e^{-x/2} & , x \geq 0 \\ 0 & , \text{otherwise} \end{cases} . \tag{7.33}$$

Eq. (7.24) gives the coefficients $a = 1$, $b = 1/12$ for square pulses, and $a = 4$, $b = 16$ for exponential pulses. Fig. (7.8) shows the short pulse absorption probabilities for these two pulse shapes. The absorption probabilities also follow the scaling relation of Eq. (7.29), using the same Δ parameter obtained from Table 7.1.

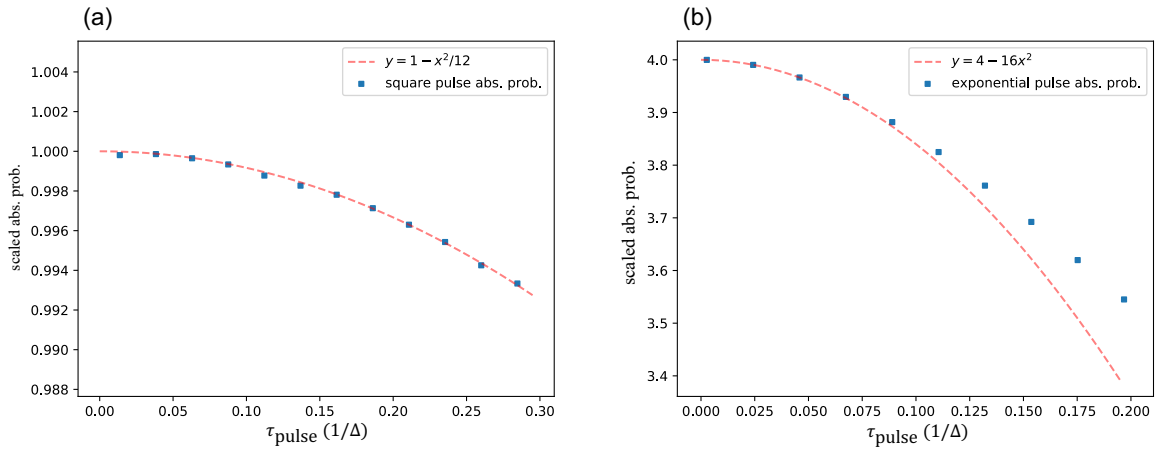

Figure 7.8: Scaled absorption probability as a function of pulse duration for (a) square pulses and (b) exponential pulses. Taking $1/\Delta = 37.1$ fs for the dimer system with phonons, as measured by Gaussian short pulses, we find good agreements between numerical results and analytical expressions.

7.2.4 Absorption Probability in the Long Pulse Regime

The long pulse regime is characterized by $\tau_{\text{sys+vib}} \ll \tau_{\text{pulse}} \ll \tau_{\text{emission}}$, where the pulse duration τ_{pulse} is much longer than the chromophore system and vibrational time scale $\tau_{\text{sys+vib}}$, but still much shorter than the emission time scale τ_{emission} so that spontaneous emission can be ignored. For many pulse shapes (e.g., Gaussian, square, exponential), $A(E\tau_{\text{pulse}})$ is a localized function peaked at $E\tau_{\text{pulse}} = 0$, and $\int dy\, A(y)$ is an $\mathcal{O}(1)$ constant. Therefore, for large τ_{pulse}, treating $A(E\tau_{\text{pulse}})$ as a function of E, we can set

$$A(E\tau_{\text{pulse}}) = \frac{k}{\tau_{\text{pulse}}} \delta_{\tau_{\text{pulse}}}(E), \tag{7.34}$$

where $k = \int dy\, A(y)$ is a pulse shape dependent $\mathcal{O}(1)$ constant and $\delta_{\tau_{\text{pulse}}}(E)$ is a sharply peaked function with width on the order of $\sim 1/\tau_{\text{pulse}}$. In the limit $\tau_{\text{pulse}} \to \infty$, $\delta_{\tau_{\text{pulse}}}(E)$ becomes a true

delta function $\delta(E)$. Substituting Eq. (7.34) into Eq. (7.21), we find

$$\text{long pulse abs. prob.}_{\text{no phonon}} = \Gamma_{\text{inc}} k \sum_n c_n \delta_{\tau_{\text{pulse}}}(E_n - E_0). \tag{7.35}$$

The physical explanation for the delta function is that long pulses have very small energy bandwidths, of order $\sim 1/\tau_{\text{pulse}}$, so the center frequency of the pulse needs to be resonant with an eigenenergy in order to have any significant absorption probability.

If an eigenenergy E_m is resonant with the pulse center frequency, the sum in the absorption probability expression (Eq. (7.21)) will be dominated by the resonant eigenstate, and we find that

$$\text{long pulse abs. prob.}_{\text{no phonon, resonant}} = \Gamma_{\text{inc}} \tau_{\text{pulse}} |\langle m|B_{\text{inc}}\rangle|^2 a, \tag{7.36}$$

where $a = A(0)$ is defined by Eq. (7.24). In this case, the absorption probability is proportional to the pulse duration τ_{pulse}, provided that $\tau_{\text{pulse}} \ll \tau_{\text{emission}}$ so that spontaneous emission can be ignored. If E_0 is not resonant with any eigenenergy, then the absorption probability is near zero in the long pulse regime due to the delta function in Eq. (7.35). Numerical verification of these results is presented below.

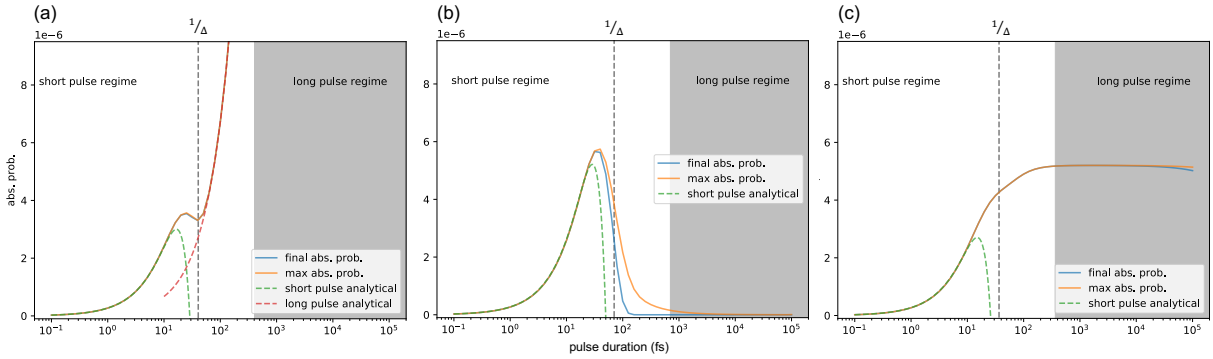

Figure 7.9: Dependence of absorption probability on pulse duration for a dimer system (a) without phonons and with pulse center frequency resonant with the upper eigenenergy (b) without phonons and with an off-resonant pulse center frequency in the middle of the two eigenenergies (c) with phonons and with an off-resonant pulse center frequency in the middle of the two eigenenergies.

Figure (7.9) shows the absorption probabilities for a dimer system under a Gaussian pulse in three different scenarios, in each case as a function of pulse duration over a range of six orders of magnitude. The Gaussian temporal profile is centered at $10\,\tau_{\text{pulse}}$,. Two types of absorption probabilities are measured. The first is the final absorption probability, which is defined as the absorption probability at $20\,\tau_{\text{pulse}}$. The second is the maximum absorption probability, defined as the maximum probability during the time interval $t = 0$ to $t = 20\,\tau_{\text{pulse}}$. We identify the characteristic system or system+vibration timescale $\tau_{\text{sys+vib}}$ as $1/\Delta$, indicated on the plots by dashed vertical lines. The short and long pulse regimes are identified by $\tau_{\text{pulse}} < 0.1/\Delta$ and $\tau_{\text{pulse}} > 10/\Delta$, respectively.

In Figure (7.9a), there is no coupling to phonons and the pulse center frequency is set to be resonant to the higher eigenenergy of the 2×2 dimer Hamiltonian. The effective energy spread parameter $\Delta = 130.8\,\text{cm}^{-1}$ (see Eq. (7.27)) corresponds to a characteristic time scale of $1/\Delta = 40.6$ fs. In the long pulse regime, the absorption probability follows the linear relationship given by Eq. (7.36) up to $\tau_{\text{pulse}} = 10^5$ fs. The long pulse absorption probability is not shown due to the small scale of the absorption probability.

Figure (7.9b) considers the same dimer system without phonons, but with the pulse center frequency set to be off-resonant at the average of the two non-degenerate eigenenergies (or equivalently, the average of the site energies). The effective energy spread parameter $\Delta = 75.3\,\mathrm{cm}^{-1}$, and $1/\Delta = 70.4$ fs. Consistent with our analysis, the final absorption probabilities in the long pulse regime are very close to zero and are smaller than the numerical accuracy of the numerical integrator. The maximum absorption probability drops to zero more slowly than the final absorption probability.

In the presence of phonons, substituting Eq. (7.34) into Eq. (7.22), we find

$$\text{long pulse abs. prob.}_{\text{thermal phonon}} = \Gamma_{\text{inc}} k \sum_{\widetilde{n},v} \widetilde{c}_{n,v} \delta_{\tau_{\text{pulse}}}(\widetilde{E}_n - E_v - E_0), \tag{7.37}$$

where $\widetilde{c}_{n,v}$ are the thermally weighted vibronic overlap with bright state, Eq. (7.18). The absorption probability is non-zero if the sum of a vibrational energy E_v and the pulse center frequency E_0 is equal to some eigenenergy $\widetilde{E}_n$ of $H_{\text{sys+vib}}$ (Eq. (6.59)). If the vibrational states are dense enough that the spacings between the vibronic energy levels are much less than $1/\tau_{\text{pulse}}$, the width of $\delta_{\tau_{\text{pulse}}}(E)$, we may treat the vibrational energies as a continuum. Defining a coarse-grained version of the bright state overlap function $\widetilde{c}_{n,v}$,

$$\widetilde{c}(\widetilde{E}_n, E_v) = \sum_{\widetilde{n}',v'} c_{n',v'} \delta(\widetilde{E}_n - \widetilde{E}_{n'}) \delta(E_v - E_{v'}) \tag{7.38}$$

and writing the sums as integrals

$$\sum_{\widetilde{n},v} \widetilde{c}_{n,v} \to \int d\widetilde{E}_n dE_v\, \widetilde{c}(\widetilde{E}_n, E_v), \tag{7.39}$$

Eq. (7.37) becomes

$$\text{long pulse abs. prob.}_{\text{thermal phonon}} = \Gamma_{\text{inc}} k \int d\widetilde{E}_n dE_v\, \widetilde{c}(\widetilde{E}_n, E_v) \delta_{\tau_{\text{pulse}}}(\widetilde{E}_n - E_v - E_0). \tag{7.40}$$

If the vibrational states are dense enough, it is reasonable to assume that $\widetilde{c}(\widetilde{E}_n, E_v)$ varies slowly on the scale of $1/\tau_{\text{pulse}}$, the width of $\delta_{\tau_{\text{pulse}}}(E)$, since we are in the regime $\tau_{\text{sys+vib}} \ll \tau_{\text{pulse}}$. Hence Eq. (7.40) can be well-approximated by replacing $\delta_{\tau_{\text{pulse}}}(\widetilde{E}_n - E_v - E_0)$ with a true delta function $\delta(\widetilde{E}_n - E_v - E_0)$, and hence

$$\text{long pulse abs. prob.}_{\text{thermal phonon}} = \Gamma_{\text{inc}} k \int dE_v\, \widetilde{c}(\widetilde{E}_n = E_v + E_0, E_v). \tag{7.41}$$

This shows that in the long pulse regime, when the system is coupled to a dense spectrum of phonons, the absorption probability is independent of pulse duration.

An alternative derivation of the long pulse absorption probability with phonons, presented in appendix J, shows that when τ_{pulse} is much longer than the time required for the system to reach a steady state due to phonon interactions, we have

$$\text{long pulse abs. prob.}_{\text{thermal phonon}} \sim \frac{\Gamma_{\text{inc}} \tau_{\text{steady}}}{N}, \tag{7.42}$$

where $\sim$ means on the order of, N is the number of chromophores and τ_{steady} is the time scale for the system to approach steady state. Note that this expression does not imply that the absorption probability is inversely proportional to N, since Γ_{inc} generally increases as N increases (see Eq. (6.12)).

Figure (7.9c) shows the absorption probability for the dimer system with phonons (calculated with 5 HEOM levels). The pulse center frequency is chosen to be the average of the two system

eigenenergies. Since the coupling to phonons broadens the frequency that the system can interact with, having the pulse center frequency equal to one of the eigenenergies will not result in any qualitative difference. For this example the effective energy spread parameter $\Delta = 145.2\,\mathrm{cm}^{-1}$, and $1/\Delta = 36.5$ fs (see table (7.1)). Consistent with our analysis, the absorption probability in the long pulse regime is quite independent of τ_{pulse} until very large τ_{pulse} values, when emission effects become significant. If we simply take τ_{steady} in Eq. (7.42) to be $1/\gamma$, where γ is the HEOM parameter characterizing the phonon dephasing rate, then the order of magnitude estimate $\Gamma_{\mathrm{inc}}\tau_{\mathrm{steady}}/2 \approx 5 \times 10^{-6}$ is also consistent with the numerical result.

To understand the general behavior of the coarse grained bright state overlap function $\widetilde{c}(\widetilde{E}_n, E_v)$, we plot this in Figure (7.10) for a model dimer system where each chromophore is coupled to two discrete vibrational modes. The total Hamiltonian is

$$H = H_{\mathrm{sys}} + H_{\mathrm{vib}} + \kappa \sum_{j=1,2} \sum_{k=1,2} \alpha_{jk} |j\rangle\langle j| (b_{jk} + b_{jk}^{\dagger}), \tag{7.43}$$

with H_{sys} expressed in the site basis as

$$H_{\mathrm{sys}} = \sum_{j=1,2} \epsilon_j |j\rangle\langle j| + J(|1\rangle\langle 2| + |2\rangle\langle 1|), \tag{7.44}$$

and

$$H_{\mathrm{vib}} = \sum_{j=1,2} \sum_{k=1,2} \omega_{jk} b_{jk}^{\dagger} b_{jk}, \tag{7.45}$$

with b_{jk} the annihilation operator for the k-th vibrational mode coupled to site j. The numerical values for the parameters in Eqs. (7.43)-(7.45) are listed in Appendix K. The parameter κ sets the overall coupling strength between the excitonic system and the vibrations. Figure (7.10) shows the discretized bright state overlap function $\widetilde{c}(\widetilde{E}_n, E_v)$ for system-vibration coupling values $\kappa = 0$, 0.1, and 1. When there is no system-vibration coupling ($\kappa = 0$), the vibronic energy is simply the sum of the system energy and the vibrational energy, i.e., $\widetilde{E}_n = E_n + E_v$. On the other hand, Eq. (7.41) requires that $\int dE_v\, \widetilde{c}(\widetilde{E}_n = E_0 + E_v, E_v)$ be non-zero for there to be a finite absorption probability. Therefore the pulse center frequency E_0 has to be equal to a system eigenenergy E_n in order to have nonzero absorption probability. The two sharp diagonal peaks in panel (a) correspond to the lines $\widetilde{E}_n = E_n + E_v$ for each of the two system energies E_n, indicating that for long pulses, the absorption probability is nonzero only when the pulse frequency is equal to one of the two system energies E_n. As the system-vibration coupling increases, the peaks broaden and their heights decrease, indicating that the pulse center frequency no longer has to be exactly equal to the system energies E_n for there to be nonzero absorption probability and consequently the resonant absorption probability at $E_0 = E_n$ decreases.

7.3 Analysis of emission

In the analytical studies of the previous section we have ignored the effect of spontaneous emission at long times. We now make use of the separation of time scales between the sys+vib dynamics and the spontaneous emission to analyze the long time emission behavior.

7.3.1 Uniform exponential decay of excited states in the presence of phonons

The HEOM reaches a steady state on the time scale of $\tau_{\mathrm{steady}} \sim 100$ fs, which is much shorter than the spontaneous emission time scale $\tau_{\mathrm{emission}} \sim 10$ ns. Therefore at a sufficiently long time after the pulse has passed, specfically, when $t - \tau_{\mathrm{pulse}} \gg \tau_{\mathrm{steady}}$, the chromophore system should reach a quasi-steady state with respect to the phonon bath that decays slowly to the ground state due to spontaneous

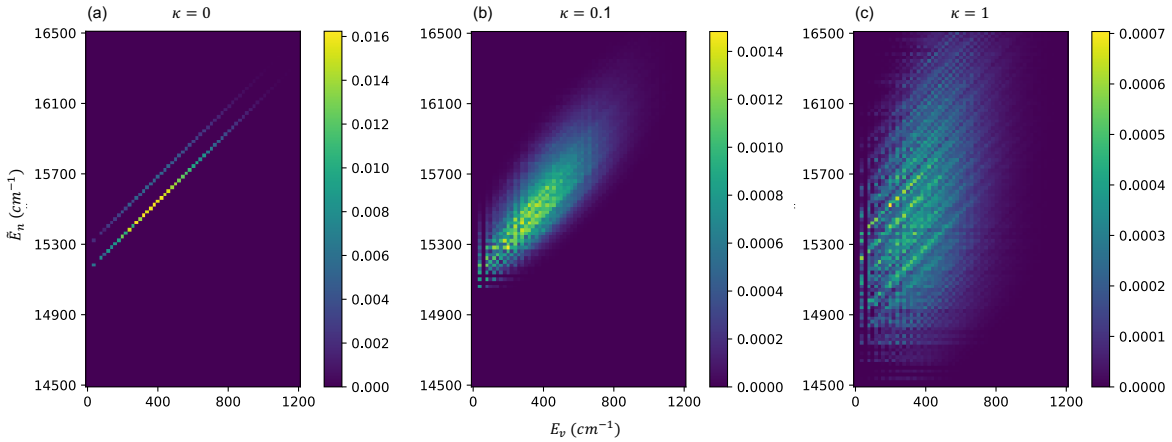

Figure 7.10: $\widetilde{c}(\widetilde{E}_n, E_v)$ for a dimer system coupled to 4 vibrational modes (2 on each chromophore). Plots (a)-(c) correspond to the exciton-phonon coupling strengths $\kappa = 0$, 0.1, and 1, respectively. At $\kappa = 0$, the two sharp diagonal peaks indicate that for long pulses, only two frequencies give rise to significant absorption probability. As κ increases, the diagonal peaks broaden, and the pulse frequency does not have to be exactly resonant to the system eigenenergy for there to be significant absorption probability.

emission. (By quasi-steady state we mean that the chromophore system is in steady state with regard to the phonon bath, but not yet with regard to the photon bath.) We claim that under an N-photon Fock state input, the long time system state takes the form

$$\rho(t) = |g\rangle\langle g| + be^{-\Gamma_{\text{long time}}t}\big(\rho_{\text{st}} - |g\rangle\langle g| + \mathcal{O}(\epsilon)\big), \tag{7.46}$$

where the decay rate $\Gamma_{\text{long time}}$ is given by

$$\Gamma_{\text{long time}} = (1 + \mathcal{O}(\epsilon)) \sum_l \text{Tr}(L_l^\dagger L_l \rho_{\text{st}}). \tag{7.47}$$

Here ρ_{st} is the normalized HEOM steady state in the excited subspace, $\epsilon \sim \tau_{\text{sys+vib}}/\tau_{\text{emission}}$ is a small parameter, and b is a constant to be determined. A detailed derivation of Eqs. (7.46) and (7.47) is provided in Appendix L. These equations show that in the quasi-steady state the excited part of the system decays to the ground state following a single exponential whose decay rate is equal to the total emission rate (see Eq. (6.50)).

The constant b has some arbitrariness in it, in the sense that b depends on where the time $t = 0$ is defined. However, once we fix the $t = 0$ point in time, we can determine the constant b numerically by first integrating $\rho(t)$ to some final time t_f that is sufficiently long enough for the system to reach a quasi-steady state. According to Eq. (7.46), the total excitation probability to the lowest order is then given by $b\exp(-\Gamma_{\text{long time}}t_f)$. Therefore we take

$$b = (\text{total excitation prob. at } t_f)e^{\Gamma_{\text{long time}}t_f}. \tag{7.48}$$

The normalized steady state ρ_{st} in Eqs. (7.46) and (7.47) can be evaluated independently of the Fock state hierarchy by propagating the HEOM with an initial state in the excited subspace to long enough time.

This long time behavior implies that we only need to solve the Fock state + HEOM equations (Eqs. (6.137) - (6.138)) numerically until the system reaches the quasi-steady state with respect with

the phonons. This happens within several mulitples of τ_{steady} after the pulse has passed. From this point onwards, the system will behave according to Eq. (7.46), with the total emission rate given by Eq.(7.47).

Figure (7.11) shows the excitation probabilities for each chromophore site on a log scale as a function of time for a dimer system. The difference between the density matrix values obtained from numerical integration of the double hierarchy of equations, Eq. (6.138), and those obtained from the lowest order long time analytical expression is quantified by the Euclidean distance

$$||\rho_{\text{num}} - \rho_{\text{ana}}|| = \sqrt{\sum_{i,j} |(\rho_{\text{num}})_{ij} - (\rho_{\text{ana}})_{ij}|^2}, \tag{7.49}$$

and is plotted in Figure (7.11). Note that we have increased the reference value of spontaneous emission rate Γ_0 by a factor of 1000 over the physically relevant value in order to see the spontaneous emission within a reasonable amount of numerical integration time. Figure (7.11) shows that in the quasi-steady state after $\sim$ 4 ps, the numerical difference $||\rho_{\text{num}} - \rho_{\text{ana}}|| \sim 10^{-5}$ is about 2 orders of magnitude smaller than the absorption probability ($\sim 10^{-3}$), indicating good convergence. Comparing the $\sim 10^{-3}$ probabilities with Eq. (7.46) indicates that for this system $b \sim 10^{-3}$ and the small parameter $\epsilon \sim 10^{-2}$. The numerically fitted value of $\Gamma_{\text{long time}}$ (2.678×10^{-2} ps, fitted from 8 to 10 ps) is in similarly good agreement with the value $\Gamma_{\text{long time}}$ (2.685×10^{-2} ps^{-1}) obtained from Eq. (7.47), with a relative difference on the order of $\epsilon \sim 10^{-2}$, in accordance with Eq. (7.47). (Note that if we had not increased Γ_0 1000 times, ϵ would be on the order of 10^{-5}, making the analytical expression even more accurate.)

7.3.2 Collective vs Independent Emission

After the incoming pulse has passed, the total emission rate of the chromophoric system is

$$R_{\text{coll}} = \sum_{l \in \{x,y,z\}} \text{Tr}(L_l^\dagger L_l \rho) = \Gamma_0 \sum_{j,k} \mathbf{d}_j^* \cdot \mathbf{d}_k \langle j|\rho|k\rangle, \tag{7.50}$$

(see Eq. (6.50)), where

$$L_x = \sqrt{\Gamma_0} \sum_j \mathbf{d}_j^* \cdot \hat{x} |g\rangle\langle j| \tag{7.51}$$

and similarly for L_y and L_z (see Eq. (6.10)). As mentioned in Section 6.2.2, Γ_0 is the unit spontaneous emission rate and $\mathbf{d}_j$ the unitless transition dipole moment of site j. The x, y, or z-polarized component of the field couples the ground state to a collective bright state $\sum_j \mathbf{d}_j \cdot \hat{x}_l |j\rangle$. Eqs. (7.50) and (7.51) constitute the correct description of emission, which is intrinsically collective [83–85].

It is sometimes assumed that the chromophores spontaneously emit independently of one another [59]. In this case, the total emission rate would be given by

$$R_{\text{indep}} = \sum_{j=1}^{N} \text{Tr}(L_j^\dagger L_j \rho) = \sum_{j=1}^{N} \Gamma_0 |\mathbf{d}_j|^2 \langle j|\rho|j\rangle, \tag{7.52}$$

with

$$L_j = \sqrt{\Gamma_0} |\mathbf{d}_j| \, |g\rangle\langle j|. \tag{7.53}$$

Here $\Gamma_0 |\mathbf{d}_j|^2$ is the spontaneous emission rate of chromophore j. We refer to the spontaneous emission described by Eqs. (7.52) - (7.53) as independent emission.

The difference between collective and independent emission rates

$$R_{\text{coll}} - R_{\text{indep}} = \Gamma_0 \sum_{j \neq k} \mathbf{d}_j^* \cdot \mathbf{d}_k \langle j|\rho|k\rangle, \tag{7.54}$$

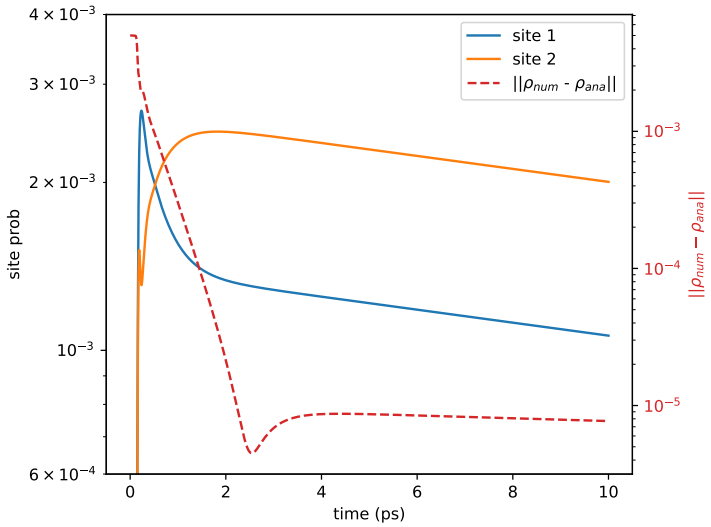

Figure 7.11: Double hierarchy calculations of the absorption probability for a selected dimer system in LHCII as a function of time. Solid blue and red lines (using the left axis) show excitation probabilities on chromophore sites 1 and 2, respectively, in a log scale as a function of time. The dashed line shows the difference (measured by the Euclidean distance, scale on the right axis) between the numerical density matrix obtained by integrating the double hierarchy of Eq. (6.138) and the lowest order analytical expression of Eq. (7.46). For these calculations the value of Γ_0 was increased by 1000 relative to the physical value in order to see emission in a reasonable amount of numerical integration time. The quasi-steady state $\rho_{\rm st}$ is found by propagating the HEOM with initial condition $\rho(0) = |1\rangle\langle 1|$ up to 20 ps, at which time each element of the density matrix remains constant up to 12 digits after the decimal point.

derives from the coherence between different excited states, i.e., from the off-diagonal terms in the density matrix, as well as from the non-orthogonality of the different transition dipoles. In an idealized system where all individual chromophores have the same emission rates Γ, then $R_{\text{indep}} = \Gamma$, but R_{coll} can vary between 0 and $N\Gamma$, depending on the dipole orientations and the extent of excitonic coherence between chromophores.

The long time emission behavior is dominated by the HEOM steady state ρ_{st} (see Eq. (7.46)). Therefore to observe the difference between collective and independent emission at long times, we need only to substitute ρ_{st} into Eqs. (7.50), (7.52), and (7.54). Since $\rho_{\text{st}} \propto \text{Tr}_{\text{vib}}(e^{-\beta H_{\text{sys+vib}}})$ [130], we find that $\rho_{\text{st}} \propto e^{-\beta H_{\text{sys}}}$ to the lowest order of the system-vibration coupling. Figure (7.12))

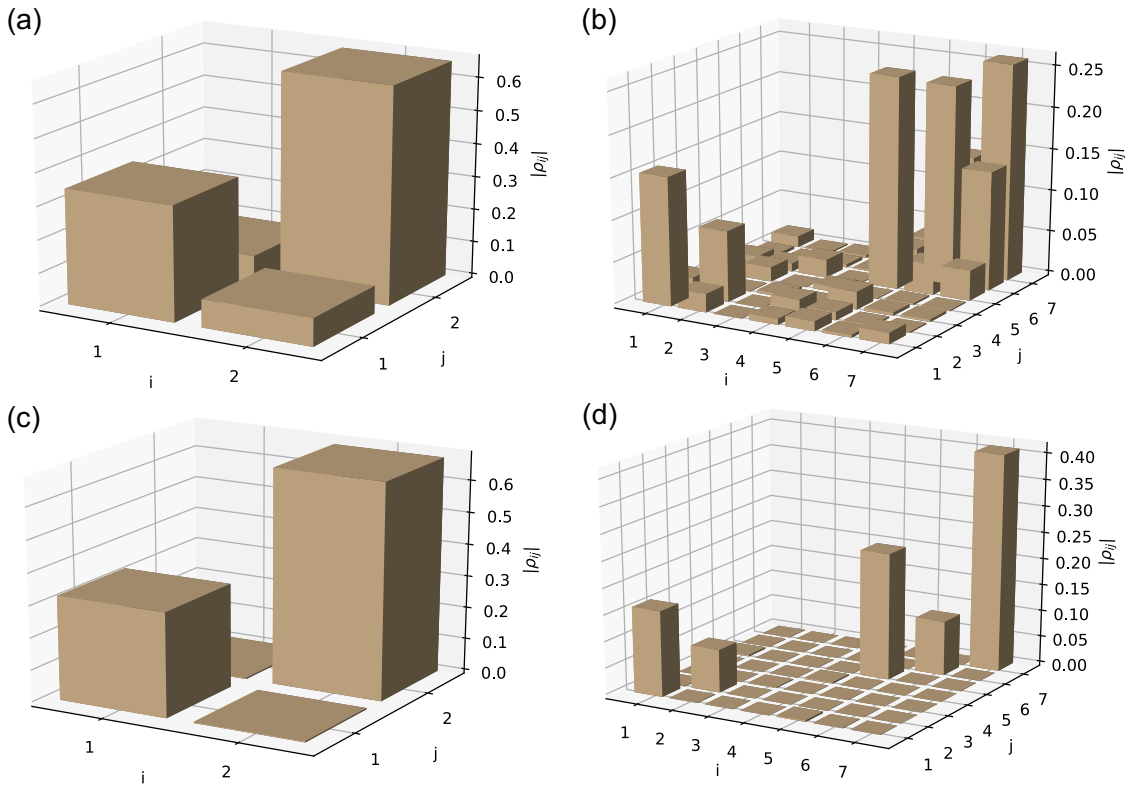

Figure 7.12: Magnitudes of matrix elements of the HEOM steady state density matrix ρ_{st} for a dimer and a 7-mer of chromophores in LHCII. (a), (b): dimer and 7-mer system, respectively, in the site basis. (c), (d): dimer and 7-mer system system, respectively on the energy basis. In the energy eigenbasis, the steady state is almost diagonal. In the site basis, coherences between different sites are present but they are generally smaller than the population terms, consistent with weakly delocalized (Frenkel) excitons.

shows the result of numerical calculations of the HEOM steady state for a selected dimer and an 7-mer system in LHCII. These show that ρ_{st} is close to being diagonal in the energy eigenbasis, and that in the site basis, the off-diagonal coherence terms are generally smaller than the diagonal population terms. This behavior is consistent with the Frenkel character of excitons in LHCII, which show delocalization over a small number of sites (2-3). Due to the random orientation of the dipoles and the smallness of the coherence between different sites, there is only a modest difference between collective and independent emission rates. In our LHCII examples, the dimer system has $R_{\text{indep}} =$

$3.23 \times 10^{-2}\,\mathrm{ns}^{-1}$ and $R_{\mathrm{coll}} = 3.59 \times 10^{-2}\,\mathrm{ns}^{-1}$; the 7-mer system has $R_{\mathrm{indep}} = 3.28 \times 10^{-2}\,\mathrm{ns}^{-1}$ and $R_{\mathrm{coll}} = 4.54 \times 10^{-2}\,\mathrm{ns}^{-1}$. These small differences are consistent with experimental results for LHCII trimers that show very little enhancement due to collective emission [131]. In contrast, bacterial LHI and LHII complexes, which have relatively ordered structures and dipole orientations, exhibit collective emission with enhancement factors of 3-4 over independent emission [132], while bacterial chlorosomes show less enhancement than might be expected from their initial delocalization lengths [133–135] because of exciton relaxation and dynamical disorder [136].

7.4 Double hierarchy solutions for LHCII with calculation of photon fluxes

In this Section we present a numerical solution of the double hierarchy for the Fock state + HEOM master equations (Eq. (6.138)) for an LHCII monomer (14-mer) system. The incoming pulse has a Gaussian temporal profile

$$\xi(t) = \Big(\frac{\Omega^2}{2\pi}\Big)^{1/4} e^{-\Omega^2(t-t_0)^2/4}, \tag{7.55}$$

where Ω is the frequency bandwidth, here chosen to be the standard deviation of the site energies ($\Omega \approx (17.7\,\mathrm{fs})^{-1}$ or $299\,\mathrm{cm}^{-1}$). t_0 is the time of the center of the pulse, chosen to be late enough in time (150 fs) that no appreciable tail of the Gaussian pulse is present before $t = 0$. The center frequency is set to be the average site energy ($\omega_0 \approx$15445 cm^{-1}) (see Figure (7.13)). An experimentally reasonable value for the incoming paraxial beam geometric factor is $\eta = 0.11$. In order to maximize the total absorption probability, the incoming field polarization was chosen to be the singular vector of the dipole matrix $\mathbf{D}$ with the largest singular value (see Appendix M). We set this singular vector to point along the +z-axis, which is found to lie approximately in the plane of the thylakoid membrane separating the stroma and lumen of a thylakoid disc (see Figure (7.13)). The other two orthogonal singular vectors are set to point along the x- and y-axes. 5 HEOM levels were included in the calculation. To check the error due to truncating the HEOM levels, we also performed the calculation with 4 HEOM levels and compare the results below. For any time-dependent quantity $f_n(t)$ obtained from n-level HEOM calculations, we determine an estimated error bar $f_n(t) \pm \mathrm{err}(t)$, where $\mathrm{err}(t)$ is the moving average of $|f_n(t) - f_{n-1}(t)|$ in the $t \pm 20\,\mathrm{fs}$ window.

Figure (7.14) shows the calculated site probabilities as functions of time. The site probabilities rise initially as the incoming pulse passes. These show oscillations over the following few hundreds of fs, due to the excitonic dipole-dipole couplings and to the interaction with phonons, as discussed in many recent studies [49, 69]. At later times the system slowly approaches a quasi-steady state due to the dephasing interaction with phonons. This is not a true steady state because the excited state site probabilities decay over the ns spontaneous emission time scale (see Section 7.3). In the absence of exciton-phonon interactions, the site probabilities will continue to oscillate due to excitonic coherence until the ns time scale spontaneous emission removes the excitation.

Figure (7.15) now shows the total excitation probability, defined as the sum of all local excitation probabilities on individual sites. Following an initial rise over the duration of the pulse, this remains nearly constant at around 4×10^{-7} after the pulse has passed over the time scale of 1 ps. The extremely low absorption probability is due to the exceedingly small magnitude of the system-light coupling $L_{\mathrm{inc}} = \sqrt{\Gamma_{\mathrm{inc}}}|g\rangle\langle B_{\mathrm{inc}}|$. This is a generic feature of natural light harvesting systems [59] which can also be related to the exceedingly slow rate of spontaneous emission (cf. Eq. (6.50)) relative to the system and system-phonon time scales.

Since the pulse bandwidth was taken here to be the same as the standard deviation of the site energies (Figure 7.13(c)), the pulse is neither in the short nor long pulse regime. However, if we apply the long pulse result that the absorption probability is on the order of $\Gamma_{\mathrm{inc}}\tau_{\mathrm{steady}}/N$ (see Eq. (7.42)),

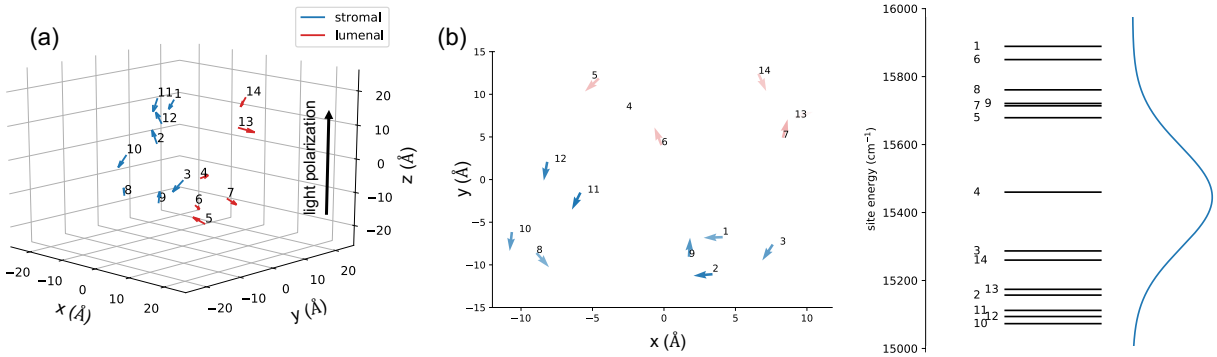

Figure 7.13: Transition dipole moments and excitonic energy levels of LHCII. (a) Relative positions and transition dipole moments of the 14 chlorophylls in a LHCII monomer. Blue arrows refer to chlorophylls on the stromal side, red arrows to chlorophylls on the lumenal side. The coordinate system is defined by the singular vector basis of the dipole matrix $\mathbf{D}$. With this convention, the z axis lies approximately in the plane separating the stroma and lumen, and polarization along z is found to maximize the total absorption probability. (b) LHCII chlorophyll transition dipole moments projected into the x-y plane. The intensity of the color of each arrow indicates the extent of overlap between the bright state and the chlorophyll at that site (i.e., $|\langle j|B_{\text{inc}}\rangle|^2$), which is proportional to the square of the z-component of the dipole momen, $|\mathbf{d}_j \cdot \hat{z}|^2$). (c) Site energies of the 14 chlorophylls in a LHCII monomer. The blue curve on the right represents the frequency distribution ($\omega_0 + |\int dt\, \xi(t) e^{i\omega t}|^2$) of the Gaussian single photon pulse.

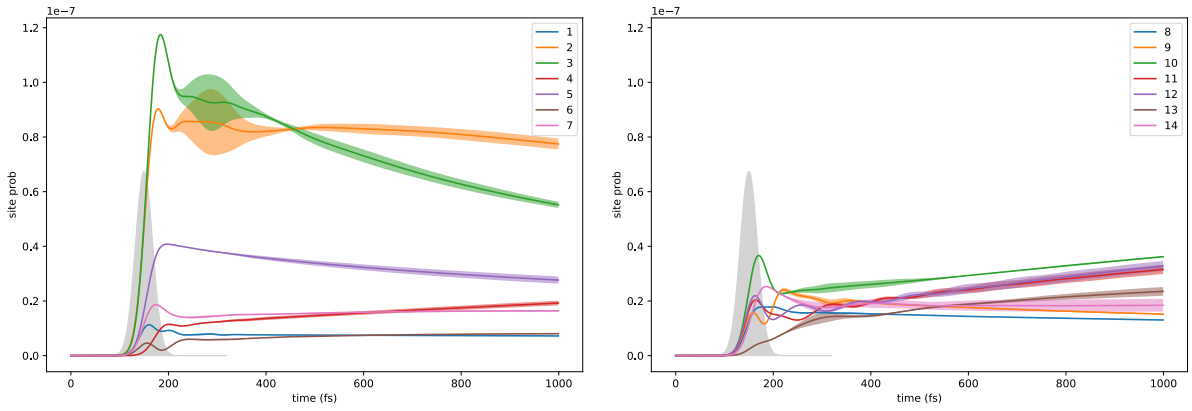

Figure 7.14: Numerical calculations of the absorption dynamics and subsequent excitonic energy transport for the LHCII monomer, a 14-mer system, using the double hierarchy for the Fock state + HEOM master equation. The 14 site probabilities as functions of time are plotted. The error due to finite HEOM levels are indicated by the colored regions around the solid lines. Gray region represent the Gaussian temporal profile squared $|\xi(t)|^2$ (see Eq. (7.8)), which has the normalization $\int |\xi(t)|^2 dt = 1$.

and taking for simplicity $\tau_{\text{steady}} = 1/\gamma \approx 150\,\text{fs}$, we arrive at an absorption probability on the order of $\sim 3 \times 10^{-7}$, consistent with the numerically observed absorption probability even though we are in the intermediate pulse regime.

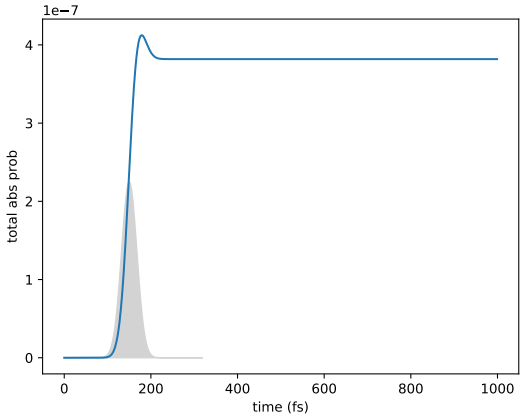

Figure 7.15: Total absorption probability for LHCII on interaction with a single Fock state photon pulse, defined as the sum over all excitation probabilities for individual sites, plotted as a function of time. The HEOM error bar here (estimated from the difference between calculations with 4 and 5 levels of the HEOM hierarchy) is smaller than the width of the curve. After the pulse, the total absorption probability remains nearly constant at around 4×10^{-7} and will decay very slowly to zero on a ns time scale due to spontaneous emission.

To analyze the change in photon flux due to absorption and emission by LHCII, the photon fluxes are partitioned into four channels. These are (1) the incoming paraxial channel, z-polarized, with a geometric factor of $\eta = 0.11$ (corresponding to a detection area of 7.3 % of the 4π solid angle, see discussion above Eq. (6.10)), (2) all other z-polarized light not captured by the incoming channel. (3) all x-polarized light, and (4) all y-polarized light. The system-light coupling operator L_l for each channel is given by Eq. (6.10), where the incoming channel has a geometric factor $\eta = 0.11$, the other z-polarized mode has $\eta = 1 - 0.11 = 0.89$, and the x- and y-polarized channels have $\eta = 1$. The photon fluxes in all four of these channels are plotted as functions of time (see Eq. (6.50)) in Figure (7.16). Due to the very small system-light coupling, most of the amplitude of the incoming single photon pulse does not excite the system and appears as outgoing flux in the incoming channel (see Figure (7.16)). The fluxes in the other channels, as well as that in the incoming channel after the pulse has passed, are on the order of s^{-1}, around 13 orders of magnitude smaller than the incoming flux before the pulse has passed the LHCII. The very small value of these fluxes after incidence of the single photon is due to the combined effects of the low, $\sim 10^{-7}$, total excitation probability, the weak emission rate, $\Gamma \sim (10\,\text{ns})^{-1}$, and the limited overlap between the system state and the bright state of each channel.

7.5 Conclusion

In Part II, we have combined an input-output formalism for optical fields with the HEOM formalism for phonon baths to study the excitonic dynamics of photosynthetic light harvesting systems interacting with N-photon Fock state pulses under the influence of coupled phonon degrees of freedom. This combined formalism results in a double hierarchy of equations of motion that need to be solved to obtain the excitonic density matrix. We demonstrated the numerical use of this double hierarchy

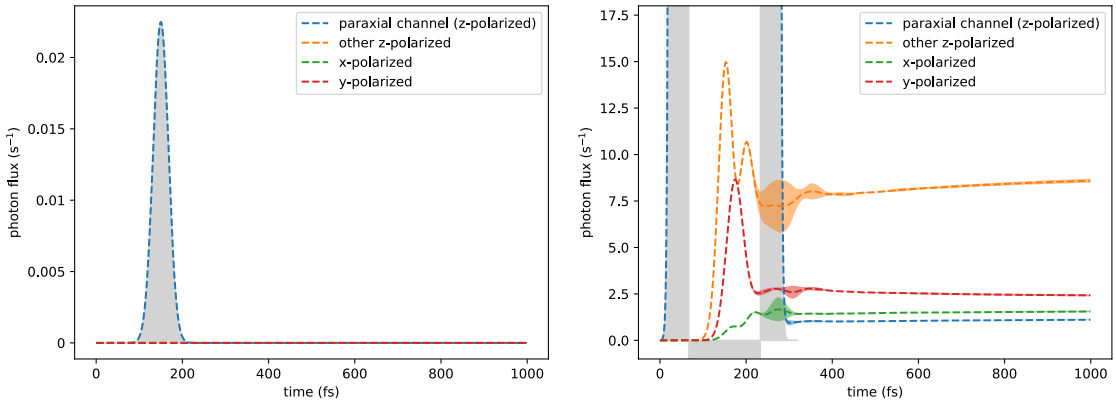

Figure 7.16: Outgoing photon flux in four different channels following excitation of LHCII by a single photon Fock state pulse. Left panel: Due to the small value of the chromophore system-light interaction, the input photon temporal profile squared $|\xi(t)|^2$ (gray region) closely overlaps with the flux in the paraxial channel (blue dashed line) Right: Zooming in on the photon flux by about 12 orders of magnitude. Notice that the photon flux is now measured in s^{-1} instead of fs^{-1}. The small difference between the input photon temporal profile and the outgoing flux in the paraxial channel is now evident.

for single photon absorption and excitonic energy transfer by the LHCII light harvesting complex, possessing 14 chlorophyll chromophores. Under the condition that the system-light coupling is very weak, as for natural light harvesting systems, we developed a number of useful analytic results that can also be applied to larger systems. These include (1) the dependence of the absorption probability on light polarization, dipole orientation, and pulse duration in the limits of short and long pulses, (2) the time evolution of the chromophore system at long times due to spontaneous emission, and (3) the close relationship between the dynamics under Fock state pulses and under coherent state pulses.

To study the absorption behavior, by neglecting the long time spontaneous emission, we could derive expressions for the system state and consequently for the absorption probability. Expressing the temporal profile of the pulse in a scaling form, we were then able to analyze the dependence of absorption probability on pulse duration. In the short pulse regime, by defining a system-dependent energy spread parameter Δ that characterizes the system+vibration time scale ($\tau_{\text{sys+vib}} \sim 1/\Delta$), we found a universal behavior for the absorption probability across all chromophoric systems up to at least the 14 chromophore LHCII system, as well as for different pulse shapes. In the long pulse regime, the absorption probability no longer shows universal behavior and needs to be treated in a case-by-case basis. Taking a chromophore dimer system as an example, we analyzed the different single photon long pulse absorption behavior in three different cases: resonant absorption without phonon coupling, off-resonant absorption without phonon coupling, and off-resonant absorption with phonon coupling. In particular, when phonon coupling is present, the long pulse absorption probability becomes independent of the pulse duration.

To study the chromophore system states at long times, we used the fact that the HEOM has a steady state to show that the chromophore system possesses a quasi-steady state, where it reaches a steady state with respect to the phonon bath but has not reached a steady state with respect to the photon bath due to the slow spontaneous emission. This enabled us to understand the chromophore system dynamics in the ps to ns timescale, where numerical integration of the double hierarchy becomes expensive. Furthermore, we used this result to analyze the difference between independent and collective emission as a function of the degree of orientational order and of excitonic coherence.

We found that for subsystems of LHCII the difference between collective and independent emission is small, implying no significant collective effects, consistent with experimental results for LHCII trimers [131] and expectations based on the non-uniform dipole orientations and the weak extent of coherence between different sites in the excitonic states for LHCII.

An important outcome of this work is the implication of the comparison of the light absorption by photosynthetic systems under excitation by Fock states of light with excitation by coherent states of light. For weak system-field couplings $N\Gamma_{\rm inc}\tau_{\rm pulse} \ll 1$ (meaning small photon numbers N, weak field-chromophore complex coupling constants $\Gamma_{\rm inc}$, and short pulse durations $\tau_{\rm pulse}$), we showed that excitation by a coherent state yields the same excited state density matrix, i.e., both populations and coherences, as does excitation by a Fock state with the same temporal profile and average photon number. This implies that simulating the excitonic dynamics under a short coherent state pulse with an average of N photons, then setting the coherence between ground and excited states to be zero gives an operationally equivalent simulation of the excitonic dynamics under an N-photon Fock state excitation. This equivalence holds both with or without phonons. Using physically relevant values of parameters, we showed this equivalence numerically for $N = 1$ and $N = 20$ photons.

This equivalence result and the analysis of absorption probabilities in the limits of short and long pulses reveal a useful complementarity between coherent state and Fock state studies. For N-photon Fock state studies, coherent states can be used to numerically simulate the more computationally expensive Fock state calculations. On the other hand, the excitation number-conserving property of single photon Fock states has provided us with clues to solve the N-photon Fock state master equations analytically in the physically relevant weak coupling limit. This analytical understanding of the absorption probability applies not only to N-photon Fock states, but also to coherent states due to the equivalence in the weak coupling limit. We see that analysis of both Fock and coherent state excitation is valuable for understanding the dynamics of light absorption by light harvesting systems in the weak coupling regime that is relevant to natural photosynthesis in vivo.

Finally, we note that the analysis in this work applies to the average state dynamics, relevant to an ensemble of light harvesting systems and an ensemble of experiments with single photons, in which only the output flux of photons is measured. For consideration of individual experiments with detection of single emitted photons, we can apply a quantum trajectory picture, as described in Ref. [53], and obtain additional information about the dynamics of the light harvesting system conditioned upon observation of individual fluorescent photons. In this interesting situation an incident single photon Fock state and an incident coherent state with an average of one photon no longer give equivalent results [53].

Contribution to other works

Vibrationlly assisted energy transfer

I have been involved in the study of vibrationally assisted energy transfer (VAET). This study is a part of a collaboration with experiments in Professor Hartmut Haeffner's group, which use ion traps to simulate the VAET process. We study the energy transfer dynamics in the case of two electronic states coupled to one vibrational mode [62] and in the the case of three electronic states coupled to two vibrational modes [61]. We simulate the dynamics by including a truncated vibrational Hilbert space, compared to for example the HEOM method, where the vibrational degrees of freedom are traced out. In the case of three electronic states coupled to two vibrational modes [61], various resonant energy transfer mechanisms are identified, where different combinations of vibrational quanta interact resonantly with the electronic energy gap. I have contributed to the perturbative analysis of these mechanisms.

In the case of two elctronic states coupled to one vibrational mode [62], the effective Hamiltonian in the single excitation subspace is written as

$$H = \frac{\Delta}{2}\sigma_z + \frac{J}{2}\sigma_x + \nu a^\dagger a + \frac{\kappa}{2}\sigma_z(a + a^\dagger),$$

where $\sigma_z = |eg\rangle\langle eg| - |ge\rangle\langle ge|$, $\sigma_x = |eg\rangle\langle ge| + |ge\rangle\langle eg|$, and a is the annihilation operator for the vibrational mode. In the absence of vibrational coupling (i.e., $\kappa = 0$), the electronic system follows a Rabi oscillation with frequency $\sqrt{\Delta^2 + J^2}$. I have contributed to the study by showing that, if the vibrational frequency is resonant with the electronic energy gap (i.e., $\nu = \sqrt{\Delta^2 + J^2}$) and if the vibrational coupling is weak (i.e., κ is the small parameter), then the electronic system follows a slow oscillation at frequency $\frac{\kappa J}{\nu}\sqrt{n}$, in addition to the fast Rabi oscillation. The parameter n is the initial Fock state number of the vibration.

I have also found that if the initial state is an eigenstate of the vibrational parity operator Π and of the Pauli operator σ_z, and if all coefficients in the initial state have the same phase modulo π, then the transfer probability $P(t)$ is invariant when simultaneously changing the signs of Δ and ν. The initial state coefficients are expressed in a basis such that the matrix representation of H is real-valued. This invariance property has practical importance in the context of trapped-ion simulation of these dynamics, since sweeping ν to negative values can be easier than sweeping Δ to negative values. This invariance is in fact a combination of three symmetries. First, if the initial state is an eigenstate of the vibrational parity operator Π, then the transfer probability $P(t)$ is invariant under the sign change $\kappa \to -\kappa$. Second, if the initial state is an eigenstate of σ_z, then $P(t)$ is invariant under the sign change $J \to -J$. Finally, if all coefficients in the initial state have the same phase modulo π, then $P(t)$ is invariant under the overall sign change $H \to -H$. Combining all three symmetries, we see that $P(t)$ is invariant under the sign change $(\Delta, \nu) \to (-\Delta, -\nu)$.

Quantum trajectories of energy transfer dynamics due to photon counting

I have also helped develop a quantum trajectory picture of the energy transfer dynamics [53], in contrast to the averaged dynamics described in Part II. The trajectories are based on photon counting measurements. Given a single photon Fock state input, when an output photon is measured, the matter system undergoes a quantum jump and collapses to the ground state. If no output photon is observed, then we can infer that the matter system is in the excited state. Thus given a single photon Fock state input, the photon counting measurement provides additional information about the matter system state. We show that given a classical-like coherent state input, not much information about the system state can be gained by photon counting measurements.

The trajectory picture is derived from a model of Markovian phonon bath. On average, the effects of the Markovian phonon bath is described by the Lindblad master equation. This is in contrast to the phonon coupling model in Part II, where the non-Markovian phonon effects are captured by the HEOM. The Markovian model for phonon effects allows us to simulate larger light harvesting systems by reducing the computational cost. We simulate the average dynamics of the PSII $C_2S_2M_2$ supercomplex containing 316 chlorophyll pigment molecules, and we obtain a simulated quantum efficiency of 92.5%, consistent with bulk experimental measurements.

A quantum algorithm for ab initio calculation of nonlinear susceptibilities

I have collaborated with quantum algorithm experts in the Whaley group to develop a quantum algorithm for ab initio calculation of nonlinear susceptibilities [63]. These nonlinear susceptibilities are used to compute the nonlinear spectra of molecules. I have used the perturbative formalism for nonlinear spectroscopy [46] to define the nonlinear susceptibilities in a form that my quantum algorithm collaborators can process readily.

Open questions and future directions

Currently, many proposals for quantum light spectroscopy make use of entangled photon pairs and require both photons interact with the matter system. In general, these types of experiments are very difficult to do, since the probability for a molecule to interact with two photons is very small. We note that entangled photon pairs have been demonstrated to be able to greatly enhance the two-photon absorption probability [137]. However, these results have not been widely accepted yet due to measurement discrepancies and a possible explanation with one-photon processes [138]. More work is needed to understand the magnitude of entangled two-photon absorption in realistic molecular systems and whether entangled two-photon absorption can be used to enhance classical spectroscopy. The use of bright squeezed light in molecular spectroscopy is also a possibility that has received little attention. These type of light would have the advantage of having a larger number of photon and retaining some non-classical properties.

Another avenue for quantum light spectroscopy is to detect the quantum properties (e.g., the $g^{(2)}$ photon correlation function) of emitted light, rather than exciting the matter system with non-classical light. In the context of photosynthetic energy transfer, $g^{(2)}$ spectroscopy has been shown theoretically to provide information about the steady state coherence and the vibronic coupling [39–42]. However, these proposals require that photon counting measurement be performed with sub-ps resolution, which is still beyond the current experimental capabilities. Outside of the context of photosynthetic energy transfer, and working in the longer ns-timescale, $g^{(2)}$ spectroscopy has been demonstrated experimentally to reveal dipole-dipole coupling between individual molecules [4], exciton-exciton annihilation [139], number of molecules [2], and molecular conformations [140]. One main difference between $g^{(2)}$ spectroscopy and typical classical light spectroscopy is that the behavior of $g^{(2)}$ depends strongly and non-trivially on the number of molecules. In classical light spectroscopy, the signal is usually simply proportional to the number of molecules. Most of the proposed or demonstrated $g^{(2)}$ spectroscopy measurements are performed with a single or a few molecules. The usefulness of $g^{(2)}$ spectroscopy for ensemble measurements is still largely unknown and should be explored, since ensemble measurements are much easier to implement.

Appendix A

Small solid angle mode in real space and time

For convenience purposes, we copy Eq. (1.19) here:

$$\tilde{f}(\mathbf{x},t) = \int d^3\mathbf{k}\, f(\mathbf{k}) e^{i\mathbf{k}\cdot\mathbf{x}} e^{-ic|\mathbf{k}|t}. \tag{A.1}$$

$f(\mathbf{k})$ is a function that has significant amplitude only in a small region R in $\mathbf{k}$-space. R is centered at $\mathbf{k}_l$. It has a transversal width of $\sigma_\perp$ and a longitudinal width of $\sigma_\parallel$. Without loss of generality, we let $\mathbf{k}_l$ to be located on the z-axis. We assume $f(\mathbf{k})$ is slowly varying such that within the small region, $|\partial f(\mathbf{k})/\partial k_x|$ and $|\partial f(\mathbf{k})/\partial k_y|$ is at most on the order of $1/\sigma_\perp$, and that $|\partial f(\mathbf{k})/\partial k_z|$ is at most on the order of $1/\sigma_\parallel$.

Without assuming a specific functional form for $f(\mathbf{k})$, we can already understand the behavior of $\tilde{f}(\mathbf{x}, t=0)$ and $\tilde{f}(\mathbf{x}, t\to\infty)$. When $t = 0$,

$$\tilde{f}(\mathbf{x},0) = \int d^3\mathbf{k}\, f(\mathbf{k}) e^{i\mathbf{k}\cdot\mathbf{x}} \tag{A.2}$$

is simply the Fourier transform of $f(\mathbf{k})$. Since $f(\mathbf{k})$ is a slowly-varying function having a transversal span of $\sim \sigma_\perp$, $\tilde{f}(\mathbf{x}, 0)$ has significant amplitude only within a transversal cross sectional area of $\sim 1/\sigma_\perp^2$. When $t \to \infty$, the the complex exponent in the integrand of Eq. (A.1) tends to be fast-varying with respect to $|\mathbf{k}|$. Therefore the integrand tends to be highly oscillatory in the k_z direction, making the integral tend to 0. For $\tilde{f}(\mathbf{x}, t)$ to be nonzero, the exponent

$$i\phi = i(\mathbf{k}\cdot\mathbf{x} - c|\mathbf{k}|t) \tag{A.3}$$

in Eq. (A.1) needs to be stationary with respect to $\mathbf{k}$, for some $\mathbf{k}$ in the small region R. The stationary condition is obtained by setting the derivative $\nabla_\mathbf{k}\phi$ to be zero. After calculating the derivative, we have the stationary condition as

$$\mathbf{x} = \hat{\mathbf{k}} ct, \tag{A.4}$$

where $\hat{\mathbf{k}} = \mathbf{k}/|\mathbf{k}|$ is the unit vector in the direction of $\mathbf{k}$. In order for the condition of (A.4) to hold for some $\mathbf{k}$ in R, $\mathbf{x}$ needs to have a magnitude of ct and a direction that lies inside the small solid angle section. Therefore, $\tilde{f}(\mathbf{x}, t\to\infty)$ has significant amplitude only when $\mathbf{x}$ lies inside the cone of the small solid angle.

To give a specific example, let $f(\mathbf{k})$ be the Gaussian function

$$f(\mathbf{k}) = \exp\Big(- \frac{k_x^2 + k_y^2}{2\sigma_\perp^2} - \frac{\zeta^2}{2\sigma_\parallel^2}\Big), \tag{A.5}$$

where $\zeta = k_z - k_0$ and $k_0 = |\mathbf{k}_l|$. To solve the integral in Eq. (A.1) approximately, we approximate $|\mathbf{k}| = \sqrt{k_x^2 + k_y^2 + k_z^2}$ in the exponent by its Taylor expansion around k_0. Keeping only the lowest order terms in k_x, k_y, and ζ,

$$|\mathbf{k}| = k_0 + \zeta + \frac{k_x^2}{2k_0} + \frac{k_y^2}{2k_0}. \tag{A.6}$$

Now the integral in Eq. (A.1) becomes

$$\begin{aligned} \tilde{f}(x,y,z,t) = e^{ik_0 z - ick_0 t} & \int dk_x \, \exp\Big(- k_x^2 \big(\frac{1}{2\sigma_\perp^2} + \frac{ict}{2k_0}\big) + ik_x x\Big) \\ & \int dk_y \, \exp\Big(- k_y^2 \big(\frac{1}{2\sigma_\perp^2} + \frac{ict}{2k_0}\big) + ik_y y\Big) \\ & \int d\zeta \, \exp\Big(- \frac{\zeta^2}{2\sigma_\perp^2} + i\zeta(z - ct)\Big). \end{aligned} \tag{A.7}$$

After performing the Gaussian integrals, we see that

$$|\tilde{f}(x,y,z,t)| = A \exp\Big(- \frac{x^2 + y^2}{2w_\perp^2} - \frac{(z-ct)^2\sigma_\parallel^2}{2}\Big), \tag{A.8}$$

where the transversal width $w_\perp$ in real space is

$$w_\perp = \frac{1}{\sigma_\perp}\sqrt{1 + \Big(\frac{ct\sigma_\perp^2}{k_0}\Big)^2}, \tag{A.9}$$

and the position-independent constant A is

$$A = \sqrt{\frac{2\sigma_\parallel^2 \pi^3}{\Big(\frac{1}{2\sigma_\perp^2}\Big)^2 + \Big(\frac{ct}{2k_0}\Big)^2}}. \tag{A.10}$$

In the longitudinal direction, $\tilde{f}(x,y,z,t)$ behaves as a wavepacket traveling at the speed of light due to the Gaussian factor centered at $z - ct$. The transverse width is time-dependent, and it is minimal at $t = 0$. When $t = 0$, $w_\perp = 1/\sigma_\perp$, so the cross section area is on the order of $1/\sigma_\perp^2$. At long enough time such that $t \gg \frac{k_0}{c\sigma_\perp^2}$, $w_\perp = \frac{ct\sigma_\perp}{k_0}$. At long times, the pulse is centered around $z = ct$ in the z-direction, so the divergence angle of the small solid angle mode in real space and time is given by $\Delta\theta = w_\perp/ct = \sigma_\perp/k_0$. Note that this divergence angle in real space is the same as the angular spread of the small region R in $\mathbf{k}$-space, given by $\sigma_\perp/k_0$.

Appendix B

Classical input-output relation

Our starting point for the derivation of the classical input-output relation is the inhomogeneous wave equation for the electric field

$$\nabla^2\mathbf{E} - \frac{1}{c^2}\frac{\partial^2\mathbf{E}}{\partial t^2} = \frac{1}{\epsilon_0 c^2}\frac{\partial^2\mathbf{P}}{\partial t^2} \tag{B.1}$$

derived from the macroscopic Maxwell's equations [141], where $\mathbf{E}$ is the electric field and $\mathbf{P}$ is the polarization field, or the density of the dipole moment. Let $\mathbf{E}$ and $\mathbf{P}$ take the form

$$\mathbf{E}(\mathbf{r},t) = \tilde{\mathbf{E}}(z,t)e^{ikz-i\omega t} + \text{c.c.} \tag{B.2a}$$

$$\mathbf{P}(\mathbf{r},t) = \tilde{\mathbf{P}}(z,t)e^{ikz-i\omega t} + \text{c.c.}, \tag{B.2b}$$

where $\omega = ck$ is the carrier wave frequency, and z is in the direction of the field propagation. The notation c.c. stands for complex conjugate. In Eq. (B.2) we have assumed that $\mathbf{E}(\mathbf{r},t)$ and $\mathbf{P}(\mathbf{r},t)$ change very slowly in the transverse x and y directions, so that the dependence on x and y is ignored. We further assume that $\tilde{\mathbf{E}}$ and $\tilde{\mathbf{P}}$ are slowly varying envelope functions such that

$$\left|\frac{\partial^2\tilde{\mathbf{E}}}{\partial t^2}\right| \ll \omega\left|\frac{\partial\tilde{\mathbf{E}}}{\partial t}\right| \ll \omega^2\left|\tilde{\mathbf{E}}\right| \quad \text{and} \quad \left|\frac{\partial^2\tilde{\mathbf{E}}}{\partial z^2}\right| \ll k\left|\frac{\partial\tilde{\mathbf{E}}}{\partial z}\right| \ll k^2\left|\tilde{\mathbf{E}}\right| \tag{B.3a}$$

and

$$\left|\frac{\partial^2\tilde{\mathbf{P}}}{\partial t^2}\right| \ll \omega\left|\frac{\partial\tilde{\mathbf{P}}}{\partial t}\right| \ll \omega^2\left|\tilde{\mathbf{P}}\right| \quad \text{and} \quad \left|\frac{\partial^2\tilde{\mathbf{P}}}{\partial z^2}\right| \ll k\left|\frac{\partial\tilde{\mathbf{P}}}{\partial z}\right| \ll k^2\left|\tilde{\mathbf{P}}\right|. \tag{B.3b}$$

Substituting Eq. (B.2) into the second order equation of Eq. (B.1) and applying the slowly varying envelope approximation (Eq. (B.3)), we obtain a first order equation

$$\frac{\partial\tilde{\mathbf{E}}}{\partial z} + \frac{1}{c}\frac{\partial\tilde{\mathbf{E}}}{\partial t} = \frac{ik}{2\epsilon_0}\tilde{\mathbf{P}}. \tag{B.4}$$

Defining a retarded time

$$s = t - \frac{z}{c} \tag{B.5}$$

and changing the variables in Eq. (B.4) from (z,t) to (s,t), we can reduce the partial differential equation in Eq. (B.4) to an ordinary differential equation of the variable t, for each fixed s, i.e.,

$$\frac{\partial}{\partial t}\tilde{\mathbf{E}}'(s,t) = \frac{ikc}{2\epsilon_0}\tilde{\mathbf{P}}'(s,t). \tag{B.6}$$

To be clear on the variables, we have defined $\tilde{\mathbf{E}}'(s,t) = \tilde{\mathbf{E}}(z,t)$ and $\tilde{\mathbf{P}}'(s,t) = \tilde{\mathbf{P}}(z,t)$. Eq. (B.6) can be solved as

$$\tilde{\mathbf{E}}'(s,t) = \tilde{\mathbf{E}}'(s,0) + \frac{ikc}{2\epsilon_0}\int_0^t d\tau\, \tilde{\mathbf{P}}'(s,\tau). \tag{B.7}$$

Let the matter sample be located between $z = -\epsilon$ and $z = \epsilon$. Then the polarization field $\tilde{\mathbf{P}}(z,t)$ is nonzero only when $|z| < \epsilon$, and $\tilde{\mathbf{P}}'(s,t)$ is nonzero only when $|t-s| < \epsilon/c$. The input field $\mathbf{F}_{\text{in}}(s)$ is defined as $\tilde{\mathbf{E}}'(s,0)$, where $s > \epsilon/c$, so that the field is upstream of the matter sample. The output field $\mathbf{F}_{\text{out}}(s)$ is defined as $= \tilde{\mathbf{E}}'(s,t)$, where $t > s + \epsilon/c$, so that the field is downstream of the matter sample. Now, we can re-write Eq. (B.7) as

$$\mathbf{F}_{\text{out}}(s) = \mathbf{F}_{\text{in}}(s) + \frac{ikc}{2\epsilon_0}\int_{s-\epsilon/c}^{s+\epsilon/c} d\tau\, \tilde{\mathbf{P}}'(s,\tau). \tag{B.8}$$

This is the classical input-output relation. Note that, given a fixed s, $\tilde{\mathbf{P}}'(s,\tau)$ is nonzero only when $\tau \in (s-\epsilon/c, s+\epsilon/c)$. By the definitions of the input and output fields, $(s-\epsilon/c, s+\epsilon/c)$ is always contained inside $(0,t)$.

To turn this into a form that is more similar to Eq. (2.5), we convert $\tilde{\mathbf{P}}'$ into $\tilde{\mathbf{P}}$ in the integral inside Eq. (B.8), and re-write the integral as

$$\int_{s-\epsilon/c}^{s+\epsilon/c} d\tau\, \tilde{\mathbf{P}}(c(\tau - s), \tau). \tag{B.9}$$

Changing the integration variable from τ to $z = c(\tau - s)$, the integral becomes

$$\frac{1}{c}\int_{-\epsilon}^{\epsilon} dz\, \tilde{\mathbf{P}}(z, s + z/c). \tag{B.10}$$

We can now write the classical input-output relation as

$$\mathbf{F}_{\text{out}}(s) = \mathbf{F}_{\text{in}}(s) + \frac{ik}{2\epsilon_0}\int_{-\epsilon}^{\epsilon} dz\, \tilde{\mathbf{P}}(z, s + z/c). \tag{B.11}$$

Comparing this to the quantum input-output relation (Eq. (2.5)), the time variable $s + z/c$ of the polarization $\tilde{\mathbf{P}}$ here corresponds to the time variable $s + \frac{\hat{\mathbf{k}}_l \cdot \mathbf{x}_j}{c}$ of the dipole operator in Eq. (2.5). The integral over z here corresponds to the sum over molecules in Eq. (2.5). The factor of i in the classical expression comes from the correspondence $ia(s) \leftrightarrow \mathbf{E}$ (ignoring a real-valued constant factor) between the field operator $a(s)$ and the classical electric field $\mathbf{E}$.

Appendix C

Fermi's golden rule rate for spontaneous emission photon flux

Consider a molecule with two electronic states, a ground state $|g\rangle$ and an excited state $|e\rangle$. The molecule may contain nuclear degrees of freedom, which will be implicit in the analysis. Let the initial electronic state of the molecule be in the excited state. Then the golden rule expression for the decay rate from $|e\rangle$ into $|g\rangle$ can be written in terms of the correlation function [142], i.e.,

$$\text{excited state decay rate} = \int_{-\infty}^{\infty} d\tau \, \langle H(\tau) H(0) \rangle. \tag{C.1}$$

Here, the expectation value is evaluated with respect to $|e\rangle|\text{vac}\rangle$, the electronically excited state of the molecule times the vacuum state of the photon field. Substituting the Hamiltonian (Eq. (1.32)) into the golden rule expression, we find the excited state decay rate is equal to

$$\text{excited state decay rate} = \sum_{l=1}^{2M} \langle e | L_l^\dagger L_l | e \rangle, \tag{C.2}$$

meaning that the total decay rate of the excited state is the sum of the spontaneous emission rates into each of the spatial modes. Given a general system state $\rho_{\text{sys}}(t)$ that may not be the excited state $|e\rangle$, the spontaneous emission photon flux in the l-th spatial mode is equal to the excited state population $\text{Tr}(|e\rangle\langle e|\rho_{\text{sys}}(t))$ times the emission rate into the l-th spatial mode $\langle e|L_l^\dagger L_l|e\rangle$. This product can be shown to be equivalent to Eq. (2.8) by noting that

$$\begin{aligned} &\text{Tr}\big(|e\rangle\langle e|\rho_{\text{sys}}(t)\big)\langle e|L_l^\dagger L_l|e\rangle \\ &= \text{Tr}\big(|e\rangle\langle e|L_l^\dagger L_l|e\rangle\langle e|\rho_{\text{sys}}(t)\big) \\ &= \text{Tr}\big(L_l^\dagger L_l \rho_{\text{sys}}(t)\big). \end{aligned} \tag{C.3}$$

The last equality is obtained by noting that in our two-level system, $L_l^\dagger L_l$ is proportional to $|e\rangle\langle e|$.

Appendix D

Perturbative expansion of Heisenberg-evolved operators

Following the notation in Sec. 3.1, we define a time-evolution superoperator $\mathcal{U}(t)$ that evolves an operator in time as

$$\mathcal{U}(t) = U^\dagger(t) \bullet U(t), \tag{D.1}$$

where the dot $\bullet$ notation means that the effect of the superoperator acting on a general operator X is to substitute the operator X into the dot $\bullet$. Specifically, $\mathcal{U}(t)X = U^\dagger(t)XU(t)$. Note that a Heisenberg picture operator $A_H(t)$ is related to the interaction picture operator $A(t)$ by

$$A_H(t) = \mathcal{U}(t)A(t) \tag{D.2}$$

(see Eq. (1.28)). Our task of expanding $A_H(t)$ from $A(t)$ now reduces to expanding the superoperator $\mathcal{U}(t)$. Just as $U(t)$ is a linear operator on the vector space of quantum states, the superoperator $\mathcal{U}(t)$ is also a linear operator on a larger vector space of operators.

Taking the time derivative of Eq. (D.1) using the Schrodinger equation (Eq. (1.26)), we obtain

$$\begin{aligned} \frac{d}{dt}\mathcal{U}(t) &= -iU^\dagger(t)[\bullet, H(t)]U(t) \\ &= -i[U^\dagger(t) \bullet U(t), H_H(t)], \end{aligned} \tag{D.3}$$

where $H_H(t) = U^\dagger(t)H(t)U(t)$ is the Hamiltonian in the Heisenberg picture. We have written the time derivative in two ways. The first line involves the interaction picture Hamiltonian $H(t)$, and the second line involves the Heisenberg picture Hamiltonian $H_H(t)$. Defining the superoperator $\mathcal{L}[A]$, where A is a general operator, as

$$\mathcal{L}[A] = -i[\bullet, A], \tag{D.4}$$

we can re-express Eq. (D.3) in superoperators in two ways. The second line in Eq. (D.3) can be written as

$$\frac{d}{dt}\mathcal{U}(t) = \mathcal{L}[H_H(t)]\mathcal{U}(t), \tag{D.5}$$

while the first line in Eq. (D.3) can be written as

$$\frac{d}{dt}\mathcal{U}(t) = \mathcal{U}(t)\mathcal{L}[H(t)]. \tag{D.6}$$

Solving Eq. (D.5) iteratively from the initial condition $\mathcal{U}(0) = 1$, we have

$$\begin{aligned}\mathcal{U}(t) =& 1 + \int_0^t dt_1\, \mathcal{L}[H_H(t_1)] \\ &+ \int_0^t dt_2 \int_0^{t_2} dt_1\, \mathcal{L}[H_H(t_2)]\mathcal{L}[H_H(t_1)] \\ &+ \int_0^t dt_3 \int_0^{t_3} dt_2 \int_0^{t_2} dt_1\, \mathcal{L}[H_H(t_3)]\mathcal{L}[H_H(t_2)]\mathcal{L}[H_H(t_1)] + \cdots .\end{aligned} \tag{D.7}$$

This result can be expressed compactly as

$$\mathcal{U}(t) = \mathcal{T}_+ \exp\bigg(\int_0^t d\tau\, \mathcal{L}[H_H(\tau)] \bigg), \tag{D.8}$$

where the forward time-ordering $\mathcal{T}_+$ orders the superoperators $\mathcal{L}$ from right to left in the order of the smallest to the largest time variable. Substituting this expansion into Eq. (D.2), we obtain the time-ordered expansion for $A_H(t)$ as

$$\begin{aligned}A_H(t) =& A(t) - i \int_0^t dt_1\, [A(t), H_H(t_1)] \\ &+ (-i)^2 \int_0^t dt_2 \int_0^{t_2} dt_1\, [[A(t), H_H(t_1)], H_H(t_2)] \\ &+ (-i)^3 \int_0^t dt_3 \int_0^{t_3} dt_2 \int_0^{t_2} dt_1\, [[[A(t), H_H(t_1)], H_H(t_2)], H_H(t_3)] + \cdots .\end{aligned} \tag{D.9}$$

On the other hand, solving Eq. (D.6) iteratively from the initial condition $\mathcal{U}(0) = 1$, we have

$$\begin{aligned}\mathcal{U}(t) =& 1 + \int_0^t dt_1\, \mathcal{L}[H(t_1)] \\ &+ \int_0^t dt_2 \int_0^{t_2} dt_1\, \mathcal{L}[H(t_1)]\mathcal{L}[H(t_2)] \\ &+ \int_0^t dt_3 \int_0^{t_3} dt_2 \int_0^{t_2} dt_1\, \mathcal{L}[H(t_1)]\mathcal{L}[H(t_2)]\mathcal{L}[H(t_3)] + \cdots .\end{aligned} \tag{D.10}$$

This result can be expressed compactly as

$$\mathcal{U}(t) = \mathcal{T}_- \exp\bigg(\int_0^t d\tau\, \mathcal{L}[H(\tau)] \bigg), \tag{D.11}$$

where the backward time-ordering $\mathcal{T}_-$ orders the superoperators $\mathcal{L}$ from right to left in the order of the largest to the smallest time variable. Substituting this expansion into Eq. (D.2), we obtain the anti-time-ordered expansion for $A_H(t)$ as

$$\begin{aligned}A_H(t) =& A(t) - i \int_0^t dt_1\, [A(t), H(t_1)] \\ &+ (-i)^2 \int_0^t dt_2 \int_0^{t_2} dt_1\, [[A(t), H(t_2)], H(t_1)] \\ &+ (-i)^3 \int_0^t dt_3 \int_0^{t_3} dt_2 \int_0^{t_2} dt_1\, [[[A(t), H(t_3)], H(t_2)], H(t_1)] + \cdots .\end{aligned} \tag{D.12}$$

We have now obtained two different expansions of the Heisenberg picture operator $A_H(t)$. Comparing Eq. (D.8) to Eq. (D.11), we find a surprisingly elegant superoperator identity:

$$\mathcal{T}_+ \exp\left(\int_0^t d\tau\, \mathcal{L}[H_H(\tau)]\right) = \mathcal{T}_- \exp\left(\int_0^t d\tau\, \mathcal{L}[H(\tau)]\right). \tag{D.13}$$

Appendix E

Relationship between Eqs. (4.13) and (4.15)

To show that the Heisenberg picture signal of Eq. (13) is equal to the interaction picture signal of Eq. (15), it suffices to show

$$\mathrm{Tr}\big(\rho(-\infty)a^{\dagger}_{\mathrm{pr,\ out}}(t_2)a_{\mathrm{pr,\ out}}(t_1)\big) = \mathrm{Tr}\big(\rho(\infty)a^{\dagger}_{\mathrm{pr}}(t_2)a_{\mathrm{pr}}(t_1)\big). \tag{E.1}$$

The presence of $\rho(\infty)$ in the interaction picture is not very intuitive, but this can be understood if we consider the following relation [52]:

$$a_{\mathrm{pr,out}}(t') = U^{\dagger}(t)a_{\mathrm{pr}}(t')U(t), \tag{E.2}$$

where $t > t'$. $U(t)$ is defined below Eq. (17). Taking a common time variable t, such that $t > t_1, t_2$. The left-hand side of Eq. (E.1) becomes

$$\mathrm{Tr}\big(\rho(-\infty)U^{\dagger}(t)a^{\dagger}_{\mathrm{pr}}(t_2)U(t)U^{\dagger}(t)a_{\mathrm{pr}}(t_1)U(t)\big). \tag{E.3}$$

Using the invariance of the trace under cyclic permutation and the unitary property $U(t)U^{\dagger}(t) = 1$, (E.3) becomes

$$\mathrm{Tr}\big(U(t)\rho(-\infty)U^{\dagger}(t)a^{\dagger}_{\mathrm{pr}}(t_2)a_{\mathrm{pr}}(t_1)\big). \tag{E.4}$$

Finally, taking $t \to \infty$, so that $U(t)\rho(-\infty)U^{\dagger}(t) \to \rho(\infty)$, we obtain the right-hand side of Eq. (E.1).

Appendix F

Numerical parameters of Sec. 4.3

Using the two-state jump model in [56] for the matter system and following the notation in that work, we take $\omega_{fe} = 11000\,\mathrm{cm}^{-1}$, $\delta = 200\,\mathrm{cm}^{-1}$, $k = 120\,\mathrm{cm}^{-1}$, and $\gamma = 100\,\mathrm{cm}^{-1}$. From Eq. (19) of [56], we derive the matter correlation function

$$\begin{aligned}\tilde{F}(\omega', \omega; t_0) = e^{-i(\omega-\omega')t_0}\Big(&\frac{1}{(\omega-\omega'+i\gamma)}\frac{1}{(\omega-\omega_+ + 2i\gamma)} \\ &+ \frac{2i\delta}{k+2i\delta}\frac{1}{(\omega-\omega'+i(k+\gamma))}\frac{1}{(\omega-\omega_- + i(k+2\gamma))} \\ &- \frac{2i\delta}{k+2i\delta}\frac{1}{(\omega-\omega'+i(k+\gamma))}\frac{1}{(\omega-\omega_+ + 2i\gamma)}\Big),\end{aligned} \tag{F.1}$$

where $\omega_\pm = \omega_{fe} \pm \delta$. We note that this is slightly different from Eq. (20) of [56]. We then multiply $\tilde{F}(\omega', \omega; t_0)$ by a factor of 20, so that around 10% of the probe is absorbed at the peak of the pump-probe spectrum. The factor of 20 effectively takes into account the light beam geometry, the molecular dipole strength, and the number of molecules in the sample.

The biphoton wavefunction of [56] takes the Gaussian form

$$\Phi(\omega, \omega_r) = \mathcal{N} e^{-\frac{(\omega+\omega_r-\omega_0)^2}{2\sigma^2}} e^{-\beta[(\omega-\omega_0/2)T_2 + (\omega_r-\omega_0/2)T_1]^2}, \tag{F.2}$$

where $\mathcal{N}$ is a normalization factor ensuring $\int d\omega d\omega_r |\Phi(\omega, \omega_r)|^2 = 1$, $\beta = 0.04822$, $\omega_0 = 22000\,\mathrm{cm}^{-1}$, $\sigma = 1000\,\mathrm{cm}^{-1}$, $T_1 = -19.69\,\mathrm{fs}$, and $T_2 = 70.31\,\mathrm{fs}$. If we choose a fixed value of ω_r, then the bivariate Gaussian biphoton wavefunction reduces to a single-variable Gaussian function $\propto e^{-(\omega-\omega_0')^2/2\sigma'^2}$ with a modified center frequency

$$\omega_0' = \big(\frac{1}{\sigma^2} + 2\gamma T_2^2\big)^{-1}\left[\frac{\omega_0 - \omega_r}{\sigma^2} + 2\gamma T_2\big(\frac{\omega_0}{2}(T_1+T_2) - \omega_r T_1\big)\right] \tag{F.3}$$

and variance

$$\sigma' = \big(\frac{1}{\sigma^2} + 2\gamma T_2^2\big)^{-1/2}. \tag{F.4}$$

This gives the explicit form of the quantum-inspired classical probe pulse corresponding to the biphoton pulse, which is thus seen to depend on the biphoton parameters γ, T_1, T_2, ω_0 and σ, in addition to ω_r. When $\omega_r = 10400\,\mathrm{cm}^{-1}$, the quantum-inspired pulse has $\omega_0' = 10874.81\,\mathrm{cm}^{-1}$ and $\sigma' = 236.09\,\mathrm{cm}^{-1}$. When $\omega_r = 11400\,\mathrm{cm}^{-1}$, the quantum-inspired pulse has $\omega_0' = 11083.46\,\mathrm{cm}^{-1}$ and $\sigma' = 236.09\,\mathrm{cm}^{-1}$.

Appendix G

Quantizing a paraxial mode

The vector potential of a paraxial beam propagating in the $+z$ direction takes the form

$$\mathbf{A}_{\text{para}}(\mathbf{x},t) = \mathbf{u}(\mathbf{x},t)e^{ik_0 z - i\omega_0 t} + \text{c.c.}, \tag{G.1}$$

where $\mathbf{u}(\mathbf{x},t)$ is a slowly varying envelope function, and k_0 and $\omega_0 = ck_0$ are the carrier wavevector and frequency, respectively. The slowly varying envelope is characterized by the conditions

$$\begin{cases} |\frac{\partial^2 \mathbf{u}}{\partial t^2}| \ll \omega_0 |\frac{\partial \mathbf{u}}{\partial t}| \ll \omega_0^2 |\mathbf{u}| \\ |\frac{\partial^2 \mathbf{u}}{\partial z^2}| \ll k_0 |\frac{\partial \mathbf{u}}{\partial z}| \ll k_0^2 |\mathbf{u}|. \end{cases} \tag{G.2}$$

Under these conditions, the wave equation $\nabla^2 \mathbf{A} = \frac{1}{c^2}\frac{\partial^2 \mathbf{A}}{\partial t^2}$ reduces to the paraxial wave equation

$$\frac{\nabla_\perp^2}{2k_0}\mathbf{u} + i(\frac{\partial \mathbf{u}}{\partial z} + \frac{1}{c}\frac{\partial \mathbf{u}}{\partial t}) = 0, \tag{G.3}$$

which is first order in z and t. Therefore we can eliminate one variable and write

$$\mathbf{u}(\mathbf{x},t) = f(t_r)\tilde{\mathbf{u}}(x,y,z), \tag{G.4}$$

where f is an arbitrary function and $t_r \equiv t - z/c$ is the retarded time. $\tilde{\mathbf{u}}(\mathbf{x})$ satisfies the Schrödinger-like equation

$$-i\frac{\partial \tilde{\mathbf{u}}}{\partial z} = \frac{\nabla_\perp^2}{2k_0}\tilde{\mathbf{u}}. \tag{G.5}$$

We normalize $\tilde{\mathbf{u}}$ according to

$$\int dxdy\, |\tilde{\mathbf{u}}(x,y,z)|^2 = 1. \tag{G.6}$$

If we fix the spatial mode $\tilde{\mathbf{u}}(\mathbf{x})$, the field degree of freedom is in the arbitrariness of $f(t_r)$. We express the Fourier components of $f(t_r)$ as

$$f(t_r)e^{-i\omega_0 t_r} = \frac{1}{\sqrt{L}}\sum_q \underbrace{\phi_q e^{-icqt}}_{\phi_q(t)} e^{iqz}, \tag{G.7}$$

where q takes the values $2\pi n/L$, $n = 0, \pm 1, \pm 2, \cdots$. L will be taken to infinity at the end of calculation. Due to the paraxial approximation, ϕ_q is localized around $q = k_0$. Substituting Eqs. (G.7) and (G.4)

into Eq. (G.1), we have

$$\begin{aligned}\mathbf{A}_{\text{para}}(\mathbf{x},t) &= \frac{1}{\sqrt{L}}\sum_q \tilde{\mathbf{u}}(\mathbf{x})\phi_q(t)e^{iqz} + \text{c.c.} \\ &= \frac{1}{\sqrt{L}}\sum_q [\tilde{\mathbf{u}}(\mathbf{x})\phi_q(t) + \tilde{\mathbf{u}}^*(\mathbf{x})\phi^*_{-q}(t)]e^{iqz}.\end{aligned} \tag{G.8}$$

From the last equality, we see that the quantity in the square bracket is simply the Fourier-transformed vector potential $\mathbf{A}_q$. Because $\mathbf{A}(\mathbf{x})$ is real-valued, $\mathbf{A}_q = \mathbf{A}^*_{-q}$, so $\{\mathbf{A}_q | q > 0\}$ completely specifies $\mathbf{A}(\mathbf{x})$. Since $\{\phi_q\}$ (containing both positive and negative q's) contains twice as many parameters as $\{\mathbf{A}_q | q > 0\}$, $\{\phi_q\}$ is a redundant description of the vector potential. To remedy this issue, we set $\phi_q = 0,\ \forall q < 0$. So

$$\mathbf{A}_{\text{para}}(\mathbf{x},t) = \frac{1}{\sqrt{L}}\sum_{q>0} \tilde{\mathbf{u}}(\mathbf{x})\phi_q(t)e^{iqz} + \text{c.c.}, \tag{G.9}$$

where the sum only ranges over positive q's. The free field electromagnetic Lagrangian in the Coulomb gauge is [113, 143]

$$\mathcal{L} = \frac{\epsilon_0}{2}\int d^3x\,(\frac{\partial \mathbf{A}}{\partial t})^2 - c^2(\nabla\times\mathbf{A})^2. \tag{G.10}$$

Using Eq. (G.9), the first term in the Lagrangian is evaluated as

$$\begin{aligned}\int d^3x\,(\frac{\partial \mathbf{A}}{\partial t})^2 &= \frac{1}{L}\int d^3x \sum_{q1,q2>0} \left[\tilde{\mathbf{u}}^2(\mathbf{x})\dot{\phi}_{q_1}\dot{\phi}_{q_2}e^{i(q_1+q_2)z} + \text{c.c.}\right] + 2|\tilde{\mathbf{u}}(\mathbf{x})|^2\dot{\phi}_{q_1}\dot{\phi}^*_{q_2}e^{i(q_1-q_2)z} \\ &\approx 2\sum_q |\dot{\phi}_q|^2,\end{aligned} \tag{G.11}$$

where $\dot{\phi}$ denotes the time derivative $d\phi/dt$. We dropped the term in the square bracket here because performing the spatial integral gives $\int dz(\int dxdy\tilde{\mathbf{u}}^2)e^{i(q_1+q_2)z}$. And since the spatial mode is slowly varying in z, this integral is non-vanishing only when $q_1+q_2 \approx 0$. However, the paraxial approximation asserts that $\dot{\phi}_q$ is non-vanishing only when $q \approx k_0$. In this respect, the quantity in the bracket is non-vanishing only when $q_1 + q_2 \approx 2k_0$, which is incompatible with $q_1 + q_2 \approx 0$. Therefore the term in the bracket is always small and can be dropped.

In the second term of the Lagrangian,

$$\nabla\times\mathbf{A} = \frac{1}{\sqrt{L}}\sum_{q>0}(\nabla\times\tilde{\mathbf{u}} + iq\hat{z}\times\tilde{\mathbf{u}})\phi_q e^{iqz} + \text{c.c.} \tag{G.12}$$

For the TEM_{00} Gaussian beam considered here, $\nabla\times\tilde{\mathbf{u}}$ is identically zero. For other beam modes $\nabla\times\tilde{\mathbf{u}}$ is generally nonzero, but it is small compared to the next term $iq\hat{z}\times\tilde{\mathbf{u}}$, because the sum $\sum_{q>0}$ is dominated by contributions from $q \approx k_0$ and in general $|\nabla\times\tilde{\mathbf{u}}|$ is much smaller than $|k_0\tilde{\mathbf{u}}|$. The spatial integral of $(\nabla\times\mathbf{A})^2$ follows similarly as above.

The Lagrangian now takes the form of a collection of harmonic oscillators

$$\mathcal{L} = \epsilon_0\sum_{q>0}|\dot{\phi}_q|^2 - \omega_q^2|\phi_q|^2, \tag{G.13}$$

where $\omega_q \equiv cq$. We first quantize the real and imaginary parts of ϕ_q using a set of bosonic operators $\tilde{a}_q^{(\text{Re})}$, and $\tilde{a}_q^{(\text{Im})}$, so that the real part of ϕ_q is quantized as

$$\text{Re}\,\phi_q = \sqrt{\frac{\hbar}{4\epsilon_0\omega_q}}(\tilde{a}_q^{(\text{Re})} + \tilde{a}_q^{(\text{Re})\dagger}) \tag{G.14}$$

and the imaginary part of ϕ_q is quantized as

$$\mathrm{Im}\,\phi_q = \sqrt{\frac{\hbar}{4\epsilon_0\omega_q}}(\tilde{a}_q^{(\mathrm{Im})} + \tilde{a}_q^{(\mathrm{Im})\dagger}) \tag{G.15}$$

Then we transform the "$\tilde{a}_q$" operators into the "a_q" operators using $a_q^{(r)} = (\tilde{a}_q^{(\mathrm{Re})} + i\tilde{a}_q^{(\mathrm{Im})})/\sqrt{2}$ and $a_q^{(l)} = (\tilde{a}_q^{(\mathrm{Re})} - i\tilde{a}_q^{(\mathrm{Im})})/\sqrt{2}$. The quantized version of the complex-valued ϕ_q becomes [144]

$$\phi_q = \mathrm{Re}\,\phi_q + i\mathrm{Im}\,\phi_q = \sqrt{\frac{\hbar}{2\epsilon_0\omega_q}}(a_q^{(r)} + a_q^{(l)\dagger}), \tag{G.16}$$

where $a_q^{(r)}$ and $a_q^{(l)}$ are two sets of bosonic operators with commutation relations $[a_q^{(\nu)}, a_{q'}^{(\nu')\dagger}] = \delta_{\nu,\nu'}\delta_{q,q'}$ and $[a_q^{(\nu)}, a_{q'}^{(\nu')}] = [a_q^{(\nu)\dagger}, a_{q'}^{(\nu')\dagger}] = 0$. The field Hamiltonian is

$$H = \sum_{q>0} \hbar\omega_q (a_q^{(r)\dagger} a_q^{(r)} + a_q^{(l)\dagger} a_q^{(l)}). \tag{G.17}$$

Substituting Eq. (G.16) into Eq. (G.9), we arrive at

$$\mathbf{A}_{\mathrm{para}}(\mathbf{x}, t) = \sum_{q>0} \sqrt{\frac{\hbar}{2\epsilon_0\omega_q L}} \tilde{\mathbf{u}}\,(\mathbf{x}) \left(a_q^{(r)} e^{-i\omega_q t} + a_q^{(l)^\dagger} e^{i\omega_q t} \right) e^{iqz} + \mathrm{h.c.} \tag{G.18}$$

Here we see that the transformed operators $a_q^{(r)}$'s and $a_q^{(l)}$'s correspond to right- and left-traveling waves, respectively. The reason that left-traveling waves appear in our quantization is because if we considered left-traveling waves in Eq. (G.1), we would have obtain the exactly same Lagrangian. Since we are only considering the right-traveling waves in this work, we will discard the $a_q^{(l)}$'s and drop the superscript (r). To obtain the continuum limit $L \to \infty$, we make the replacements $\sum_{q>0} \to L/(2\pi c)\int_0^\infty d\omega$ and $a_q \to \sqrt{2\pi c/L}a(\omega)$, to ensure the commutation relation $[a(\omega), a^\dagger(\omega')] = \delta(\omega - \omega')$. Finally, using the relation $\mathbf{E} = -\partial\mathbf{A}/\partial t$, we have

$$\mathbf{E}_{\mathrm{para}}(\mathbf{x}, t) = \int_0^\infty d\omega \sqrt{\frac{\hbar\omega}{4\pi\epsilon_0 c}} (i\tilde{\mathbf{u}}(\mathbf{x}) a(\omega) e^{-i\omega t_r} + \mathrm{h.c.}). \tag{G.19}$$

Since the size of the chromophoric system is much smaller than the wavelength of visible light, we can apply the dipole approximation and set the light-matter interaction to the form $-\mathbf{d}\cdot\mathbf{E}(\mathbf{x_0})$, where $\mathbf{d}$ is the dipole moment operator of the chromophoric system, and $\mathbf{x_0}$ is the position of this, which is considered as fixed. Without loss of generality, let $\mathbf{x_0} = \mathbf{0}$, and let $\tilde{\mathbf{u}}(\mathbf{0})$ be real-valued. We then rewrite the electric field of the paraxial mode at location $\mathbf{0}$ as

$$\mathbf{E}_{\mathrm{para}}(\mathbf{x} = \mathbf{0}, t) = \int_0^\infty d\omega \sqrt{\frac{\hbar\omega}{4\pi\epsilon_0 c}} \tilde{\mathbf{u}}(\mathbf{0}) (ia(\omega) e^{-i\omega t_r} + \mathrm{h.c.}). \tag{G.20}$$

Appendix H

Chromophore system parameters

Matrix elements of the Hamiltonian H and the HEOM parameters λ and γ are expressed in units of cm^{-1}. The dipole matrix $\mathbf{D}$ is in units of Debye. The i-th row of $\mathbf{D}$ contains the transition dipole moment of the i-th site.

H.1 monomer

$$H = 15222$$

$$d = \begin{pmatrix} 4 & 0 & 0 \end{pmatrix}$$

$$\lambda = 37$$

$$\gamma = 30$$

H.2 dimer

We choose the a602 and a603 chlorophylls in the LHCII monomer (parameters given below) as the dimer system. Both dipole moments have a magnitude of 4 Debye. The angle between the dipole moments is $\phi = 2.282$ rad.

H.3 7-mer

The 7-mer system consists of chlorophylls a602, a603, b608, b609, a610, a611, and a612 in the LHCII monomer (parameters given below).

H.4 LHCII monomer

The LHCII monomer consists of 14 chlorophylls. In the basis of singly excited states the chlorophylls are listed in the order b601, a602, a603, a604, b605, b606, b607, b608, b609, a610, a611, a612, a613, a614. The Hamiltonian is taken from [112]. The dipole moments are taken from [112, 122, 145, 146] and the HEOM parameters are taken from [112, 122].

$$H = \begin{pmatrix}
15889 & 49.64 & -5.89 & -2.51 & 0.77 & -1.87 & -2.49 & 2.78 & 3.79 & -5.95 & 24.89 & 9.13 & -10.79 & 3.59 \\
49.64 & 15157 & 38.11 & 6.42 & -0.71 & 5.6 & 7.13 & -5.84 & -19.25 & -11.39 & 9.69 & 15.83 & -4.96 & 0.69 \\
-5.89 & 38.11 & 15287 & -3.28 & 1.13 & -8.89 & 1.23 & 6.72 & 96.66 & 12.97 & -2.7 & -0.76 & 2.68 & -6.7 \\
-2.51 & 6.42 & -3.28 & 15460 & 3.35 & 104.56 & 35.93 & -2.76 & -7.28 & -4.18 & -3.8 & 4.67 & 2.12 & -3.42 \\
0.77 & -0.71 & 1.13 & 3.35 & 15679 & 29.71 & -4.47 & -5.13 & -0.77 & 1.61 & 1.33 & -2.85 & -1.4 & 0.37 \\
-1.87 & 5.6 & -8.89 & 104.56 & 29.71 & 15850 & 59.38 & -4.99 & -0.16 & -3.28 & -2.52 & 3.1 & 1.47 & -2.16 \\
-2.49 & 7.13 & 1.23 & 35.93 & -4.47 & 59.38 & 15714 & -4.43 & -11.99 & -0.14 & -2.78 & 3.07 & 2.2 & -3.25 \\
2.78 & -5.84 & 6.72 & -2.76 & -5.13 & -4.99 & -4.43 & 15761 & 36.07 & 61.97 & 4.35 & -1.08 & -2.01 & 1.3 \\
3.79 & -19.25 & 96.66 & -7.28 & -0.77 & -0.16 & -11.99 & 36.07 & 15721 & 3.86 & 4.3 & -2.57 & -2.92 & 2.33 \\
-5.95 & -11.39 & 12.97 & -4.18 & 1.61 & -3.28 & -0.14 & 61.97 & 3.86 & 15073 & -24.96 & 23.1 & 7.21 & -1.55 \\
24.89 & 9.69 & -2.7 & -3.8 & 1.33 & -2.52 & -2.78 & 4.35 & 4.3 & -24.96 & 15112 & 126.92 & -6.15 & 4.55 \\
9.13 & 15.83 & -0.76 & 4.67 & -2.85 & 3.1 & 3.07 & -1.08 & -2.57 & 23.1 & 126.92 & 15094 & -0.47 & -0.18 \\
-10.79 & -4.96 & 2.68 & 2.12 & -1.4 & 1.47 & 2.2 & -2.01 & -2.92 & 7.21 & -6.15 & -0.47 & 15174 & -50.22 \\
3.59 & 0.69 & -6.7 & -3.42 & 0.37 & -2.16 & -3.25 & 1.3 & 2.33 & -1.55 & 4.55 & -0.18 & -50.22 & 15260
\end{pmatrix}$$

$$\mathbf{D} = \begin{pmatrix}
-3.04018928 & -1.51919464 & -0.09641966 \\
1.42230404 & 3.46070983 & -1.41440402 \\
-2.58738817 & -2.60418809 & -1.58859273 \\
-1.81480538 & 2.10130623 & 2.87940854 \\
0.29193785 & 1.81308663 & -2.86137889 \\
-2.62012348 & -0.01673115 & 2.16671942 \\
-1.55037969 & -1.03298647 & 2.84416275 \\
2.98160121 & 1.07250043 & -1.2328005 \\
2.08379809 & 2.66109756 & -0.36924966 \\
-1.77671903 & -3.27783512 & -1.44881552 \\
-2.58650849 & -3.04210998 & -0.23567077 \\
2.46647094 & 2.26807328 & -2.18457426 \\
1.96630894 & -2.09060951 & 2.78621267 \\
0.5585345 & -3.51332832 & -1.82881474
\end{pmatrix}$$

$$\lambda = \begin{pmatrix} 37 & 37 & 37 & 37 & 37 & 37 & 37 & 37 & 37 & 37 & 37 & 37 & 37 & 37 \end{pmatrix}$$

$$\gamma = \begin{pmatrix} 48 & 30 & 30 & 30 & 48 & 48 & 48 & 48 & 48 & 30 & 30 & 30 & 30 & 30 \end{pmatrix}$$

Appendix I

Second order perturbation analysis of coherent state input

Neglecting the slow spontaneous emission, the coherent state master equation (Eq. (6.26)) becomes

$$\frac{d}{dt}\rho = -i[H - i\alpha(t)L_{\rm inc}^{\dagger} + i\alpha^{*}(t)L_{\rm inc}, \rho]. \tag{I.1}$$

Rotating out the Hamiltonian H, the interaction frame density matrix $\tilde{\rho}(t) = e^{iHt}\rho(t)e^{-iHt}$ follows the equation

$$\frac{d}{dt}\tilde{\rho}(t) = [-\alpha(t)L_{\rm inc}^{\dagger}(t) + \alpha^{*}(t)L_{\rm inc}(t), \tilde{\rho(t)}], \tag{I.2}$$

where $L_{\rm inc}(t) \equiv e^{iHt}L_{\rm inc}e^{-iHt}$. Given the initial state $\tilde{\rho}(0) = |g\rangle\langle g|$, to second order perturbation we have,

$$\begin{aligned}\tilde{\rho}(t) = |g\rangle\langle g| + \int_0^t dt_1 \; & -\alpha(t_1)L_{\rm inc}^{\dagger}(t_1)|g\rangle\langle g| - \alpha^{*}(t_1)|g\rangle\langle g|L_{\rm inc}(t_1) \\ + \int_0^t dt_2 \int_0^{t_2} dt_1 \; & -\alpha^{*}(t_2)\alpha(t_1)L_{\rm inc}(t_2)L_{\rm inc}^{\dagger}(t_1)|g\rangle\langle g| - \alpha(t_2)\alpha^{*}(t_1)|g\rangle\langle g|L_{\rm inc}(t_1)L_{\rm inc}^{\dagger}(t_2) \\ & + \alpha^{*}(t_2)\alpha(t_1)L_{\rm inc}^{\dagger}(t_1)|g\rangle\langle g|L_{\rm inc}(t_2) + \alpha(t_2)\alpha^{*}(t_1)L_{\rm inc}^{\dagger}(t_2)|g\rangle\langle g|L_{\rm inc}(t_1).\end{aligned} \tag{I.3}$$

In obtaining the equation above, terms involving $L_{\rm inc}(t)|g\rangle\langle g|$ and $|g\rangle\langle g|L_{\rm inc}^{\dagger}(t)$ were dropped. Since $L_{\rm inc} = \sqrt{\Gamma_{\rm inc}}|g\rangle\langle B_{\rm inc}|$ (see Eq. (6.11)), these terms are identically zero. Using the fact that $e^{-iHt}|g\rangle = |g\rangle$, $L_{\rm inc}(t)$ can be simplified as $L_{\rm inc}e^{-iHt}$, and $L_{\rm inc}^{\dagger}(t)$ can be simplified as $e^{iHt}L_{\rm inc}^{\dagger}(t)$. Switching the time index t_1 and t_2 in the first and the third terms in the double integral,

$$\begin{aligned}\tilde{\rho}(t) = |g\rangle\langle g| + \int_0^t dt_1 \; & -\alpha(t_1)e^{iHt_1}L_{\rm inc}^{\dagger}|g\rangle\langle g| - \alpha^{*}(t_1)|g\rangle\langle g|L_{\rm inc}e^{-iHt_1} \\ + \int_0^t dt_2 \int_0^{t_2} dt_1 \; & -\alpha(t_2)\alpha^{*}(t_1)|g\rangle\langle g|L_{\rm inc}e^{iH(t_2-t_1)}L_{\rm inc}^{\dagger} + \alpha(t_2)\alpha^{*}(t_1)e^{iHt_2}L_{\rm inc}^{\dagger}|g\rangle\langle g|L_{\rm inc}e^{-iHt_1} \\ + \int_0^t dt_1 \int_0^{t_1} dt_2 \; & -\alpha(t_2)\alpha^{*}(t_1)L_{\rm inc}e^{iH(t_2-t_1)}L_{\rm inc}^{\dagger}|g\rangle\langle g| + \alpha(t_2)\alpha^{*}(t_1)e^{iHt_2}L_{\rm inc}^{\dagger}|g\rangle\langle g|L_{\rm inc}e^{-iHt_1}.\end{aligned} \tag{I.4}$$

The first term in the first double integral is in fact equal to the first term in the second double integral. To see this, notice that

$$|g\rangle\langle g|L_{\rm inc}e^{iH(t_2-t_1)}L_{\rm inc}^\dagger = L_{\rm inc}e^{iH(t_2-t_1)}L_{\rm inc}^\dagger|g\rangle\langle g| = \langle g|L_{\rm inc}e^{iH(t_2-t_1)}L_{\rm inc}^\dagger|g\rangle|g\rangle\langle g|. \tag{I.5}$$

Now using the property $\int_0^t dt_2\int_0^{t_2}dt_1 + \int_0^t dt_1\int_0^{t_1}dt_2 = \int_0^t dt_2\int_0^t dt_1$ to combine the double integrals and rotating back to the original frame, i.e., $\rho(t) = e^{-iHt}\tilde{\rho}(t)e^{iHt}$, we write $\rho(t)$ in block matrix form as

$$\rho(t) = \begin{pmatrix} \big(1-\langle\beta'_\alpha(t)|\beta'_\alpha(t)\rangle\big)|g\rangle\langle g| & |g\rangle\langle\beta'_\alpha(t)| \\ |\beta'_\alpha(t)\rangle\langle g| & |\beta'_\alpha(t)\rangle\langle\beta'_\alpha(t)| \end{pmatrix}, \tag{I.6}$$

where

$$|\beta'_\alpha(t)\rangle \equiv -\int_0^t d\tau\,\alpha(\tau)e^{-iH(t-\tau)}L_{\rm inc}^\dagger|g\rangle. \tag{I.7}$$

Generalization to include an initial phonon pure state follows similarly. Specifically, given an initial pure state $|g\rangle|v\rangle$ that is a product state of the chromophore ground state and a pure vibrational state $|v\rangle$, we first compute the chromophore system + vibration density matrix to the second order perturbation. Tracing out the vibrational degrees of freedom, we obtain the reduced chromophore system density matrix $\rho_{\rm phonon,\ pure}(t)$ as

$$\rho_{\rm phonon,\ pure}(t) = \begin{pmatrix} \big(1-\langle\gamma'_{\alpha,v}(t)|\gamma'_{\alpha,v}(t)\rangle\big)|g\rangle\langle g| & {\rm Tr}_{\rm vib}\,|g\rangle\langle\gamma'_{\alpha,v}(t)| \\ {\rm Tr}_{\rm vib}\,|\gamma'_{\alpha,v}(t)\rangle\langle g| & {\rm Tr}_{\rm vib}\,|\gamma'_{\alpha,v}(t)\rangle\langle\gamma'_{\alpha,v}(t)| \end{pmatrix}, \tag{I.8}$$

where

$$|\gamma'_{\xi,v}(t)\rangle \equiv -\int_0^t d\tau\,\xi(\tau)e^{-iH_{\rm sys+vib}(t-\tau)}L_{\rm inc}^\dagger|g\rangle e^{-iH_{\rm vib}\tau}|v\rangle. \tag{I.9}$$

If the initial phonon state is a thermal mixture of pure states $\sum_v P_v|v\rangle\langle v|$, where each pure state $|v\rangle$ has the Boltzmann weight P_v, then the reduced chromophore system state in the second order perturbation is simply a thermal mixture of the states Eq. (I.8).

$$\rho_{\rm phonon,\ mixed}(t) = \sum_v P_v \begin{pmatrix} \big(1-\langle\gamma'_{\alpha,v}(t)|\gamma'_{\alpha,v}(t)\rangle\big)|g\rangle\langle g| & {\rm Tr}_{\rm vib}\,|g\rangle\langle\gamma'_{\alpha,v}(t)| \\ {\rm Tr}_{\rm vib}\,|\gamma'_{\alpha,v}(t)\rangle\langle g| & {\rm Tr}_{\rm vib}\,|\gamma'_{\alpha,v}(t)\rangle\langle\gamma'_{\alpha,v}(t)| \end{pmatrix}. \tag{I.10}$$

Appendix J

Absorption probability with phonon in the long pulse regime

In our typical HEOM parameter regimes, the time scale for the system to reach the steady state, τ_{steady}, is on the order of 100 fs. Then if $\tau_{\text{steady}} \ll \tau_{\text{pulse}}$, the system essentially remains in a steady state with respect to the HEOM during τ_{pulse}. Using the notation of appendix L, we write the physical density matrix as

$$\rho^{\vec{0}}_{1,1}(t) = P(t)\rho_{\text{st}} + (1 - P(t))\rho_{\text{g}}, \tag{J.1}$$

where $P(t)$ is the excitation probability. Substituting this ansatz into the Fock state + HEOM master equations, Eq. (6.138), and applying Eq. (L.7), we can write the time dependence of the excitation probability as

$$\frac{d}{dt}P(t) = -\xi(t)\text{Tr}(L^{\dagger}_{\text{inc}}\rho^{\vec{0}}_{0,1}) + \text{c.c.} \tag{J.2}$$

The time derivative of $P(t)$ depends on $\rho^{\vec{0}}_{0,1}$. To solve for $\rho^{\vec{0}}_{0,1}$, we first write the equations for the auxiliary density matrices with Fock state index $(0, 1)$ in the vectorized form

$$\frac{d}{dt}\mathbf{v}_{0,1}(t) = -\xi^*(t)\mathbf{v}_{0,0}L_{\text{inc}} + \mathbf{A}\mathbf{v}_{0,1}, \tag{J.3}$$

where $\mathbf{v}_{m,n}$ represents the vectorized form of all $\rho^{\vec{n}}_{m,n}$. $\mathbf{v}_{0,0}$ is independent of time and consists of $|g\rangle\langle g|$ in the $\vec{n} = \vec{0}$ component and 0 in all other components. The notation $\mathbf{v}_{0,0}L_{\text{inc}}$ means right multiplying every auxiliary density matrix in $\mathbf{v}_{0,0}$ by L_{inc}. Solving formally for $\mathbf{v}_{0,1}$,

$$\mathbf{v}_{0,1}(t) = -\int_0^t d\tau\, e^{\mathbf{A}(t-\tau)}\xi^*(\tau)\big(\mathbf{v}_{0,0}L_{\text{inc}}\big). \tag{J.4}$$

Since the HEOM does not connect different excitation subspaces, and the only two HEOM steady states are in the $|\text{ground}\rangle\langle\text{ground}|$ and $|\text{excited}\rangle\langle\text{excited}|$ blocks, the fact that $|g\rangle\langle g|L$ is in the $|\text{ground}\rangle\langle\text{excited}|$ block implies that $\mathbf{v}_{0,0}L$ only contains the transients of HEOM that decay to zero on the time scale of τ_{steady}. Therefore the factor $e^{\mathbf{A}(t-\tau)}$ only contributes significantly when $\tau \in [t - \mathcal{O}(\tau_{\text{steady}}), t]$. Within this time interval, the pulse temporal profile $\xi(\tau)$ is essentially constant. Using Eq. (6.11), we can then approximate $\mathbf{v}_{0,1}$ as

$$\mathbf{v}_{0,1}(t) = -\sqrt{\Gamma_{\text{inc}}}\xi^*(t)\int_0^{\mathcal{O}(\tau_{\text{steady}})} d\tau\, e^{\mathbf{A}\tau}\big(\mathbf{v}_{0,0}|g\rangle\langle B_{\text{inc}}|\big). \tag{J.5}$$

The physical HEOM index $\vec{n} = \vec{0}$ component of the integrand $e^{\mathbf{A}\tau}\big(\mathbf{v}_{0,0}|g\rangle\langle B_{\text{inc}}|\big)$ is strictly in the $|\text{ground}\rangle\langle\text{excited}|$ block for all τ, and we write the integrand as $|g\rangle\langle\zeta(\tau)|$, where $|\zeta(\tau)\rangle$ is some unnormalized state in the singly excited subspace. This is because the action of the HEOM, $e^{\mathbf{A}\tau}$, does not change the excitation number, and the $\vec{n} = \vec{0}$ component of the initial state $\mathbf{v}_{0,0}|g\rangle\langle B_{\text{inc}}|$ (i.e., $|g\rangle\langle B_{\text{inc}}|$) lies in the $|\text{ground}\rangle\langle\text{excited}|$ block. We now write the $\vec{n} = \vec{0}$ component of the integral in Eq. (J.5) in the form

$$\int_0^{\mathcal{O}(\tau_{\text{steady}})} d\tau\, |g\rangle\langle\zeta(\tau)|, \tag{J.6}$$

where $|\zeta(0)\rangle = |B_{\text{inc}}\rangle$, the normalized bright state, and $|\zeta(\tau)\rangle$ decays to 0 on the order of $\tau = \tau_{\text{steady}}$. Therefore the value of this integral is in the $|\text{ground}\rangle\langle\text{excited}|$ block and has magnitude on the order of τ_{steady}. We write this order of magnitude estimate as $\tau_{\text{steady}}|g\rangle\langle\phi|$, where $|\phi\rangle$ is some normalized excited state induced by the HEOM. Now we can express the order of magnitude estimate of the $\vec{n} = \vec{0}$ component of $\mathbf{v}_{0,1}$ in Eq. (J.5) as

$$\rho^{\vec{0}}_{0,1}(t) \sim -\sqrt{\Gamma_{\text{inc}}}\xi^*(t)\tau_{\text{steady}}|g\rangle\langle\phi|. \tag{J.7}$$

Substituting this into Eq. (J.2), we find

$$\frac{d}{dt}P(t) \sim \Gamma_{\text{inc}}|\xi(t)|^2\tau_{\text{steady}}\big|\langle\phi|B_{\text{inc}}\rangle\big|^2. \tag{J.8}$$

Because $|\phi\rangle$ arises from the HEOM and $|B_{\text{inc}}\rangle$ arises from the dipole orientations, they are quite independent of each other, and we expect $|\langle\phi|B_{\text{inc}}\rangle|^2 \sim 1/N$, where N is the number of chromophores. (To obtain this scaling we used the fact that the average square overlap of two independent, uniformly distributed normalized vectors in an N-dimensional Hilbert space is $1/N$.) Integrating $P(t)$ over the pulse duration, we have

$$\text{long pulse abs. prob. with phonon} \sim \frac{\Gamma_{\text{inc}}\tau_{\text{steady}}}{N}. \tag{J.9}$$

We have now arrived at the important result that in the long pulse regime, i.e., $\tau_{\text{pulse}} \gg \tau_{\text{steady}}$, the absorption probability in the presence of phonon coupling is independent of the pulse duration.

Appendix K

Numerical parameters for $\tilde{c}(\tilde{E}_n, E_\nu)$

In Section 7.2.4, we discuss the long pulse absorption probability using a model dimer system. Each chromophore of the dimer system is coupled to two discrete vibrational modes. The parameters are listed in Table K.1 below.

parameter	value (cm^{-1})
α_{j1}	42.5
α_{j2}	50.9
ω_{j1}	40
ω_{j2}	100
ϵ_1	15287
ϵ_2	15157
J	38.1
k_BT	200

Table K.1: Numerical values for the parameters of Eqs. (7.43) - (7.45) in the main text. The values are used to generate Figure (7.10). The α_{jk}'s and ω_{jk}'s are the same for both sites and thus independent of the site index j.

For ease of calculation, instead of treating $c(E_n, E_v)$ as a function of continuous variables as in Eq. (7.38), we discretized E_n and E_v into 20 cm^{-1} bins and replaced the delta function $\delta(E_1 - E_2)$ in Eq. (7.38) by the binning function

$$\chi(E_1, E_2) = \begin{cases} \frac{1}{20\,\mathrm{cm}^{-1}} & E_1 \text{ and } E_2 \text{ are in the same bin} \\ 0 & \text{otherwise,} \end{cases} \tag{K.1}$$

where the factor $1/20\,\mathrm{cm}^{-1}$ ensures proper normalization $\int dE_1\, \chi(E_1, E_2) = 1$. Then the discretized $\widetilde{c}(\widetilde{E}_n, E_v)$ takes the form

$$\widetilde{c}(\widetilde{E}_n, E_v) = \sum_{\widetilde{n}', v'} \widetilde{c}_{n',v'} \chi(\widetilde{E}_n, \widetilde{E}'_n) \chi(E_v, E'_v). \tag{K.2}$$

Appendix L

Detailed proof of the long time emission behavior (Eqs. 7.46 and 7.47)

We first note that on restriction to the ground and singly excited subspaces of the system Hilbert space, the HEOM has two steady state solutions. One is the ground state $\rho_{\mathrm{g}} = |g\rangle\langle g|$, and the other lies in the singly excited subspace. We denote the normalized steady state in the singly excited subspace as ρ_{st}. We express the HEOM in a vectorized form as $d\mathbf{v}/dt = \mathbf{A}\mathbf{v}$, where the vector $\mathbf{v}$ contains the vectorized physical system density matrix and all vectorized HEOM auxiliary density matrices, and $\mathbf{A}$ is a matrix such that $\mathbf{A}\mathbf{v}$ gives the HEOM time derivative. The two steady states $\mathbf{v}_1$ and $\mathbf{v}_2$ satisfy $\mathbf{A}\mathbf{v}_1 = \mathbf{A}\mathbf{v}_2 = 0$, and are degenerate eigenvectors of $\mathbf{A}$ with eigenvalue 0. $\mathbf{v}_1$ consists of ρ_{g} in the physical density matrix and 0 in all other auxiliary density matrices. $\mathbf{v}_2$ consists of ρ_{st} in the physical density matrix and takes some nonzero values in other auxiliary density matrices.

After the single photon pulse has passed (i.e.. when $\xi(t)$ becomes negligibly small), the Fock state indices in Eq. (6.138) decouple from each other, and the physical $(1,1)$ component of the Fock state hierarchy evolves with the HEOM plus the Lindblad dissipators that account for spontaneous emission. We therefore write the system dynamics as $d\mathbf{v}/dt = (\mathbf{A} + \mathbf{D})\mathbf{v}$, where $\mathbf{D}$ is the Lindblad dissipator $\sum_l \mathcal{D}[L_l]$. Since the energy scale of $\mathbf{D}$ is much smaller than the energy scale of $\mathbf{A}$, we can think of $\mathbf{D}$ as a perturbation on $\mathbf{A}$ that breaks the degeneracy of $\mathbf{v}_1$ and $\mathbf{v}_2$. $\mathbf{v}_1$ remains the eigenvector with zero eigenvalue, since one can check directly that $\mathbf{D}\mathbf{v}_1 = 0$. Following a degenerate perturbation theory approach, to the lowest order the other perturbed eigenvector $\mathbf{v}_2'$ can be written as a linear combination of the unperturbed eigenvectors plus a correction of order $\epsilon \sim |\mathbf{D}|/|\mathbf{A}| \sim \tau_{\mathrm{sys+vib}}/\tau_{\mathrm{emission}}$:

$$\mathbf{v}_2' = c_1\mathbf{v}_1 + c_2\mathbf{v}_2 + \mathcal{O}(\epsilon). \tag{L.1}$$

The corresponding eigenvalue (denoted as $-\Gamma_{\text{long time}}$ for reasons to be clear in a moment) is small in magnitude, on the energy scale of spontaneous emission. Note that we do not assume the eigenvectors are orthogonal, since $\mathbf{A}$ and $\mathbf{A} + \mathbf{D}$ are in general not normal operators.

At long times, when the transients of HEOM decay away, the vectorized system plus auxiliary density matrices take the form

$$\mathbf{v}(t) = d_1\mathbf{v}_1 + d_2\mathbf{v}_2' e^{-\Gamma_{\text{long time}}t}. \tag{L.2}$$

Using Eq. (L.1), we write the physical density matrix at long times as

$$\rho(t) = d_1\rho_{\rm g} + d_2 e^{-\Gamma_{\text{long time}}t}(c_1\rho_{\rm g} + c_2\rho_{\rm st} + \mathcal{O}(\epsilon)). \tag{L.3}$$

Since the excited state will eventually decay to the ground state, $\Gamma_{\text{long time}}$ has a positive real part. In fact, we will see below that to the lowest order $\Gamma_{\text{long time}}$ is purely real. Using the fact that $\rho(\infty) = \rho_{\rm g}$ and $\mathrm{Tr}\rho = 1$, we obtain $d_1 = 1$ and $c_1 = -c_2$, and hence

$$\rho(t) = \rho_g + be^{-\Gamma_{\text{long time}}t}(\rho_{\rm st} - \rho_{\rm g} + \mathcal{O}(\epsilon)), \tag{L.4}$$

where $b = d_2c_2$. Thus the excited portion of the system density matrix follows a single exponential decay into the ground state.

To determine the value of $\Gamma_{\text{long time}}$, we first take the time derivative of Eq. (L.4)

$$\frac{d}{dt}\rho(t) = -b\Gamma_{\text{long time}}e^{-\Gamma_{\text{long time}}t}(\rho_{\rm st} - \rho_{\rm g} + \mathcal{O}(\epsilon)). \tag{L.5}$$

On the other hand, substituting Eq. (L.4) into the Fock state + HEOM master equation (Eq. (6.138)), we have

$$\frac{d}{dt}\rho(t) = \big(\text{HEOM} + \sum_l \mathcal{D}[L_l]\big)\big(\rho_{\rm g} + be^{-\Gamma_{\text{long time}}t}(\rho_{\rm st} - \rho_{\rm g} + \mathcal{O}(\epsilon))\big), \tag{L.6}$$

where "HEOM" is used as shorthand for the Hamiltonian evolution term together with the HEOM part of the Fock state + HEOM master equation, Eq. (6.138).

The rate of change of the total excited subspace probability is

$$\frac{dP}{dt} = \mathrm{Tr}(\Pi_{\rm ex}\frac{d\rho}{dt}), \tag{L.7}$$

where $\Pi_{\rm ex} \equiv \sum_j |j\rangle\langle j|$ is the excited subspace projector. From Eq. (L.5), we have

$$\frac{dP}{dt} = b\Gamma_{\text{long time}}e^{-\Gamma_{\text{long time}}t}(1 + \mathcal{O}(\epsilon)), \tag{L.8}$$

and from Eq. (L.6), we have

$$\frac{dP}{dt} = be^{-\Gamma_{\text{long time}}t}\sum_l \mathrm{Tr}(L_l^\dagger L_l\rho_{\rm st} + \mathcal{O}(\epsilon)). \tag{L.9}$$

The HEOM term does not contribute to dP/dt, since HEOM does not change the system excitation number. Comparing Eq. (L.8) to Eq. (L.9), we then arrive at the identification

$$\Gamma_{\text{long time}} = (1 + \mathcal{O}(\epsilon))\sum_l \mathrm{Tr}(L_l^\dagger L_l\rho_{\rm st}). \tag{L.10}$$

Appendix M

Using singular value decomposition to obtain collective dipole moments

To understand the effect of light polarization, it is useful to re-express $\sum_j |\mathbf{d}_j \cdot \hat{\epsilon}|^2$ as the matrix product $\epsilon^\dagger \mathbf{D}^\dagger \mathbf{D} \epsilon$, where ϵ is a 3×1 unit vector representing the light polarization and $\mathbf{D}$ is an $N \times 3$ matrix with the j-th row being the transition dipole moment of the j-th chromophore. We then perform a singular value decomposition on $\mathbf{D}$ by writing the orthonormal eigenvectors of $\mathbf{D}^\dagger \mathbf{D}$ (or singular vectors of $\mathbf{D}$) as e_1, e_2, and e_3, corresponding to the non-negative eigenvalues d_1^2, d_2^2, and d_3^2, where d_1, d_2, and d_3 are the non-negative singular values. Without loss of generality, we let $d_1 \geq d_2 \geq d_3 \geq 0$. Light polarized in e_1 maximizes $\epsilon^\dagger \mathbf{D}^\dagger \mathbf{D} \epsilon$, therefore maximizing the absorption probability. Expressing everything in the singular vector basis, given a light polarization $\hat{\epsilon} = a_1 e_1 + a_2 e_2 + a_3 e_3$, then

$$\sum_j |\mathbf{d}_j \cdot \hat{\epsilon}|^2 = a_1^2 d_1^2 + a_2^2 d_2^2 + a_3^2 d_3^2. \tag{M.1}$$

To confirm numerically the linear dependence of the absorption probability on $\sum_j |\mathbf{d}_j \cdot \hat{\epsilon}|^2$, we consider single photon excitation of a dimer system coupled to a vibrational bath via the double hierarchy of photon field and HEOM bath. We let each chromophore have a transition dipole moment of 4 Debye, the relevant value for chlorophyll molecules [112]. Since any two vectors in 3-dimensional space have a common plane, we only need to consider two singular vectors. The third singular vector is perpendicular to the common plane, and has 0 singular value. On the plane, one of the singular vectors lies in the middle of the two dipoles, corresponding to a singular value of $d_{\text{inner}} = 4\sqrt{1 + \cos\phi}$, where ϕ (satisfying $0 \leq \phi \leq \pi$) is the angle between the two dipoles. We call this singular vector the inner singular vector. The other singular vector, labeled as the outer singular vector, is orthogonal to the inner singular vector on the common plane, and corresponds to a singular value of $d_{\text{outer}} = 4\sqrt{1 - \cos\phi}$. When $0 \leq \phi \leq \pi/2$, $d_{\text{inner}} \geq d_{\text{outer}}$, so the inner singular vector maximizes the absorption probability. When $\pi/2 \leq \phi \leq \pi$, $d_{\text{outer}} \geq d_{\text{inner}}$, and the outer singular vector maximizes the absorption probability.

As a first example, we fix the angle between the two dipole moments to be $\phi \approx 2.28$ rad, corresponding to the dipole orientations of chlorophylls a602 and a603 in LHCII. We vary the light polarization along the plane that contains both dipole moments, and parameterize the polarization

by the angle θ to the outer singular vector (see Figure (M.1)). Using Eq. (M.1), one can show that

$$\sum_j |\mathbf{d}_j \cdot \hat{\epsilon}|^2 = 16(1 - \cos\phi \cos 2\theta). \tag{M.2}$$

Figure (M.1) shows the results of numerical calculations with the double hierarchy. These show that the maximum absorption probability is indeed proportional to Eq. (M.2) across all θ. Since ϕ is between $\pi/2$ and π, the maximal (minimal) absorption probability occurs at the outer (inner) singular vector.

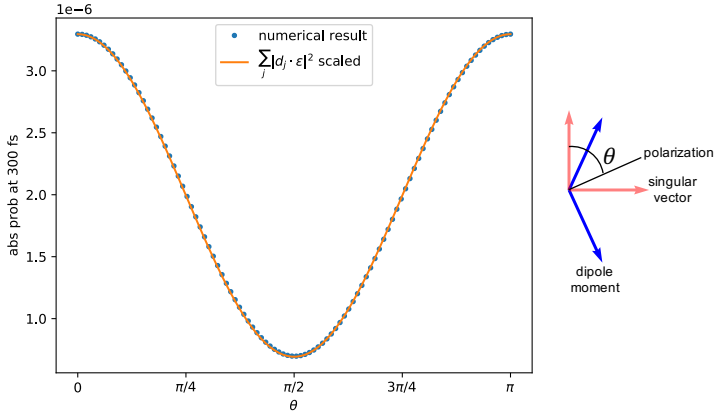

Figure M.1: Double hierarchy calculations of single photon absorption for a chromophore dimer system within LHCII, fixing the dipole orientations and varying the light polarization, which is parameterized by θ. The maximum absorption probability is proportional to Eq. (M.2). 5 HEOM levels were included in the calculation. See text for details of the dimer system.

In another example, we fix the polarization to be either the inner singular vector or the outer singular vector, and vary the angle ϕ between the dipole moments. Substituting the appropriate θ into Eq. (M.2), when the polarization is the inner singular vector, $\sum_j |\mathbf{d}_j \cdot \hat{\epsilon}|^2 = 32\cos^2(\phi/2)$, and when the polarization is the outer singular vector, $\sum_j |\mathbf{d}_j \cdot \hat{\epsilon}|^2 = 32\sin^2(\phi/2)$. Figure (M.2) shows the linear dependence of the maximum absorption probability on $\sum_j |\mathbf{d}_j \cdot \hat{\epsilon}|^2$ again. When $\phi = 0$, the inner singular vector aligns with both dipoles, maximizing the absorption probability, while the outer singular vector is perpendicular to both dipoles, giving zero absorption probability. The opposite is true when $\phi = \pi$.

This type of singular value analysis can be applied to more general chromophore systems to understand the dependence of the absorption probability on the polarization of the incident Fock state photon and the dipole orientations.

Experimentally, the light harvesting systems are typically randomly oriented in solution. Assuming a uniform distribution over all orientations, averaging over all system orientations while fixing the polarization is equivalent to averaging over all polarization directions while fixing the system orientation. Note that rotating the system around the polarization direction does not change $\sum_j |\mathbf{d}_j \cdot \hat{\epsilon}|^2$. Averaging the polarization over all solid angles Ω , we have

$$\text{avg}\Big(\sum_j |\mathbf{d}_j \cdot \hat{\epsilon}|^2\Big) = \frac{1}{4\pi}\int d\Omega \sum_j |\mathbf{d}_j \cdot \hat{\epsilon}(\Omega)|^2 = \frac{1}{3}\sum_j |\mathbf{d}_j|^2, \tag{M.3}$$

which depends only on the magnitude and not on the relative orientation of the dipole moments.

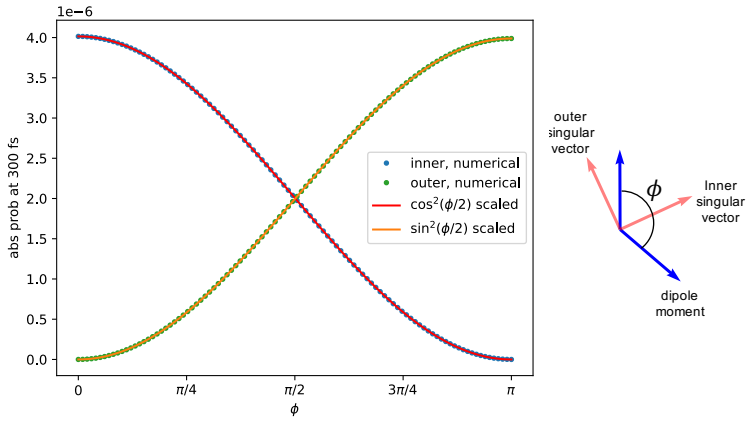

Figure M.2: Double hierarchy calculations of single photon absorption for a chromophore dimer system, varying the angle ϕ between the dipoles, and letting the light polarization to be either the inner or outer singular vector. The maximum absorption probability is proportional to Eq. (M.2). 5 HEOM levels were included in the calculation. See text for details of the dimer system.

Bibliography

[1] E. Wientjes, J. Renger, A. G. Curto, R. Cogdell, and N. F. Van Hulst. Strong antenna-enhanced fluorescence of a single light-harvesting complex shows photon antibunching. Nat. Commun., 5(1):4236, 2014.

[2] J. M. Cui, F. W Sun, X.D. Chen, Z. J. Gong, and G. C. Guo. Quantum statistical imaging of particles without restriction of the diffraction limit. Phys. Rev. Lett., 110(15):153901, 2013.

[3] J. M. Lupton and J. Vogelsang. Photon correlations probe the quantized nature of light emission from optoelectronic materials. Appl. Phys. Rev., 8(4):041302, 2021.

[4] C. Hettich, C. Schmitt, J. Zitzmann, S. Kuhn, I. Gerhardt, and V. Sandoghdar. Nanometer resolution and coherent optical dipole coupling of two individual molecules. Science, 298(5592):385–389, 2002.

[5] H. J. Kimble, M. Dagenais, and L. Mandel. Photon antibunching in resonance fluorescence. Phys. Rev. Lett., 39(11):691–695, 1977.

[6] P. J. Shadbolt, M. R. Verde, A. Peruzzo, A. Politi, A. Laing, M. Lobino, J. C. F. Matthews, M. G. Thompson, and J. L. O'Brien. Generating, manipulating and measuring entanglement and mixture with a reconfigurable photonic circuit. Nat. Photonics, 6(1):45–49, 2012.

[7] K. Edamatsu, G. Oohata, R. Shimizu, and T. Itoh. Generation of ultraviolet entangled photons in a semiconductor. Nature, 431(7005):167–170, 2004.

[8] R. M. Stevenson, A. J. Hudson, R. J. Young, P. Atkinson, K. Cooper, D. A. Ritchie, and A. J. Shields. Biphoton interference with a quantum dot entangled light source. Opt. Express, 15(10):6507–6512, 2007.

[9] P. G. Kwiat, K. Mattle, H. Weinfurter, A. Zeilinger, A. V. Sergienko, and Y. Shih. New high-intensity source of polarization-entangled photon pairs. Phys. Rev. Lett., 75(24):4337–4341, 1995.

[10] V. Sultanov, A. Kavčič, E. Kokkinakis, N. Sebastián, M. V. Chekhova, and M. Humar. Tunable entangled photon-pair generation in a liquid crystal. Nature, 631(8020):294–299, 2024.

[11] L. A. Wu, M. Xiao, and H. J. Kimble. Squeezed states of light from an optical parametric oscillator. J. Opt. Soc. Am. B, 4(10):1465–1475, 1987.

[12] N. Aggarwal, T. J. Cullen, J. Cripe, G. D. Cole, R. Lanza, A. Libson, D. Follman, P. Heu, T. Corbitt, and N. Mavalvala. Room-temperature optomechanical squeezing. Nat. Phys., 16(7):784–788, 2020.

[13] A. Ourjoumtsev, A. Kubanek, M. Koch, C. Sames, P. W. H. Pinkse, G. Rempe, and K. Murr. Observation of squeezed light from one atom excited with two photons. Nature, 474(7353):623–626, 2011.

[14] L. A. Wu, H. J. Kimble, J. L. Hall, and H. Wu. Generation of squeezed states by parametric down conversion. Phys. Rev. Lett., 57(20):2520–2523, 1986.

[15] A. H. Safavi-Naeini, S. Gröblacher, J. T. Hill, J. Chan, M. Aspelmeyer, and O. Painter. Squeezed light from a silicon micromechanical resonator. Nature, 500(7461):185–189, 2013.

[16] D. A. Kalashnikov, E. V. Melik-Gaykazyan, A. A. Kalachev, Y. F. Yu, A. I. Kuznetsov, and L. A. Krivitsky. Quantum interference in the presence of a resonant medium. Sci. Rep., 7(1):11444, 2017.

[17] C. K. Hong, Z. Y. Ou, and L. Mandel. Measurement of subpicosecond time intervals between two photons by interference. Phys. Rev. Lett., 59(18):2044, 1987.

[18] R. Lettow, Y. L. A. Rezus, A. Renn, G. Zumofen, E. Ikonen, S. Götzinger, and V. Sandoghdar. Quantum interference of tunably indistinguishable photons from remote organic molecules. Phys. Rev. Lett., 104(12):123605, 2010.

[19] A. Sipahigil, K. D. Jahnke, L. J. Rogers, T. Teraji, J. Isoya, A. S. Zibrov, F. Jelezko, and M. D. Lukin. Indistinguishable photons from separated silicon-vacancy centers in diamond. Phys. Rev. Lett., 113(11):113602, 2014.

[20] Y. H. Deng, H. Wang, X. Ding, Z. C. Duan, J. Qin, M. C. Chen, Y. He, Y. M. He, J. P. Li, Y. H. Li, L. C. Peng, E. S. Matekole, T. Byrnes, C. Schneider, M. Kamp, D. W. Wang, J. P. Dowling, S. Höfling, C. Y. Lu, M. O. Scully, and J. W. Pan. Quantum interference between light sources separated by 150 million kilometers. Phys. Rev. Lett., 123(8):080401, 2019.

[21] H. S. Zhong, H. Wang, Y. H. Deng, M. C. Chen, L. C. Peng, Y. H. Luo, J. Qin, D. Wu, X. Ding, Y. Hu, P. Hu, X. Y. Yang, W. J. Zhang, G. Li, Y. X. Li, X. Jiang, L. Gan, G. W. Yang, L. X. You, Z. Wang, L. Li, N. L. Liu, C. Y. Lu, and J. W. Pan. Quantum computational advantage using photons. Science, 370(6523):1460–1463, 2020.

[22] S. Slussarenko and G. J. Pryde. Photonic quantum information processing: A concise review. Appl. Phys. Rev., 6(4):041303, 2019.

[23] J. L. O'brien, A. Furusawa, and J. Vučković. Photonic quantum technologies. Nat. Photonics, 3(12):687–695, 2009.

[24] C. M. Caves. Quantum-mechanical noise in an interferometer. Phys. Rev. D, 23(8):1693, 1981.

[25] J. Aasi, J. Abadie, B. P. Abbott, R. Abbott, T. D. Abbott, M. R. Abernathy, C. Adams, T. Adams, P. Addesso, R. X. Adhikari, et al. Enhanced sensitivity of the ligo gravitational wave detector by using squeezed states of light. Nat. Photonics, 7(8):613–619, 2013.

[26] A. F. Abouraddy, M. B. Nasr, B. E. A. Saleh, A. V. Sergienko, and M. C. Teich. Quantum-optical coherence tomography with dispersion cancellation. Phys. Rev. A, 65(5):053817, 2002.

[27] G. B. Lemos, V. Borish, G. D. Cole, S. Ramelow, R. Lapkiewicz, and A. Zeilinger. Quantum imaging with undetected photons. Nature, 512(7515):409–412, 2014.

[28] S. Asban, K. E. Dorfman, and S. Mukamel. Quantum phase-sensitive diffraction and imaging

using entangled photons. Proc. Natl. Acad. Sci. U.S.A., 116(24):11673–11678, 2019.

[29] A. N. Boto, P. Kok, D. S. Abrams, S. L. Braunstein, C. P. Williams, and J. P. Dowling. Quantum interferometric optical lithography: Exploiting entanglement to beat the diffraction limit. Phys. Rev. Lett., 85(13):2733–2736, 2000.

[30] K. E. Dorfman, F. Schlawin, and S. Mukamel. Nonlinear optical signals and spectroscopy with quantum light. Rev. Mod. Phys., 88(4):045008, 2016.

[31] F. Schlawin. Entangled photon spectroscopy. J. Phys. B: At., Mol. Opt. Phys., 50(20):203001, 2017.

[32] K. Matsuzaki and T. Tahara. Superresolution concentration measurement realized by sub-shot-noise absorption spectroscopy. Nat. Commun., 13(1):953, 2022.

[33] F. Schlawin, K. E. Dorfman, B. P. Fingerhut, and S. Mukamel. Manipulation of two-photon-induced fluorescence spectra of chromophore aggregates with entangled photons: A simulation study. Phys. Rev. A, 86(2):023851, 2012.

[34] A. Ishizaki. Probing excited-state dynamics with quantum entangled photons: Correspondence to coherent multidimensional spectroscopy. J. Chem. Phys., 153(5), 2020.

[35] F. Schlawin, K. E. Dorfman, and S. Mukamel. Entangled two-photon absorption spectroscopy. Acc. Chem. Res., 51(9):2207–2214, 2018.

[36] M. G. Raymer, T. Landes, and A. H. Marcus. Entangled two-photon absorption by atoms and molecules: A quantum optics tutorial. J. Chem. Phys., 155(8):081501, 2021.

[37] P. Grangier, R. E. Slusher, B. Yurke, and A. LaPorta. Squeezed-light–enhanced polarization interferometer. Phys. Rev. Lett., 59(19):2153, 1987.

[38] E. S. Polzik, J. Carri, and H. J. Kimble. Spectroscopy with squeezed light. Phys. Rev. Lett., 68(20):3020, 1992.

[39] C. S. Muñoz and F. Schlawin. Photon correlation spectroscopy as a witness for quantum coherence. Phys. Rev. Lett., 124(20):203601, 2020.

[40] D. I. H. Holdaway, V. Notararigo, and A. Olaya-Castro. Perturbation approach for computing frequency- and time-resolved photon correlation functions. Phys. Rev. A, 98(6):063828, 2018.

[41] C. Nation, H. O. Gestsson, and A. Olaya-Castro. Photon correlation time-asymmetry and dynamical coherence in multichromophoric systems. arXiv:2404.16892, 2024.

[42] C. Nation, V. Notararigo, H. O. Gestsson, L. Sapienza, and A. Olaya-Castro. Two-colour photon correlations probe coherent vibronic contributions to electronic excitation transport under incoherent illumination. arXiv:2403.00857, 2024.

[43] D. Zigmantas, T. Polívka, P. Persson, and V. Sundström. Ultrafast laser spectroscopy uncovers mechanisms of light energy conversion in photosynthesis and sustainable energy materials. Chem. Phys. Rev., 3(4):041303, 2022.

[44] R. van Grondelle and V. I. Novoderezhkin. Energy transfer in photosynthesis: experimental insights and quantitative models. Chem. Phys. Phys. Chem., 8(7):793–807, 2006.

[45] E. A. Arsenault, P. Bhattacharyya, Y. Yoneda, and G. R. Fleming. Two-dimensional electronic–vibrational spectroscopy: Exploring the interplay of electrons and nuclei in excited state molecular dynamics. J. Chem. Phys., 155(2):020901, 2021.

[46] S. Mukamel. Principles of Nonlinear Optical Spectroscopy. Oxford series in optical and imaging sciences. Oxford University Press, 1995.

[47] B. Q. Baragiola, R. L. Cook, A. M. Brańczyk, and J. Combes. N-photon wave packets interacting with an arbitrary quantum system. Phys. Rev. A, 86(1):013811, 2012.

[48] Y. Tanimura and R. Kubo. Time evolution of a quantum system in contact with a nearly Gaussian-Markoffian noise bath. J. Phys. Soc. Jpn., 58(1):101–114, 1989.

[49] A. Ishizaki and G. R. Fleming. Unified treatment of quantum coherent and incoherent hopping dynamics in electronic energy transfer: Reduced hierarchy equation approach. J. Chem. Phys., 130(23):234111, 2009.

[50] C. W. Gardiner and M. J. Collett. Input and output in damped quantum systems: Quantum stochastic differential equations and the master equation. Phys. Rev. A, 31(6):3761, 1985.

[51] J. Combes, J. Kerckhoff, and M. Sarovar. The SLH framework for modeling quantum input-output networks. Adv. Phys.: X, 2(3):784–888, 2017.

[52] L. Ko, R. L. Cook, and K. B. Whaley. Dynamics of photosynthetic light harvesting systems interacting with n-photon fock states. J. Chem. Phys., 156(24):244108, 2022.

[53] R. L. Cook, L. Ko, and K. B. Whaley. A quantum trajectory picture of single photon absorption and energy transport in photosystem II. J. Chem. Phys., 159(13):134108, 2023.

[54] Q. Li, K. Orcutt, R. L. Cook, J. Sabines-Chesterking, A. L. Tong, G. S. Schlau-Cohen, X. Zhang, G. R. Fleming, and K. B. Whaley. Single-photon absorption and emission from a natural photosynthetic complex. Nature, 619(7969):300–304, 2023.

[55] A. Ishizaki. Probing excited-state dynamics with quantum entangled photons: Correspondence to coherent multidimensional spectroscopy. J. Chem. Phys., 153(5):051102, 2020.

[56] F. Schlawin, K. E. Dorfman, and S. Mukamel. Pump-probe spectroscopy using quantum light with two-photon coincidence detection. Phys. Rev. A, 93(2):023807, 2016.

[57] S. Asban and S. Mukamel. Distinguishability and "which pathway" information in multidimensional interferometric spectroscopy with a single entangled photon-pair. Sci. Adv., 7(39):eabj4566, 2021.

[58] S. Asban, V. Y. Chernyak, and S. Mukamel. Nonlinear quantum interferometric spectroscopy with entangled photon pairs. J. Chem. Phys., 156(9):094202, 2022.

[59] H. C. H. Chan, O. E. Gamel, G. R. Fleming, and K. B. Whaley. Single-photon absorption by single photosynthetic light-harvesting complexes. J. Phys. B-At. Mol. Opt., 51(5):054002, 2018.

[60] L. Ko, R. L. Cook, and K. B. Whaley. Emulating quantum entangled biphoton spectroscopy using classical light pulses. J. Phys. Chem. Lett., 14(36):8050–8059, 2023.

[61] Z. Z. Li, L. Ko, Z. Yang, M. Sarovar, and K. B. Whaley. Unraveling excitation energy transfer assisted by collective behaviors of vibrations. New J. Phys., 23(7):073012, 2021.

[62] Z. Z. Li, L. Ko, Z. Yang, M. Sarovar, and K. B. Whaley. Interplay of vibration-and environment-assisted energy transfer. New J. Phys., 24(3):033032, 2022.

[63] T. Kharazi, T. F. Stetina, L. Ko, G. H. Low, and K. B. Whaley. An efficient quantum algorithm for generation of ab initio n-th order susceptibilities for non-linear spectroscopies. arXiv:2404.01454, 2024.

[64] L. Ko, R. L. Cook, and K. B. Whaley. Input-output formulation of quantum nonlinear spectroscopy. To be published.

[65] H. M. Wiseman and G. J. Milburn. Quantum Measurement and Control. Cambridge University Press, 2009.

[66] L. Ye and S. Mukamel. Interferometric two-photon-absorption spectroscopy with three entangled photons. Appl. Phys. Lett., 116(17):174003, 2020.

[67] R. Loudon. The quantum theory of light. Oxford University Press, 2000.

[68] C. Kreisbeck and A. Aspuru-Guzik. Efficiency of energy funneling in the photosystem II supercomplex of higher plants. Chem. Sci., 7(7):4174–4183, 2016.

[69] S. Kundu and N. Makri. Real-time path integral simulation of exciton-vibration dynamics in light-harvesting bacteriochlorophyll aggregates. J. Phys. Chem. Lett., 11(20):8783–8789, 2020.

[70] T. C. Berkelbach, T. E. Markland, and D. R. Reichman. Reduced density matrix hybrid approach: Application to electronic energy transfer. J. Chem. Phys., 136(8):084104, 2012.

[71] J. J. J. Roden, D. I. G. Bennett, and K. B. Whaley. Long-range energy transport in photosystem II. J. Chem. Phys., 144(24):245101, 2016.

[72] R. E. Blankenship. Molecular mechanisms of photosynthesis. John Wiley & Sons, 3rd edition, 2021.

[73] J. Olšina, A. G. Dijkstra, C. Wang, and J. Cao. Can natural sunlight induce coherent exciton dynamics? arXiv:1408.5385, 2014.

[74] P. Y. Yang and J. Cao. Steady-state analysis of light-harvesting energy transfer driven by incoherent light: From dimers to networks. J. Phys. Chem. Lett., 11(17):7204–7211, 2020.

[75] T. Mančal and L. Valkunas. Exciton dynamics in photosynthetic complexes: excitation by coherent and incoherent light. New J. Phys., 12(6):065044, 2010.

[76] P. Brumer and M. Shapiro. Molecular response in one-photon absorption via natural thermal light vs. pulsed laser excitation. Proc. Natl. Acad. Sci. U.S.A., 109(48):19575–19578, 2012.

[77] T. V. Tscherbul and P. Brumer. Non-equilibrium stationary coherences in photosynthetic energy transfer under weak-field incoherent illumination. J. Chem. Phys., 148(12):124114, 2018.

[78] L. A. Pachón, J. D. Botero, and P. Brumer. Open system perspective on incoherent excitation of light-harvesting systems. J. Phys. B: At. Mol. Opt., 50(18):184003, 2017.

[79] P. Brumer. Shedding (incoherent) light on quantum effects in light-induced biological processes. J. Phys. Chem. Lett., 9(11):2946–2955, 2018.

[80] J. Jin, S. Welack, J. Y. Luo, X. Q. Li, P. Cui, R. X. Xu, and Y. J. Yan. Dynamics of quantum dissipation systems interacting with fermion and boson grand canonical bath ensembles: Hierarchical equations of motion approach. J. Chem. Phys., 126(13):134113, 2007.

[81] J. Bätge, Y. Ke, C. Kaspar, and M. Thoss. Nonequilibrium open quantum systems with multiple bosonic and fermionic environments: A hierarchical equations of motion approach. Phys. Rev. B, 103(23):235413, 2021.

[82] R. H. Dicke. Coherence in Spontaneous Radiation Processes. Phys. Rev., 93(1):99, 1954.

[83] R. H. Lehmberg. Radiation from an N-atom system. I. general formalism. Phys. Rev. A, 2(3):883–888, 1970.

[84] M. Gross and S. Haroche. Superradiance: An essay on the theory of collective spontaneous emission. Phys. Rep., 93(5):301–396, 1982.

[85] F. C. Spano and S. Mukamel. Superradiance in molecular aggregates. J. Chem. Phys., 91(2):683–700, 1989.

[86] C. Gardiner and P. Zoller. Quantum noise: a handbook of Markovian and non-Markovian quantum stochastic methods with applications to quantum optics. Springer Science & Business Media, 2004.

[87] E. del Valle, A. Gonzalez-Tudela, F. P. Laussy, C. Tejedor, and M. J. Hartmann. Theory of frequency-filtered and time-resolved n-photon correlations. Phys. Rev. Lett., 109(18):183601, 2012.

[88] C. W. Gardiner. Driving a quantum system with the output field from another driven quantum system. Phys. Rev. Lett., 70(15):2269, 1993.

[89] T. Caneva, M. T. Manzoni, T. Shi, J. S. Douglas, J. I. Cirac, and D. E. Chang. Quantum dynamics of propagating photons with strong interactions: a generalized input–output formalism. New J. Phys., 17(11):113001, 2015.

[90] R. Glenn, K. Bennett, K. E. Dorfman, and S. Mukamel. Photon-exchange induces optical nonlinearities in harmonic systems. J. Phys. B: At. Mol. Opt., 48(6):065401, 2015.

[91] E. A. Arsenault, Y. Yoneda, M. Iwai, K. K. Niyogi, and G. R. Fleming. Vibronic mixing enables ultrafast energy flow in light-harvesting complex ii. Nat. Commun., 11(1):1460, 2020.

[92] A. Niedringhaus, V. R. Policht, R. Sechrist, A. Konar, P. D. Laible, D. F. Bocian, D. Holten, C. Kirmaier, and J. P. Ogilvie. Primary processes in the bacterial reaction center probed by two-dimensional electronic spectroscopy. Proc. Natl. Acad. Sci. U.S.A., 115(14):3563–3568, 2018.

[93] F. Ma, E. Romero, M. R. Jones, V. I. Novoderezhkin, and R. van Grondelle. Both electronic and vibrational coherences are involved in primary electron transfer in bacterial reaction center. Nat. Commun., 10(1):933, 2019.

[94] L. Bolzonello, F. Bernal-Texca, L. G. Gerling, J. Ockova, E. Collini, J. Martorell, and N. F. Van Hulst. Photocurrent-detected 2D electronic spectroscopy reveals ultrafast hole transfer in operating PM6/Y6 organic solar cells. J. Phys. Chem. Lett., 12(16):3983–3988, 2021.

[95] Y. Fujihashi, K. Miwa, M. Higashi, and A. Ishizaki. Probing exciton dynamics with spectral selectivity through the use of quantum entangled photons. J. Chem. Phys., 159(11):114201,

2023.

[96] S. Mukamel, M. Freyberger, W. Schleich, M. Bellini, A. Zavatta, G. Leuchs, C. Silberhorn, R. W. Boyd, L. L. Sánchez-Soto, A. Stefanov, M. Barbieri, A. Paterova, L. Krivitsky, S. Shwartz, K. Tamasaku, K. Dorfman, F. Schlawin, V. Sandoghdar, M. Raymer, A. Marcus, O. Varnavski, T. Goodson, Z. Y. Zhou, B. S. Shi, S. Asban, M. Scully, G. Agarwal, T. Peng, A. V. Sokolov, Z. D. Zhang, M. S. Zubairy, I. A. Vartanyants, E. del Valle, and F. Laussy. Roadmap on quantum light spectroscopy. J. Phys. B: At., Mol. Opt. Phys., 53(7):072002, 2020.

[97] S. Szoke, H. Liu, B. P. Hickam, M. He, and S. K. Cushing. Entangled light-matter interactions and spectroscopy. J. Mater. Chem. C, 8(31):10732–10741, 2020.

[98] G. Scarcelli, A. Valencia, S. Gompers, and Y. Shih. Remote spectral measurement using entangled photons. Appl. Phys. Lett., 83(26):5560–5562, 2003.

[99] A. Yabushita and T. Kobayashi. Spectroscopy by frequency-entangled photon pairs. Phys. Rev. A, 69(1):013806, 2004.

[100] A. A. Kalachev, D. A. Kalashnikov, A. A. Kalinkin, T. G. Mitrofanova, A. V. Shkalikov, and V. V. Samartsev. Biphoton spectroscopy of YAG:Er^{3+} crystal. Laser Phys. Lett., 4(10):722, 2007.

[101] K. E. Dorfman, F. Schlawin, and S. Mukamel. Stimulated raman spectroscopy with entangled light: Enhanced resolution and pathway selection. J. Phys. Chem. Lett., 5(16):2843–2849, 2014.

[102] D. A. Kalashnikov, Z. Pan, A. I. Kuznetsov, and L. A. Krivitsky. Quantum spectroscopy of plasmonic nanostructures. Phys. Rev. X, 4(1):011049, 2014.

[103] D. A. Kalashnikov, A. V. Paterova, S. P. Kulik, and L. A. Krivitsky. Infrared spectroscopy with visible light. Nat. Photon, 10(2):98–101, 2016.

[104] C. Ye, Y. Sun, and X. Zhang. Entanglement-assisted quantum chiral spectroscopy. J. Phys. Chem. Lett., 12(35):8591–8597, 2021.

[105] Z. Zhang, T. Peng, X. Nie, G. S. Agarwal, and M. O. Scully. Entangled photons enabled time-frequency-resolved coherent raman spectroscopy and applications to electronic coherences at femtosecond scale. Light Sci. Appl., 11(1):274, 2022.

[106] A. Stefanov. On the role of entanglement in two-photon metrology. Quantum Sci. Technol., 2(2):025004, 2017.

[107] F. Albarelli, E. Bisketzi, A. Khan, and A. Datta. Fundamental limits of pulsed quantum light spectroscopy: Dipole moment estimation. Phys. Rev. A, 107(6):062601, 2023.

[108] A. Khan, F. Albarelli, and A. Datta. Does entanglement enhance single-molecule pulsed biphoton spectroscopy? Quantum Sci. Technol., 9(3):035004, 2024.

[109] P. J. Mosley, J. S. Lundeen, B. J. Smith, P. Wasylczyk, A. B. U'Ren, C. Silberhorn, and I. A. Walmsley. Heralded generation of ultrafast single photons in pure quantum states. Phys. Rev. Lett., 100(13):133601, 2008.

[110] P. Hamm and M. Zanni. Concepts and Methods of 2D Infrared Spectroscopy. Cambridge University Press, 2011. Published in New York.

[111] P. Rebentrost, M. Mohseni, I. Kassal, S. Lloyd, and A. Aspuru-Guzik. Environment-assisted quantum transport. New J. Phys., 11(3):033003, 2009.

[112] V. Novoderezhkin, A. Marin, and R. van Grondelle. Intra- and inter-monomeric transfers in the light harvesting LHCII complex: the Redfield-Forster picture. Phys. Chem. Chem. Phys., 13(38):17093–17103, 2011.

[113] C. Cohen-Tannoudji, J. Dupont-Roc, and G. Grynberg. Photons and Atoms-Introduction to Quantum Electrodynamics. John Wiley & Sons, Ltd, 1997.

[114] R. L. Cook. Continuous measurement and stochastic methods in quantum optical systems. PhD thesis, University of New Mexico, 2013.

[115] B. Q. Baragiola, L. M. Norris, E. Montaño, P. G. Mickelson, P. S. Jessen, and I. H. Deutsch. Three-dimensional light-matter interface for collective spin squeezing in atomic ensembles. Phys. Rev. A, 89(3):033850, 2014.

[116] C. W. Gardiner. Handbook of stochastic methods springer-verlag. New York, 1983.

[117] J. Gough. Quantum Stratonovich calculus and the quantum Wong-Zakai theorem. J. Math. Phys., 47(11):113509, 2006.

[118] A. Ishizaki, T. R. Calhoun, G. S. Schlau-Cohen, and G. R. Fleming. Quantum coherence and its interplay with protein environments in photosynthetic electronic energy transfer. Phys. Chem. Chem. Phys., 12(27):7319–7337, 2010.

[119] T. Renger, A. Klinger, F. Steinecker, M. Schmidt am Busch, J. Numata, and F. Müh. Normal mode analysis of the spectral density of the Fenna–Matthews–Olson light-harvesting protein: how the protein dissipates the excess energy of excitons. J. Phys. Chem. B, 116(50):14565–14580, 2012.

[120] J. Rammer. Quantum Field Theory of Non-equilibrium States. Cambridge University Press, 2007.

[121] R. Kubo. Generalized cumulant expansion method. J. Phys. Soc. Jpn., 17(7):1100–1120, 1962.

[122] D. I. G. Bennett, K. Amarnath, and G. R. Fleming. A structure-based model of energy transfer reveals the principles of light harvesting in Photosystem II supercomplexes. J. Am. Chem. Soc., 135(24):9164–9173, 2013.

[123] C. Kreisbeck, T. Kramer, M. Rodriguez, and B. Hein. High-performance solution of hierarchical equations of motion for studying energy transfer in light-harvesting complexes. J. Chem. Theory Comput., 7(7):2166–2174, 2011.

[124] H. D. Zhang, Q. Qiao, R. X. Xu, and Y. J. Yan. Effects of herzberg–teller vibronic coupling on coherent excitation energy transfer. J. Chem. Phys., 145(20):204109, 2016.

[125] E. A. Arsenault, A. J. Schile, D. T. Limmer, and G. R. Fleming. Vibronic coupling in light-harvesting complex ii revisited. J. Chem. Phys., 155(9):096101, 2021.

[126] Y. Kano and E. Wolf. Temporal coherence of black body radiation. Proc. Phys. Soc. (1958-1967), 80(6):1273, 1962.

[127] Y. Wang, J. Minář, L. Sheridan, and V. Scarani. Efficient excitation of a two-level atom by a

single photon in a propagating mode. Phys. Rev. A, 83(6):063842, 2011.

[128] ASTM G03.09. Standard tables for reference solar spectral irradiances. ASTM International G173, 14.01, 2012. "Standard Tables for Reference Solar Spectral Irradiances".

[129] In Ref. [109], two identically prepared single photons produce a Hong-Ou-Mandel dip of 92 fs FWHM. Assuming Gaussian temporal profiles, $\tau_{\text{pulse}} = \text{FWHM}/(4\sqrt{\ln 2})$ (see for example [67]).

[130] Y. Tanimura. Numerically exact approach to open quantum dynamics: The hierarchical equations of motion (HEOM). J. Chem. Phys., 153(2):020901, 2020.

[131] M. A. Palacios, F. L. de Weerd, J. A. Ihalainen, R. van Grondelle, and H. van Amerongen. Superradiance and exciton (de)localization in light-harvesting complex II from green plants? J. Phys. Chem. B, 106(22):5782–5787, 2002.

[132] R. Monshouwer, M. Abrahamsson, F. van Mourik, and R. van Grondelle. Superradiance and exciton delocalization in bacterial photosynthetic light-harvesting systems. J. Phys. Chem. B, 101(37):7241–7248, 1997.

[133] S. Savikhin, D. R. Buck, W. S. Struve, R. E. Blankenship, A. S. Taisova, V. I. Novoderezhkin, and Z. G. Fetisova. Excitation delocalization in the bacteriochlorophyll c antenna of the green bacterium chloroflexus aurantiacus as revealed by ultrafast pump-probe spectroscopy. FEBS Lett., 430(3):323–326, 1998.

[134] A. Yakovlev, V. Novoderezhkin, A. Taisova, and Z. Fetisova. Exciton dynamics in the chlorosomal antenna of the green bacterium chloroflexus aurantiacus: experimental and theoretical studies of femtosecond pump-probe spectra. Photosynth. Res., 71(1):19–32, 2002.

[135] V. I. Prokhorenko, D. B. Steensgaard, and A. R. Holzwarth. Exciton dynamics in the chlorosomal antennae of the green bacteria chloroflexus aurantiacus and chlorobium tepidum. Biophys. J., 79(4):2105–2120, 2000.

[136] T. Malina, R. Koehorst, D. Bína, J. Pšenčík, and H. van Amerongen. Superradiance of bacteriochlorophyll c aggregates in chlorosomes of green photosynthetic bacteria. Sci. Rep., 11(1):8354, 2021.

[137] O. Varnavski, S. K. Giri, T. M. Chiang, C. J. Zeman IV, G. C. Schatz, and T. Goodson III. Colors of entangled two-photon absorption. Proc. Natl. Acad. Sci. U.S.A., 120(35):e2307719120, 2023.

[138] A. Mikhaylov, R. N. Wilson, K. M. Parzuchowski, M. D. Mazurek, C. H. Camp Jr., M. J. Stevens, and R. Jimenez. Hot-band absorption can mimic entangled two-photon absorption. J. Phys. Chem. Lett., 13(6):1489–1493, 2022.

[139] J. Hofkens, M. Cotlet, T. Vosch, P. Tinnefeld, K. D. Weston, C. Ego, A. Grimsdale, K. Müllen, D. Beljonne, J. L. Brédas, et al. Revealing competitive förster-type resonance energy-transfer pathways in single bichromophoric molecules. Proc. Natl. Acad. Sci. U.S.A., 100(23):13146–13151, 2003.

[140] T. Adachi, J. Vogelsang, and J. M. Lupton. Chromophore bending controls fluorescence lifetime in single conjugated polymer chains. J. Phys. Chem. Lett., 5(12):2165–2170, 2014.

[141] R. W. Boyd. Nonlinear optics. Academic press, 2020.

[142] A. Nitzan. Chemical Dynamics in Condensed Phases: Relaxation, Transfer, and Reactions in Condensed Molecular Systems. Oxford Graduate Texts. OUP Oxford, 2013.

[143] D. A. Steck. Quantum and Atom Optics. available online at `http://steck.us/teaching` (revision 0.13.9, 22 July 2021).

[144] M. E. Peskin and D. V. Schroeder. An Introduction To Quantum Field Theory. Frontiers in Physics. Avalon Publishing, 1995.

[145] Z. Liu, H. Yan, K. Wang, T. Kuang, J. Zhang, L. Gui, X. An, and W. Chang. Crystal structure of spinach major light-harvesting complex at 2.72 Å resolution. Nature, 428(6980):287–292, 2004.

[146] Z. Liu, H. Yan, K. Wang, T. Kuang, J. Zhang, L. Gui, X. An, and W. Chang. Crystal structure of spinach major light-harvesting complex at 2.72 angstrom resolution. doi:10.2210/pdb1rwt/pdb, 2004.